MAGNETISM AND SPIN TRANSPORT STUDIES ON INDIUM TIN OXIDE

Ali Moraad Hakimi

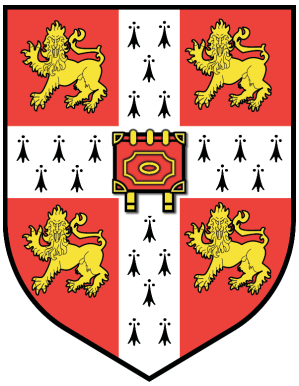

Darwin College

University of Cambridge

A dissertation submitted for the degree of Doctor of Philosophy
at the University of Cambridge

February 2011

In loving memory of my Grandfathers, Cyrus and Peter

Abstract

This dissertation reports on a detailed systematic study of the investigation into using Indium Oxide based materials in next generation spin-transport electronic applications.

Initial studies focused on the optimisation of the electrical properties of Indium Oxide (In_2O_3) and Tin(Sn)-doped Indium Oxide (ITO) thin films grown using DC magnetron sputtering. The manipulation of various deposition parameters allowed the electrical properties to be tuned effectively.

With the desire to create multi-functional spintronic devices, a dilute magnetic oxide system is developed where the In_2O_3 and ITO matrices are doped with low levels of transition metals, in particular, Co. Using a number of characterisation techniques, the origins of the magnetic response in these thin films is explored in great detail. In particular, powerful probes such as x-ray and optical magnetic circular dichroism are utilised. The major finding from these investigations is that the magnetism does not necessarily emanate from the Co dopants alone. In fact, Co dopants give a strictly paramagnetic response, suggesting that the magnetism observed may be a result of polarised electrons in localised donor states in the In_2O_3 and ITO hosts. Therefore, we believe that the origins of magnetism in these films is related to a hybridisation and charge transfer of electrons from a broad donor/defect-derived impurity band to a band of unoccupied $3d$ states at the Fermi level. The emergence of a very weak magnetic signal in pure ITO raises further questions as to the true origins of the ferromagnetic behaviour and supports a defect-related mechanism.

To explore the suitability of ITO for a future in spintronics further, the performance of some metal ferromagnet/oxide multilayered structures was investigated. The investigations revealed a significant contribution to both the magnetic and magneto-transport properties from a superparamagnetic component giving some insight into the importance of the quality of interfaces between the metal ferromagnet/oxide layers and heterostructures.

Using a three-dimensional focused-ion beam etching technique to fabricate submicron spin-valve devices with ITO spacer layers, current-perpendicular-to-plane magnetoresistance measurements were carried out to estimate the spin diffusion length of ITO at room temperature. In conjunction with a simplified Valet-Fert model, a spin asymmetry ratio for Co of 0.55 and spin diffusion length of 6 ± 1 nm in semiconducting ITO at room temperature was estimated. These findings imply that spin information can be conserved and transported through In_2O_3 and ITO even up to and beyond room temperature.

Preface

This dissertation is submitted for the degree of Doctor of Philosophy at the University of Cambridge. Except where specific references are made, this work is entirely the result of my own work and includes nothing that is the outcome of work done in collaboration. No part of this work has been, or is being submitted for any other qualification at this, or any other university. This dissertation does not exceed 60,000 words.

Some of the significant results and interpretations derived in this work have been published or submitted for publication and presented at international conferences, as listed below. Original copies of these papers are reproduced in the appendix.

- "Estimation of the spin diffusion length of semiconducting Indium Tin Oxide using Co/Indium Tin Oxide/Co spin valve junctions"
  A. M. H. R. Hakimi, N. Banerjee, A. Aziz, J. W. A. Robinson, M. G. Blamire, Applied Physics Letters **96**, 102514, (2010).

- "Origin of magnetism in Cobalt-doped Indium Tin Oxide thin films"
  A. M. H. R. Hakimi, F. Schoofs, R. Bali, N. A. Stelmashenko, M. G. Blamire, S. Langridge, S. A. Cavill, G. van der Laan, S. S. Dhesi Physical Review B, (2010).

- "Probing the origins of magnetism in Dilute Magnetic Oxides"
  A. M. H. R. Hakimi and S. S. Dhesi, Diamond Light Source Annual Report, (2011).

- "Role of Superparamagnetism in [Co/ITO] multilayers"
  A. M. H. R. Hakimi, M. Egilmez, J. W. A. Robinson, F. Schoofs, S. L. Sahonta, M. G. Blamire, submitted, (2011).

- "Donor band ferromagnetism in cobalt-doped indium oxide"
  A. M. H. R. Hakimi, M. G. Blamire, S. M. Heald, M. Alshammari, M. Al-Qahtani, D. S. Score, H. J. Blythe, A. M. Fox and G. A. Gehring, submitted, (2011).

- "Indium Tin Oxide thin films for Spintronics"
  A. M. H. R. Hakimi, N. Banerjee, A. Aziz, J. W. A. Robinson, F. Schoofs, M. G. Blamire, S. A. Cavill, G. van der Laan, S. S. Dhesi, 17th Workshop on Oxide Electronics, Poster Session, Awaji Island, Japan, (2010)

Collaborations with other members of the Device Materials Group have been fruitful and I have been lucky enough to be part of some other peer-reviewed articles;

- "Strain dependent defect mediated ferromagnetism in Mn-doped and undoped ZnO thin films"
  F. Schoofs, T. Fix, **A. M. H. R. Hakimi**, S. S. Dhesi, G. van der Laan, S. A. Cavill, S. Langridge, J. L. MacManus-Driscoll, M. G. Blamire, J. Appl. Phys. 108, 053911, (2010).

- "Origin of Magnetism in La and Fe doped $SrTiO_{3-\delta}$ films"
  M. Egilmez, G. W. Leung, **A. M. H. R. Hakimi**, M. G. Blamire, J. Appl. Phys. 108, 123912, (2010).

Acknowledgements

The list of people who have supported me throughout these years is endless. I convey my utmost appreciation to all those I speak of. In particular, I must thank my supervisor Mark Blamire for his guidance throughout. Other members of the Device Materials Group and beyond who deserve a special mention are Nadia Stelmashenko, Jason Robinson, Mehmet Egilmez, Stuart Wimbush and Mary Vickers who have all helped me with many scientific issues since I started working in the group. The office of Room 221 has also seen some real characters passing through and I am happy to say that I have made some dear friends during my time here - Rantej Bali, Sophie Harrington, Jamie Young and Niladri Banerjee (along with Frank Schoofs who wishes he was in Room 221) have been wonderful to both socialise and work with. I also thank the Engineering and Physical Science Research Council and the Magnetism Group from the Institute of Physics for their generous financial support.

I have spent many of my days here in Cambridge either on a football pitch or Real tennis court. I therefore thank the Cambridge University Association Football Club, Darwin College Football Club, Cambridge University Press Football Club and the Cambridge University Real Tennis Club as well as the British Real Tennis Academy for being such an excellent source of distraction.

A healthy portion of the work in this thesis has been performed in laboratories elsewhere in the country. Our visits to Diamond Light Source were extremely valuable and I thank all at Beamline IO6 for their devoted help, in particular Sarnjeet Dhesi. My collaboration with the Magnetic Oxides group at the University of Sheffield under the close supervision of Gillian Gehring has been extremely rewarding. I have spent a great deal of time with them in Sheffield and thank them for always making me feel so welcome and making our collaboration so fruitful. Gillian in particular has been a wonderful source of knowledge and inspiration over the last one and a half years or so. Sean Langridge has also been extremely kind in measuring a number of samples on the SQUID in my absence at the Rutherford Appleton Laboratory.

I would also like to extend my gratitude to the Pearson family for being so good to me during my time in Cambridge. In particular, I would like to offer my love and appreciation to their wonderful daughter Laura.

This ramble would not be complete without me giving thanks to my wonderful family. I have been away from them now for over 7 years and am grateful for their patience in waiting for me to come home. That thought alone has been one of the special things which has kept me going for all these years of study. My mother and father have supported me throughout and I cannot thank them enough.

AMHR Hakimi
February 2011

Contents

Chapter 1

Introduction

1.1 Setting the scene: Motivation for *Spintronics*

The concept of transparent conducting oxide films was born out of the discoveries made by Badeker [1] over one hundred years ago. Since then, these materials have formed integral components in a wide variety of modern day optoelectronic applications such as liquid crystal displays and transparent electrodes of solar cells. In order to achieve the simultaneous occurrence of high optical transmittance within the visible region together with good electrical conductivity, an electron degeneracy must be created within the band gap, usually obtained via the introduction of non-stoichiometry and/or appropriate dopants. Tin-doped Indium Oxide, commonly know as Indium Tin Oxide (ITO), has been in practical use for most transparent optoelectronic applications for many years now.

The relentless drive for greater information storage capacity in physically smaller devices has pushed the size of components to scales where quantum mechanical effects become important. To aid such an increase in information density, both the electron spin and charge are exploited in the field of spin transport electronics; hence the portmanteau *spintronics*. The basic idea is to combine the characteristics of existing magnetic devices with semiconductor devices in order to realise a new generation of devices that are much smaller, more energy efficient, non-volatile, and much faster than presently available [2,3]. Spintronics may lead to devices such as spin-polarised LEDs, spin-field effect transistors, and spin-based qubits for quantum computers. The key requirement in the development of such devices is an efficient injection, transfer and detection of spin-polarised current from a ferromagnetic material into a semiconductor. Due to the well known problem of a resistance mismatch at metal/semiconductor interfaces, hindering an effective spin injection, much interest now concentrates on the development of room-temperature ferromagnetic semiconductors [4]. A candidate class of materials are the dilute magnetic semiconductors (DMS), in which magnetic moments are incorporated into a semiconducting lattice.

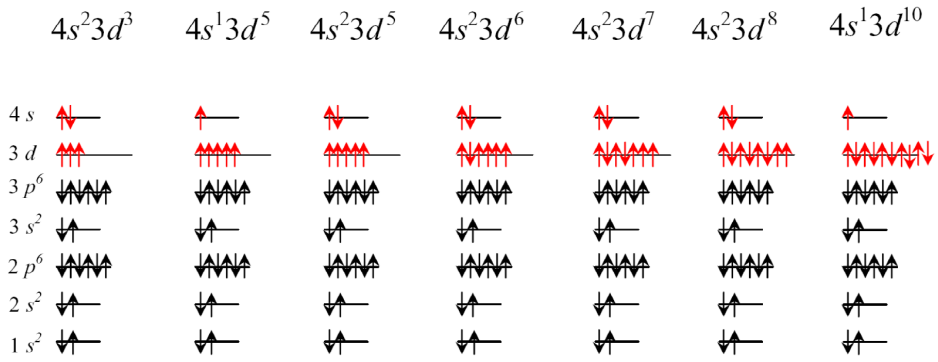

Figure 1.1: Electronic configuration of the $3d$-states and $4s$-states of transition metal elements (from right to left: V to Cu).

1.2 Dilute Magnetic Semiconductors

A DMS is a compound with properties intermediate between a non-magnetic semiconductor and a magnetic element, and is obtained by doping a non-magnetic semiconductor with transition metal (TM) elements (elements with valence electrons corresponding to the $4s$ orbital with a partially filled $3d$ shell). Figure 1.1 illustrates the electronic configuration of these states for the TM elements. A DMS is characterised by the random substitution of a fraction of the original host semiconducting atoms by a homogeneous or "uniform" dilute concentration of magnetic impurity atoms. Since one cannot normally get an ordered distribution of dopants, homogeneous or uniform essentially means a statistically uniform dopant distribution wherein the number distribution of near neighbour dopant-dopant separation is not too broad. These mixed crystal systems may essentially be considered as two interacting subsystems. The first of these is the system of delocalised conduction and valence band electrons. The second is the random, diluted system of localised magnetic moments associated with the magnetic atoms. A "true" DMS is one in which the magnetic dopant spins retain remanent alignment in the presence of spin polarised carriers.

Figure 1.2 depicts the simple idea behind a DMS. The coupling between localised magnetic moments leads to the existence of a number of magnetic phases. Mechanisms that control the ferromagnetic ordering in these materials are therefore dictated by the properties of the magnetic impurities. Coupling interactions between moments will generally depend on the location of the dopants within the host lattice, the doping properties of the impurities as well as on other dopants and defects that may be present within the material.

A DMS should ideally offer the following [5];

- Ferromagnetic Curie temperature greater than 500 K
- A close connection between the ferromagnetism and the population of a spin-split

band of carriers

- A choice of p- or n-type doping
- High mobility and long spin diffusion length
- Magneto-optic effects including magnetic circular dichroism
- Anomalous Hall effect.

The discovery of carrier-mediated ferromagnetism in Mn-doped GaAs ($Mn_xGa_{1-x}As$ or GaMnAs) revamped the field of DMSs and created renewed interest in discovering new and novel DMSs [6]. However, GaMnAs, and indeed other so-called DMS systems (other TM-doped III-V semiconductors) are limited by their low ferromagnetic Curie temperature ($T_C \approx 170$ K) and so their practical applications are limited. The quest for new high-T_C DMSs was given a breath of new life after pioneering theoretical predictions based on the Zener mean-field model of ferromagnetism [7] by Dietl *et al.* [8]. Here it was predicted that the T_c of DMSs could be increased above room temperature for p-type DMSs, and that ferromagnetism would be stable in DMSs based on wide-bandgap semiconductors, i.e. ZnO and GaN.

Soon after, several oxide-based DMS (DMO) have been reported to be robust, room temperature ferromagnets. In particular, Matsumoto *et al.* claimed intrinsic ferromagnetism in Co-doped TiO_2 thin films grown using pulsed laser deposition [9,10]. These results prompted extensive experimental work and theoretical studies on other oxide systems such as ZnO (see chapter 5 and references within), SnO_2 [11–14], (La,Sr)TiO_3 [15] and In_2O_3 (see chapter 5 and references within), however, the most heavily studied are those of Co- and Mn-doped ZnO and Co-doped TiO_2. Although a considerable amount of experimental data and corresponding mechanisms have been accumulated over recent years, the origins of the ferromagnetic ordering in DMOs still remain unclear. Early experiments relied on simple magnetic characterisation using superconducting quantum interference device magnetometry to classify the validity of the DMO. However, it is difficult to distinguish "intrinsic" ferromagnetism from that which is "extrinsic", such as ferromagnetic precipitations or secondary phases because all the magnetisation signals are measured together, i.e. it is a volume sensitive measurement. Therefore, magnetisation alone is not enough to verify intrinsic magnetism. Thus, it is critical to distinguish those which are true DMOs from those which merely show magnetic hysteresis.

One of the most troubling issues surrounding this area of research is the disparity of results obtained by different laboratories across the world. It has become acceptable to acknowledge the fact that the magnetic properties of these materials are strongly dependent on the conditions in which they were prepared. As a result, the properties are not even entirely reproducible from one growth to another, even in the same laboratory. Therefore, the field is starving for a universal, unified theory which can shed

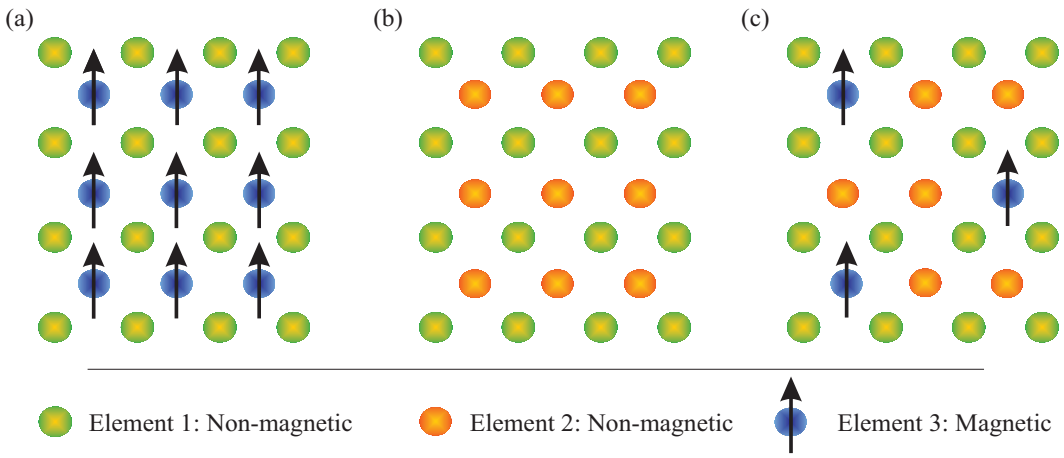

Figure 1.2: Illustration of the basic idea behind a dilute magnetic system: (a) a magnetic semiconductor exhibiting ferromagnetism due to carrier mediated alignment of a periodic array of impurity transition metal dopants, (b) a non-magnetic semiconductor which contains no magnetic ions, and (c) a dilute magnetic semiconductor where only a small fraction of the host semiconductor sites are substituted by transition metal dopants. Adapted from reference [6].

light on some of these unanswered questions.

1.3 Thesis Overview

Given its tried and tested practical use, Indium oxide-based materials form the basis for the developing field of transparent spintronics as well as the theme of this thesis. Having introduced the dilute magnetic semiconductor and oxide family, this dissertation proceeds further by reminding the reader of some of the basic principles of magnetism. In addition, a brief history is given of the numerous theories which have been proposed in recent years to aid the understanding of magnetism in the dilute magnetic semiconductor and oxide systems. The experimental procedures and measurement techniques used to characterise the materials are described in chapter 3.

Chapters 4 through to 10 contain a mixture of background and first principles and experimental results. Because the nature of the work presented here is rather diverse, it was decided that it would be better to introduce the important concepts in each chapter as a prerequisite to the results. Therefore, chapter 4 is concerned with the basic introduction to the Indium Oxide system and a systematic study into the electrical properties of the material as a function of various deposition parameters and extrinsic doping. Chapter 5 is an account of the struggle to develop a dilute magnetic oxide system using Indium Oxide and ITO, and also touches upon the controversies surrounding the field. Following the development of an adequate DMO, powerful probes such as synchrotron radiation x-ray (chapter 6) and optical (chapter 7) magnetic circular dichroism techniques were used to try and better understand the origins of magnetism

in these materials. The last three chapters describe the gradual transition toward integration of Indium Oxide based materials into spintronic devices. Ferromagnetic metal/oxide multilayers (chapters 8 and 9) and spin valve junctions (chapter 10) show the potential of Indium Tin Oxide based materials for future spintronic applications. The thesis is summarily closed in chapter 11 before suggesting some potential avenues that this area of research may wish to take in the near future (chapter 12).

Bibliography

[1] K. Badeker, Ann. Phys. (Leipzig) **22**, 749, (1907).

[2] S. Datta and B. Das, Appl. Phys. Lett. 56, 665, (1990).

[3] S. A. Wolf, D. D. Awschalom, R. A. Buhrman, J. Daughton, S. von Molnar, M. L. Roukes, A. Y. Chtchelkanova, D. M. Treger Science, 294, 1488, (2001).

[4] G. Schmidt, D. Ferrand, L. W. Molenkamp, B. J. van Wees, Phys. Rev. B. 62, R4790, (2000).

[5] J. M. D. Coey, Curr. Opin. Solid State and Materials Science 10, 8392, (2006).

[6] H. Ohno Science, 281, 951, (1998).

[7] C. Zener, Physics Review, 81, 440 (1951); 82, 403, (1995).

[8] T. Dietl, H. Ohno, F. Matsukura, J. Cibert, D. Ferrand, Science 287, 1019, (2000).

[9] Y. Matsumoto, M. Murakami, T. Shono, T. Hasegawa, T. Fukumura, M. Kawasaki, P. Ahmet, T. Chikyow, S.-Y. Koshihara, H. Koinuma, Science 291, 854, (2001).

[10] Y. Matsumoto, M. Murakami, K. Hasegawa, T. Fukumura, M. Kawasaki, P. Ahmet, K. Nakajima, T. Chikyow, H. Koinuma, Appl. Surf. Sci. 189, 344, (2002).

[11] N. H. Hong, J. Sakai, W. Prellier, A. Hassini, J. Phys.: Condens. Matter 17, 1697-1702, (2005).

[12] N. H. Hong, J. Sakai, N. T. Huong, N. Poirot, A. Ruyter, Phys. Rev. B 72, 045336, (2005).

[13] S. B. Ogale, R. J. Choudhary, J. P. Buban, S. E. Lofland, S. R. Shinde, S. N. Kale, V. N. Kulkarni, J. Higgins, C. Lanci, J. R. Simpson, N. D. Browning, S. Das Sarma, H. D. Drew, R. L. Greene, T. Venkatesan, Phys. Rev. Lett. 91, 7, (2003).

[14] K. Gopinadhan, D. K. Pandya, S. C. Kshyap, S. Chaudhary, J. Appl. Phys. 99, 126106, (2006).

[15] S. X. Zhang, W. Yu, S. B. Ogale, S. R. Shinde, D. C. Kundaliya, W. K. Tse, S. Y. Young, J. S. Higgins, L. G. Salamanca-Riba, M. Herrera, L. F. Fu, N. D. Browning, R. L. Greene, T. Venkatesan, Phys. Rev. B 76, 085323, (2007).

Chapter 2

Background Theory and First Principles

This chapter introduces some of the fundamental physics which govern the phenomena investigated in this volume of work. The majority of the physical concepts explained in the following sections have been formulated using references [1], [2] and [3]. More detailed descriptions of specific effects will be described in subsequent chapters.

2.1 Origins of Magnetism

Magnetism is a quantum mechanical phenomenon in which it is known that the magnetic properties arise from spin magnetic moments contributing to an overall molecular field. There are three principal sources of a magnetic moment in a free atom: electron spin, orbital angular momentum about the nucleus and change in orbital momentum with an applied magnetic field [1]. An orbiting electron has a spin quantum number, s, and angular momentum quantum number, l, which can be summed over all electrons in an atom to calculate its total orbital moment, L, and spin angular moment, S, respectively.

The Pauli exclusion principle states that no two fermions can simultaneously occupy the same quantum state. This becomes significant when considering the exchange interactions between atoms and how electron orbitals overlap. It is also important to consider Hund's rules, which govern how useful energy interactions dictate the ground state terms. Using these rules, one can calculate the values for J, the total angular momentum, L and S for the ground states of the transition metal ions.

Therefore, to summarise, the universal origin of magnetism is almost always the interplay between the electronic spin degree of freedom, the repulsive Coulomb interactions between electrons, and the fermionic quantum statistics of electrons. However, one universal theory of magnetism is yet to be agreed upon as it continues to be amongst one of the most challenging of solid-state physics problems.

2.1.1 Magnetic materials

The magnetic moment per unit volume of a material is defined as $\vec{M}$ and the macroscopic field within the material is defined as $\vec{H}$. The magnetic susceptibility, χ, describes the ability of a material to become magnetised and is defined as

$$\chi = \frac{\vec{M}}{\vec{H}}. \tag{2.1}$$

The permeability, μ, is a material property that defines the degree to which a material's magnetisation responds to a linear magnetic field. The induced magnetic field, $\vec{B}$, is the net magnetic effect from an externally applied magnetic field. When in the presence of a magnetic material, the external magnetic field is made up of contributions from the current elements and the magnetic material such that

$$\vec{B} = \mu_0\vec{H} + \mu_0\vec{M} = \mu_0\vec{H} + \mu_0\chi\vec{H}. \tag{2.2}$$

The relative permeability of the material, μ_r, is the ratio of a material's permeability, μ, to that of free space, μ_0 (which is constant). It is known that μ_r is equal to $1 + \chi$. Therefore, we now have

$$\vec{B} = \mu_0\vec{H}(1 + \chi) = \mu_r\mu_0\vec{H}. \tag{2.3}$$

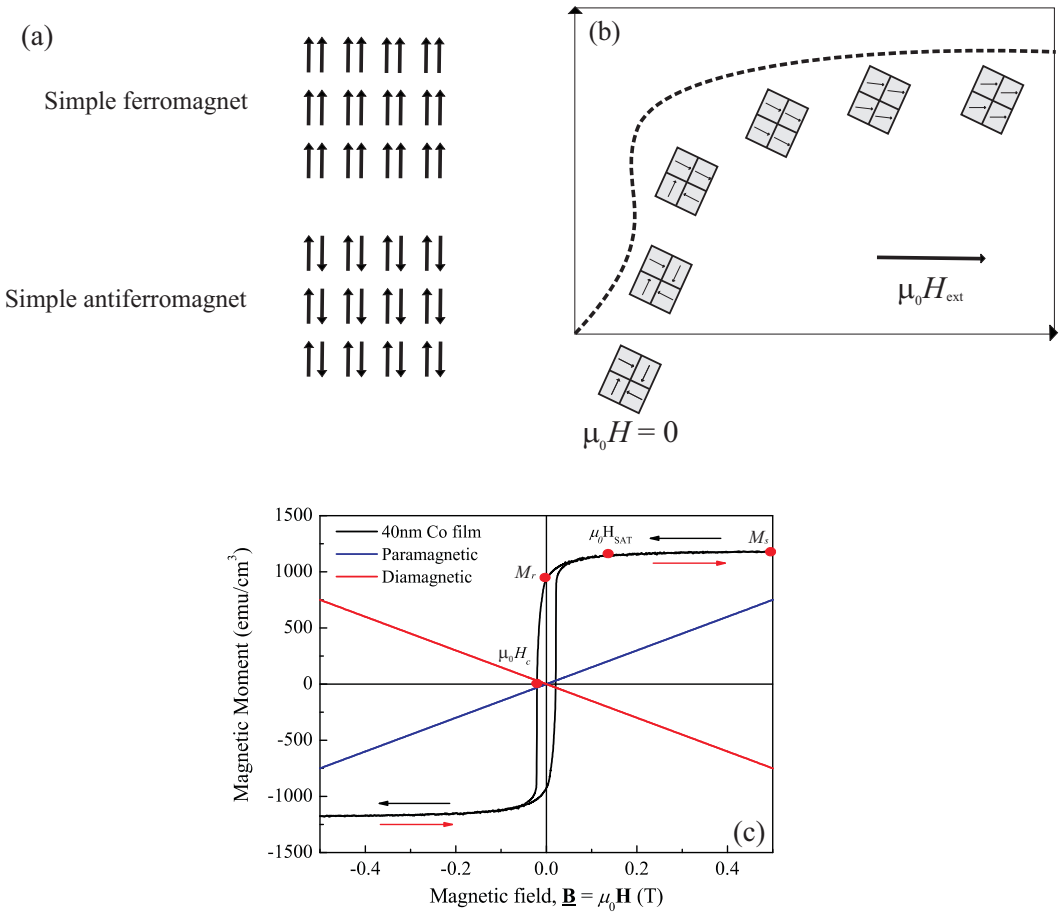

Figure 2.1: (a) Illustration of the typical dipole alignments in ferromagnetic (top) and antiferromagnetic (bottom) materials using a linear array of localised moments; (b) Schematic illustration of the process of domain rotation within an applied field which gives a magnetic hysteresis; (c) Typical responses to an applied magnetic field for a ferromagnetic (40 nm thick Co film, solid black line), paramagnetic (solid blue line) and diamagnetic (solid red line) materials. As the external magnetic field (μ_0H) is increased, the induced magnetic moment also increases. The induced magnetisation eventually saturates at a point M_s. Upon reversal of the external field the material retains a certain permanent magnetisation termed the remanant magnetisation, M_r. The value of the reversed field when the sample is fully demagnetised is called the coercive field, $\mu_0 H_c$.

The values of μ_r and χ can be used to classify magnetic materials which can be summarised in the following points:

- χ is small and negative, typically $\chi \approx$ - 10^{-5}. These materials are *diamagnetic*. This occurs when an external magnetic field is applied to a material, causing an induced electromotive force (e.m.f) to accelerate the material's electrons. When the field is constantly applied, the induced e.m.f returns to zero, but the current remains. This is because the currents are sufficiently stable to screen the material from the applied magnetic field and so the material has acquired a weak magnetisation which opposes the applied field. A very small diamagnetic moment is induced in all materials, although it will only be observed with no other dipole moments present in an externally applied magnetic field.

- χ is small and positive ($\chi \approx 10^{-5}$ - 10^{-3}). These materials are *paramagnetic*. This is seen in materials in which a number of the atoms possess, in the absence of an applied field, a permanent magnetic dipole moment. However, these moments are randomly orientated and so in the absence of an external field the net magnetisation will be zero. Upon the application of an external field, the moments begin to align with the field and the magnetisation is non-zero. There is competition between the aligning effect of the field and thermal disorder. The material will have, on average, greater alignment with the field than against it so that magnetisation varies linearly with applied magnetic field. As temperature increases, thermal disorder will also increase and so the paramagnetic susceptibility decreases.

- $\chi \gg 1$ and positive ($\chi \approx$ 50 - 10,000). These materials are *ferromagnetic*. The dependence of χ on an applied magnetic field is non-linear in ferromagnetic materials. Ferromagnets also have a spontaneous magnetisation in the absence of an external magnetic field (see section 2.1.3). As with paramagnets, magnetisation occurs due to the alignment of dipoles at low temperatures [Fig. 2.1 (a)]. The difference is that ferromagnets remain ordered to higher temperatures below a ferromagnetic Curie temperature (T_C), indicating that there are stronger exchange interactions present. Below T_C the magnetic moments align and the material is ferromagnetic, whilst above T_c, thermal fluctuations destroy this alignment so the material is paramagnetic.

- χ is small and positive, but with a different magnetic structure and temperature dependence - these materials are classified as *antiferromagnetic*. For an antiferromagnet, exactly half of the dipoles are aligned in one direction and half in the opposite [Fig. 2.1 (a)]. This means that, overall, there is no spontaneous magnetisation. Similar to T_C for ferromagnets, there is a critical temperature, known as the Neel temperature, T_N, above which the moments are disordered

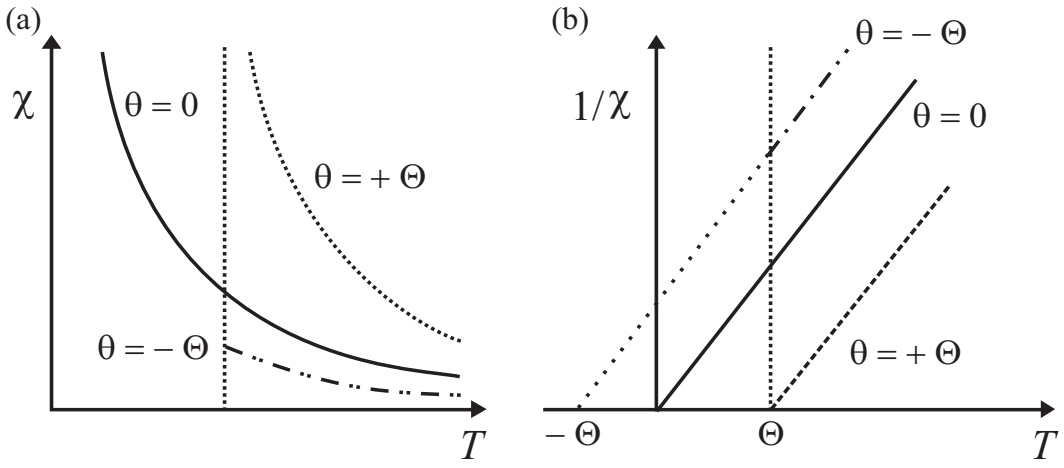

Figure 2.2: The Curie-Weiss law states that $\chi \propto 1$ / (T - θ) for $T > \theta$. This can be found in (a) for each of the three magnetic cases: $\theta = 0$ (paramagnet), $\theta = \Theta > 0$ (ferromagnet) and $\theta =$ - $\Theta < 0$ (antiferromagnet). Plotting $1/\chi$ versus T gives results in straight lines as shown in (b) with the intercept on the temperature axis yielding θ. Adapted from reference [3].

paramagnetically and below which they are alternatively arranged parallel and antiparallel.

2.1.2 Temperature dependence of magnetic susceptibility

The change in the susceptibility χ with temperature can be described by the Curie-Weiss law only for $T > \theta$ (i.e. for temperatures above the transition to magnetic order in the paramagnetic state) and is given in Eqn. 2.4, where C is the Curie constant, T is the absolute temperature and θ is the Curie-Weiss temperature. The relationship is shown graphically in Fig. 2.2.

$$\chi = \frac{C}{T - \theta} \tag{2.4}$$

If;

- $\theta = 0$, the the material is a paramagnet,
- $\theta > 0$, the material is a ferromagnet and we would expect $\theta = T_C$,
- $\theta < 0$, the material is an antiferromagnet and we expect $\theta =$ - T_N (see Fig. 2.2).

2.1.3 Ferromagnetism

According to band theory, the magnetic moment is defined as the number of band states per atom, per unit energy and per spin [4]. Figure 2.3 shows the density of states (DOS) calculated for non-magnetic Cu and strongly ferromagnetic Co metals. The shapes of the DOS in both scenarios are very similar, however, in the case of

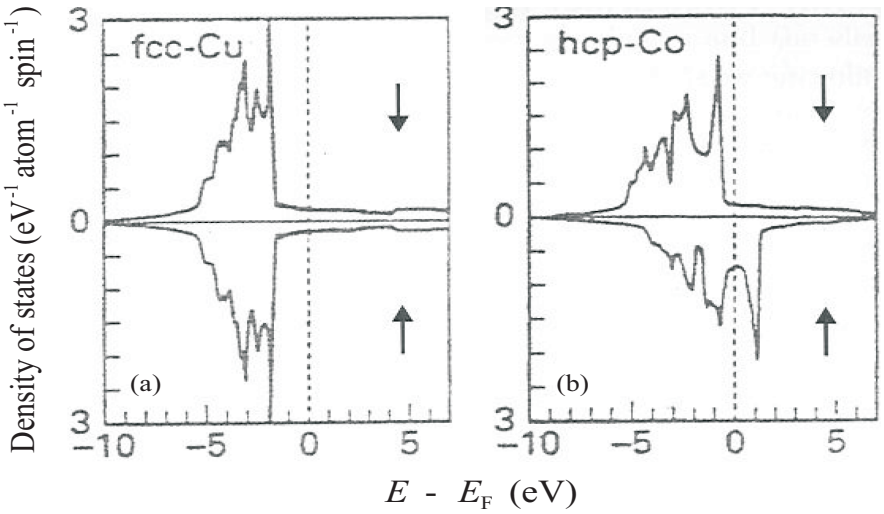

Figure 2.3: Density of states of Cu (a) and Co (b) metals for the majority and minority spins. The Fermi energy E_F is set to zero. Cu is non-magnetic due to the absence of exchange splitting. Co is a strong ferromagnet due to total occupancy of the majority spin band. The dashed line in each figure indicates the different position of the Fermi energy, E_F - it separates the occupied from the unoccupied states. After reference [4].

Cu no exchange splitting is observed, as expected. The exchange splitting, Δ, can be defined as the relative shift of spin-up and -down electron bands. The difference in the number of spin-up and spin-down electrons gives rise to an observed spontaneous magnetisation - ferromagnetism. Via consideration of the energy exchange involved in a resultant spontaneous ferromagnetic signal we can define a condition that must be met before this can occur. This is known as the *Stoner criterion* and is defined as

$$Ug(E_F) \geq 1, \tag{2.5}$$

where U is a measure of the Coulomb energy and $g(E_F)$ is the density of states at the Fermi level. The condition for the ferromagnetic instability requires that the Coulomb effects are strong and the density of states at the Fermi energy is large.

In order to explain the fact that ferromagnetic materials do not remain saturated when the applied field is removed, Weiss [5, 6] introduced the classical concept of magnetic domains which form as a consequence of *energy minimisation*. He proposed that a ferromagnet is divided into regions called "domains", in which the magnetisation within the domain is almost saturated. The magnetisation in different domains is in different directions, so that the magnetisation of a ferromagnetic specimen could be small or even zero. The consequences of this development were [1]:

1. the permanent existence of atomic magnetic moments which make up the magnetic domains and are aligned due to a Weiss mean (or "molecular") field [5],

2. in the demagnetised state, the atomic moments were aligned,

3. the magnetic domains were randomly aligned in the demagnetised state,

4. the magnetisation process involved the reorientation of the magnetic domains to the applied magnetic field.

As point (4) states, M_s is achieved by aligning the magnetisation of each domain with the applied magnetic field [Fig. 2.1 (b)]. A direct consequence of ferromagnetic domains is the existence of a magnetic hysteresis upon the application of an increasing field to a magnetic sample. The process of magnetising a sample to saturation consists of converting it to a single domain system, and can be described as a three-step process:

1. Low-field region - domains orientated favourably with respect to the applied magnetic field may grow, by displacement of domain walls, at the expense of those orientated unfavourably.

2. Intermediate-field region - atomic magnetic moments within an unfavourably aligned domain overcome the anisotropy energy and rotate into a crystallographic "easy" direction nearest to the direction of the applied field. This is called "domain rotation".

3. High-field region - the domains aligned along the preferred easy axis close to the field direction are gradually rotated so they are completely aligned with the applied magnetic field. This occurs as the field is increased as is known as "coherent domain rotation".

Such processes are described by a ferromagnet's hysteresis loop where magnetisation is measured as a function of the applied field and is characterised by four material and system dependent parameters: M_s; M_r; coercive field ($\mu_0 H_c$); and saturation field ($\mu_0 \mathrm{H}_{SAT}$). The magnetisation process and the important parameters can be found in Fig. 2.1 (c).

There is, however, another aspect of the magnetisation process which must be acknowledged. Consider a ferromagnetic body exposed to an external magnetic field. When the magnetisation inside a magnetic body meets the surface it suddenly has to stop. Therefore, we have a divergence in the magnetisation and an equal but opposite effect in the magnetic field. The result is a "demagnetising field". In the scenario of a thin film, if the magnetisation lies in the plane of the film, the only divergence of magnetisation is at the ends, which we assume are an infinite distance away and therefore, there is no demagnetising field. If the field is perpendicular to the film, magnetic poles are created on the top and bottom surfaces and give rise to a demagnetising field. The effect is dependent upon the strength of the magnetisation and geometry of the material.

2.1.4 Superparamagnetism

Superparamagnetism is a rather special scenario. It is a size effect of ferromagnetism, i.e. one cannot reduce the size of magnetic particles indefinitely and still retain useful

magnetic properties [2]. As already explained using Weiss's theory, a ferromagnetic sample divides itself into an array of magnetic domains in order to minimise its energy. Below a certain size, moments are released from their constraints so we can think of the particle as a single-domain structure, where the M_r is no longer fixed in the direction dictated by the particle shape or crystal anisotropy: instead, magnetisation can randomly flip direction under the influence of thermal energy. The reason for the small ferromagnetic particles becoming single-domain is simply due to the fact that the energy *cost* of domain wall formation does not outweigh any *saving* in demagnetising energy. A particle of volume V will need an activation energy equal to KV, where K is a constant which quantifies the energy density associated with the anisotropy, to minimise its energy and thus flip its magnetisation. For very small particles, such that KV is small compared to the thermal energy, $k_B T$, the magnetisation can be easily flipped in this way by thermal fluctuations. If we now consider a distribution of the small ferromagnetic particles throughout a non-magnetic matrix and assume that the particles are far enough apart, then we can also assume that interparticle interactions can be neglected, and for $k_B T \gg KV$, the system will behave like a typical paramagnet [3]. At high enough temperatures the moments on the particles are able to fluctuate rapidly and the relaxation time (the time between spin flips), τ, of the moment on a particle is given by

$$\tau = \tau_0 exp\left(\frac{KV}{k_B T}\right), \tag{2.6}$$

where τ_0 is typically 10^{-9}s. Another important parameter in the determination of superparamagnetic effects is the measuring time, t, of a particular laboratory experimental technique. The detection of superparamagnetism is time-dependent and hence the relationship between τ and t is very important. If $t \gg \tau$ in the absence of an applied magnetic field then the magnetisation of the nanoparticles averages to zero and the system is said to be in the superparamagnetic state. However, if $t \ll \tau$, the magnetisation will not flip during the measurement and will be equivalent to the instantaneous magnetisation. The nanoparticles now appear to be "blocked". A transition between superparamagnetism and blocked states occurs when $t = \tau$.

Similar to a paramagnetic material, the superparamagnetic particles can become aligned and magnetised via the application of an applied external magnetic field, however, they have a magnetic susceptibility somewhere in between a paramagnetic and ferromagnetic material. In the presence of a magnetic field, the magnetisation loop has a characteristic "*s*"- shape [Fig. 2.4 (a)], and can be described well by a Brillouin function;

$$M = M_s \left[\left(\frac{2J+1}{2J}\right) \coth\left[\frac{(2J+1)y}{2J}\right] - \left(\frac{1}{2J}\right) \coth\left(\frac{y}{2J}\right)\right] \tag{2.7}$$

where M_s is the saturation magnetisation, $y = g\mu_B JH/k_B T$ (where g is the Lande g-factor, μ_B is the Bohr magneton, H is the applied magnetic field, k_B is Boltzmann's

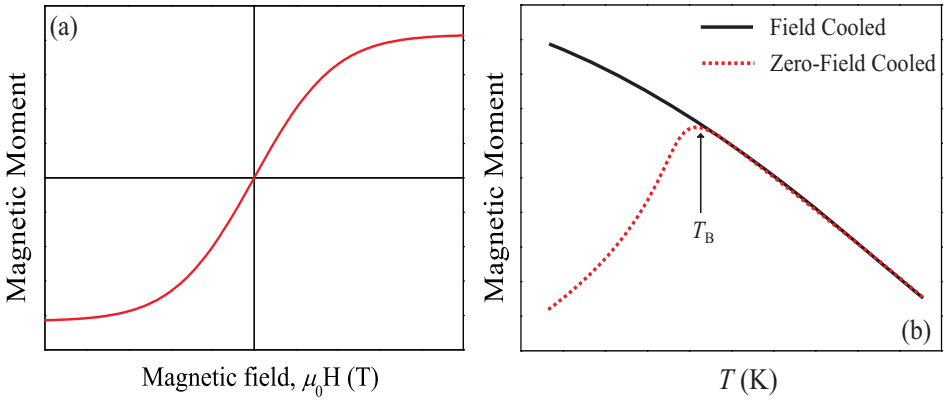

Figure 2.4: (a) Simulated magnetic hysteresis loop for a superparamagnetic sample using the Brillouin function (Eqn. 2.7), (b) Schematic of typical magnetisation versus temperature curves (field- and zero-field cooled) for a superparamagnetic material showing the blocking temperature, T_B, in the zero-field cooled curve only.

constant and T is temperature) and J is the total angular momentum. Important features of the magnetisation loop for a superparamagnet are the distinct absence of hysteresis (low coercive fields) and large saturation fields.

Superparamagnetism can be destroyed by cooling. This follows because the characteristic fluctuation time for a particle's moment varies exponentially with temperature, so the magnetisation appears to switch sharply to a stable state as the temperature is reduced. The temperature at which this occurs is called the blocking temperature (occurs when $t{=}\tau$), T_B, and depends linearly on the sample volume and on the magnitude of the crystal-field anisotropy. T_B is usually identified through field- and zero-field cooling magnetometry [see Fig. 2.4 (b)]. Below T_B the material loses its preferred magnetisation direction in zero field (ZFC) and will begin to average to zero. Through rearrangement of Eqn. 2.6 T_B can be defined as

$$T_B = \frac{KV}{k_B ln\left(\frac{\alpha t}{\tau_0}\right)}. \tag{2.8}$$

Therefore, from Eqn. 2.6 we can see that T_B is dependent on the applied field, particle size as well as the size distribution.

2.1.5 Competing interactions, frustration and randomness

It is not always possible to satisfy all the interactions in a system and settle on a single unique ground state. This results in a variety of similar low energy states distributed around the system and means that energy minimisation is not achieved. As a result, system is now said to show "frustration". This usually occurs in situations where it is not possible to orient a spin on a neighbouring lattice so that the other nearest neighbours can achieve energy minimisation and the system contains a multiplicity of equally unsatisfied states [3].

There are other consequences to energy imbalances within a magnetic system. *Spin glasses* are defined as a random, mixed-interaction magnetic system characterised by a random, yet cooperative, freezing of spins at a well defined temperature, below which no long range magnetic ordering is present. Randomness within the system can be introduced in a number of ways, namely via site- and bond-randomness. Equally important to the inherent randomness of a spin glass is the presence of competing interactions and random anisotropy which may lead to a locally varying easy-axis for magnetisation. Competing interactions will lead to frustration so that there is a multidegenerate ground state. Another feature of spin glass materials is the *cooperative freezing transition* which occurs at a certain temperature, T_f. At high temperature the behaviour of spins within the spin glass material is dominated by thermal fluctuations (in fact, this is true for all magnetic materials) so that the spins can be considered independent. As the temperature cools, the independent spins slow down and start to cluster. Those not in the cluster will help to mediate interactions between clusters. As the temperature nears T_f the fluctuations in the clusters begins to slow down so that interactions between clusters becomes more long range. At T_f the system finds one of its many ground states and freezes. Below T_f the system is said to be "glassy". This is seen in a magnetisation versus temperature curve where there is a divergence between the field cooled and zero-field cooled magnetic susceptibility below T_f.

A signature of both spin glass and superparamagnetic materials is a sharp peak close to either T_f or T_B in the real part of AC susceptibility where the position of the peak should vary with the frequency of the alternating magnetic field.

2.1.6 A quantum description of magnetism

Although Weiss developed a very successful phenomenological theory based on an internal *molecular* field [5], it was not until the advent of quantum mechanics that the origin of the interaction became clear. The interaction responsible for magnetic order is the *exchange interaction*. This interaction results from the fact that electrons are identical and obey the Pauli exclusion principle. Heisenberg showed that a quantum mechanical exchange interaction between neighbouring electrons with overlapping wavefunctions plays a decisive role in explaining ferromagnetism. If we consider two localised electrons on neighbouring atoms with spins i and j, then the Hamiltonian exchange between them is given by;

$$< H >= -2J_{ij}s_i \cdot s_j, \tag{2.9}$$

where J_{ij} is the exchange integral between the i^{th} and j^{th} spins. However, when considering a solid then it is necessary to sum the exchange over all the electrons which can contribute to the energy, so that

$$< H >= -2\sum_{ij} J_{ij}s_i \cdot s_j. \tag{2.10}$$

In most cases, our interest lies only in the nearest-neighbour (n-n) interactions, which simplifies the Heisenberg Hamiltonian

$$< H >= -2J \sum_{n-n} s_i \cdot s_j, \tag{2.11}$$

where it is assumed that the exchange integral J is the same for all nearest-neighbour pairs. If $J < 0$, the lowest energy state results from antiparallel spins (antiferromagnetism). $J > 0$ gives ferromagnetism due to the alignment of spin moments on adjacent atoms. This type of exchange interaction is known as *direct exchange* where electrons on neighbouring magnetic atoms interact with each other.

In many transition metal oxides, magnetic interactions between the transition metal ions are mediated by the conduction electrons and intermediate anions. These types of magnetic coupling are known as *indirect exchange* interactions, which can still be described by the Heisenberg Hamiltonian. These interactions form the basis for the theories used to describe the possible origins of magnetism in the dilute magnetic systems (see next section).

2.2 Existing theories for ferromagnetic origin in DMS and DMO systems

In light of the results mentioned in chapter 1 regarding DMS and DMO materials, many have speculated as to the origins of the magnetic behaviour in these materials. The mechanisms responsible for the origin of ferromagnetism in DMOs are far from being well understood and it is this aspect which makes this area of research so exciting. It was discussed briefly in chapter 1 that in a DMO a sizable portion of atoms are randomly substituted by transition metal elements, giving rise to localised magnetic moments in the oxide host matrix. The presence of magnetic ions affects the free carrier behaviour through an *sp-d* exchange interaction between localised magnetic moments and the spins of the itinerant carriers. However, as we shall see in chapter 5, this simple picture of $3d$ cations with localised moments causing ferromagnetism is now being strongly contested (see section 5.5). Since for dilute concentrations of magnetic dopants the mean separation between neighbouring dopants is larger than that required for any conventional mechanism of ferromagnetic exchange between neighbouring ions to be operative, the occurrence of ferromagnetism in many cases is termed as "carrier" mediated.

This section aims to describe the models that are most commonly used to describe the magnetic interactions in dilute systems. Some, such as the double-exchange interaction, exclusively promote ferromagnetism, whereas the others can result in ferromagnetic or antiferromagnetic interactions, depending on the geometry, defect structure and carrier concentration.

2.2.1 Carrier-mediated exchange

The RKKY model

Early attempts to understand the magnetic behaviour in DMS and DMO systems are based on models in which the local magnetic moments are assumed to interact with each other via Rudeman-Kittel-Kasuya-Yosida (RKKY) interactions [7]. The RKKY model describes the interaction between the delocalised conduction band electrons and a lone, localised magnetic ion. Nearby conduction electrons are duely magnetised by the magnetic ion. These act as an effective field and influence the polarisation of nearby magnetic ions. This polarisation and sign of the exchange interaction, J_{ex}, decays in an oscillatory manner mediating either ferromagnetic or antiferromagnetic coupling depending on the separation of the magnetic ions, r, and the density of electrons, in the following manner;

$$J_{ex}(r) = \frac{m^* k_F^4}{\hbar^2} F(2k_F r) \tag{2.12}$$

where m^* is the effective mass and k_F is the Fermi wavevector of the electron gas. The oscillating function follows Eqn. 2.13

$$F(x) = \frac{x\cos x - \sin x}{x^4}. \tag{2.13}$$

In general, this model is applicable when there is a high concentration of delocalised carriers present in the host oxide.

The Zener-based models

Interested by the interactions between d-shells in the transition metals, Zener explained how direct coupling between d-shells is antiferromagnetic whereas indirect coupling via conduction electrons is ferromagnetic [8]. These $3d$ spin and conduction electron interactions were thought to be long-range.

The origin of ferromagnetism however is more complicated, and cannot be explained by RKKY or Zener-like interactions alone. One of the prominent models is the Zener model of carrier-mediated ferromagnetism developed by Dietl *et al* [9]. It is a mean-field model in which there is a long range ferromagnetic exchange interaction between TM (Mn) spins and p-type hole carriers. The model includes antiferromagnetic superexchange interactions [10] and so goes a step further than simply considering spin and free electrons. It also takes into account the anisotropy of the carrier-mediated exchange interaction associated with the spin-orbit coupling in the host material. It was this theory that predicted that Mn-doped p-type ZnO (and GaN) would have a ferromagnetic Curie temperature above room temperature.

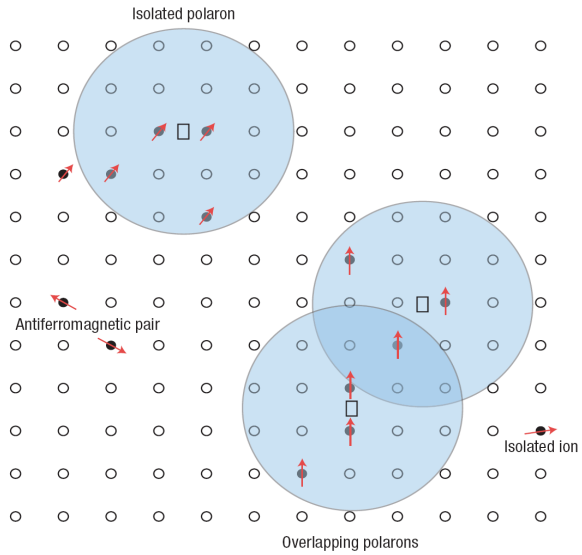

Figure 2.5: Representation of bound magnetic polarons. Cation sites are illustrated by the small open circles. The unoccupied oxygen sites (oxygen vacancies) are represented by the squares. Oxygen is not shown. Impurity ions within a BMP will tend to align to minimise energy. BMPs overlap when their energies align. After Reference [13].

The Double Exchange Model

This model is based on another model proposed by Zener to explain the experimentally observed ferromagnetism in manganite materials [11]. The model is characterised by the *hopping* of electrons between two neighbouring TM ions. In the DMO materials, the $3d$ levels of the TM ions are split by the crystal field into higher energy doublet e_g and lower energy triplet t_{2g} levels (10 electrons are spread over a total of five levels in the d orbital). Spin-up and spin-down states are also split by the exchange splitting. If neighbouring TM ions are aligned in parallel with each other, the electrons in the partially filled $3d$-orbitals of the TM ions are allowed to hop from one ion to the other and stabilise the ferromagnetic ground state.

2.2.2 The Bound Magnetic Polaron Model

The model developed by Dietl *et al.* [9] predicts ferromagnetism arising from a ferromagnetic exchange provided by holes in the conduction band. In most samples however, n-type electron doping is employed and so ferromagnetism is more likely to be mediated by electron carriers.

The bound magnetic polaron (BMP) model is described by the exchange interaction between many localised TM ions spins via a much lower number of weakly localised charge carriers. The localised holes of the polarons act on the TM impurities surrounding them, thus producing an effective magnetic field and aligning all the spins. Therefore, a BMP can be defined as a localised hole centre containing magnetic

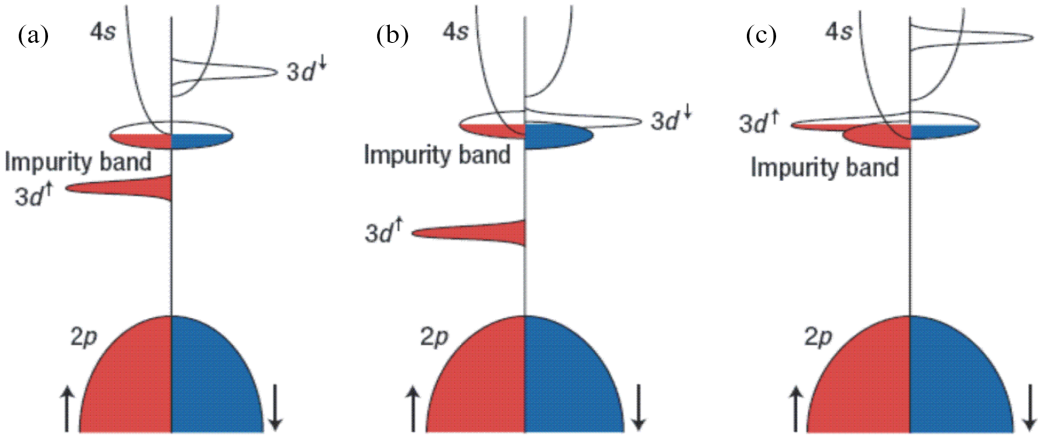

Figure 2.6: Schematic band structure of an oxide with different $3d$ TM impurities. (a) The position of the $3d$ level for low T_c, when the splitting of the impurity band is small. (b) and (c) show positions of the spin-down (b) and spin-up (c) $3d$ levels, respectively, leading to high T_C. After Reference [13].

impurity spins. Overlapping of neighbouring magnetic polarons leads to a long-range ferromagnetic state, and tends to take place more readily if the temperature is decreased so that impurity spins in neighbouring BMPs are aligned. Coey *et al.* applied this model to DMOs [12, 13] and proposed that ferromagnetic exchange coupling of TM ions in n-type DMOs is mediated by the shallow donor electrons trapped by the oxygen vacancies that tend to form BMPs within their hydrogenic orbits (Fig 2.5).

The general formula for the DMOs is;

$$(A_{1-x}M_x)(O \diamond \delta)_n \tag{2.14}$$

where A is a nonmagnetic cation, M is a magnetic TM cation, O is the oxygen, $\diamond$ represents a donor defect and n= 1 or 2. The exchange interaction ΔE_{ex} between the hydrogenic electron and TM cation can be written in terms of the s-d exchange parameter J_{sd} as;

$$\Delta E_{ex} = -J_{sd} S \cdot s |\psi(r)|^2 \Omega \tag{2.15}$$

where S is the spin of the TM cation with a volume $\Omega = (4/3)\pi {r_c}^3$, r_c is the TM cation radius, and s is the spin of donor electron. The wave function of the donor electron in a 1s orbital is given by $\psi(r) = (\pi {r_H}^3)^{-1/2} \exp(-r/r_H)$, where r_H and r are the hydrogenic orbital radius of the donor electron and the distance from the nucleus, respectively.

Therefore, in order to increase the the exchange interaction and ferromagnetic Curie temperature one needs to increase the donor electron density in the vicinity of the TM cation. As the donor defect concentration, δ, increases, the hydrogenic orbitals associated with the defects will begin to overlap to form a spin-split donor impurity band (Fig. 2.6) [13]. At low concentrations, the electrons may remain localised because of the influence of correlations and potential fluctuations in a narrow band, but above

a critical donor concentration the impurity band states would become delocalised. An increasing density of defects would eventually lead to the hydrogenic orbitals associated with the randomly situated defects overlapping. The model implies that high T_c requires hybridisation and charge transfer from a donor-derived impurity band to unoccupied $3d$ states at the Fermi level. This is shown in Fig. 2.6 (b) and (c) where a high T_c is only achieved when empty minority- or majority-spin "d" states lie at the Fermi energy level *within* the impurity band.

The BMP model works on the basis of direct exchange interactions which as has been discussed, we know are antiferromagnetic. However, the interaction between BMPs may be ferromagnetic for sufficiently large concentrations of magnetic impurities.

Courtesy of the BMP model applied to the DMO materials, the knowledge of defects (oxygen vacancies in particular) in DMOs and their influence on the ferromagnetic behaviour became very important.

2.3 Magnetoresistance

Magnetoresistance (MR) is defined as a change in the electrical resistance of a substance in the presence of a magnetic field. The signal response of a device is often characterised by the percentage MR, as shown by Eqn. 2.16, where ΔR is the change in resistance in an applied field (R(H) - $R(0)$) and $R(0)$ is the resistance in the absence of an applied field

$$MR(\%) = \frac{R(H) - R(0)}{R(0)} = \frac{\Delta R}{R(0)}. \tag{2.16}$$

Many different forms of MR have been researched, using a variety of different materials and multilayer architectures. This section will concentrate on the "ordinary" MR effect in metal, semiconducting and doped semiconducting thin films, leaving more specific phenomena such as the giant magnetoresistance (GMR) effect seen in multilayer systems to later chapters of the thesis.

2.3.1 Magnetoresistance of non-magnetic metals and ferromagnets

When a metal carries an electrical current, the displacement of the electrons to different parts of the Fermi surface is such that the scattering is minimised, i.e. the electrons find the path of least dissipation to cross the sample. On application of a magnetic field, the electrons are then forced to take another path which increases the scattering rate and gives a positive MR (increasing R with increasing field). A negative MR can be achieved through application of a magnetic field in the plane of the sample but perpendicular to the current direction which results in reduced electron orbits and

hence scattering.

The situation in ferromagnets however is more complicated and can be visualised by considering the "two-current model" proposed by Mott and involves electrons from the s- and d-bands of the ferromagnet. The band structures and electron behaviour for the s- and d bands are very different. The d-band is very narrow so that the density of states at the Fermi energy level is large and the Stoner criterion is satisfied, and the respective effective masses of the electrons follow ${m_d}^* \gg m_e$. The electrons in the s-bands are nearly free so that ${m_s}^* \sim m_e$. Therefore, the conductivity, σ, defined by

$$\sigma = \frac{n_s e^2 \tau_s}{m_s^*} + \frac{n_d e^2 \tau_d}{m_d^*}, \tag{2.17}$$

will be dominated by the first term and conduction is mainly governed by the s electrons. $n_{s,d}$ are the number of electrons in the s- and d-bands respectively, and $\tau_{s,d}$ are the respective scattering times. The transition probability is therefore due to $s \rightarrow d$ electrons and is strongly temperature dependent. Generally at low temperatures (below T_c) there are few $s \rightarrow d$ transitions due to all unoccupied d-states being antiparallel. At higher temperatures (above T_c), all s electrons can make transitions and there is a rise in the scattering rate. Once a magnetic field is applied the degree of spin polarisation is increased which allows fewer $s \rightarrow d$ transitions, giving a negative MR.

2.3.2 Anisotropic magnetoresistance

Magnetoresistance which depends strongly on the orientation of the magnetisation is known as "anisotropic" magnetoresistance (AMR). Its origins are connected with the spin-orbit interaction and its influence on s-d scattering which leads to anisotropic scattering [3]. It is however, a rather small effect.

Investigating the MR of a system will therefore provide fundamental information about the scattering mechanisms of carriers as well as giving insight into potential technological applications. In particular, in regards to the origins of magnetism in the DMO materials, any distinctive magnetotransport results might be used as a way of identifying interactions, such as those between s-like conduction electrons and $3d$ localised magnetic ions.

Bibliography

[1] D. Jiles, Introduction to Magnetism and Magnetic Materials, Second Edition, Chapman & Hall, (1998).

[2] R. C. O'Handley, Modern Magnetic Materials - Principles and Applications, John Wiley & Sons, Inc. (1999).

[3] S. Blundell, Magnetism in Condensed Matter, Oxford University Press, Oxford, p. 93, (2001).

[4] J. Stohr and H. C. Siegmann, Magnetism - From fundamentals to Nanoscale Dynamics, Springer, pg. 524, (2006)

[5] P. Weiss, Compt. Rend., 143, 1136, (1906).

[6] P. Weiss, J. Phys., 6, 661, (1907).

[7] M. A. Ruderman, C. Kittel, Phys. Rev. 96, 99, (1954) ; T. Kasuya, Prog. Theor. Phys. 16, 45, (1956) ; K. Yosida, Phys. Rev. 106, 893, (1957).

[8] C. Zener Phys. Rev., 81, 440, (1951).

[9] T. Dietl, H. Ohno, F. Matsukura, J. Cibert, D. Ferrand, Science 287, 1019, (2000).

[10] P. W. Anderson Phys. Rev., 79, 350, (1950).

[11] C. Zener, Physics Review, 82, 403, (1995).

[12] J. M. D. Coey, J. Appl. Phys. 97, 10D313, (2005).

[13] J. M. D. Coey, M. Venkatesan, C. B. Fitzgerald, Nature, 4, (2005).

Chapter 3

Experimental procedures

All structures used in this work were prepared using DC magnetron sputtering under ultra high vacuum conditions. Characterisation was performed using a number of techniques. This chapter describes the techniques used and the key principles behind each of them. Several of these are revisited in forthcoming chapters where further explanation is required.

3.1 Principles of Sputtering

Many factors must be considered and demands met when deciding upon a suitable film deposition technique for a particular application. One must consider issues such as the required substrate along with film coverage, residual or induced film strain, thickness uniformity, sticking coefficients of the substrate and successful transfer of stoichiometric properties [1]. One of the major challenges in film deposition is acquiring the desired phase and structure upon a substrate during deposition. The structural development of the film requires the species arriving on the substrate to be able to migrate on the growth surface. This surface mobility must be optimised allowing adatoms to reach equilibrium sites. Therefore, the structure and properties of a thin film is critically dependent on the film growth parameters.

The basic principle behind the sputtering process involves the ejection of species from a solid target surface which has been subjected to energetic ion bombardment. This provides the source of the vapour flux in sputter deposition, which eventually condenses onto a strategically positioned substrate surface. The energy of the sputtered species depends on a number of factors, such as the atomic mass, the nature of the target, the type of energy of the bombarding species, *etc.* [1].

Sputtering requires a gas in order to maintain a discharge in front of the sputtering target, which is held at a high negative potential, producing an electric field. The ion source is usually a plasma generated by the impact of electrons within the noble gas (predominantly argon (Ar) gas as well as mixtures containing oxygen in this work). These positively charged gas ions from the discharge are accelerated in the electric field and bombard the target surface to produce the sputtered flux. Eventually, the ejected or sputtered atoms condense onto a substrate to form a thin film.

3.1.1 DC magnetron sputtering

In this work, DC magnetron sputtering was used. For a full review of DC magnetron sputtering, the reader can refer to reference [4] of this chapter. The action of the electric field is to accelerate electrons (e^*) to collide with inert Ar atoms according to the relationship; $e^*+Ar \rightarrow Ar^+ + e$. This yields positively charged Ar ions as well as free electrons to form the glow discharge. Therefore, the electric field will determine the momentum at impact of the plasma ions and also the momentum of the ejected material. However, unlike a conventional DC sputtering target, the target has been mounted upon a magnetron (stage containing SmCo permanent magnets) whose magnetic field lines permeate through the target. The field lines serve to provide effective toroidal confinement of secondary electrons generated by ion bombardment of the target surface along a "race-track" by virtue of a Lorentz force $e\vec{V}\times B$. The electron race track is visible on the magnetron surface due to the higher sputtering rate along this track [see figure 3.1 (a) - (c)]. The use of a magnetic backing and its effects on the motion of

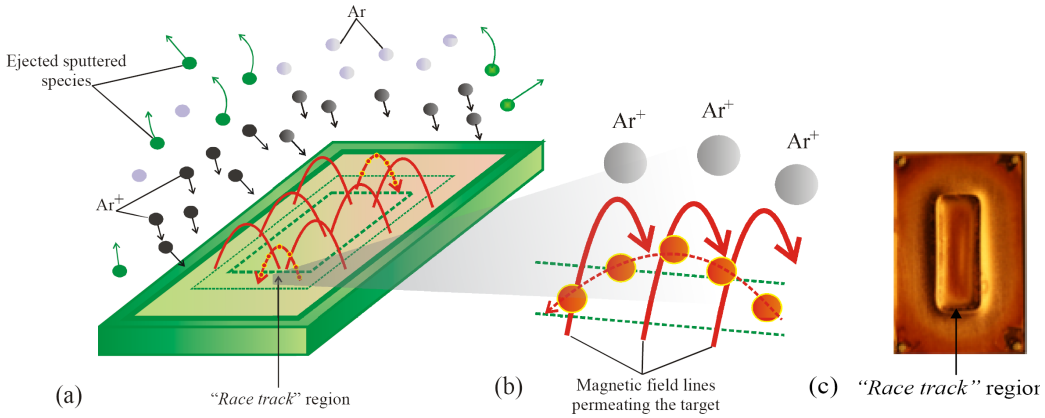

Figure 3.1: Magnetron sputtering: (a) illustration of a standard rectangular dc magnetron target showing the magnetic field lines, an Ar plasma and an electron race track; (b) enlargement of the electron race track; (c) photograph of a Cu target (35×55 mm). Adapted from J. W. A. Robinson thesis [2].

the electrons within its vicinity enhances the ionisation of the plasma near the target leading to a higher sputtering rate and improving its efficiency. It also means that the plasma can be sustained at a lower pressure. The sputtered atoms are neutrally charged and so are unaffected by the magnetic trap. Controlling the pressure of the plasma and/or the power supplied to the magnetron enables the manipulation of the kinetic energy of the Ar^+ ions; this in turn controls the sputtering yield of the target and the deposition rate on the substrate surface. There are a host of other sputtering parameters that have an influence over the final outcome of the process such as the substrate temperature, the oxygen/Ar gas pressure ratio, the total gas pressure, the substrate-target distance, *etc.*

3.2 Substrates

3.2.1 Types of Substrates

The various thin film structures were grown on four different types of substrates; fused amorphous silica glass, *r*- and *c*-plane sapphire (Al_2O_3) and single crystal silicon (Si) substrates with a (100) crystallographic orientation and a 250 nm thermally grown oxide on the surface (now termed Si (100)/SiO_2 substrates). Each chapter will specify which of these has been used for the different structures investigated in this work. In particular, silica glass is the typical substrate used for ITO thin films due to its excellent optical transparency. Furthermore, ITO has been known to maintain favourable properties even when amorphous and grown on silica glass. Silica glass substrates were used for preliminary experiments where basic structural and electronic characterisation of pure In_2O_2 and ITO were carried out. However, it was found that there were some

odd magnetic contributions coming from the silica glass substrates, and we therefore decided to switch to using r and c-Al_2O_3 for all measurements where magnetic characterisation was required.

3.2.2 Substrate Preparation

Substrates were typically cut using a diamond dicing saw. During this dicing process the substrate was held in position under the saw by a transparent, acetone-soluble wax to a glass microscope slide. Once cut, the chips were heated and removed from the glass slide. The process leaves remains of various substances and dirt particles which are in need of removal so to prevent the disruption of any nucleation and growth processes or formation of impurities during thin film growth. Substrates were placed in a beaker containing acetone and treated in an ultrasonic bath for 12 minutes. This process was repeated three times before the substrates were finally soaked in ethanol and dried by compressed air until optically clear. Prior to loading, the substrates were cleaned once again.

3.3 The MKII Sputter Deposition System

Thin films investigated in this work were prepared in the Mark II ultra-high vacuum (UHV) sputter deposition system (Fig. 3.2). Once the substrate(s) had been loaded into the system, it is roughed and then evacuated with a diffusion pump whilst baking out overnight for 8 - 10 hours. This process removes material which has been absorbed onto the chamber walls. The number of impurities within the chamber will be directly proportional to the number of impurities incorporated into the growing films, and so baking is of paramount importance. Typical base pressures achieved after baking and over-night pumping are approximately 1×10^{-6} Pa as measured by an *in-situ* residual gas analyser.

Two different flanges were used during the course of these investigations. Both enabled three targets to be used simultaneously. Pure and doped In_2O_3 and ITO films were grown using a single target source with predetermined element composition. Substrates were placed onto a Platinum (Pt) heater. The temperature calibration of the Pt heater was performed using a pyrometer. All layered and stacked structures were made using a rotating sample turntable which sits below the three magnetrons. Note that when discussing growth temperatures in this thesis I am referring explicitly to the temperature of the heater or sample stage. It is important to be aware that the heater temperature *is not* the same as the substrate temperature or substrate surface temperature. In fact, the difference can be as much as 120 - 150 °C [3], and will be dependent on factors such as the type of substrate, the sputtering target, *etc.*

For sputtering, argon and oxygen gases of purity better than 99.999 % were used.

Both argon and oxygen gases were bled into the gas reservoir one after the other. The reservoir is closed off from the deposition chamber and allowed to mix for 20 minutes. The reservoir is then roughed momentarily to create a turbulence to encourage further mixing of the oxygen and argon gases before being injected into the main deposition chamber.

3.4 Deposition parameters

The deposition rate of the sputtering target depends on a number of factors, namely; rate of rotation of the sample stage as it moves below the target, the gas pressure, the substrate-target distance, and linearly on the power supplied to the magnetron. In this work, the deposition process was controlled using each of these parameters, except for the gas pressure which was kept constant (1.50±0.01 Pa) for all film structures deposited in these investigations. All layered structures (grown using the rotating turntable) had a constant substrate-target distance of 40 - 50 mm. The only additional changes which were made to the rate of sputtering for these materials were done by changing the width of the slit windows. Typically these were 7 mm wide and help to control the substrate exposure time to the target [see Fig. 3.2 (c)]. The rate of rotation was controlled using a LabView program [5] in conjunction with a stepper motor. For pure and alloyed films grown on the Pt heater, the target-substrate distance varied across the heater resulting in a concentration gradient along the heater.

Deposition rates for each target were calibrated in separate deposition runs, using atomic force microscopy (AFM) (see section 3.5.2) in tapping mode from a step-edge across a lift-off sample; this involved masking, with photoresist or permanent marker pen, part of a substrate and depositing onto it. This created a step which was then measured by the AFM. The rates were then back calculated using our knowledge of deposition time, rotation speeds, *etc.*

3.5 Thin Film Characterisation

3.5.1 X-Ray Diffraction studies

X-ray diffraction (XRD) was used for phase identification (θ-2θ scan) as well as low-angle reflectivity (LAR) measurements to estimate film thicknesses and quality of multilayer structures. A Bruker D8 Advance was used for the θ-2θ scans and a Bruker axs D8 Discover was used for the LAR measurements. The diffractometer used a CuKα (λ = 1.5406 Å) x-ray source. The peak positions in the θ-2θ scans were then later verified using a diffraction PCPDFwin database. The vertical size of a crystal grain is a measure of the size of a coherently diffracting domain. Scherrer derived an equation

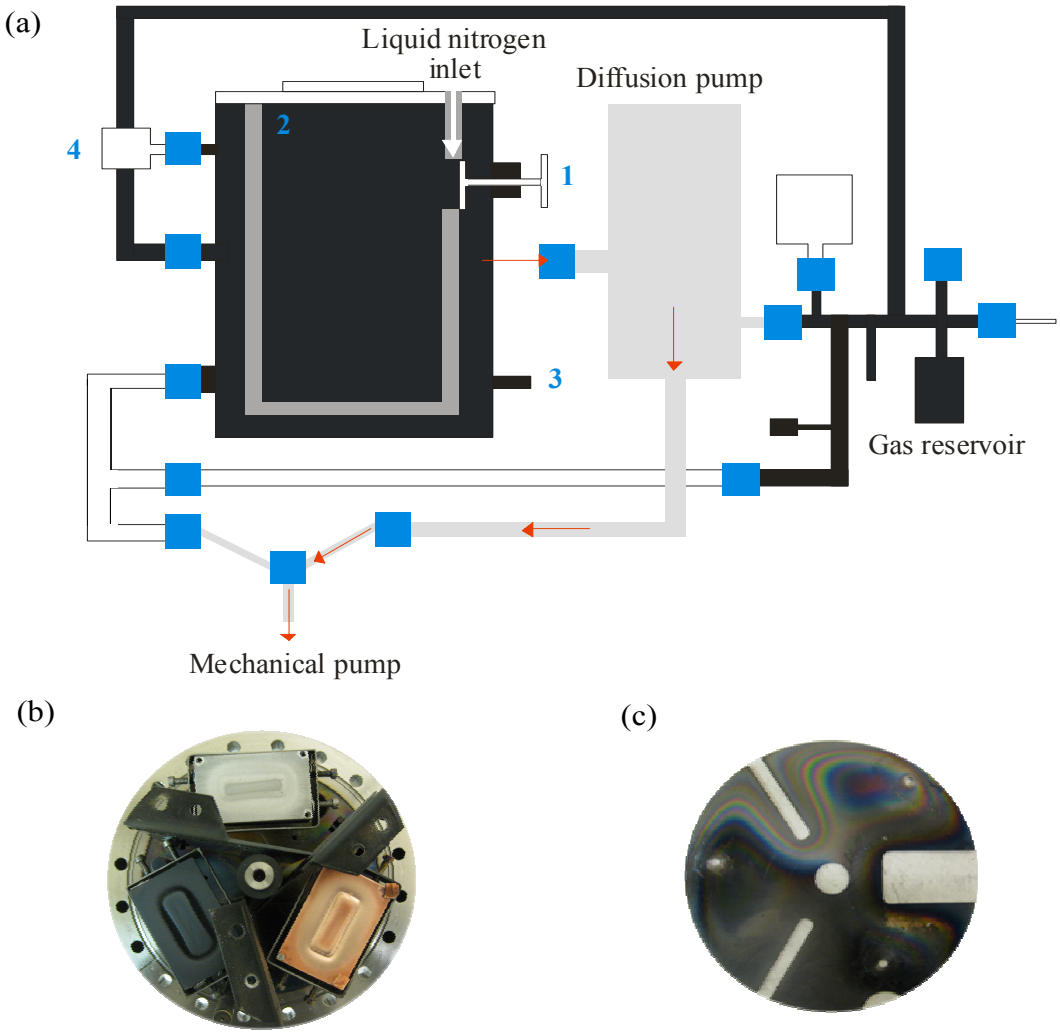

Figure 3.2: Schematic of the MKII sputtering system. The black filled regions indicate the flow of the mixture of sputtering gases. The grey regions accompanied by red arrows indicate the pumping direction. (1) = inner-to-outer chamber valve, (2) = main sputtering chamber, (3) digital pressure sensing Baratron, (4) mass spectrometer. Adapted from J. W. A. Robinson thesis [2]; (b) a photograph of the tri-target sputtering flange with targets installed; (c) a photograph of the sputtering shield with exposure slits.

which relates the broadening of the diffraction peaks to the vertical size of a crystal [6],

$$d_{hkl} = \frac{k_s \lambda}{\beta \cos\theta}, \tag{3.1}$$

where d_{hkl} is the mean grain size perpendicular to the reflecting plane, k_s is the Scherrer constant (somewhat arbitrary, but usually between 0.89 and 1, however, unity is assumed here), λ is the wavelength of the chosen radiation (1.5406 Å) and β is the integral breadth of a reflection in radians at peak position 2θ identified from a standard θ-2θ scan. Using the Scherrer formula, one is able to calculate a value for the average vertical grain size of the films and gain some insight in to the crystallographic coherence throughout the film.

X-ray reflectivity is a powerful tool for investigating multilayered thin film structures and allows one to derive information on the interfaces, mass density of the layers, and to estimate the corresponding stack thickness normal to the film surface with a high degree of accuracy. Using this technique, x-rays are reflected from, and refracted at, the interfaces which separate materials with different electron densities and therefore different refractive indices by virtue of electron - x-ray interaction. These scans have a critical angle $2\theta_c$, which relates to the average electron density, and interference Kiessig fringes which have periods relating to the total film thickness. As the scanning angle increases beyond $2\theta_c$ the x-rays penetrate deeper into the film resulting in an exponential decrease in the recorded intensity. The film density and thickness can generally be found using a modified Bragg law [7]. The thickness was extracted by fitting the Kiessig fringe periods to a simulated scan using "Reflectivity" software.

3.5.2 Atomic Force Microscopy

The AFM Multiscope Nanoscope III (Digital Instruments) reveals topographic information of the film, by scanning the surface with a microfabricated Si tip of nominal radius 30 - 50 nm. The instrument was used in the *tapping mode*, wherein a piezoelectric crystal is used to oscillate the tip over the film surface. The vertical resolution of this instrument is around 0.10 nm. Information obtained from an AFM image can provide us with insight into possible growth processes which may have dictated the growth of the film.

3.5.3 Magnetometry

The magnetic properties were characterised using both DC and AC magnetometry. In DC magnetometry the sample is magnetised by a constant magnetic field and the magnetic moment of the sample is measured, producing a DC magnetisation curve. In AC magnetic measurements, a small AC drive magnetic field is superimposed on top

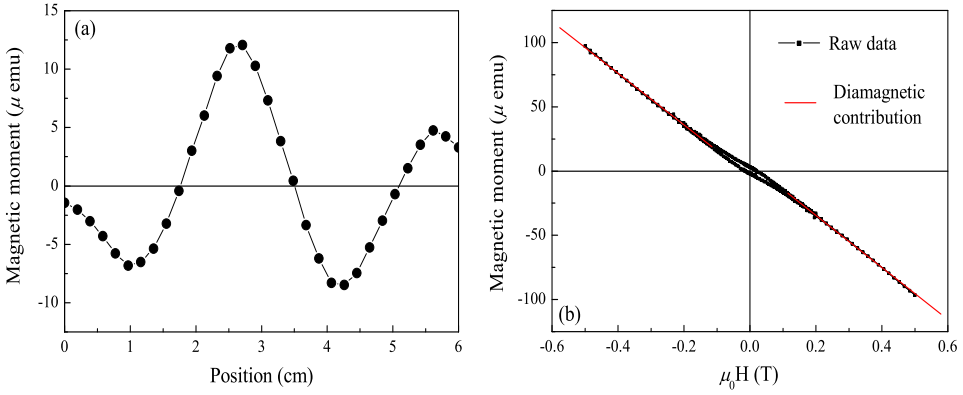

Figure 3.3: (a) Centering measurement over a scanning range of 6 cm to find the optimum magnetisation signal within the SQUID sample space, (b) raw data for a typical magnetisation loop at 2 K for a Co-doped ITO(10) thin film with linear components arising from the diamagnetic background of the substrate (red line).

of the DC field, causing a time-dependent magnetic moment in the sample. Two different methods of DC magnetometry were used: vibrating sample magnetometry (VSM) and superconducting quantum interference device magnetometry (SQUID). The raw magnetisation data from a sample will consist of two clear contributions. There is a low field, saturating ferromagnetic contribution from the sample and a high field linear dependency that is due to the diamagnetic contribution from the substrate [Fig. 3.3 (b)]. This may contain a paramagnetic contribution from unreacted components of the film, which would also be linear in this high field range. To separate the ferromagnetic contribution from the rest, we use a scan of the sample holder and blank substrate (giving our linear diamagnetic background) and subtract it from the scan where a film has been grown on top of a substrate. A source of error in this technique will be the differences in volume of the substrates. The volume of the substrate is orders of magnitude larger than that of the film and so we must be careful when performing the background subtraction. One way to overcome this problem would be to measure the same blank substrate that will be deposited upon later.

Vibrating Sample Magnetometry

VSM measures the magnetic induction in a region where the sample is vibrated within a magnetic field. The forced vibration induces an oscillatory change in the permeability of the sample which is recorded as an alternating current signal by pick up coils. For best results, it is advised that the entire sample must remain within the space bound by the pick up coils. The maximum sensitivity of the VSM is approximately 2μemu. An illustration of the VSM process can be found in Fig. 3.4.

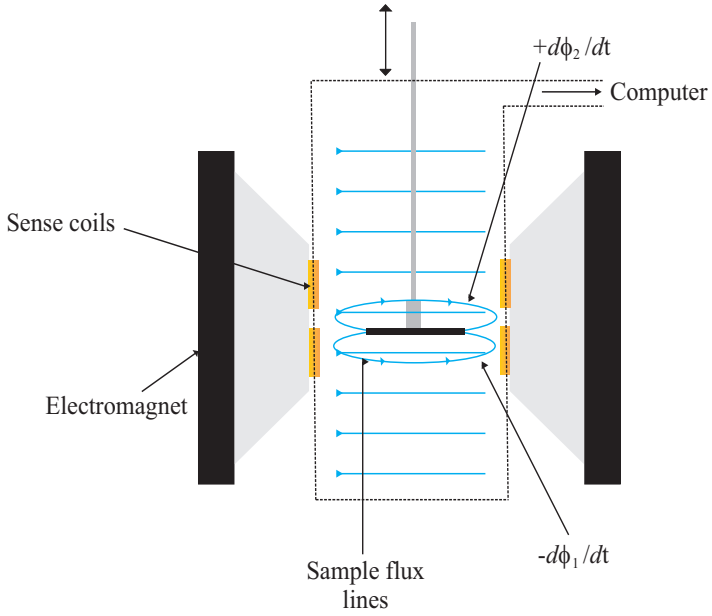

Figure 3.4: An illustration of the VSM used to measure the magnetic properties of some of the samples discussed in this thesis. Figure adapted from J. W. A. Robinson thesis [2].

Superconducting Quantum Interference Device Magnetometry

A superconducting quantum interference device magnetometer, or SQUID, is a very sensitive device used for making magnetisation measurements and is typically 100 times more sensitive than a VSM. A SQUID works on the principle of measuring a voltage induced by the magnetic field from a sample in a field-sensing coil. The SQUID consists of a superconducting ring with a small insulating layer called a Josephson junction. The flux passing through the ring is quantised once the ring has become superconducting but the Josephson junction enables the trapped flux within the ring to change by discrete amounts. Without the Josephson junction, flux cannot enter the ring. Therefore, the device can be used to measure the changes in flux quanta within the ring. The system must be kept at liquid helium temperatures to operate. A least-squares fitting program converts the variation in flux to a theoretical expression that gives a magnetisation value.

Once in the system, the sample must be positioned so that the centre of the sample corresponds to the centre of the field-sensing coils. A scan over a length of 6 cm is used to identify where the sample is located [Fig. 3.3 (a)], after which it can be centred either manually or automatically.

AC susceptibility

As explained above, the induced sample moment is time-dependent for AC measurements such that the measurement yields information about magnetisation dynamics which are not obtained in DC measurements. When the alternating magnetic field has a very low frequency the measurement is most similar to DC magnetometry. However, at much higher frequencies the AC moment of the sample does not follow along the DC magnetisation curve due to dynamic effects in the sample - for this reason, AC susceptibility is often know as the dynamic susceptibility. At these higher frequencies, the magnetisation will in fact lag behind the drive field, creating a phase shift.

The AC susceptibility measurement yields two quantities: the magnitude of the susceptibility, χ, and the phase-shift, ψ relative to the drive signal. The susceptibility can be thought of in an alternative manner: an in-phase or real component, χ', or an out-of-phase or imaginary component, χ". Using AC susceptibility measurements superparamagnetism and spin glass behaviour may be probed where we expect to see shifts in χ' and χ" as a function of the alternating magnetic field frequency when measured as a function of temperature.

AC susceptibility measurements were performed using CRYOGENIC LIMITED cryogen-free system multipurpose system in "VSM" mode where it was possible to apply a small AC drive magnetic field over a DC field and measure the susceptibility as a function of temperature.

3.5.4 Electrical Measurements

Resistivity Probe

Measurement of the sample resistance as a function of temperature was carried out by four-point resistance measurements (in a colinear arrangement) using a custom-built probe. This technique separates the voltage and current connections so that the interfacial effects (from the connection of the contact points to the sample) are circumvented and it is purely the resistance of the sample area of interest that is measured [8]. Sample films are carefully inserted into the space between the contact pogo pins and the insulating base platform. An adjustable head containing the contact pin arrangement is then brought into contact with the film. This ensemble is then placed into a liquid helium dewar, where the temperature of the sample is varied by the height of the sample with respect to the level of helium. A minimum temperature of 4.8 K was achieved resulting from almost complete submersion.

Transport measurements

Magnetotransport measurements were performed through standard four-point measurements on a CRYOGENIC LIMITED cryogen-free system. In some cases gold

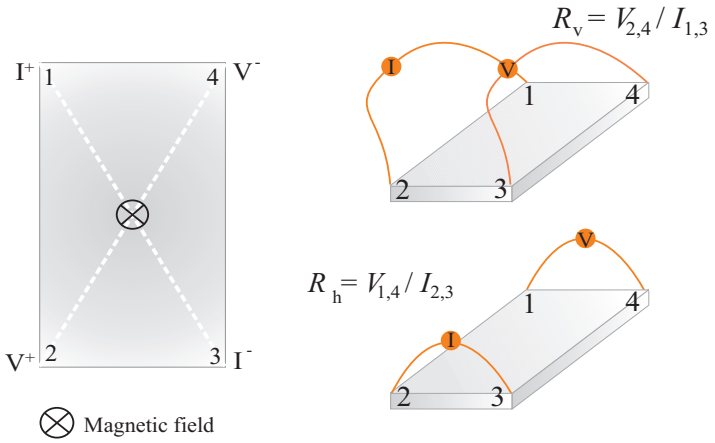

Figure 3.5: Schematic of the configurations used in a Hall measurement to determine V_H.

contacts were sputtered prior to the measurements in order to improve the electrical contact between the wire bonds and the film surface. Magnetoresistance measurements used a colinear contact configuration with an applied magnetic field applied either parallel or perpendicular to the applied current. The carrier concentration and mobility were extracted using Hall measurements in a van der Pauw contact arrangement [8] (see Fig. 3.5).

Charge carriers within an electric current flowing through a magnetic field in a conductor will experience a transverse force which will tend to drift carriers away from the original current direction, resulting in an excess surface electrical charge on one side of the sample. This charge results in the Hall voltage (V_H), and is measured as the potential drop across the two sides of the sample. The resulting transverse force is V_H, expressed as;

$$V_H = \frac{I\mu_0 H}{qn_s}, \tag{3.2}$$

where I is the applied current through the sample, $\mu_0 H$ is the applied magnetic field, q is the charge on a single electron and n_s is the sheet carrier density (cm^{-2}). Mobility (μ_H) can be obtained once a value for the sheet resistance, R_s, has been determined through the relationship;

$$\mu_H = \frac{V_H}{R_s I \mu_0 H} = \frac{1}{qn_s R_s} \tag{3.3}$$

A value for R_s can be obtained by considering two characteristic resistances: the vertical, R_v, and horizontal, R_h, related by the van der Pauw equation;

$$e^{-\pi R_v/R_s} + e^{-\pi R_h/R_s} = 1 \tag{3.4}$$

Measurement of V_H consists of making a series of voltage measurements with a constant current and a magnetic field perpendicular to the sample and measured by applying a current through diagonal contacts (e.g. $I_{1,3}$, measuring $V_{2,4}$). Eight measurements of V_H, similar in nature are made ($V_{2,4}$, $V_{4,2}$, $V_{1,3}$, $V_{3,1}$) for both positive

and negative fields (see Fig. 3.5).

3.5.5 Magnetic Circular Dichroism (MCD)

Optical MCD (O-MCD)

Magneto-optical (MO) measurements presented in this thesis were made at the University of Sheffield. The experimental set-up is based upon the Sato [9, 10] transmission method that allows the simultaneous measurement of two magneto-optical parameters, MCD and Faraday rotation. The principles of the MO effects are explained in more detail in chapter 7.

The sample is mounted on a disc with an aperture, in a cold finger cryostat which allows measurements to be made in the range of 5 - 400 K. The sample space is located between two electromagnetic poles which can achieve applied magnetic fields of up to approximately 0.50 T, applied perpendicular to the sample. There is also another option available, whereby the sample is not mounted using the cryostat. In this configuration it is possible to bring the electromagnetic poles much closer together, thereby increasing the maximum applied magnetic field. Here the calibrated maximum applied magnetic field was approximately 1.80 T.

As shown in Fig. 3.6, the setup can be altered between Kerr and Faraday geometry which are used for samples that reflect and transmit light respectively. This is achieved by simply moving the photoelastic modulator (PEM), analyser and photolultiplier tube (PMT) to the position required in the arrangement shown. The setup uses a xenon lamp which is useful over spectral ranges of 1.5 - 4.5 eV respectively.

The light propagates through a Spectro-275 spectrometer to produce monochromatic light. This has three diffraction gratings blazed at different wavelengths for improved accuracy across a wide spectral range. We can select the diffraction grating most appropriate for the wavelength of light required. However there are still unwanted wavelengths and so a bandpass filter is used in the setup. Before it passes through the sample, the light must be plane polarised. To do so, it is passed through a UV prism polariser.

The light beam is focused to a size similar to that of the aperture which it is to pass through onto the sample surface, and is achieved with a series of mirrors. The mirrors must be optimised regularly to keep the maximum amount of light passing through the sample. Any scattering will directly reduce the sensitivity of the experiment. The role of the PEM is to produce a signal that is proportional to the rotation and ellipticity, allowing them to be measured simultaneously. It consists of a birefringent crystal mounted on a piezo-vibrator of characteristic modulating frequency, f [12]. The birefringent crystal is vibrated, causing a periodic advancement and retardation of the transversing light phase, which occurs parallel to the vibration direction. This means that the light that emerges will alternate between LCP and RCP light with a

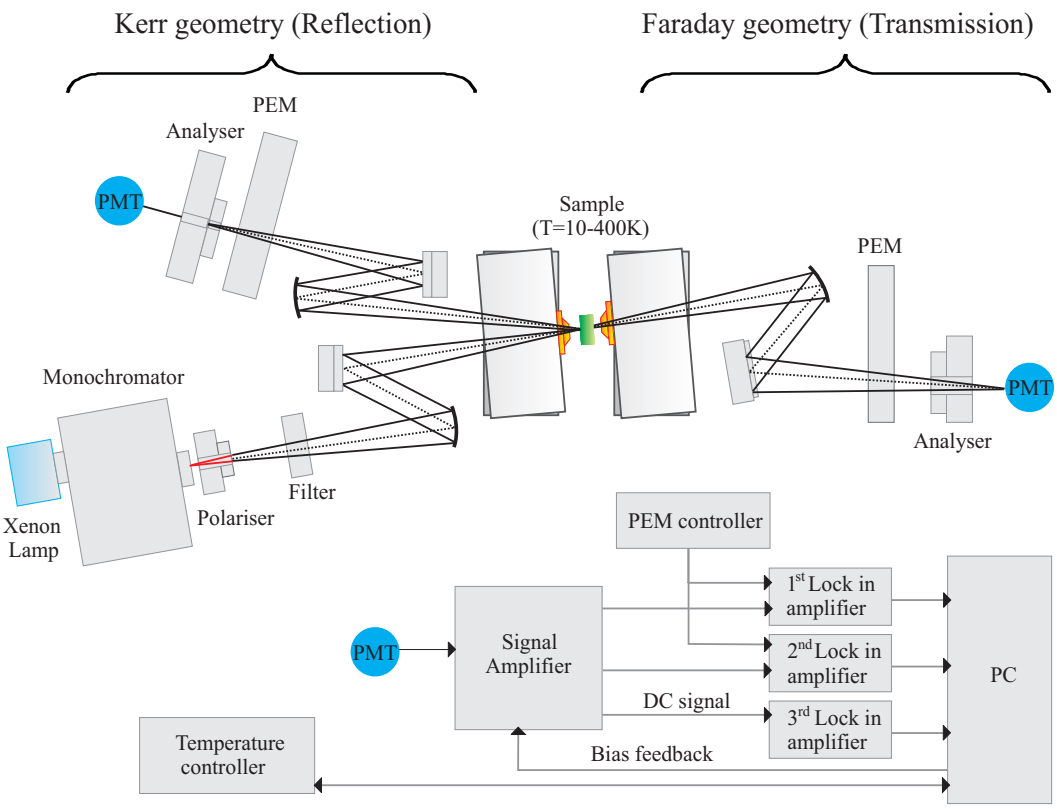

Figure 3.6: Magneto-Optic setup for measurements in either Faraday or Kerr geometry. Adapted from A. J. Behan thesis [11].

frequency f.

The light then passes through an analyser before it is focused on the PMT. Any MCD or rotation exhibited by the sample will introduce oscillations in the light intensity with a frequency f or $2f$ respectively. Therefore, if no MCD effect is present, the intensity at the detector will remain constant.

The PMT will then convert the light intensity into an electrical signal. The signal amplifier unit is initially used to amplify the signal and after, split it into the AC and DC components respectively. Using a Keithley voltmeter, the DC voltage is read and kept constant by controlling the gain of the PMT to maintain a constant sensitivity. The AC component is measured using two lock-in amplifiers. Sato shows in ref. [9] using complex theory how the measurement of the three intensities (I_0, I_f, and I_{2f}) can then be translated to obtain values for the MCD and Faraday rotation.

The system is automated with instruments that are controlled from a PC using LabVIEW. The measurements of the magneto-optical spectra are automatically repeated to give an average and hence reduce the noise levels. The current of the electromagnet can be swept to produce a magneto-optical hysteresis loop, or the wavelength swept to produce a spectra.

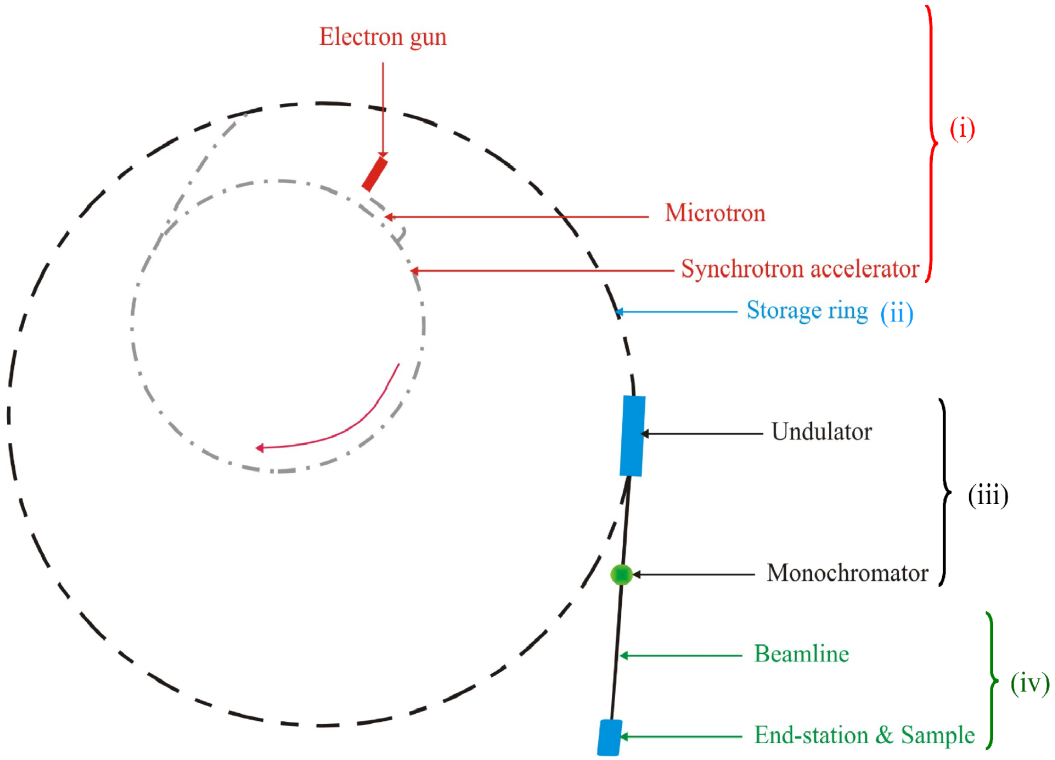

Figure 3.7: Schematic representation of a typical synchrotron radiation facility. (i) initial acceleration stages, (ii) the storage ring, (iii) insertion devices used to manipulate and polarise the beam, and (iv) reaching the end station where the sample is located and can be characterised.

X-Ray MCD (XMCD)

High intensity, tuned x-rays available at a synchrotron radiation facility has allowed unparalleled access in the observation of magnetic phenomena. Synchrotron radiation is emitted when charged particles are accelerated close to the speed of light and are deflected by a magnetic field. The availability of its high brilliance and other superior properties compared to conventional light sources make synchrotron radiation an extremely versatile tool. The XMCD measurements presented in this thesis were performed at Beamline I06 at Diamond Light Source. The principles of XMCD effects are explained in more detail in chapter 6.

Production of synchrotron radiation requires several components: a primary electron accelerating system, a synchrotron accelerator for further acceleration of electrons, a storage ring to store the accelerated electrons, insertion devices in the storage ring to produce the radiation, beamline systems equipped with monochromators to tune and direct the radiation to an experimental end-station, and an undulator to provide polarisation of the synchrotron source (see Fig. 3.7).

Electrons are initially emitted by a hot cathode through thermionic emission in high vacuum and accelerated by an anode voltage before being accelerated again in the microtron. The microtron is a linear accelerator where electrons pass through an elec-

tric field many times before being redirected on larger growing trajectories by a strong magnetic field. The electrons then pass through to the synchrotron accelerator where they are focused on their final trajectory and energy (approximately 3 GeV at Diamond Light Source). The electrons then enter the storage ring through a transfer channel where they gradually decay and are reinjected every 12 hours. In order to maximise the density of electrons which have near total circular polarisation, undulators (a periodic array of magnets) are often inserted in the storage ring. In an undulator, the electron beam is periodically deflected by weak magnetic fields. The electrons emit radiation at the wavelength of their periodic motion in the undulator. The spectral resolution of the emitted radiation is proportional to the number of undulator periods and the radiation wavelength can be changed by varying the magnetic field. The x-rays then pass through an arrangement of slits, mirrors and monochromators to deliver light of desired energy and polarisation to the beamline end station.

Bibliography

[1] Z. Barber, Journal of Materials Chemistry, 16, 334-344, (2006).

[2] J. W. A. Robinson, PhD Thesis, Zero to Pi Oscillations in Ferromagnetic Josephson Junctions, University of Cambridge, (2007).

[3] Z. Barber, Private communication.

[4] R. E. Somekh and Z. H. Barber, Journal of Physics E: Scientific Instruments, 21(11):1029-1033, (1988).

[5] Program created and coded by Gavin Burnell

[6] B. D. Cullity, Elements of X-Ray Diffraction, 2nd Edition MA: Addison Wesley, Page 102, (1978).

[7] A. Segmuller, Thin Solid Films, 18(2):287-294, (1973).

[8] I. J. van der Pauw, Philip. Res. Repts., 13:1-9, (1958).

[9] K. Sato, Jpn. J. Appl. Phys. 20, No. 12, (1981).

[10] W.P. van Drent and T. Suzuki, J. Magn. Magn. Mater., 175, 53 (1997).

[11] A. J. Behan, PhD Thesis, Characterisation of Doped ZnO Thin Films for Spintronic Applications, (2008).

[12] K.W. Hipps and G.A. Crosby, J. Physical Chemistry, 83, 555, (1979).

Chapter 4

The Indium Oxide system

This chapter introduces the Indium Oxide system, and how it can be manipulated to obtain Indium Tin Oxide, the primary material system used for our investigations. Previous work performed by others is described and related to the findings in this thesis. The suitability of these materials for successful transfer to the field of oxide spintronics is considered.

4.1 Introduction

Transparent conducting oxide (TCO) thin films and techniques for their fabrication have been investigated for many years because of their unique properties and extensive application potential [1]. The mass interest in Indium Oxide (In_2O_3) thin films stems from its dual ownership of high optical transparency together with electronic conductivity. In view of the high practical importance of In_2O_3 thin films, a great deal of research and development has been carried out on the electrical and optical properties. Rupprecht [2] performed some of the earliest experiments on the In_2O_3 semiconductor. Inspired by this pioneering work, others later followed suit investigating the various methods to produce In_2O_3-based materials such as direct current (DC) magnetron sputtering, radio frequency (rf) sputtering, chemical vapour deposition (CVD), vacuum evaporation (VE), sol gel reaction, *etc*, in an attempt to meet both economic and technological needs. In particular, considerable interest has been devoted to the study of Tin (Sn)-doped In_2O_3 (ITO). This product of In_2O_3 also holds very similar optical and electrical properties as pure, undoped In_2O_3, and so is also of great technological interest.

There is a fundamental interest in the conduction mechanisms within TCO material systems. A great deal of work has been carried out in trying to correlate the microstructural characteristics in an attempt to explain the physical reasons behind conduction in In_2O_3 and ITO-based thin films. One of the most important aspects of working with these materials from a technological point of view is the balance between the electrical and optical properties, i.e. achieving high optical transmission whilst maintaining minimal sheet resistance. However, these two properties are not independent, and optical transparency in the visible region is strongly affected by the electrical properties of the film. Usually, good electrical properties can be achieved but at the expense of transmission.

The electrical properties of the oxides depend heavily on the oxidation state of the metal component, i.e. the stoichiometry of the oxide, and on the nature and quantity of the impurities incorporated within the film. A perfectly stoichiometric oxide will be insulating. Effective doping can be achieved provided that the dopant is of the same size or smaller than the host ion it will be replacing, and that no secondary compounds are formed between the dopant and host atoms.

The properties of ITO films are strongly dependent on the preparation techniques. A huge archive of data collected on the various electrical and optical parameters of ITO exist, none of which are identical. Because of this, understanding the limiting physical phenomena in these materials is difficult. This chapter aims to introduce the In_2O_3 and ITO system and provide a relatively up-to-date picture of the work done on the electrical and optical properties of In_2O_3 and ITO based thin films and the various methods used to make them. The conduction mechanisms which govern the electrical properties will also be discussed along with the the results obtained with our materials.

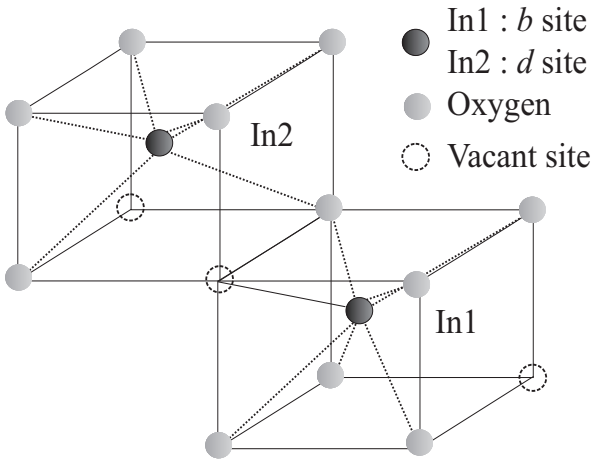

Figure 4.1: The crystal structure of In_2O_3.

4.2 The Indium Oxide system

In_2O_3 exists in a modified cubic crystallographic phase (space group Ia^3) called the *bixbyite* structure (also called *c*-type rare earth oxide structure) [3]. A conventional unit cell consists of 16 formula units of In_2O_3 where one fourth of the oxygen anions located along the four <111> axes are missing. Indium cations are located in two non-equivalent sites (see Figure 4.1), with 8 In^{3+} ions located in the centre of trigonally distorted oxygen octahedrons (*b* site). The remaining 24 In^{3+} ions located in the centre of the more distorted octahedrons (*d* site) [4]. In_2O_3 is reported to have a lattice constant of 1.012 nm [5].

In_2O_3 is a poor conducting material when stoichiometric. However, as deposited

In_2O_3 generally lacks stoichiometry due to oxygen vacancies. At high concentrations of oxygen vacancies, an oxygen vacancy impurity band forms and overlaps E_c at the bottom of the conduction band producing a degenerate semiconductor. Oxygen vacancies act as doubly ionised donors, contributing two electrons to the conductivity. The material composition can be represented as In_2O_{3-x}. As well as providing conduction electrons, the oxygen vacancies also allow for O^{2-} ion mobility. Generally, additional electron carriers can be supplied by doping In_2O_3 with four or more valence electrons. In Sn-doped In_2O_3 (ITO), Sn acts as a cationic dopant in the In_2O_3 lattice and substitutes for In, which has a valence of three (In^{3+}). This results in *n*-type doping of the In_2O_3 lattice by providing an electron to the conduction band. High electron concentrations (10^{17}- 10^{20} cm^{-3}) can be achieved either with an oxygen deficiency (e.g., In_2O_{3-x}) or an excess of metal atoms (e.g. $In_{2+y}O_3$).

The Sn dopant essentially forms an interstitial bond with oxygen present in the system and will exist as either SnO (valency +2) or SnO_2 (valency +4), the outcome of which will have a direct influence on the overall conductivity of the ITO film. A valency of +2 will result in a reduction in the conductivity of the ITO film as it will create a hole, which subsequently behaves as a "carrier trap", reducing the overall car-

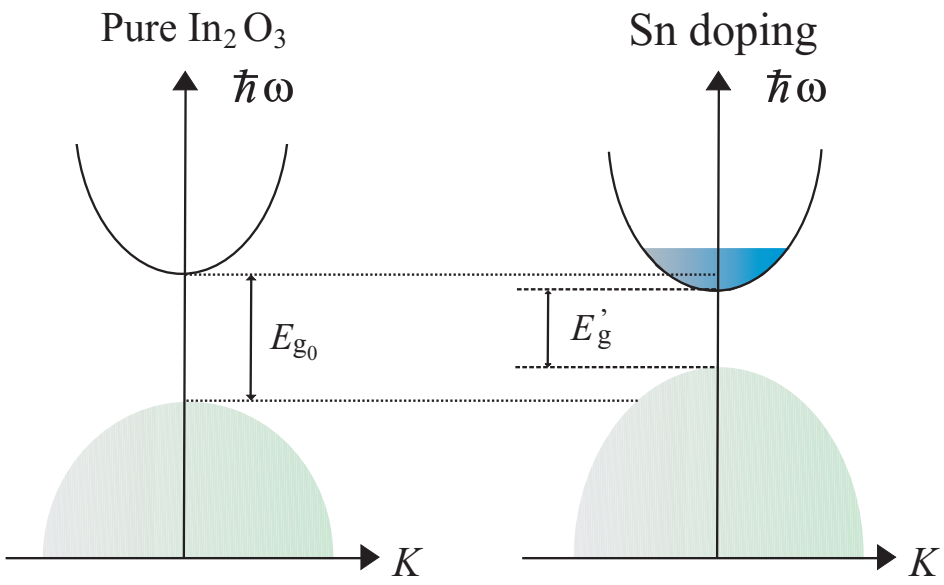

Figure 4.2: The assumed parabolic band structure of pure, undoped In_2O_3 (left) as well as the effect of doping the lattice with Sn (right). Adapted from [7].

rier concentration. On the other hand, predominance of the SnO_2 state results in the Sn^{4+} acting as an n-type donor that releases electrons to the ITO conduction band, thus improving ITO conductivity.

Sn^{4+} ions also have another role to play in the electrical behaviour of ITO: they act as scattering centres for electrons inside the In_2O_3 lattice. This creates a trade-off between electron carrier density and mobility when trying to optimise the conductivity of an ITO film. The formal description of ITO can thus be written as $In_{2-x}Sn_xO_{3-2x}$.

Optoelectronic properties of materials are dominated by the electronic structure near the bandgap. The understanding of the band structure of ITO is based on the theory behind In_2O_3. In order to explain the conductivity mechanism of In_2O_3 when doped with Sn, Hamberg and Granqvist have assumed a simple parabolic band structure (Fig. 4.2) with an intrinsic wide semiconductor bandgap of 3.75 eV [6]. Addition of Sn dopants results in the formation of donor states just below the conduction band. As the doping levels increase, these donor states will eventually merge with the conduction band. Once the material becomes degenerate, the mutual exchange and Coulombic interactions shift the conduction band downwards and the valence band upwards - effectively narrowing the band gap, E_g, from E_{g0} to $E_g^{'}$ [7].

4.3 Electrical Conduction mechanisms

Electrical conductivity (σ) depends on the concentration (n_c) and mobility (μ_H) of a free electron carrier according to the relationship:

$$\sigma = n_c \mu_H q, \tag{4.1}$$

or, in terms of resistivity, ρ,

$$\rho = \frac{1}{n_c \mu_H q}, \tag{4.2}$$

where q is the electron charge. Therefore, it is clear that to obtain high conductivity, it is important to have a high carrier concentration and mobility simultaneously.

Most efforts to improve the conductivity of ITO thin films have focused on increasing the number of free carriers via extrinsic doping. However, this technique is self-limiting, as the process of increased doping will naturally impair the electron mobility. Therefore, obtaining the highest conductivity is a trade-off between carrier concentration and electron mobility. The two subsections below describe the limiting factors to these two important conduction parameters. For a more detailed review the reader is referred to reference [8].

4.3.1 Free carrier concentration

Previously it was stated that a high carrier concentration can be achieved either by introducing non-stoichiometry, i.e. creating oxygen vacancies, or an excess of metal atoms, or extrinsic doping, e.g., with Sn. Frank and Kostlin have performed extensive studies into the electrical properties of ITO films as a function of varying Sn concentration [9]. Doping does not always result in a continual rise in carrier concentration and improved electrical properties. The dopants can behave in a number of different ways, e.g., they may occupy interstitial sites, form defects acting as carrier traps, or be the cause of phonon or impurity scattering centres, leading to a fall in carrier mobility. Frank and Kostlin listed four dominating lattice defects which they believe influence the electrical properties of ITO films:

1. *Impurity ions* - Sn acts as a cationic dopant resulting in n-type doping by providing an electron to the conduction band.

2. *Neutral defects* - Two neutral defects exist; those Sn^{4+} ions remote from nearest neighbour positions become loosely bound to an interstitial oxygen anion and form a neutral compound ($Sn_2{}^{+}O_i{}^{2-}$). This interstitial neutral defect will dissociate on annealing under reducing conditions, such that the O^{2-} can drift out. If the Sn^{4+} ions are close enough to be bound to the three nearest neighbours on regular anion sites as well as an additional interstitial oxygen ion, $(Sn_2O_4)_i$ is formed. This is usually the case at high Sn doping levels. A rise in Sn doping is likely to result in an increase in the neutral scattering centre density.

3. *Compound neutral defect* - if there is a surplus of Sn as well as loosely bound oxygen, the two neutral defects described above may combine.

4. *Oxygen vacancy* - oxygen vacancies will act as doubly ionised donors. Deposition within oxygen rich conditions will result in a film saturated with oxygen which

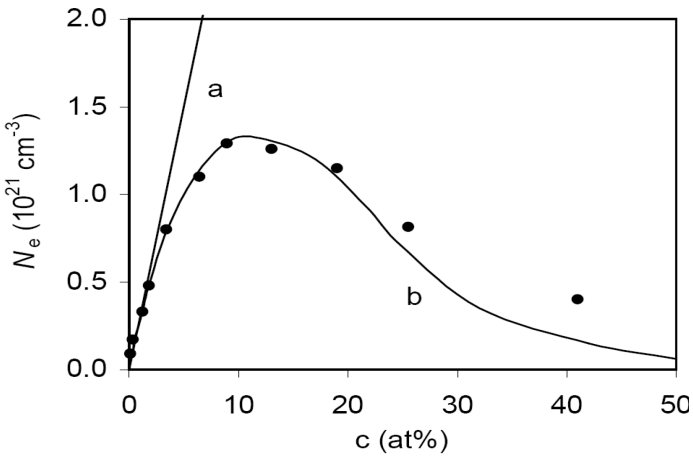

Figure 4.3: Dependence of the free-electron density N_e on the Sn concentration, c. a indicates the region where Sn doping is low and the rise in carrier concentration is linear, indicating that every Sn atom behaves as a donor. b represents the region beyond 8% doping where the carrier concentration soon begins to fall off likely due to Sn ions occupying nearest neighbour anion sites and forming neutral defects. After reference [10].

for the purposes of improving the electrical properties is highly undesirable. Interstitial oxygen can diffuse through the ITO lattice reaching grain boundaries. Exposing the film to higher temperatures has the potential to create free electrons and dissolve interstitial oxygen to promote substitutional Sn.

It has been found that very high dopant concentrations (beyond a critical limit) result in the observed ITO film carrier concentration being lower than expected. This implies that a portion of Sn atoms are electrically inactive and is likely due to an increased probability of the occupation of adjacent cation positions by two or more Sn atoms. Figure 4.3 illustrates the dependence of the free carrier concentration on the level of Sn doping [10]. The highest carrier concentration, which corresponds to the lowest resistivity, occurs when the Sn doping level is approximately 10%. The solid solubility of Sn in In_2O_3 is approximately 8%. Beyond this range, a Sn oxide phase may form and distort the lattice structure resulting in a decrease in the carrier concentration.

4.3.2 Carrier mobility

From equation 4.1 we can see that to improve conductivity, we require an increase in carrier concentration or mobility, or both. However, increasing carrier concentration can lead to an increase in visible absorption and hence a reduction in transparency. Therefore, increasing the mobility is extremely vital for ITO films in order to achieve good electrical and optical properties.

The free carrier mobility, μ_H, can be defined as:

$$\mu_H = q\tau/m^*, \tag{4.3}$$

where q is the electron charge, τ is the average collision time of electrons and m^* is the effective electron mass in the conduction band. The mobility of the charge carriers is strongly influenced by the disorder within the crystal structure. Mobility of the free carriers is therefore strongly affected by the different scattering processes of free charge carriers. These are summarised below.

1. *Grain boundary scattering* - these play a significant role in polycrystalline films. Films of this nature tend to contain high densities of interface states which are capable of trapping free carriers from the bulk of the grain [11]. The mobility due to grain boundary scattering, μ_g, can be expressed as [12]:

$$\mu_g = qD(2\pi m^* k_B T)^{-1/2} exp\left(-\frac{q\phi_b}{k_B T}\right), \tag{4.4}$$

   where D is the grain size, ϕ_b is the grain boundary potential barrier, q is the charge of a single electron, k_B is Boltzmann constant, T is the absolute temperature in Kelvin and m^* is as before. From equation 4.4, it is evident that films possessing larger grains and hence smaller grain boundary potential suffer less from grain boundary scattering.

2. *Ionised impurity scattering* - it has been suggested in some models of degenerate semiconductors that the contribution from these impurities to the mobility of free charge carriers can be described as follows [13]:

$$\mu_i = \frac{4e}{3}\left(\frac{\pi}{3}\right) n_i^{-2/3}, \tag{4.5}$$

   where n_i is the impurity concentration and the free electron carrier concentration is usually assumed to be equal to the impurity concentration. Mobility therefore decreases with the concentration of impurities.

3. *Lattice scattering* - propagation of acoustic or optical waves through a lattice can cause as electron-phonon scatter event inducing vibrations within the lattice. The mobility due to this kind of scattering depends strongly on the temperature. An increase in the temperature will result in more lattice vibration and therefore a decrease in carrier mobility [14]:

$$\mu_l = \frac{(8\pi)^{1/2} q\hbar^4 C}{3E_L m^{*5/2}(k_B T)^{3/2}}, \tag{4.6}$$

   where C is the elastic constant, E_L is the shift in the edge of the conduction band with temperature and the other constants are as before.

The total mobility, μ_{total}, as a result of all the scattering sources can be represented by the sum of the reciprocal values for μ_g, μ_i, μ_l.

$$\frac{1}{\mu_{total}} = \frac{1}{\mu_g} + \frac{1}{\mu_i} + \frac{1}{\mu_l} + \ldots + \ldots \tag{4.7}$$

4.4 Previous Work

A large portion of the previous research has focused on the influence that the numerous deposition techniques and conditions (table 4.1), post growth treatments [15–18] and substrate effects [19, 20] may have on the electrical and optical properties of the ITO films. Bel Hadj Tahar *et al.* provide a comprehensive review of the varying properties of ITO when grown using a variety of deposition techniques [8].

4.4.1 Effects of substrate temperature

Lee performed an investigation into the behaviour of the carrier concentration and mobility for reactive DC magnetron sputtered ITO thin films grown on alkaline-free glass substrates at various process temperatures (70 - 380°C) [38]. It was suggested that the dependence of carrier concentration and mobility on the substrate temperature could be divided into two distinct regions based on a shift in dominant scattering mechanisms. In region 1 carrier concentration and mobility both increase with substrate temperature as a result of increasing crystallinity and grain size; in region 2 carrier concentration continues to rise but mobility falls due to ionised impurities which act as scattering centres and trap the free electron carriers. Electron carriers have a much clearer conduction path in well-ordered crystalline structures as opposed to a disordered amorphous structure. The rise in substrate temperature also promotes favourable conditions for Sn adatomic substitution.

4.4.2 Effects of oxygen partial pressure

It is widely accepted that excess oxygen present during the growth of ITO films is detrimental to the electronic properties of the film. Many argue that this is largely due to two main factors. The first one is connected to the fact that crystallinity worsens compounded with a decreasing average grain size and hence a greater number of grain boundaries. Also, adsorption of oxygen into the films could inhibit the surface migration of In or Sn atoms leading to structural disorder. The second factor relates to excess oxygen filling oxygen vacancies and thus deactivating the substituted Sn^{4+} ions by forming $Sn^{+}O^{-}$ complexes. Ultimately, this results in a decrease in carrier concentration.

However, again we meet the compromise between the best electrical and optical properties. High oxygen partial pressures yields films with superior optical transparency but lower carrier concentration and therefore, reduced electrical quality.

4.4.3 Post-growth annealing treatment

The most common method of manipulating the as-deposited films is to use some form of post-growth annealing treatment [15–18]. Changes observed with the annealing temperature have been associated with transformations in the local ordering of the material during re-crystallisation such as the reduction in structural distortion and increases in mean crystallite size. Annealing treatment may also lead to the creation or annihilation of oxygen vacancies by releasing trapped donor sites at grain boundaries and dislocations as well as encouraging the out-diffusion of oxygen atoms from interstitial positions.

4.4.4 Crystallographically oriented films

In a drive to improve the carrier mobility research has been carried out focusing on developing preferentially oriented or epitaxial In_2O_3 and ITO films on substrates such as yttria-stablised zirconia (YSZ) [39]. It was thought that by improving the crystalline quality, thus minimising large angle grain boundaries and defects, the conduction mechanisms of ITO could be understood better. Comparing the electrical properties of the epitaxial ITO film with that of a polycrystalline film grown on glass, Kamei *et al.* found no improvement and concluded that neither large angle grain boundaries nor crystalline orientation were dominant electron scattering factors in ITO films. In fact, they claim that the dominant factors are electron scattering events at point defects such as ionised or neutral impurity scattering. Similarly, Fan *et al.* found that the electrical properties of ITO films grown on single crystal Al_2O_3 are not significantly influenced by cystallographic orientation or the substrate material [40].

Table 4.1: Summary of the electrical (ρ = resistivity, n_c = carrier concentration, μ_H = electron carrier mobility) and optical properties of ITO thin films at room temperature grown using a variety of deposition techniques. DCMS = DC magnetron sputtering, RFS = radio frequency sputtering, PLD = pulsed laser deposition, CVD = chemical vapour deposition, VE = vacuum evaporation.

Technique	ρ ($\times 10^{-4}\Omega$cm)	n_c ($\times 10^{20}$cm^{-3})	μ_H (cm^2 V^{-1} s^{-1})	Substrate	Transparency (%)	Reference
DCMS	7.00	6.00	25.00	Glass	...	[21]
DCMS	3.00	4.00	40.00	Glass	>80	[22]
DCMS	1.40	9.00	46.00	Glass	> 90	[23]
DCMS	370	7.00	24.50	Glass	...	[24]
DCMS	1.60	8.10	47.00	...	...	[25]
RFS	4.00	4.60	18.00	Glass	$\approx$ 90	[26]
RFS	0.68	36	27.00	...	...	[27]
RFS	2.55	15.9	15.4	...	...	[28]
RFS	13.8	2.60	17.39	...	...	[29]
PLD	8.00	10-12	...	...	$\approx$ 90	[30]
PLD	3.00	5.00	40.00	...	80	[31]
PLD	1.30	10	35.00	Si, Glass	85	[32]
CVD	1.60-1.80	9.00	43.00	...	...	[33]
Sol-gel	12	1.20	7.00	...	...	[34]
Sol-gel	3.30	10	21	...	...	[35]
VE	0.70	20-30	$\approx$ 10	...	...	[36]
VE	0.44	13.8	103	...	...	[37]
VE	6.80	5.70	16	...	...	[37]

Table 4.2: Comparison of the room temperature electrical properties (resistivity, ρ, carrier concentration, n_c, and electron mobility, μ_H) of pure In_2O_3 and ITO grown using a heater temperature of 300°C and an oxygen partial pressure of 0.15 Pa with varying levels of extrinsic Sn doping.

Sn concentration (at. %)	ρ (Ω cm)	n_c (cm^{-3})	μ_H ($cm^2\ V^{-1}\ s^{-1}$)
0.0	$3.00\pm0.32\times10^{-1}$	$7.90\pm0.36\times10^{18}$	2.65 ± 0.28
5.0	$1.45\pm0.09\times10^{-3}$	$1.83\pm0.15\times10^{20}$	23.58 ± 0.14
10.0	$2.33\pm0.08\times10^{-4}$	$8.84\pm0.08\times10^{20}$	25.22 ± 0.14

4.5 Experimental Results

In_2O_3 and Sn-doped In_2O_3 films were grown using DC magnetron sputtering from single commercial targets onto silica glass substrates as described in chapter 3. The power applied to the targets was kept constant at 20 W in both cases resulting in a deposition rate of approximately 40 nm/min for each target. The gas pressure was maintained at 1.50 ± 0.01 Pa with a gas flow rate of approximately 0.10 ± 0.01 Pa/s. To investigate the effects of temperature on the samples, heater temperatures were varied between room temperature and 600°C. When investigating the effects of oxygen partial pressure, an oxygen partial pressure range of 0 - 0.60 Pa was used.

4.6 Electrical properties

Dependence on Sn concentration

The Sn content in In_2O_3 was varied in the range from 0 to 10 at%. Table 4.2 summarises the values for resistivity (ρ), carrier concentration (n_c) and electron mobility (μ_H) at room temperature for thin films of pure In_2O_3 and Sn-doped (5 and 10 at.%) In_2O_3 [now called ITO(5) and ITO(10)]. The electronic properties of the films improve with increasing Sn doping. Pure In_2O_3 samples were semicondcuting whereas those doped with Sn showed metallic behaviour. The best electrical properties are found for ITO(10) films. For this reason, the majority of the work presented in the rest of the thesis is concerned with ITO(10).

Magnetoresistance (MR) measurements of a series of pure In_2O_3, ITO(5) and ITO(10) grown using an oxygen partial pressure of 0.15 Pa and heater temperature of 300°C are shown in Fig. 4.4 (a). The samples doped with Sn show characteristics typical of the ordinary MR effect for a semiconducting or metal thin film, indicating weak localisation behaviour. Magnetoresistance is negative for all films suggesting the reduction in spin disorder as the alignment increases with field. A plot of how the magnitude of MR (at an applied magnetic field of 5 T) depends on the carrier

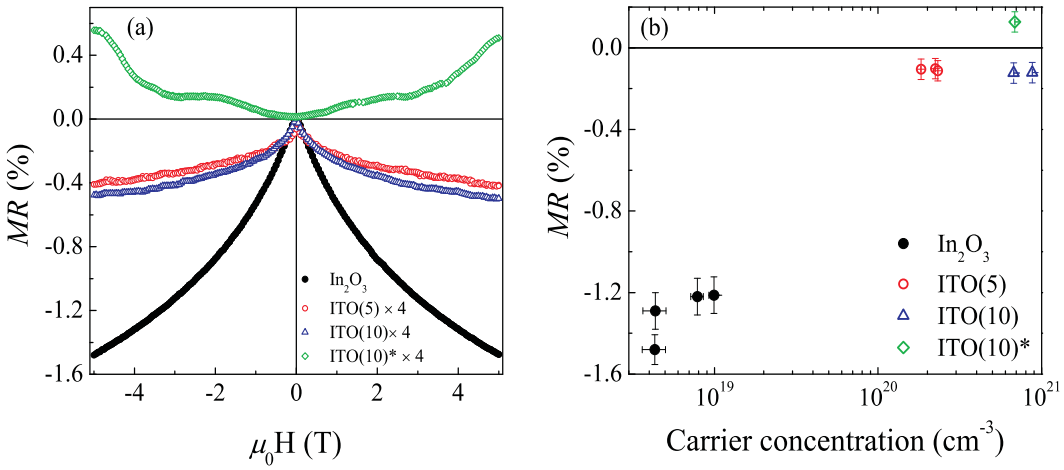

Figure 4.4: (a) Magnetoresistance curves for pure In_2O_3 (black), ITO(5) (red) and ITO(10) (blue) thin films grown using an oxygen partial pressure of 0.15 Pa and a heater temperature of 300°C at 10 K. MR curves of ITO(5) and ITO(10) have been multiplied by a factor of 4. An ITO(10) film grown on an unheated substrate is shown in green [ITO(10)*] and has also been multiplied by a factor of 4, (b) Dependence of MR at 10 K on the carrier concentration under an applied magnetic field of 5 T.

concentration can be found in Fig. 4.4 (b). Samples with lower carrier concentration possess a much larger negative MR, which is largest for non-Sn-doped samples. Two electron waves may travel in opposite directions along the same closed path, being elastically scattered by the same impurities. This will lead to a constructive interference and an additional resistance. Upon application of a magnetic field, the two waves will acquire a phase difference and the additional resistance present in the absence of a magnetic field will decrease. Therefore, the addition of Sn may reduce the weak localisation effect and the constructive interference. The observation of negative MR in these samples may be related to the high density of oxygen vacancies. The suggestion we make about a reduction in spin disorder with increasing field implies that the samples may be also be magnetic (see section 5.6.6).

Effects of substrate temperature

Figure 4.5 shows the θ-2θ XRD diffractogram for approximately 300 nm thick ITO(10) films grown on silica glass substrates at varying heater temperatures using an oxygen partial pressure of 0.15 Pa. The films were highly polycrystalline showing diffraction peaks from a number of reflection planes. It seems that there may be a shift in preferred orientation from the ITO (400) to the ITO (222) for films grown above 300°C. A rise in the calculated peak intensity ratio of ITO (222) to ITO (400) [$I_{(222)}/I_{(400)}$] confirms the change in orientation. For heater temperatures above 300°C it is clear that the ITO (222) peaks become more pronounced and sharper, suggesting an increase in the average grain size.

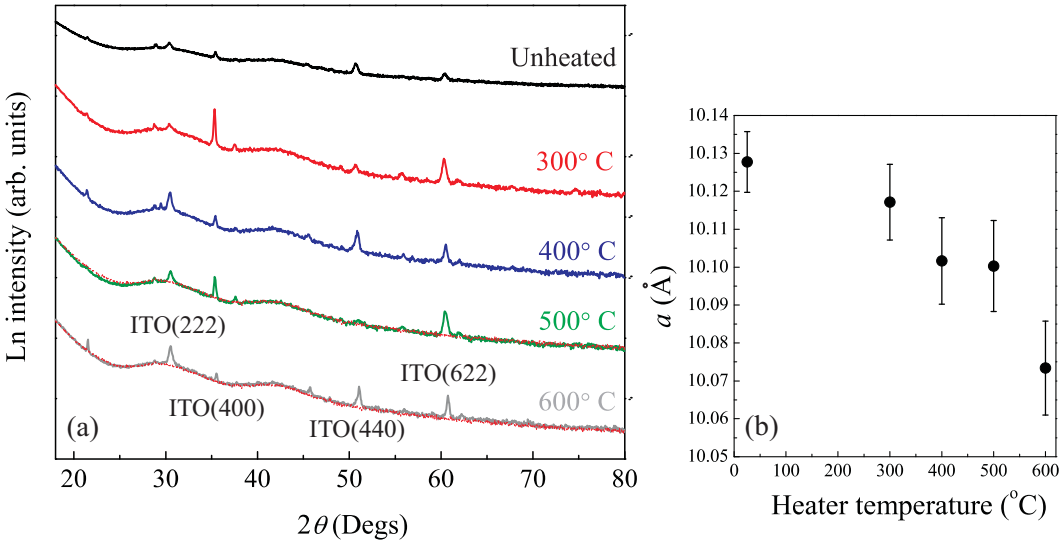

Figure 4.5: (a) X-ray diffraction patterns for 300 nm thick ITO(10) films grown on silica glass substrates at different heater temperatures. The oxygen partial pressure during deposition was 0.15 Pa. Scans of the silica substrates are superimposed (dotted red lines). (b) Variation in the out-of-plane lattice parameter, a, with heater temperature during growth.

Any observed peak shifting may be related to the level of Sn incorporation or uniform (macro)strain effects, each of which may result in chemical and lattice disorder. Figure 4.5 (b) shows a decreasing out-of-plane lattice parameter, a, as the heater temperature during growth increases. This suggests that raising the heater temperature results in greater Sn substitution for In within the lattice as the ionic radius for $Sn^{4}+$ (0.81 Å) is smaller than that of In^{3+} (0.94 Å).

Calculation of the average vertical grain size was made by applying the Scherrer equation (Eqn. 3.1) to the ITO (222) peak. The results of these calculations are shown in table 4.3 and clearly shows an increase in the average vertical grain size as the heater temperature increases. At higher temperatures atoms within the film have excess energy which they use to diffuse throughout the material to form larger grains. Also, at higher temperatures it is common for grains to coalesce.

AFM studies on these films show an obvious change in film morphology as the substrate temperature increased (Fig. 4.6). It appears that the crystal size begins to increase forming elongated crystalline outgrowths (heater temperature of 600°C) instead of smaller grains seen in the films grown at lower temperatures. Analysis of these images using the AFM Nanoscope software allows us to make an estimate of the average root mean square surface roughness of these films. The root mean square surface roughness increased steadily from a minimum of 2.30±0.20 nm at 300°C, to a maximum at the highest substrate temperature of 3.30±0.15 nm over a $1\times1\mu m^2$ area at 600°C.

The heater temperature during growth was found to affect the electrical proper-

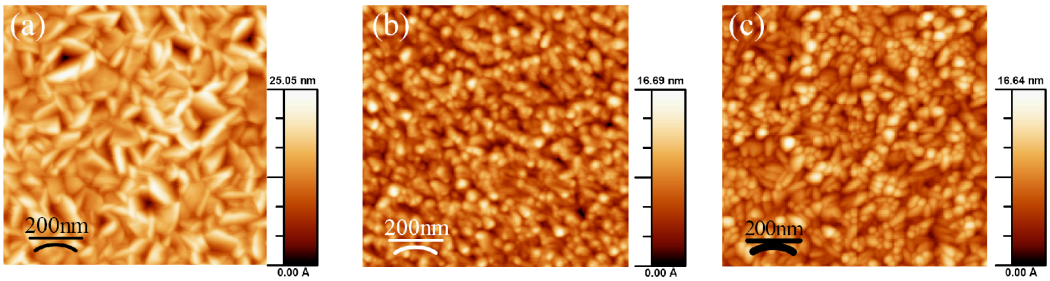

Figure 4.6: 1×1 μm^2 AFM micrographs showing the film evolution of ITO(10) thin films grown on silica glass substrates at varying heater temperatures, (a) 600°C, (b) 300°C and (c) unheated. A second order flattening procedure has been applied to these images to reduce scanner bow.

Table 4.3: Summary of the variation of calculated vertical grain size for the ITO(10) films grown at different heater temperatures. All films were deposited using an oxygen partial pressure of 0.15 Pa.

Heater temperature (°C)	Film thickness (nm)	Vertical grain size (nm)
300	290±11	27±2
400	280±11	38±2
500	295±10	41±2
600	290±11	49±2

ties of the ITO films. A selection of typical resistivity versus temperature curves for ITO films grown at varying substrate temperatures are shown in Fig. 4.7. ITO films grown on unheated substrates (labelled 25°C) show a negative temperature coefficient of resistance (TCR), i.e. semiconducting characteristics over the temperature range of 5 - 290 K. All films grown with a substrate temperature over 100°C exhibit a positive TCR, i.e. metallic characteristics.

Figure 4.8 shows the variation of ρ, n_c, and μ_H, as a function of the substrate temperature for the ITO films deposited using an oxygen partial pressure of 0.15 Pa. The resistivity of the ITO films decreased from 13.83×10^{-4} to 1.65×10^{-4} Ωcm as the heater temperature increased from 25 to 600°C. In these samples, n_c rose substantially when the heater temperature was increased from 25 to 100°C, after which the change was very small. The increase in n_c with heater temperature may be due to an increase in diffusion of Sn atoms from interstitial locations and grain boundaries into the In cation sites. The decrease in resistivity with increasing heater temperature can be explained by the fact that the crystallite size increases with increasing substrate temperature (table 4.3), thus reducing the grain boundary scattering. This is reflected by the rise in μ_H.

The magnetoresistance response of an unheated ITO(10) thin film is shown in Fig.

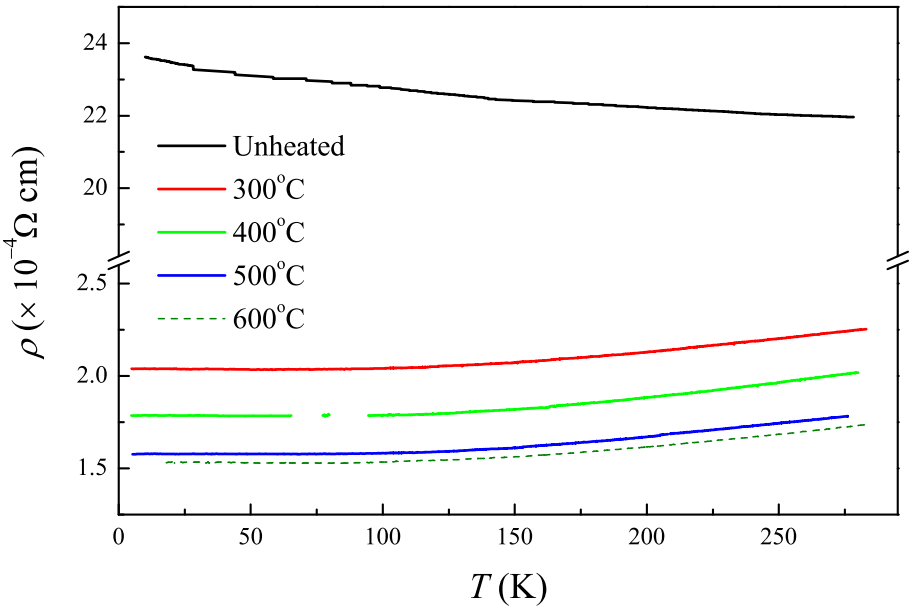

Figure 4.7: Resistivity (ρ) versus temperature curves for ITO(10) films grown at varying heater temperatures using an oxygen partial pressure of 0.15 Pa.

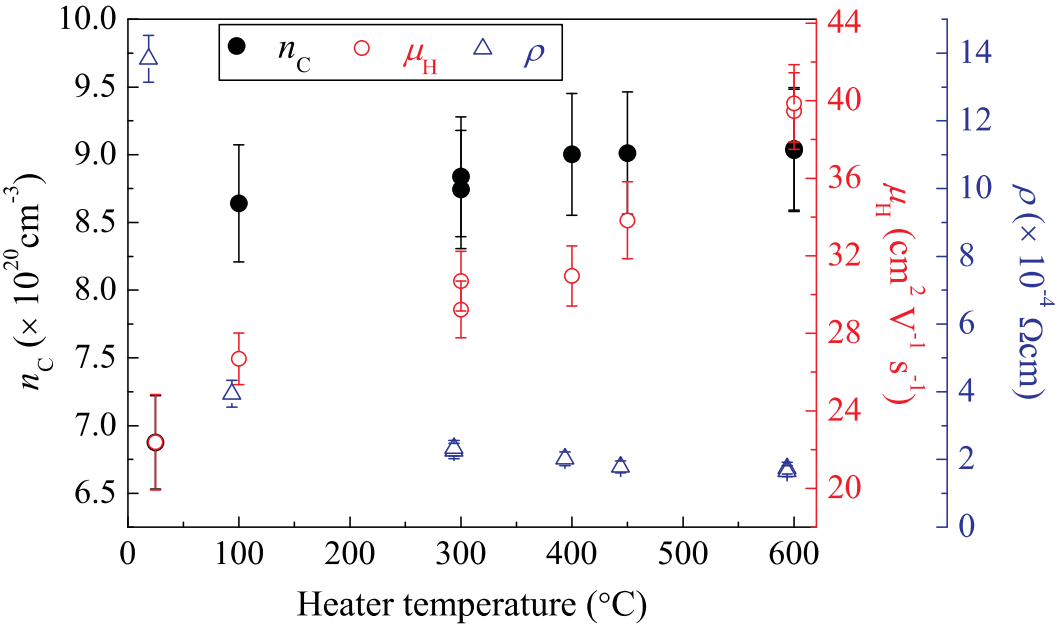

Figure 4.8: Variation of room temperature resistivity (ρ), carrier density (n_c), and Hall mobility (μ_H) as a function of heater temperature for the ITO(10) films deposited using an oxygen partial pressure of 0.15 Pa.

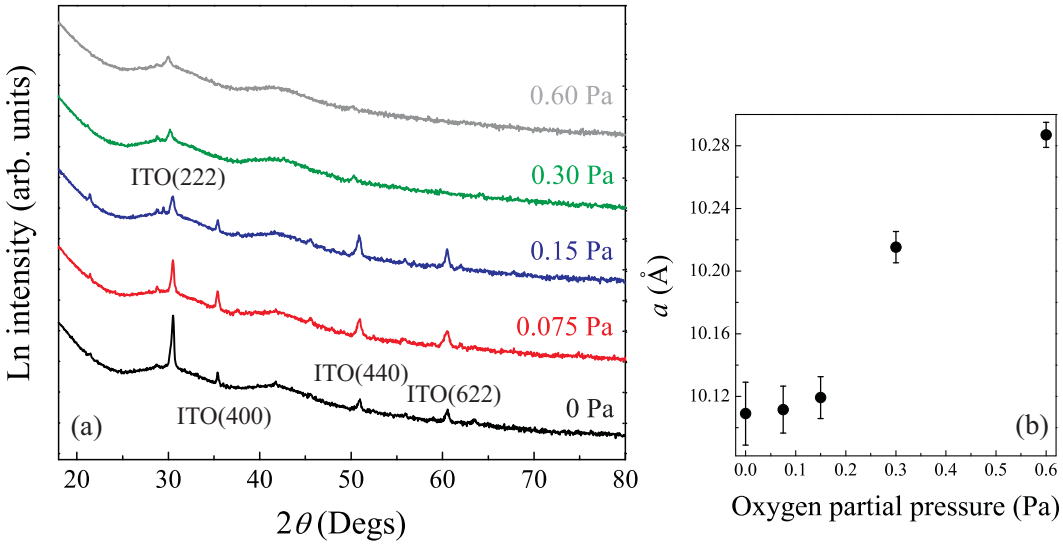

Figure 4.9: (a) X-ray diffraction patterns for 300 nm thick ITO films grown on silica glass at different oxygen partial pressures. The heater temperature was 300°C. (b) Variation in the out-of-plane lattice parameter, a, as a function of oxygen partial pressure.

4.4 (a) (green). MR becomes positive rather than more negative and is typical of an ordinary MR effect due to a Lorentz force. This is likely to be related to the changes in film microstructure as we now have a material which is richer in defects and grain boundaries. This may result in changes to the phonon periodicity which will naturally influence the scattering mechanisms contributing to the MR.

Effects of oxygen partial pressure

Figure 4.9 shows the θ-2θ XRD diffractogram for approximately 300 nm thick ITO(10) films grown on silica glass substrates at varying oxygen partial pressures (0 - 0.60 Pa) using a constant heater temperature of 300°C. With decreasing levels of oxygen, the ITO films become increasingly polycrystalline and the ITO (222) peak becomes very well pronounced. The out-of-plane lattice parameter is significantly reduced for films grown in increasingly oxygen deficient conditions and suggests a rise in the level of Sn substitution for In.

Table 4.4 summarises some of the properties of films grown at different oxygen partial pressures. The vertical grain size of the films decreases as oxygen partial pressure increases. Excess oxygen may migrate towards grain boundaries and interstitial sites, inhibiting the movement of grain boundaries and hence grain growth.

The oxygen pressure was also found to affect the electrical properties of the ITO films. Typical resistivity versus temperature curves for ITO(10) films grown at varying oxygen partial pressures are plotted in Fig. 4.10. It is clear that the film resistivity increases with the addition of more oxygen during the growth process. All films grown

Table 4.4: Summary of the variation of calculated vertical grain size for the ITO(10) films grown at different oxygen partial pressures. All films were deposited using a heater temperature of 300°C.

Oxygen partial pressure (Pa)	Film thickness (nm)	Vertical grain size (nm)
0.000	290±10	45±2
0.075	270±10	44±2
0.150	285±10	32±2
0.300	280±10	30±2
0.600	290±10	26±2

in oxygen partial pressure ≤ 0.15 Pa showed a positive TCR and were metallic, however, those grown at much higher levels of oxygen possessed a negative TCR and were semiconducting.

Figure 4.11 illustrates the variation of ρ, n_c and μ_H as a function of oxygen pressure for the ITO(10) films grown using a heater temperature of 300°C. As already mentioned above, resistivity is highest for films grown with the highest levels of oxygen partial pressure. This decrease in resistivity with decreasing oxygen pressure can be explained by the number of oxygen vacancies in the ITO films. The oxygen vacancies create free electrons in the films as one oxygen vacancy is capable of creating two extra electrons. The increase in the number of oxygen vacancies leads to an increase in carrier density and a consequent increase in conductivity. Growing the films in higher oxygen pressure leads to the filling of oxygen vacancies and hence a fall in the carrier concentration. Therefore, we can conclude that the carrier concentration in our ITO(10) films is strongly influenced by the concentration of oxygen vacancies as well as the level of Sn doping.

Investigations into the effects of oxygen partial pressure on pure In_2O_3 and ITO(5) were also carried out, and the results are summarised in table 4.5. Like the case of the ITO(10), electrical transport properties of these films deteriorated as the partial pressure of oxygen used during the growth process increased.

4.6.1 Brief discussion

From the XRD and AFM analysis, it has been shown that the grains become larger as the substrate growth temperature increases or oxygen partial pressure levels fall. Free electron carriers conduct faster in well-ordered crystalline structures, rather than in those with more grain boundaries which would act as blocking barriers in carrier transfer.

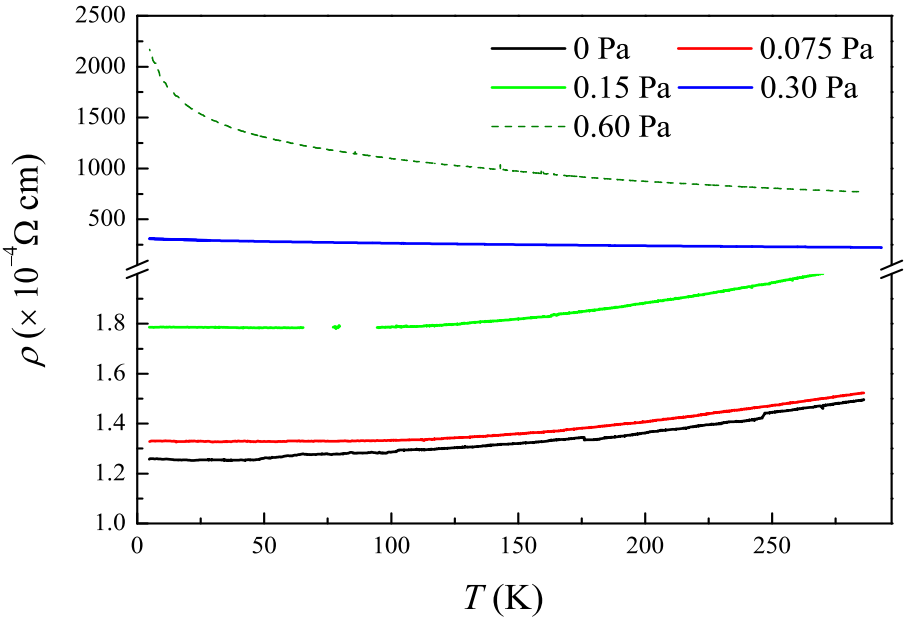

Figure 4.10: Resistivity (ρ) versus temperature curves for ITO(10) films grown at varying oxygen partial pressures using a heater temperature of 300°C.

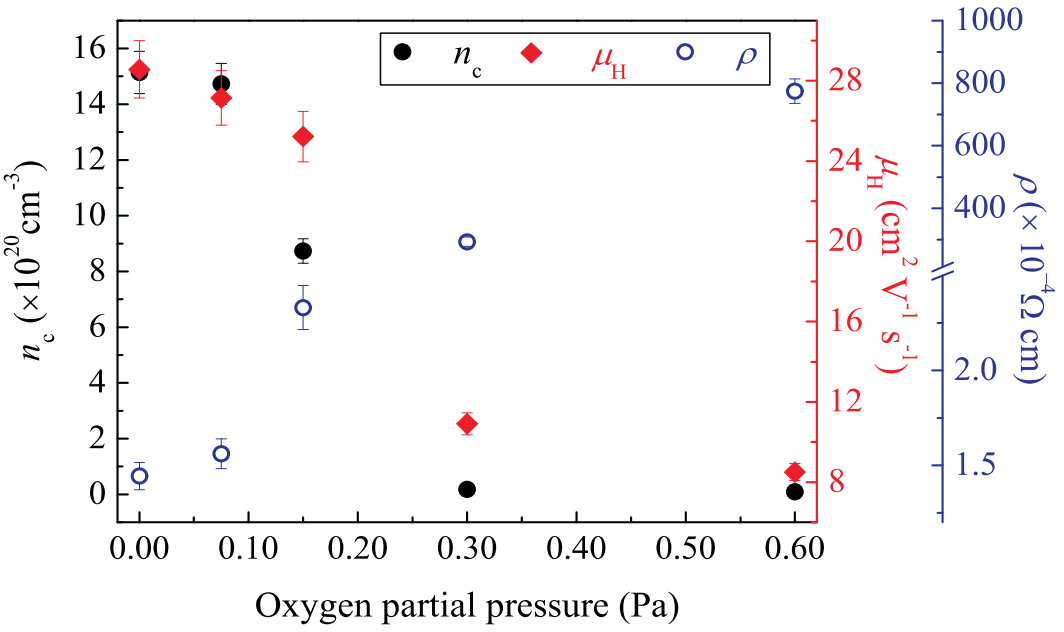

Figure 4.11: Variation of room temperature resistivity (ρ), carrier density (n_c), and Hall mobility (μ_H) as a function of oxygen deposition partial pressure for the films grown at 300°C.

If grain boundary scattering is assumed to be the predominant scattering mechanism we find that ρ can be expressed by combining Eqns. 4.2 and 4.4;

$$\rho = \frac{1}{N\mu_H q} = \frac{1}{(ne)eD(2\pi m^* kT)^{-1/2} exp\left(-\frac{e\phi_b}{kT}\right)}. \tag{4.8}$$

Therefore, ρ is inversely proportional to the grain size, D. We have seen that the average vertical grain size increases with increasing substrate temperature and subsequently ρ decreases, however, it does not follow an inverse relationship. As for the films grown with varying oxygen partial pressure, increasing oxygen levels led to large increases in ρ. It is likely that in the regions with excess oxygen, the oxygen may do any of the following: (i) incorporate into the bixbyite lattice; (ii) become segragted to grain boundaries; or (iii) become complexed with Sn ions, forming Sn^+O^-. Excess oxygen can therefore lead to two types of electron scattering centres : those which form SnO complexes and distort the lattice, creating neutral scattering centres, and those segregated to become charge carrier traps, therefore acting as negatively charged scattering centres.

4.7 Summary and Conclusions

Transparent In_2O_3 and Sn-doped In_2O_3 films with n-type conductivity were successfully made using DC magnetron sputtering. The results show that the progressive increase in the level of Sn doping leads to increasing carrier concentration and improved electrical properties. Variation of growth parameters such as the heater temperature and oxygen partial pressure allowed the tuning of the electrical properties: in general, higher heater temperatures and lower oxygen partial pressures lead to more crystalline films with greater levels of electrically active substitutional Sn, and as a result, much improved electrical characteristics. Experiments where the oxygen partial pressure was varied highlighted the role that oxygen vacancies play in determining the electrical properties of the films. Excess oxygen is seen to be detrimental to the conductive nature of the films, and is believed to be the cause of a rise in the density of electron scattering centres.

With this level of understanding for the In_2O_3 and ITO systems, the goal is to now use these materials for the development of a dilute magnetic oxide material by doping with a variety of transition metal ions. The next 3 chapters will tell this story.

Table 4.5: Summary of the room temperature transport properties (resistivity, ρ, carrier concentration, n_c, and electron mobility, μ_H) of In_2O_3 and ITO(5) thin films grown under various oxygen partial pressures using a heater temperature of 300 °C.

Material	Oxygen partial pressure (Pa)	ρ (Ω cm)	n_c (cm^{-3})	μ_H ($cm^2\ V^{-1}\ s^{-1}$)
In_2O_3	0.000	$2.71\pm0.15\times10^{-3}$	$6.87\pm0.15\times10^{19}$	33.50 ± 0.12
In_2O_3	0.075	$5.55\pm0.11\times10^{-3}$	$4.54\pm0.17\times10^{19}$	24.79 ± 0.16
In_2O_3	0.150	$3.00\pm0.32\times10^{-1}$	$7.86\pm0.26\times10^{18}$	5.65 ± 0.20
In_2O_3	0.300	$2.41\pm0.08\times10^{1}$	$5.18\pm0.47\times10^{17}$	4.99 ± 0.26
In_2O_3	0.600	$5.85\pm0.07\times10^{1}$	$1.43\pm0.54\times10^{16}$	3.03 ± 0.31
ITO(5)	0.000	$2.53\pm0.09\times10^{-4}$	$7.00\pm0.08\times10^{20}$	35.23 ± 0.15
ITO(5)	0.150	$1.45\pm0.11\times10^{-3}$	$1.83\pm0.08\times10^{20}$	23.58 ± 0.14
ITO(5)	0.300	$2.54\pm0.17\times10^{-2}$	$1.39\pm0.12\times10^{19}$	17.59 ± 0.24

Bibliography

[1] K. L. Chopra, S. Major, D. K. Pandya, Thin Solid Films 102, 1, (1983).

[2] G. Rupprecht, Z. Phys. 139, 504, (1954).

[3] F. S. Galasso, Structure and properties of inorganic solids. Oxford New,York, Toronto, Sydney, Branschweig, Pergamon Press. pp. 90-102, (1970).

[4] N. Nadaud, N. Lequeux, M. Nanot, J. Jov, T. Roisnel, J. Solid State Chem. 135, 140-148, (1998).

[5] P.Nath, R.Bunshah, Thin solid films 69, 63, (1980).

[6] I. Hamberg, C. Granqvist, Journal of Applied Physics, 60, R123, (1986).

[7] L. Gupta, A. Mansingh, P. K. Srivastava, Thin Solid Films, 176, 33-44, (1989).

[8] R. Bel Hadj Tahar, T. Ban, Y. Ohya, Y. Takahashi, J. Appl. Phys. 83, 5, (1998).

[9] G. Frank, H. Kostlin, Appl. Phys. A27, 197-206, (1982).

[10] H. Kostlin, R. Jost, W. Lems, Phys. Stat. Sol. (a)29, 87-93, (1975).

[11] H. Hartnagel, A. Dawar, A. Jain, C. Jagadish, Institute of Physics Publishing, (1995).

[12] J. Seto, Journal of Applied Physics, 46, 5247, (1975).

[13] V. Johnson, K. Lark Horovitz, Physical Review, 71, 374, (1947).

[14] K. Ramaiah, V. Raja, A. Bhatnagar, R. Tomlinson, R. Pilkington, A. Hill, S. Chang, Y. Su, F. Juang, Semiconductor Science and Technology, 15, 676, (2000).

[15] S-S. Kim, S-Y. Choi, C-G. Park, H-W. Jin, Thin Solid Films, 347, 155-160, (1997).

[16] Y. Hoshi, Y. Kiyomura, Thin Solid Films, 411, 36-41(2002).

[17] C. Guillen, J. Herrero, Thin Solid Films, 510, 260-264, (2006).

[18] N. Mori, S. Ooki, N. Masubuchi, A. Tanaka, M. Kogoma, T. Ito, Thin Solid Films, 411, 6, (2002).

[19] G. M. Zhen, S. Hi-Gang, R. Job, L. Pa-Shen, W. R. Fahrner, Chinese Physical Letters, Vol. 22, No. 5, 1228, (2005).

[20] L. J. Meng, M. P. D. Santos, Thin Solid Films, 322, 56, (1998).

[21] S. Takayama, A. Tanaka, T. Sugawara, T. Himuro, Jpn. J. App. Phys. 41, 619-621, (2002).

[22] R. P. Howson, I. Safi, G. W. Hall, N. Danson, NIMB, 121, 96-101, (1997).

[23] H-C. Lee, J-Y. Soo, Y-W. Choi, D-W. Lee, Vacuum, 72, 269-276, (2004).

[24] N. Kikuchi, E. Kusano, H. Nanto, A. Kinbara, H. Hosono, Vacuum 59, 492-499, (2000).

[25] C. H. L. Weijtens, J. Electrochem. Soc. 138, 3432, (1991).

[26] G. Franz, B. Lange, S. Sotier, J. Vac. Sci. Tehnol. A, 19(5), (2001).

[27] S. Ray, R. Banerjee, N.Basu, A. K. Batabayal, A. K. Barua, J. Appl. Phys. 54, 3497, (1983).

[28] H. Nanto, T. Minami, S. Orito, S. Takata, J. Appl. Phys. 63, 2711, (1988).

[29] L. J. Meng, M. P. D. Santos, Thin Solid Films, 289, 65, (1996).

[30] H. Kim, J. S. Horwitz, W. H. Kim, Z Kafafi, D. B.Chrisey, Materials Research Society Symposium Proceedings, 780, 21-32, (2003).

[31] C. Coutal, A. Azema, J.C. Rostau, Thin Solid Films, 288, 248-253, (1996).

[32] F. O. Adurodija, H. Izumi, T. Ishihara, H. Yoshioka, H. Matsui, M. Motoyama, Jpn. J. App. Phys. 38, 2710-2716, (1999).

[33] L. A. Ryabova, V. S. Salun, I. A. Serbinov, Thin Solid Films 92, 327, (1982).

[34] K. Nishio, T. Sei, T. Tsushiya, J. Mater. Sci. 31, 1761, (1996).

[35] Y. Takahashi, H. Hayashi, Y. Ohya, Mater. Res. Soc. Symp. Proc. 271, 401, (1992).

[36] P. Nath, R. F. Bunshah, B. M. Basol, O. M. Staffsud, Thin Solid Films 72, 463, (1980).

[37] I. A. Rauf, J. Appl. Phys. 79, 4057, (1996).

[38] H-C. Lee, Applied Surface Science, 252, 2647-2656, (2006).

[39] M. Kamei, Y. Shigesato, S. Takaki, Thin Solid Films 259, 38, (1995).

[40] J. C. C. Fan, F. J. Bachner, J. Electrochem. Soc. 122, 1719, (1975).

Chapter 5

The Quest for a Dilute Magnetic Oxide

This chapter begins by discussing previous work in the field of dilute magnetic oxides. Common problems associated with the characterisation of these materials which continue to puzzle the wider scientific community are also introduced. The chapter closes with magnetic and magnetotransport characterisation measurements made on Co-doped In_2O_3 and ITO films.

5.1 Introduction

Chapter 1 has already expressed the principal goal in the field of DMS and DMO materials for implementation within the emerging field of spintronic device applications: the capability to exhibit substantial carrier spin polarisation at and above room temperature.

The large electronegativity of oxygen in DMOs is expected to produce strong *sp-d* exchange interactions between band carriers and localised spins [1]. As a result, the wide bandgap oxides are considered to be well suited to the cause as they are capable of providing a multi-functional foundation for next generation spintronic devices. The combination of high optical transparency, electrical conductivity and potential ferromagnetic behaviour opens up many new attractive avenues for the future.

This chapter introduces the experimental techniques used to investigate the magnetic behaviour of DMS and DMO systems. An extensive review on DMO materials, in particular In_2O_3 and ITO, is given, and a discussion on the more popular systems studied such as ZnO and TiO_2 is provided. A dilute magnetic oxide system based on In_2O_3 and ITO is then developed and described.

5.2 Examination of ferromagnetism

5.2.1 Magnetometry

Early experiments relied heavily on SQUID magnetometry to classify the origins of magnetism in DMOs. However, it is difficult to distinguish "intrinsic" ferromagnetism from that which is "extrinsic", such as ferromagnetic precipitations or secondary phases because all the magnetisation signals are measured together, i.e. it is a volume sensitive measurement. Therefore, magnetisation alone is not enough to verify the formation of a "true" DMO.

5.2.2 Magneto-optical effects

As a consequence of a coupling interaction between *s*- and *p*-carriers in the host oxide/semiconductor with the *d*-electrons of the TM ions, photoexcited charge carriers in the host oxide show a sizeable magneto-optical effect. MCD is the difference in the absorption coefficients for two circularly polarised waves of light and is proportional to the energy derivative of the absorption coefficient. Therefore, MCD is largest around the onset of absorption. This gives a clear indication of the extent to which the states involved in the transition at that particular energy are influenced by the magnetism. More on this matter will follow in chapter 7.

5.2.3 The Anomalous Hall Effect

For an introduction to the Hall effect, the reader is referred to reference [2] of this chapter, which is the original report of Edwin H. Hall's momentous discovery. In addition to the ordinary Hall effect (OHE) that is present in all semiconductors and metals, there is an additional voltage present in magnetic materials which is proportional to the magnetisation, called the "Anomalous Hall effect" (AHE). It was found that the Hall resistivity ρ_{xy} in an applied perpendicular magnetic field $\mu_0 H_z$ is qualitatively different in ferromagnetic and non-magnetic conductors. In the latter, ρ_{xy} increases linearly with $\mu_0 H_z$ as expected from the Lorentz force; in ferromagnets, however, ρ_{xy} initially increases steeply in weak $\mu_0 H_z$, but saturates at a large value that is nearly independent of $\mu_0 H_z$. The point of saturation is roughly proportional to the magnetisation M_z. Therefore, ρ_{xy} in ferromagnetic materials can be expressed as

$$\rho_{xy} = R_0 \mu_0 H_z + R_s M_z, \tag{5.1}$$

where the first term denotes the OHE and the second the contribution from the spontaneous magnetisation (AHE). This additional term to the electron group motion has been attributed to the asymmetric carrier scattering by magnetic impurities in the presence of a spin-orbit interaction [3] [Fig. 5.1 (b)]. Imagine that each carrier has an associated orbital angular momentum about the magnetic scattering centre, the sign of which depends on whether the carrier passes on one side or the other. The spin-orbit coupling between the orbital angular momentum of the carrier and spin angular momentum of the magnetic impurity means that the electron carriers will find it energetically favourable to pass on one side rather than the other, resulting in the asymmetry in scattering. Because of this term, it was believed that ferromagnetic ordering will generate the AHE, and so it therefore became sought after as evidence for the direct manifestation of intrinsic ferromagnetism in DMO materials. An encouraging sign for detecting a genuine intrinsic ferromagnetic signal using AHE measurements is the quantitative scaling with the magnetisation loops. This has been reported in Co:TiO_2 [3–5] [see Fig. 5.1 (c)] and Co:ZnO [6] systems.

Observing the AHE alone is not adequate to conclude a material is an intrinsic DMO. The AHE response has also been detected in samples where the presence of metallic Co clusters has been confirmed [7, 8]. They conclude that the weak AHE originates from the spin-interaction in close proximity to the clustered Co, in complete contrast to Toyosaki's proposal described and illustrated in Fig. 5.11 (a) and (b). Surprisingly, the AHE effect appears in the non-magnetic material $Zn_{0.985}Cu_{0.015}O$ [9].

Figure 5.2 (a) - (c) summarises the effects described in sections 5.2.1 to 5.2.3 in trying to determine the nature of magnetism in the DMO systems along with the general phenomenological scheme behind each characterisation technique [10].

With the difficulty in gaining access to MCD-centred techniques such as optical

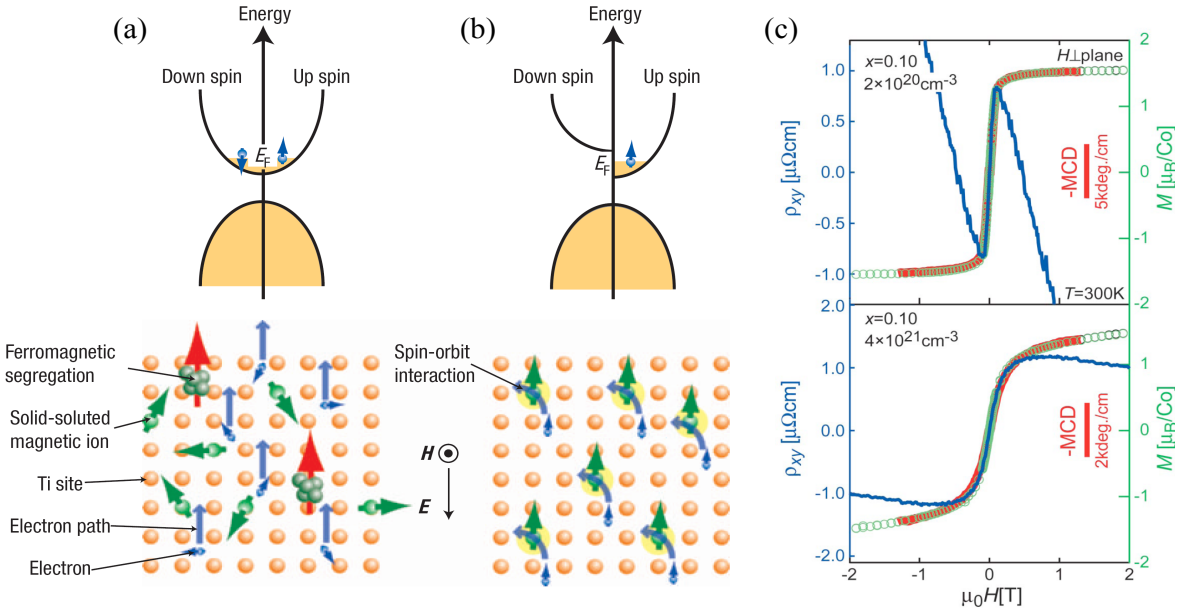

Figure 5.1: Sources of extrinsic and intrinsic ferromagnetism in DMO materials proposed in reference [3]: (a) ferromagnetic secondary phase (red arrows) segregates causing ferromagnetic magnetisation, regardless of the non-ferromagnetic ordering of the incorporated magnetic dopants (green arrows); (b) an exchange interaction between magnetic dopants and charge carriers (blue arrows) results in ferromagnetic ordering. Spin-orbit interaction between the two leads to ferromagnetic spin polarisation of charge carriers, generating an AHE (light blue curves); (c) quantitative scaling of the magnetic field dependence of MCD (red curve), resistivity (blue curve) and magnetisation (green curve) for Co:TiO_2 samples at room temperature with varying carrier concentrations. After references [3, 4].

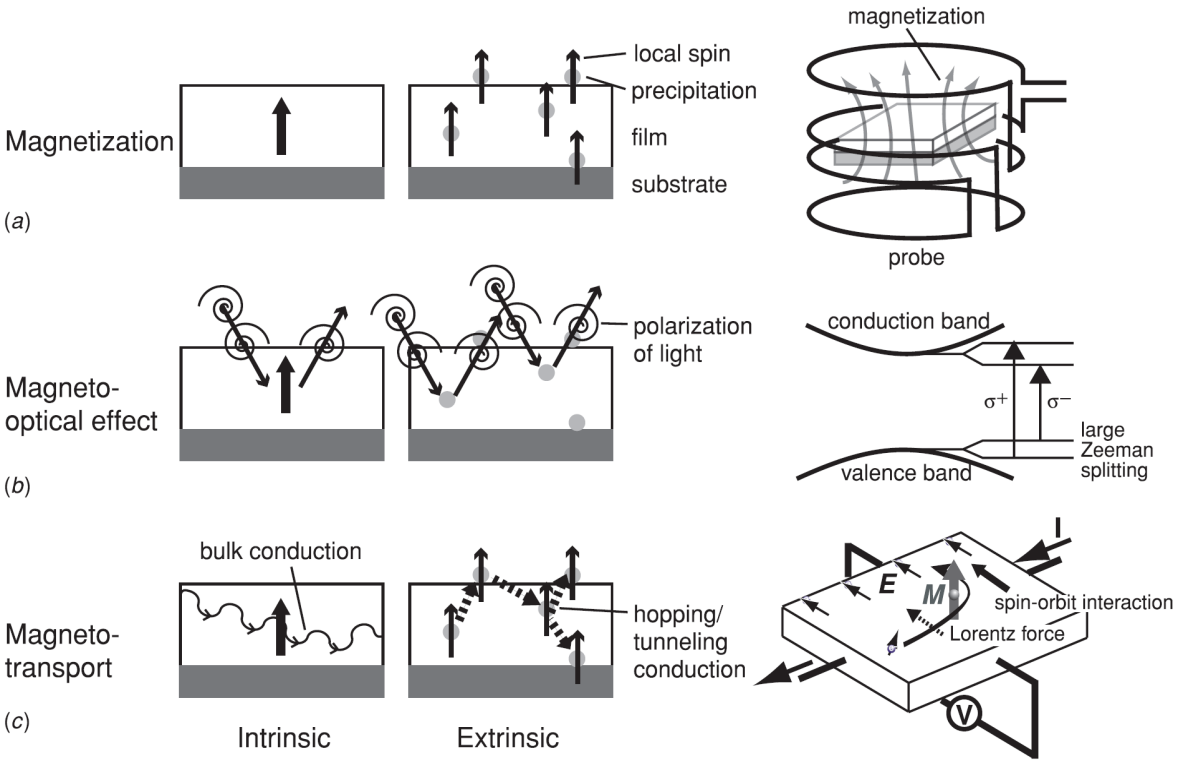

Figure 5.2: Schematic diagrams of intrinsic and extrinsic sources of ferromagnetism for (a) magnetisation, (b) magneto-optical effects, and (c) magneto-transport measurements. The left hand side and central diagrams represent intrinsic and extrinsic ferromagnetism respectively. The diagrams on the right show the phenomenological scheme for each measurement. After reference [10].

and x-ray MCD, many researchers must make do with what they have. In this volume of work we have managed to use both forms of MCD characterisation (see chapters 6 and 7), as well the more widely accessible techniques such as x-ray diffraction, SQUID magnetometry, transport measurements, *etc.*

5.3 Previous work

5.3.1 Ferromagnetism in In_2O_3 and ITO thin films

Compared to ZnO and TiO_2, In_2O_3 and ITO are relatively unexplored materials for dilute magnetic oxide materials. However, a host of authors have published reports on the observation of room temperature ferromagnetism in a variety of TM-doped and undoped In_2O_3-based materials; table 5.1 summarises a selection of these results.

One of the most important practical goals of this research area is to produce a magnetic oxide system with *tunable* ferromagnetic behaviour, capable of exhibiting independently controlled carrier and magnetic doping along with a high Curie temperature. Early work by Philip and co-workers identified Cr-doped In_2O_3 as a material system where electrical and magnetic behaviour, from ferromagnetic metal-like to ferromagnetic semiconducting to paramagnetic insulator, can be controllably tuned through the defect concentration [11]. They proposed that both the electronic and magnetic properties can be enhanced by making the films more oxygen deficient. By altering the oxygen partial pressure during the growth process, the investigators were able to tune the defect concentration and hence the carrier concentration. The fall in n_c results in both electrical and magnetic phase transitions. The authors estimate a critical concentration of oxygen vacancies of 6.0×10^{22} cm^{-3} and equivalent carrier concentration of 2.0×10^{19} cm^{-3} to observe ferromagnetism.

Kim *et al.* investigated the effects of carrier concentration on the magnetic and magnetotransport behaviour of Cr-doped ITO(10) films. They found that the anomalous Hall effect only appeared in the presence of a very high carrier concentration (1.32×10^{21} cm^{-3}) and again this pointed towards a carrier mediated ferromagnetic response [12].

Using density-functional calculations, Raebiger *et al.* showed that long range ferromagnetic Cr-Cr coupling can exist in Cr-doped In_2O_3 films, via the inclusion of extrinsic dopants in the form of Sn, which will provide free electrons [13] (see Fig. 5.3). Essentially, the authors present an idea where the ferromagnetism can be turned "on" and "off" simply by tuning the carrier concentration via external Sn doping. In the absence of free carriers, Cr-doped In_2O_3 is paramagnetic, whereas in the degenerate doping regime (using Sn), Cr-doped In_2O_3 is ferromagnetic. The onset of ferromagnetism occurs as the free-electron concentration reaches half of the Cr dopant concentration.

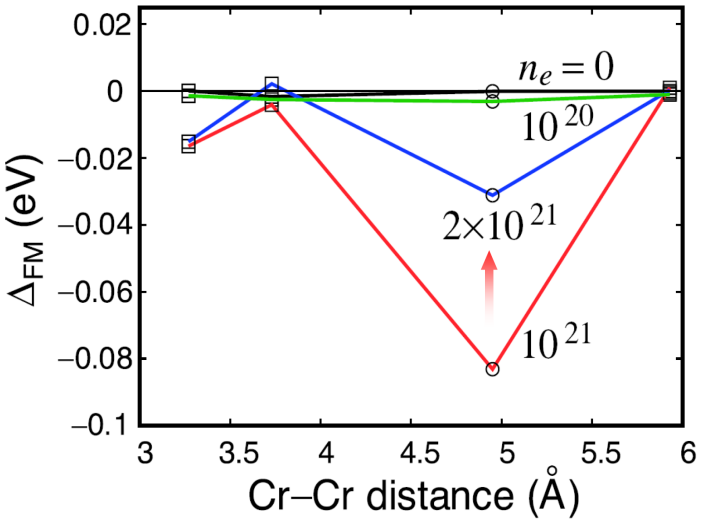

Figure 5.3: Ferromagnetic stabilisation energy, Δ_{FM}, at room temperature as a function of Cr-Cr distance, r. The black line denotes Δ_{FM} in the absence of free carriers (n_e=0), while green, red and blue lines correspond to electron concentrations of n_e= 10^{20}, 10^{21} and 2×10^{21}cm^{-3} respectively. The red arrow indicates the shift in Δ_{FM} after exceeding the limit for n_e. After reference [13].

Jiang *et al.* showed experimental evidence consistent with the predictions made by Raebiger, whereby the ferromagnetism of Mn-doped In_2O_3 films show reversible behaviour, which can be switched between on and off by controlling the carrier density [14]. In addition to this, increasing the carrier concentration through additional Sn doping led to marked increases in ferromagnetic response in Cr-doped In_2O_3 films.

Panguluri *et al.* recently opened up another dimension to the discussions surrounding the origin of magnetism in these oxide materials, particularly in those which are pure and undoped [15]. As-deposited samples of pure, undoped In_2O_3 were non-magnetic, but those doped with Cr were weakly ferromagnetic at room temperature. After a vacuum annealing treatment, both sets of samples are ferromagnetic, showing the need for a high concentration of oxygen vacancies to mediate magnetism. To investigate the coupling interaction between the charge carriers and the ferromagnetic moment in In_2O_3 and Cr-doped In_2O_3 films, point contact Andreev reflection was used. This revealed a spin polarisation of approximately 50% at 1.3 K in both pure In_2O_3 and the samples doped with Cr. In addition to this, a model was described which predicts that room temperature ferromagnetism should emerge in undoped In_2O_3 above a critical carrier concentration of 4.0×10^{19} cm^{-3}. The model also predicts a carrier concentration dependent T_C, as was suggested by Philip *et al* [11]. These findings raised doubts over the necessity to have transition metal dopants to produce carrier-mediated ferromagnetism.

Contrary to the findings described above where increasing carrier concentration generally leads to improved magnetic properties, Wang *et al.* have shown that in Mn-doped In_2O_3, increasing the Sn level leads to a degradation of the magnetic response [16]. In

the $In_{1.90-x}Mn_{0.1}Sn_xO_3$ samples, increasing x from 0 to 0.06 resulted in a suppression of the coercive field. Furthermore, the magnetisation loops resembled something more like a paramagnetic material. It was suggested that the introduction of Sn into the system caused a larger amount of magnetic ions to couple antiferromagnetically. This may be connected to the fact that the Sn and TM dopant ions are both competing for the In lattice sites.

Codoping TM-doped In_2O_3 with Cu has also been investigated [17, 18]. In particular, the magnetic properties of (Cu/Fe)-codoped In_2O_3 (IFCO), are not directly related to the Cu doping. Using detailed analysis of anomalous Hall effect measurements, Yu *et al.* ascribe the ferromagnetic properties of their IFCO samples to an exchange coupling between magnetic ions which is mediated by mobile electrons rather than localised ones, i.e. much like the behaviour expected for a typical ferromagnet where the anomalous Hall coefficient is proportional to the carrier density. In contrast, Brize *et al.* have reported worsened magnetic properties of (Cu,Mn)-doped In_2O_3 thin films, suggesting that doping with Cu promotes the formation of undesirable precipitates which degrade the magnetic properties [19].

Stankiewicz *et al.* and more recently Subias *et al.*, have performed extensive studies into the Co-doped In_2O_3 and ITO(10) systems by studying the local structural environment of Co through x-ray absorption studies at the Co K-edge in conjunction with x-ray photoelectron spectroscopy [21, 22] (Fig. 5.4). It was concluded that different contributions of oxidised (Co^{2+}) and metallic (Co^0) cobalt to the observed ferromagnetism are found depending on the host oxide and the Co doping content. The threshold was estimated to be less than 7.0 at.% Co, after which the Co doping is no longer within the dilute limit (Co substitutes for In lattice sites) and metal Co clusters form. Magnetisation characterisation of these samples showed a lack of saturation at low temperatures even up to magnetic fields of 5 T, clearly indicating that a large portion of the Co^{2+} ions are giving a paramagnetic response, and not contributing to the ferromagnetism directly.

There have been a number of surprising results where room temperature ferromagnetism has been observed in pure, undoped oxide materials (see section 5.2.3): In_2O_3 is one of these. We have described above that Panguluri *et al.* have even estimated the extent of spin polarisation in pure In_2O_3. Hong *et al.* reported that room temperature ferromagnetism is present in a host of undoped oxides [31]. The controversy surrounding these kinds of reports will be discussed further later, where the sources of error in measuring nanomagnetism will be also be raised.

Some of these results have caused former supporters and pioneers of this area to turn on their previous ideas and look at the situation from another angle. J. M. D. Coey in particular is certainly one who has recently begun to change his attitude towards these materials (see section 5.4). Recently, Venkatesan *et al.* reported measurements on Fe- and Mn-doped ITO(10) films where it is claimed that the ferromagnetism in the Fe-doped samples is due to secondary ferromagnetic Fe_3O_4 grains, but are unable to

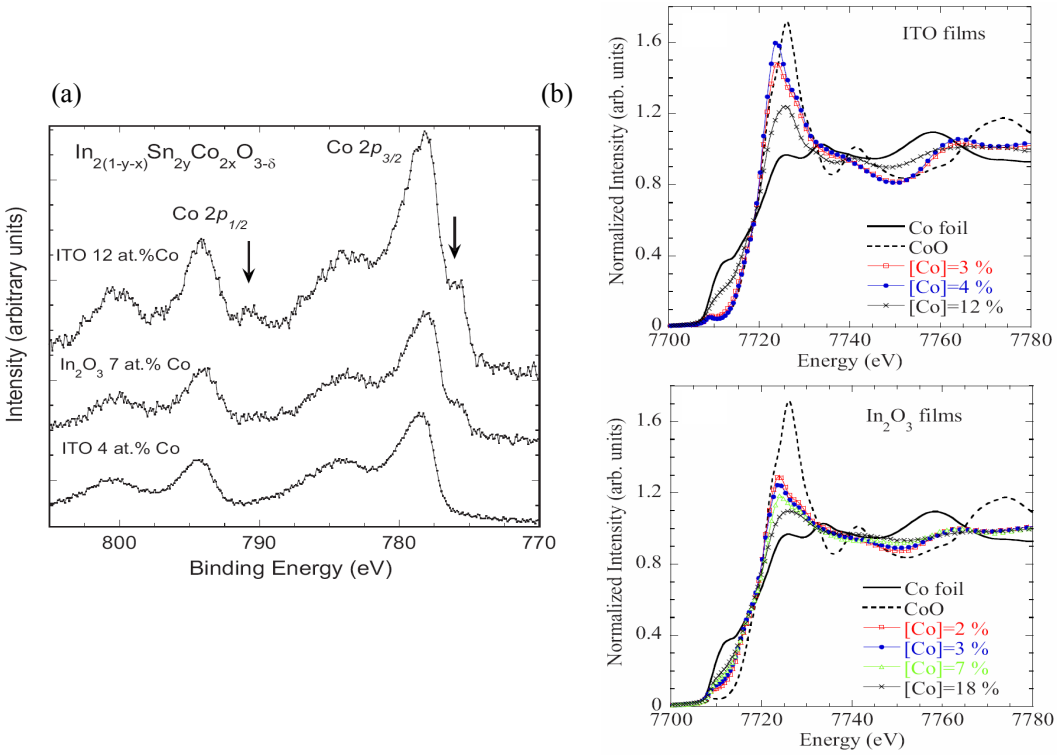

Figure 5.4: (a) X-ray photoemission spectra at the Co $2p$ core-level for varying levels of Co doping in ITO(10) samples. Increasing the level of Co leads to the formation of metallic Co clusters, implied by the extra features appearing in the spectra, and indicated by the arrows. (b) X-ray absorption near edge structure analysis at the Co K-edge for ITO(10) and In_2O_3 films for varying levels of Co content. Again, low doping levels reveal spectra which resemble divalent CoO, whereas, high levels of doping lead to features emerging in the spectra which would suggest Co metal segregation. After reference [22].

identify the source of the magnetism in those doped with Mn [15]. The authors conclude by claiming that these materials cannot be regarded as a DMS in the accepted sense.

It is clear with the varying results described above that there is still much to understand regarding the origins of magnetism in these materials.

Table 5.1: Summary of a selection of TM-doped In_2O_3 and ITO thin films. DCMS = DC magnetron sputtering, RFS = radio frequency sputtering, PLD = pulsed laser deposition, RE = reactive thermal evaporation.

System	TM content (at.%)	Substrate	Growth technique	T_C (K)	Magnetisation features ($300K$)	Reference
Cr:In_2O_3	2.0	(0001) sapphire	RFS	...	0.50 emu/cm^{-3}	[15]
Cr:ITO	5.0	Si/SiO_2	PLD	...	0.70 emu/cm^{-3}	[12]
Cr:In_2O_3	2.0	Si/SiO_2	RE	...	1.5 μ_B/Cr	[11]
Cr:In_2O_3	3.0	*c*-sapphire	PLD	...	0.95 μ_B/Cr	[14]
Cr:ITO	3.0	*c*-sapphire	PLD	...	2.10 μ_B/Cr	[14]
Cr:ITO	2..0	(0001) sapphire	Sol-gel	...	0.22 μ_B/Cr	[23]
Ni:In_2O_3	5.3	MgO	PLD	>400	0.40-0.70 μ_B/Ni	[24]
Ni:In_2O_3	5.3	sapphire	PLD	>400	0.70 μ_B/Ni	[24]
Ni:In_2O_3	6.0	...	Sol-gel	...	0.06 μ_B/Ni	[25]
Ni:ITO	6.0	...	Sol-gel	...	0.03 μ_B/Ni	[25]
Mn:ITO	5.0	(0001) sapphire	RE	$\gg$300	0.80 μ_B/Mn	[20]
Mn:ITO	5.0	Si/SiO_2	RE	$\gg$300	0.08-0.12 μ_B/Mn	[20]
Mn:ITO	5.0	Silica glass	RFS	>400	8.0 emu/cm^{-3}	[26]
Mn:ITO	3.2	Silica glass	Sol-gel	$\geq$600	0.39 μ_B/Mn	[27]
Mn:In_2O_3	5.0	*c*-sapphire	PLD	...	0.10 μ_B/Mn	[14]
Mn:ITO	5.0	*c*-sapphire	PLD	...	0.18 μ_B/Mn	[14]
Co:ITO	8.0	Silica glass	DCMS	$\leq$40	0.26 μ_B/Co	[29]
Co:ITO	30.0	Fused quartz	DCMS	...	1.10μ_B/Co$\rightarrow$metal clusters	[30]
Co:In_2O_3	3.0	Fused quartz	DCMS	...	0.06μ_B/Co	[22]
Co:ITO	4.0	Fused quartz	DCMS	...	0.02μ_B/Co	[22]
Co:ITO	12.0	Fused quartz	DCMS	...	1.05μ_B/Co$\rightarrow$metal clusters	[22]

5.3.2 Other ferromagnetic TM-doped oxide systems

It is not possible, nor entirely necessary for a long discussion on the other ferromagnetic DMOs which have been reported. Due to the rapidly growing number of reports in this field, some references have been overlooked. Instead, the reader is referred to other, more comprehensive reviews, and the references within, on the DMO family [10,33–36].

TM:ZnO has been adopted as the prototypical model DMO system (analogous to the GaMnAs DMS system) and has received the majority of attention from researchers globally. The problem has been approached both experimentally and theoretically. Pan *et al.* provided a detailed overview of the recent progress in the TM-doped ZnO system, highlighting the importance of influential factors such as growth techniques, substrate, strain and post-annealing effects and the role that codoping can play [36]. Here, we focus on those systems which have been doped using Co (Co:ZnO in particular), as this is the dopant which has been studied in detail in this thesis.

A myriad of studies are available on the Co-doped ZnO system where the investigators strive to determine the exact role of the TM dopants. Is it that they are uniformly distributed and substituting for host matrix ions, or perhaps, are they forming metal or secondary oxide phase clusters or lying in interstitial positions? In most cases where extrinsic ferromagnetism has been claimed as the source of magnetism in Co:ZnO, the investigators report clustering of Co [38]. However, antiferromagnetic CoO has also been reported to result in weak ferromagnetism in Al-doped Co:ZnO [39]. Here, Dietl *et al.* argue that the magnetic behaviour in their films are a result of uncompensated spins at CoO nanocrystal surfaces formed via spinodal decomposition, and also from Co precipitates exchange biased by the surrounding Co-rich Co:ZnO lattice. Chang *et al.* attribute the lack of ferromagnetism in their Co:ZnO samples to the lack of free electron carriers and direct Co-Co interactions [40]. Through first-principle calculations, they conclude that interactions between substitutional Co atoms (at Zn lattice sites) only induces antiferromagnetic coupling, similar to that described above by Dietl and also later suggested through XMCD studies [41]. The authors suggest that in addition to free charge carriers, an exchange interaction between substitutional and interstitial Co through cluster formation is required for high T_c ferromagnetism. So, from these two reports, it is implied that magnetism in Co:ZnO can only come about via an extrinsic source.

Once again, from first-principle calculations of the oxygen surfaces in Co:ZnO, Sanchez *et al.* show that the spin polarisation induced by the substitutional Co atoms is enhanced depending on the proximity to the surface [42]. It is also predicted that the oxygen atoms are spin polarised only at the surface, and not the bulk, and that this surface stability is reinforced by Co. This polarised oxygen surface may also explain the spontaneous magnetisation reported in ZnO (and indeed others) structures in the absence of TM dopants [43].

To exercise the feasibility that uncompensated spins at the surface of CoO nanoclusters embedded in ZnO are a source of magnetism, Hanafin *et al.* used a combination of

density-functional theory and Monte Carlo simulations to show that these finite sized particles (of various shapes) cannot be considered as the origin of ferromagnetism in Co:ZnO [44].

However, with each of the scenarios described above, there are many simplifications, assumptions and parameterisations of the possible magnetic interactions within the Co:ZnO system. These models will neglect important parameters such as grain boundaries, interfaces with the substrate (Co clusters have been reported at the interface between film and substrate in Co:ZnO [8]), as well as intrinsic defects, each of which can alter the local magnetic order.

Experimentally, we must consider factors such as the growth conditions, sample morphology and microstructure in addition to the spatial distribution of the Co atoms when determining the magnetic properties. In particular, there is now an emerging view that samples of Co:ZnO with high structural quality (and uniform Co distribution as some report above) will not result in long-range ferromagnetism at high temperature, and that the magnetism may be related to structural [45] or point-defects (e.g. oxygen vacancies, *etc*,.) [46].

As with the Co:ZnO scenario, the Co:TiO_2 system is intensely debated. After initial reports of intrinsic ferromagnetism in this system [3,8,47,48], the general consensus has now become that ferromagnetism in Co:TiO_2 is a result of metal Co clustering [49–52].

5.3.3 d^0 ferromagnetism

Perhaps one of the most interesting, if not the most controversial, wrinkles in the field of high temperature DMOs, is that oxygen vacancy defects in closed-shell d^0 transition metal oxides can result in room temperature ferromagnetism. This phenomenon has now been termed "d^0 ferromagnetism". The idea was born after experiments by Venkatesan *et al.* who had prepared pure, undoped HfO_2 by PLD and observed anisotropic ferromagnetic behaviour up to 500 K [53]. In bulk form, these oxides are diamagnetic, however, in the thin film form, they produce a modest magnetic response, likely to be due to the creation of defects or oxygen vacancies on transformation to the thin film form. A theory was put forward which postulates the hybridisation of these oxygen vacancy defect states with unoccupied Hf-derived $5d$ states in the conduction band, forming an impurity band. Mixing and transference of electrons between the impurity band and the unoccupied Hf $5d$ states was thought to be enough to polarise the impurity band and lead to ferromagnetism. Later predictions by the same group proposed that a finite magnetisation per unit area of film as a function of dopant concentration for ZnO and SnO_2 host oxides, doped with a variety of TM dopants, could be extrapolated to zero [54]. Therefore, room temperature ferromagnetism can occur in the absence of TM dopants in other closed-shell transition metal oxides. This highlighted the apparent importance of defects as a critical driver of ferromagnetism in these systems. Following this work, room temperature ferromagnetism was observed

in other undoped oxides such as TiO_2 and In_2O_3 [55].

A report which directly challenges the findings of Hong *et al.*, is that of Berardan *et al.*, where they show that pure In_2O_3 is diamagnetic, as would be expected for a d^{10} element [56]. In fact, Berardan goes a step further to say that their findings imply that all magnetic transitions which occur in the TM-doped In_2O_3 thin films are due to the presence of small amounts of secondary phases.

These results make us reconsider the role that $3d$ element doping has in introducing ferromagnetism in the oxide hosts. Does the doping genuinely introduce ferromagnetism? Or does it simply enhance the magnetism that already exists in the oxide hosts when in thin film form? (see section 5.4).

Rather embarrassing, yet highly relevant, results which have come out of other research groups attempting to repeat and build on the results of HfO_2, have discovered that their films only become magnetic once handled with stainless steel tweezers [57]. These troubling aspects of the data compounded with the distinct lack of reproducibility has cast much doubt over their validity.

5.4 Problems associated with Dilute Magnetism

Given the fact that there is still no unified theory or model to explain the phenomena observed when non-magnetic oxides become ferromagnetic in thin film form (but not in bulk) at room temperature after being doped (or not at all) with only a few percent of TM dopants, the field is naturally met with great sceptism.

We must not overlook some of the technical issues accompanied with measuring dilute magnetism. For one, typical magnetic signal levels are generally of the order of 10^{-6} emu. Therefore, for magnetic characterisation, SQUID magnetometry and not VSM should be used, as its sensitivity levels are generally 100 times better. The presence of small measuring artifacts, which are not so important when measuring traditional bulk ferromagnets, can completely modify the results, leading to surprising yet incorrect results. Thin film heterogeneity cannot be ignored. There is no reason to believe that the profile of the dopant element is uniform over the entire film without good elemental profile analysis such as Rutherford backscattering. Already a case has been referenced where clustered material was found at the interface between film and substrate [8]. It is difficult to rule out the possibility of the $3d$ dopant not being uniformly diluted in the oxide lattice, instead tending to form secondary phases such as metallic clusters. Coey reminded us in his recent article that the "*Absence of evidence is not evidence of absence*" [58]. It was discussed in section 5.2 that phenomena such as the AHE and MCD can take place in the presence of non-uniform dopant distributions where the dopants may be fully or partially clustered. One could then take a view arguing that even if some secondary phase clusters are present why worry if there is still a chance of the properties being application-worthy? The main reason is simply the

lack of reproducibility in extrinsic states that lead to these phenomena. It is far more sensible to pursue achieving a statistically homogenous dopant dispersion whereby the properties can be influenced by manipulating the carrier density, *etc.*

However, secondary phases cannot be a general explanation for all that we see in the DMOs for the following reasons:

- The moment per cation at low concentrations can exceed that of any known ferromagnetic phase [59];
- An unusual anisotropy of the saturation magnetisation, unlike that of known ferromagnetic phases [53, 60].

Contamination is also a major concern and must be treated extremely seriously. Typically we are only dealing with 10 - 30 μg of material on top of a substrate which is approximately 50 mg. Therefore, only the slightest speck of contamination could be sufficient to produce a spurious magnetic moment in a SQUID magnetometer. The substrate holder must also be cleaned thoroughly. The general protocol is to always measure the substrate holder and a blank substrate before any measurement of the film and make sure that there is no trace of ferromagnetism. Garcia *et al.* give a comprehensive review of the possible sources of experimental errors in nanoscale magnetism, and give examples of magnetic signals which have emanated from Kapton tape, iron based tools (tweezers, *etc*), silver paste amongst others [61].

Above all, the reproducibility of the magnetisation from one sample to the next can in some cases be very poor. Small changes in the deposition environment may lead to drastic changes in the magnetisation.

The issues described above are all symptoms of the limited information that we can get from simple magnetometry. If, for some laboratories, this is to be the sole source of characterisation, then the work must be carried out carefully and in extremely clean conditions.

5.5 Can a DMO be classed as a DMS?

With all of the above taken into account, Coey *et al.* [62] recently produced a report whereby the right to classify a DMO as a DMS in the strictest sense is questioned. They coin the irreproducibility in magnetic behaviour as "phantom ferromagnetism", and suggest a new model for ferromagnetism in DMO materials based on the spin-split band (Stoner model) theory rather than a Heisenberg exchange coupling of localised spins. The model has been named the "charge-transfer model". In fact, the model suggests that the spins of $3d$ dopant electrons plays no significant role in the ferromagnetic order in DMOs (contrary to DMS models based on the Heisenberg exchange interaction).

The basic idea is that a narrow, structured local density of states $N(E)$ is associated with defects, but the Fermi level (which may lie above or below a mobility edge) will

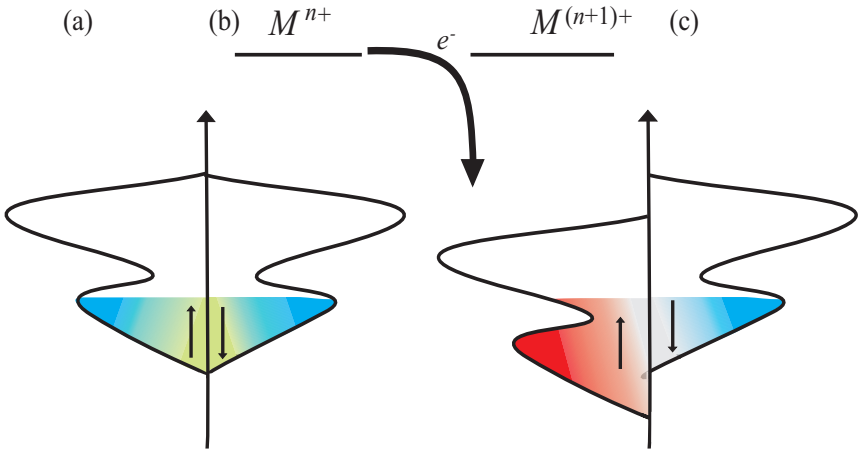

Figure 5.5: A representation of the charge-transfer ferromagmetism model showing the charge transfer involved with a ferromagnetic instability. (a) Defect related density of states is linked to an electron reservoir. (b) By electron transfer to or from the defects, the Fermi level can be shifted to a position where spontaneous ferromagnetic splitting of the defect related density of states occurs. Adapted from reference [62].

not normally coincide with a peak in N(E). However, if there is a local charge reservoir, such as a dopant cation coexisting in two different charge states or a charge-transfer complex at the surface, then it may be possible for electron transfer to raise the Fermi level to a peak in the local density of states, provided that the energy gain from spin splitting exceeds the energy cost of the charge transfer. This leads to a Stoner splitting of $N(E)$ (Fig. 5.5). In the case of TM-doped oxides, the charge transfer in doped oxides is facilitated by mixed-valence TM ions. Note that in this model the enabling feature of the TM ions is not that they carry a localised magnetic moment, but it is their ability to feed electrons into the local density of states (or to accept charge from it) that explains the dopant cations ability to promote ferromagnetism, i.e. the $3d$ dopants act as a charge reservoir from which electrons are transferred to and from local defect states. This general theory is able to explain a wide range of experimental observations, but needs solid experimental proof. Furthermore, spontaneous Stoner ferromagnetism can arise in percolating defect-rich regions, such as the nanoparticle surface, and is therefore not uniform, and instead is restricted to some defect-rich regions.

A selection of the different defects and segregations that may form are represented in Fig. 5.6. Defects may be distributed uniformly throughout the material [Fig. 5.6 (a)] or form via spinodal decomposition [Fig. 5.6 (b)]. They may also be associated with the surface or interface of a thin film [Fig. 5.6 (c)] or with grain boundaries [Fig. 5.6 (d)]. In this way, only a small fraction of the total volume of the sample need be involved.

Through consideration of the total electronic energy involving the Stoner integral in the defect band, the defect bandwidth, the total number of electrons (including the defect band and reservoir) and the on-site Coulomb energy for the multi-valent TM

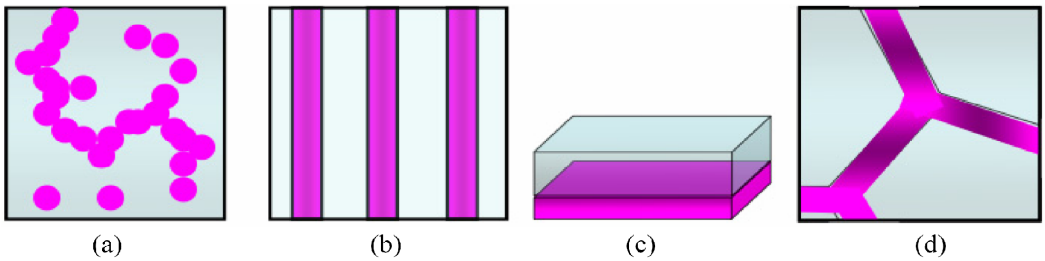

Figure 5.6: Possible distributions of defects: (a) random distribution of point defects at the percolation threshold; (b) spinodal decomposition; (c) interface defects; and (d) grain boundary defects. After reference [63].

dopants within the charge reservoir, Coey *et al.* have been able to devise a magnetic phase diagram for the charge transfer ferromagnetism model.

It is also noted that the magnetic moment measured is not limited by the magnitude of the charge transfer. It reflects the occupancy of the defect band, which becomes spin-split as electrons are transferred to or from the charge reservoir. In fact, the moment may exceed the number of transferred electrons. The charge reservoir simply serves to push the energy balance of the defect band in favour of Stoner splitting. This model is not only limited to the DMOs, but can also apply to d^0 ferromagnets as well, provided there is a charge reservoir.

5.6 Experimental Results

5.6.1 Preliminary experiments

The reader must by now understand the difficulties experienced when working with DMO materials. The struggle to develop my own dilute magnetic oxide system began by first using a range of different transition metal dopants. In this work in particular, those included Cr, Mn, Cu and Co. All films grown using Cu doping were diamagnetic. Those ITO films doped with Cr and Mn were more promising, however, the success rate for obtaining a ferromagnetic signal was at best 1 in 8. In addition, the Cr and Mn-doped samples were only characterised using a VSM rather than a more sensitive SQUID magnetometer. Altering the oxygen partial pressure during the growth process as well as post-growth annealing did not improve the situation in the slightest. As we will describe below, those samples doped with dilute amounts of Co were found to be ferromagnetic and with a much better success rate: it was therefore decided that these would be studied in greater detail, the results of which will follow in this chapter and subsequent chapters 6 and 7. Due to the relatively low signals recorded we assume that there are minimal demagnetising effects present in these samples.

Table 5.2: Summary of the magnetic and transport characteristics of 5.4 at.% Co-doped In_2O_3 thins films with Sn doping levels of 0, 5, and 10 at.% at room temperature. Samples were grown using an oxygen partial pressure of 0.075 Pa in an Ar:O_2 mix and heater temperature of 300°C.

Sn concentration (at. %)	n_c ($\times 10^{20}$ cm^{-3})	M_s (emu/cm^3)	$\mu_0 H_c$ (mT)
0.0	$4.60\pm0.21\times10^{19}$	0.48±0.06	10.0±0.25
5.0	$3.36\pm0.14\times10^{20}$	0.67±0.10	7.76±0.25
10.0	$6.17\pm0.10\times10^{20}$	1.11±0.07	8.14±0.25

5.6.2 Dependence on extrinsic Sn doping concentration

The magnetisation was strongly influenced by the level of extrinsic Sn doping introduced into the In_2O_3 matrix. Table 5.2 summarises the influence that external Sn doping had on In_2O_3, ITO(5) and ITO(10) films each doped with 5.4 at.% Co. Increasing levels of Sn doping leads to a rise in the bulk magnetisation of the film, contrary to the findings in reference [16]. The rise in magnetisation was accompanied by a steady increase in the carrier concentration. This suggests that there may be some correlation between the carrier concentration and magnetisation in these films and more importantly, that the magnetisation is stronger with increasing levels of extrinsic carrier doping. The films doped with Sn are metallic whereas those without Sn exhibit semiconducting properties. However, in both such cases, the magnetisation increases sharply upon cooling. In the case of the Co-doped In_2O_3 this seems rather counter-intuitive as the carrier concentration will decrease slightly with decreasing temperature. So why does the magnetisation continue to rise in these semiconducting films? One possible explanation may be as follows: the carrier density at room temperature is the density of ionised donor states; at low temperatures the donors will become neutral and these localised states can also contribute to magnetism. The temperature dependent data shows us that the localised states are actually more efficient at generating a magnetic moment than the delocalised states. The magnetisation versus temperature scans of the Co-doped films with 0, 5 and 10 at.% Sn follow similar paths with no sign of a superparamagnetic blocking temperature. The zero-field cooled (ZFC) and field-cooled (FC) magnetisation versus temperature curves for a 5.4 at.% Co-doped In_2O_3 thin film with an applied magnetic field of 20 mT is shown in Fig. 5.7.

From here onwards in this chapter, the data presented will focus on measurements performed on Co-doped ITO(10) thin films as these provided us with the largest ferromagnetic response.

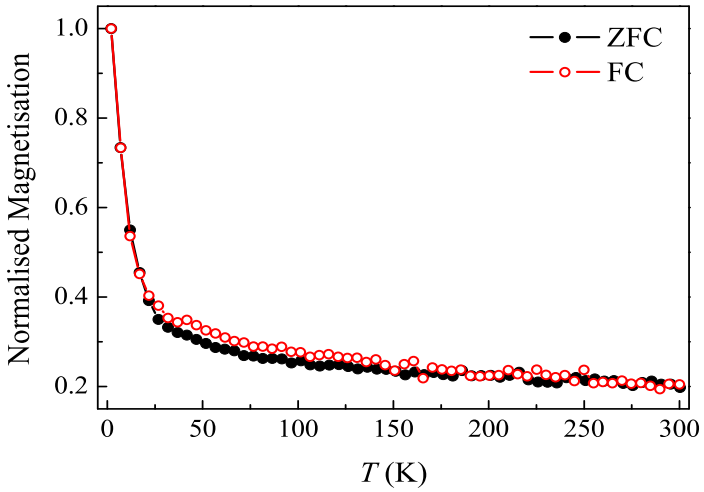

Figure 5.7: ZFC-FC normalised magnetisation versus temperature scans for a 5.4 at.% Co-doped In_2O_3 film. The applied field was 20 mT.

5.6.3 Co-doped ITO(10) films

A series of Co-doped ITO(10) ($In_{2-x}Sn_{x-1}(Co_x)O_{3-2x}$ with $x = 0.016$-0.054) thin films ($\approx$ 250 nm thick) were co-deposited (two targets, one of pure Co and the other a commercially made ITO(10) target) on r-plane sapphire substrates by DC magnetron sputtering in a UHV system. A power of 20 and 25 W was applied to the ITO(10) and Co targets respectively. The heater was maintained at a temperature of 300°C during deposition. The system base pressure was better than 1×10^{-6} Pa. Films were sputtered in 1.50±0.01 Pa of an Ar-O_2 (95:5) mix (0.075 Pa O_2) with a gas flow rate of approximately 0.10±0.01 Pa/s.

Structural Properties

Figure 5.8 shows the θ-2θ XRD scans of Co-ITO films grown on r-plane sapphire for a range of Co doping levels. All peaks displayed on the diffractogram could be indexed assuming the same cubic bixbyite structure as pure ITO. Peaks were sharp, suggesting that the films are crystalline. At first glance, no detectable peaks corresponding to any secondary Co oxides or Co metal were found. This is often the case in DMOs which appear to be phase-pure and of high crystalline quality. To verify these findings, the integration time per point was raised to 100 seconds - a route also taken by Opel *et al.* [64] for Co:ZnO, where they increased the integration time further to 400 seconds and only then detected reflection peaks corresponding to the (111) reflection peak of fcc Co metal as well as $ZnCo_2O_4$ (400) and Co_3O_4 (400). Still, with this adjustment and within the detection limit of the instrument, we were unable to identify any diffraction

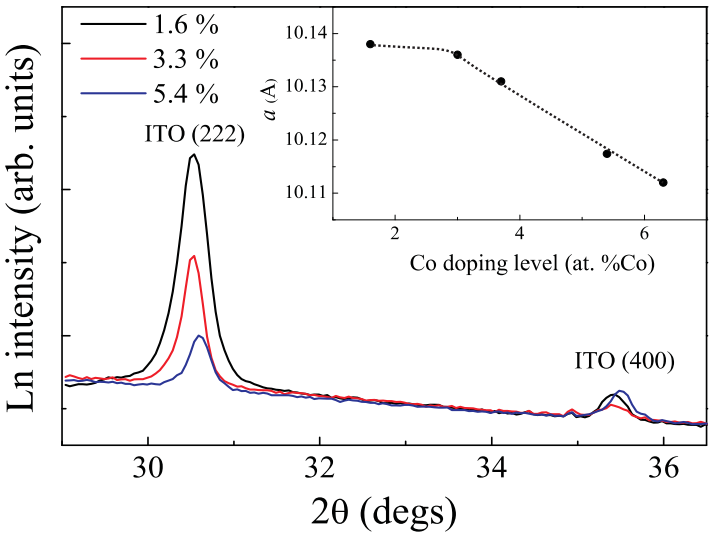

Figure 5.8: (a) θ-2θ XRD diffractograms focusing on the ITO (222) and ITO (400) peaks for Co-ITO films of varying Co concentrations, demonstrating the shift in the peak position and intensity upon Co doping. Inset: lattice parameter, a (Å), as a function of Co doping. The dotted line serves as a guide to the eye.

peaks which would suggest the presence of metallic Co clusters or any other secondary Co oxide phases.

A shift in the peaks (predominantly the highly pronounced ITO (222) diffraction peak) towards higher values of 2θ with increasing level of Co doping is observed and suggests a gradual decrease in the out-of-plane lattice parameter, a (inset, Fig. 5.8). This is evidence that the smaller Co^{2+} ions (ionic radius 0.74 Å) substitute for the larger In^{3+} ions (ionic radius 0.94 Å) at In sites rather than forming a defect phase.

We know that this characterisation technique has its limitations in terms of detecting dilute levels of transition metal dopants. A more detailed study involving the use of high-resolution cross-sectional transmission electron microscopy would certainly help and give a more representative picture of the microstructure. Co is renowned for forming clusters and in the past has been shown to accumulate close to the substrate/film interface [8] (see Fig. 5.9), and so caution must be exercised.

Magnetometry

In-plane magnetisation (M) versus field (μ_0H) measurements showed clear evidence for ferromagnetism in each of the samples. The diamagnetic background of the substrate and sample holder has been subtracted from all the magnetisation data shown here. Figures 5.10 - 5.12 (a) show the magnetisation loops for $x = 0.016$, 0.03 and 0.054 respectively over a temperature range of 2 - 300 K. A noticeable difference in the shape of the magnetisation curves between the 1.6 at.% doped sample and those of the 3.0 and 5.4 at.% Co-doped samples is apparent. The 1.6 at.% doped sample appears to

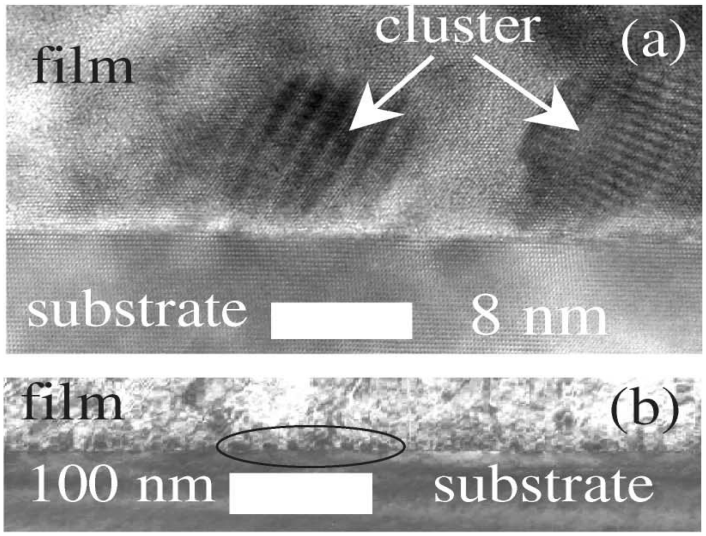

Figure 5.9: TEM images of a Co:TiO_2 film at different magnifications showing the formation of Co clusters close to the substrate interface with the film [8].

have magnetisation curves which are more "square" than those of the other doping levels, i.e. a larger remanent magnetisation. This is confirmed by a simple calculation of the ratio between the saturation and remanent magnetisation (m_r/m_s). The average m_r/m_s for the 1.6 at.% Co-doped sample was 0.41, compared to values of approximately 0.20 in the other samples with higher doping levels (calculated by averaging over all temperatures). Interestingly, it is at 2 K in the 1.6 at.% doped sample that m_r/m_s is at its minimum value (≈ 0.31). It is only at temperatures ≥ 10 K that the magnetisation curves become more square. The magnetisation saturation fields for the samples are typically between 0.20 - 0.45 T, the largest values arising at 2 K.

Figures 5.10 - 5.12 (b) provide an expanded view of the low-field data to demonstrate the nature of the coercive field ($\mu_0 H_c$) and how it changes between 2 and 300 K. Hysteretic behaviour is observed, consistent with ferromagnetism, with values for $\mu_0 H_c$ ranging from 8 - 75 mT across the Co doping range.

Figures 5.10 - 5.12 (c) and 5.13 (c) summarise the behaviour of $\mu_0 H_c$ as a function of the temperature. For each doping level $\mu_0 H_c$ decreases steadily with temperature, and in the case where we have 5.4 at.% Co-doped ITO [Fig. 5.12 (c)], $\mu_0 H_c$ falls according to an inverse relationship to the temperature. Fig. 5.13 (c) in particular gives a clearer picture of how $\mu_0 H_c$ behaves as a function of temperature for each of the doping levels. By displaying the normalised $\mu_0 H_c$ (normalised to the maximum $\mu_0 H_c$(2 K) for each data set) we can see that in the changes in $\mu_0 H_c$ over the temperature range become more drastic as the level of Co doping increases.

The magnetisation loops at 300 K for the 1.6, 3.0 and 5.4 at.% Co-doped samples are shown in Fig. 5.13 (a). The magnetisation rises almost linearly with increasing levels of Co content. This implies that the Co dopants are acting independently of each other. Had there been an exponential rise with Co content, it would have implied ferromagnetic clustering, whereas a negative parabolic trend would suggest antiferro-

magnetic clusters.

Figures 5.10 - 5.12 (d) show the normalised FC magnetisation of the 1.6, 3.0 and 5.4 at. % Co-doped ITO films as a function of temperature in a constant applied magnetic field of 20 mT in the 5 - 300 K temperature range. In each case, the sample magnetisation decreases rapidly particularly between 2 - 40 K. This implies that the sample possesses a strong paramagnetic component in addition to a weak ferromagnetic component, as seen in other DMO systems [27]. Initially we attempted to fit the data using a purely paramagnetic relationship, however, this proved unsuccessful. Assuming that we have the coexistence of magnetic phases within this sample, we were able to model the magnetic susceptibility, χ, using a modified Curie-Weiss relationship in combination with a standard mean-field model for a weak itinerant ferromagnet [65] using the relation:

$$\chi = [1-\alpha]\left(\chi_0 + \frac{C}{T-\theta}\right) + \alpha\sqrt{1-\frac{T^2}{T_C^2}}, \tag{5.2}$$

where α is magnetic phase fraction (the ferromagnetic fraction), χ_0 is a constant non-paramagnetic contribution to the magnetic susceptibility, C is the Curie constant ($= n\mu^2/3k_B$, where k_B is Boltzmann's constant, n number of magnetic ions and μ the magnetic moment of the ion), θ is the Curie-Weiss temperature and describes the magnetic interactions between the paramagnetic spins, T is the measurement temperature, and T_C is the Curie temperature of the ferromagnet. The values for α are found to be 17.8, 17.2 and 17.6% for the 1.6, 3.0 and 5.4 at.% Co-doped ITO films respectively, confirming that the paramagnetic contribution is dominant in these samples. The fit estimates values for T_C of approximately 500 K in each case. There was no sign of a blocking temperature, thus suggesting the absence of secondary Co metal nanoclusters within the bulk of the film. However, it has been suggested that a magnetisation versus temperature measurement is not necessarily the most rigorous method to expose a superparamagnetic blocking temperature (T_B). It is believed that T_B can sometimes be suppressed by the ever present superexchange coupling between the Co particles [66].

5.6.4 Dependence on oxygen partial pressure

As one would expect, changes in the oxygen partial pressure during the growth process influenced the magnetic properties of the samples. It was found that samples grown in more oxygen deficient atmospheres produced a greater magnetic response than those grown in environments which were richer in oxygen. The majority of films which were metallic (generally those grown in oxygen partial pressures of ≤ 0.15 Pa) showed some level of ferromagnetic response, whereas those which were grown and possessed semiconducting properties were found to be diamagnetic. Figure 5.14 shows the mag-

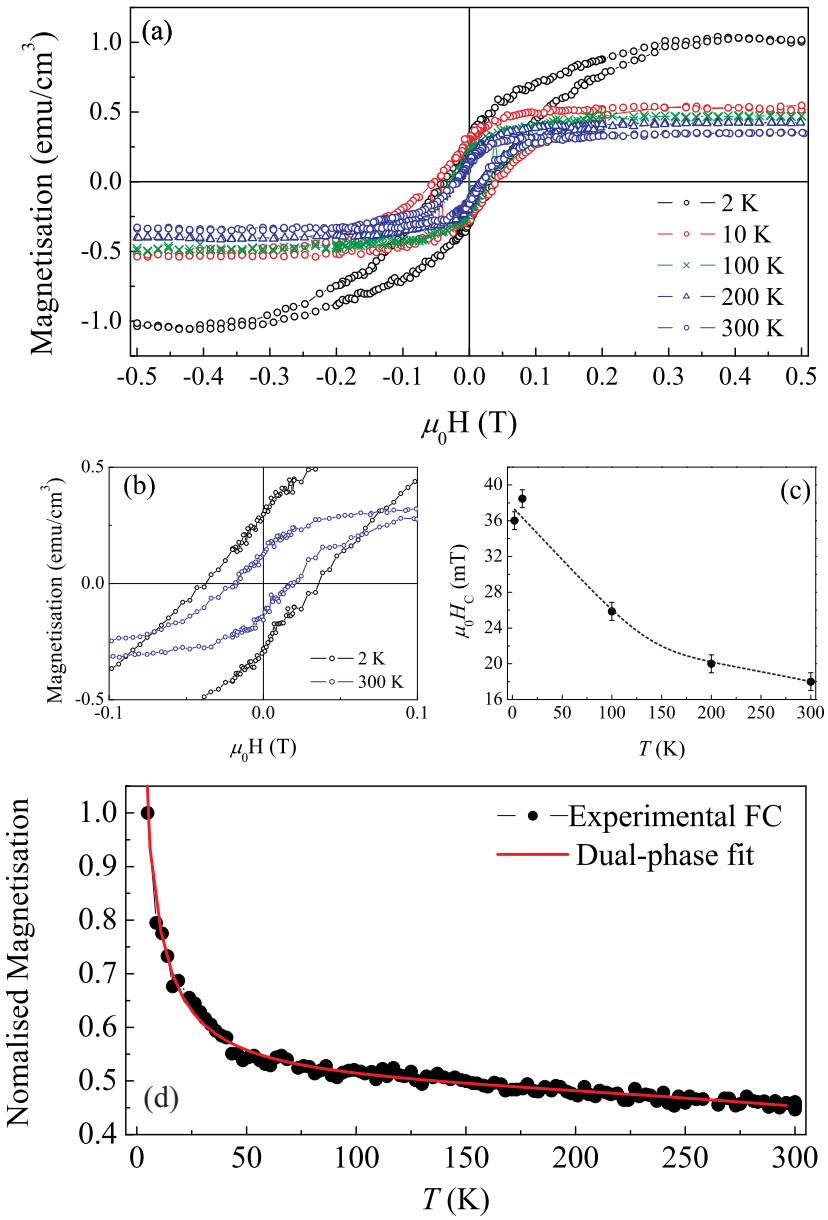

Figure 5.10: (a) Magnetic hysteresis loops using a SQUID magnetometer for a 1.6 at.% Co-doped ITO film at varying temperatures. (b) Magnified image showing the large change in coercive field between 2 K and 300 K. (c) Variation in coercive field as a function of temperature; the dotted line is a guide to the eye. (d) Normalized field-cooled magnetization for a 1.6 at.% Co-doped ITO film as a function of temperature in an applied magnetic field of 20 mT; the solid line fits the experimental data to the magnetic dual-phase model described in Eqn. 5.2.

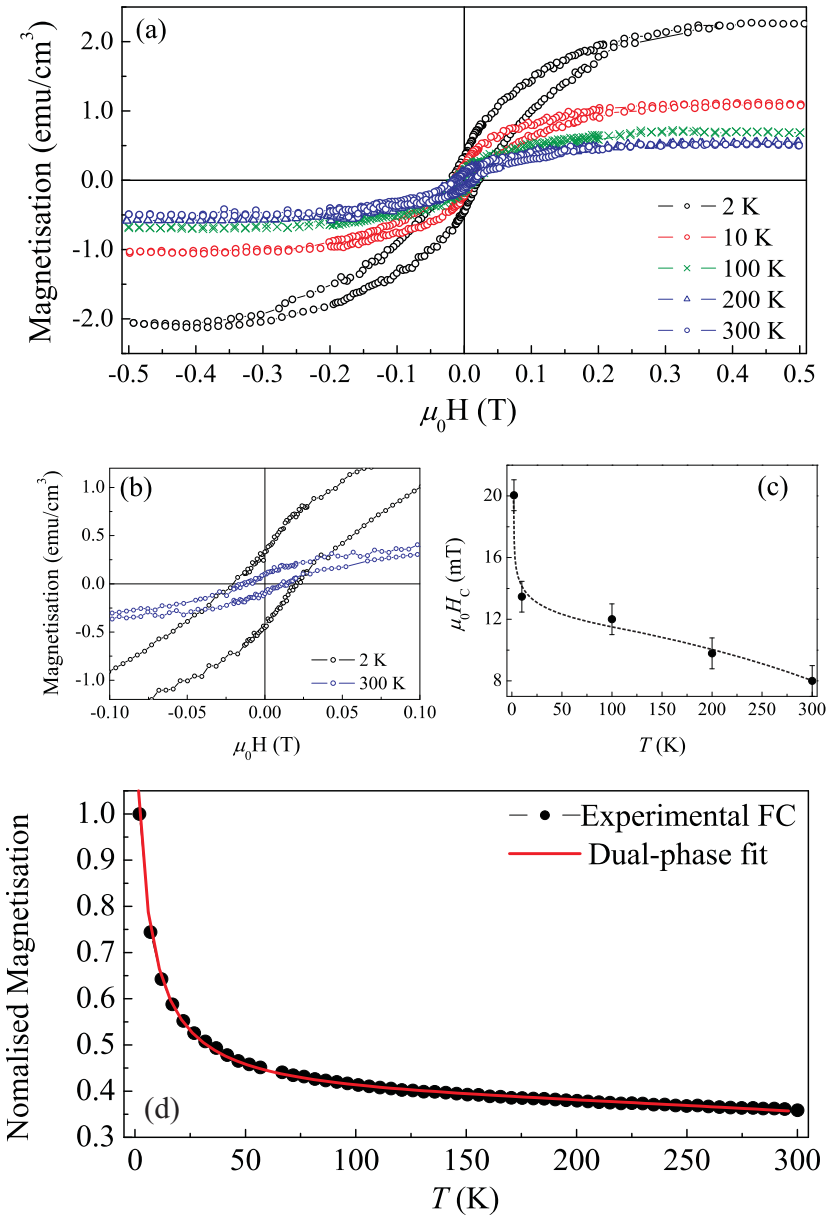

Figure 5.11: (a) Magnetic hysteresis loops using a SQUID magnetometer for a 3.0 at.% Co-doped ITO film at varying temperatures (b) Magnified image showing the large change in coercive field between 2 K and 300 K (c) Variation in coercive field as a function of temperature; the dotted line is a guide to the eye. (d) Normalized field-cooled magnetization for a 3.0 at.% Co-doped ITO film as a function of temperature in an applied magnetic field of 20 mT; the solid line fits the experimental data to the magnetic dual-phase model described in Eqn. 5.2.

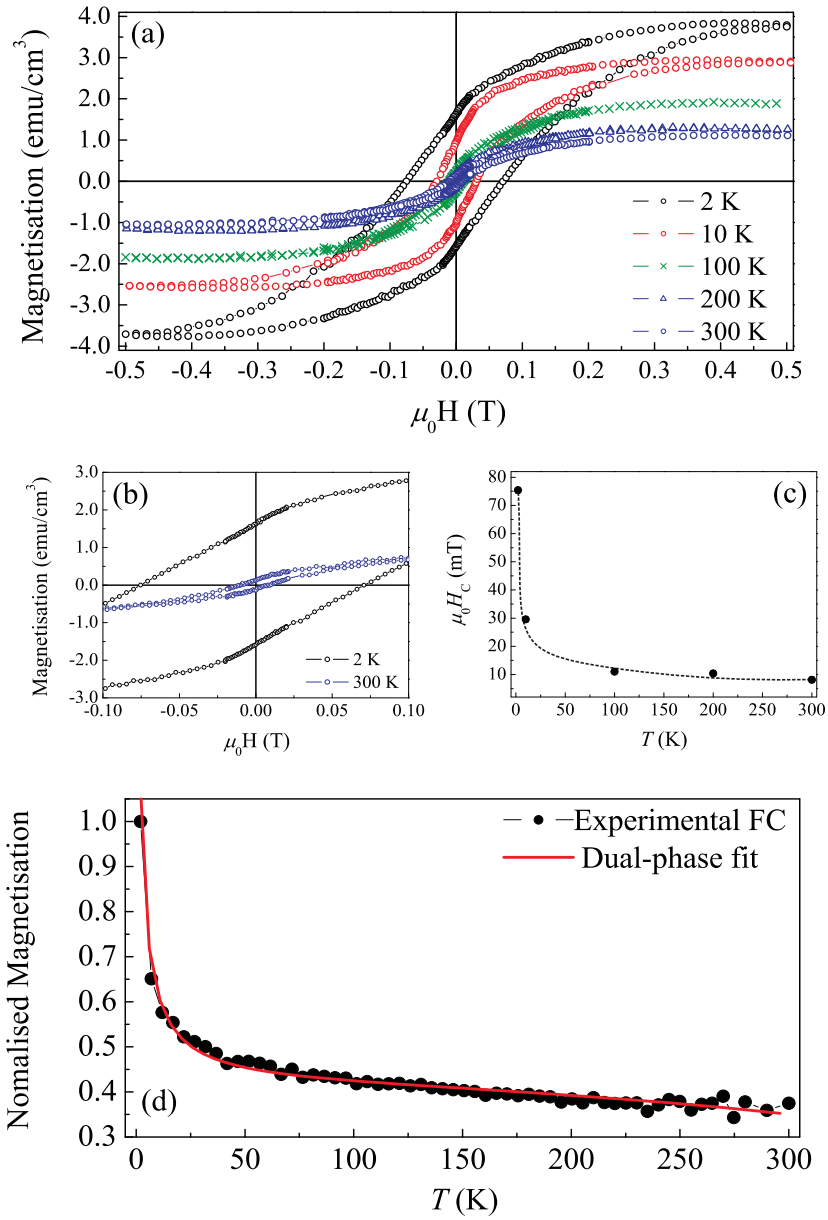

Figure 5.12: (a) Magnetic hysteresis loops using a SQUID magnetometer for a 5.4 at.% Co-doped ITO film at varying temperatures. (b) Magnified image showing the large change in coercive field between 2 K and 300 K. (c) Variation in coercive field as a function of temperature; the dotted line is a guide to the eye. (d) Normalized field-cooled magnetization for a 5.4 at.% Co-doped ITO film as a function of temperature in an applied magnetic field of 20 mT; the solid line fits the experimental data to the magnetic dual-phase model described in Eqn. 5.2.

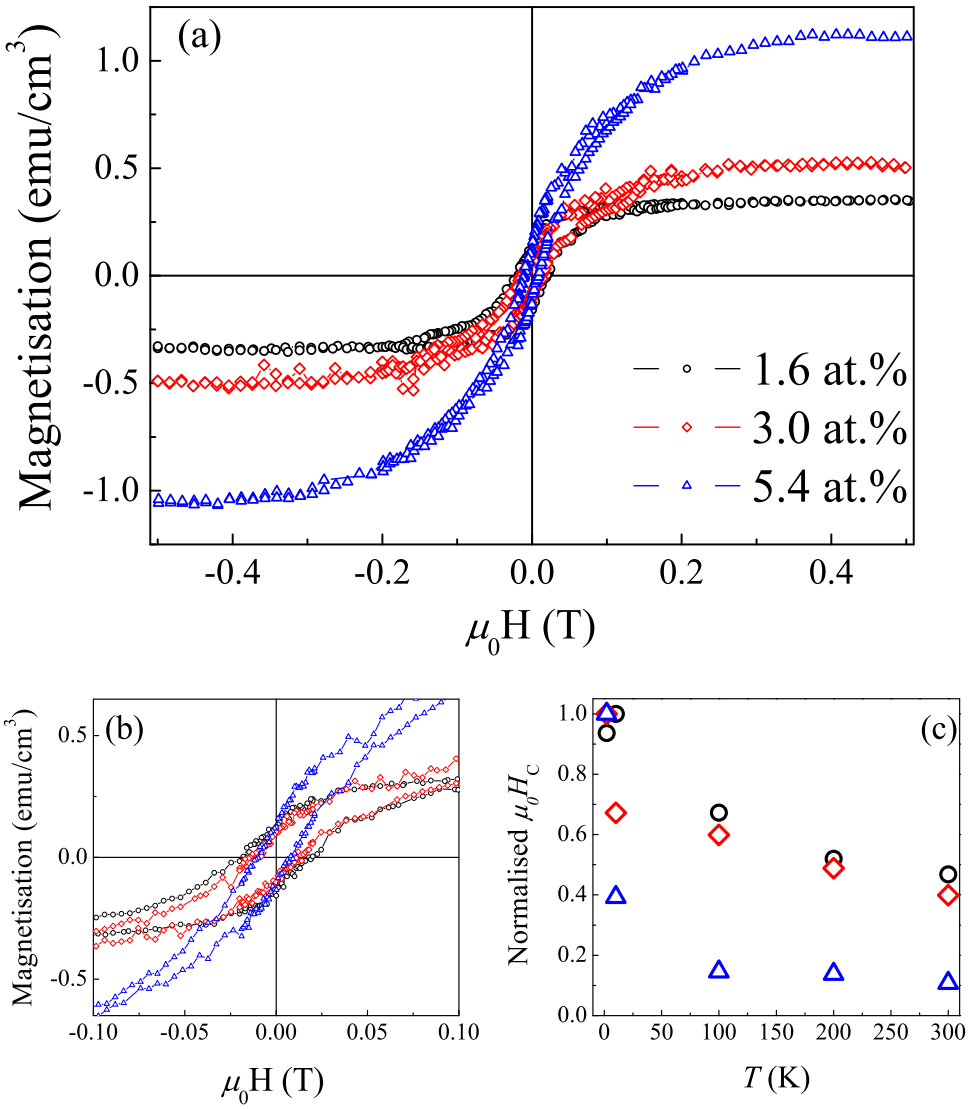

Figure 5.13: (a) Magnetisation versus applied field loops at 300 K, (b) expanded view of the low-field region for the magnetisation curves shown in (a) at 300 K, and (c) normalised coercive field, H_c, as a function of temperature for 1.6 (open black circles), 3.0 (open red diamonds) and 5.4 at.% (open blue triangles) Co-doped ITO films.

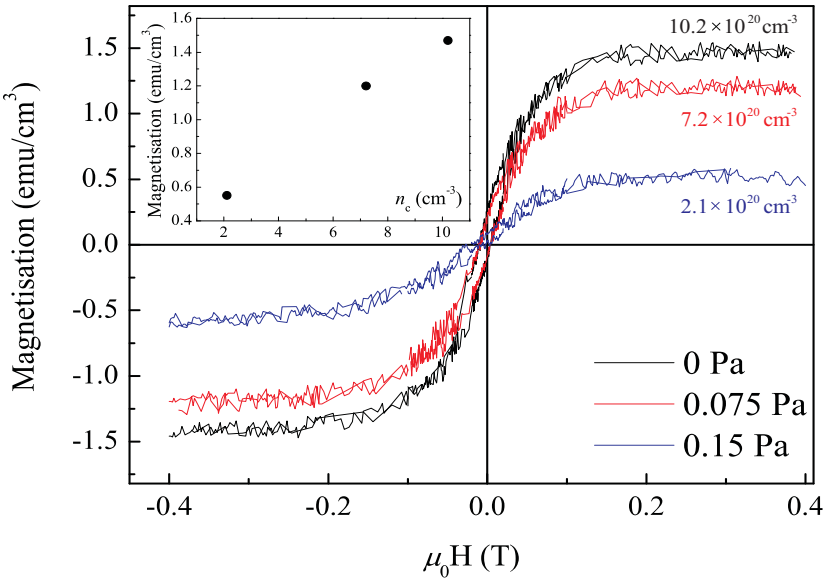

Figure 5.14: Room temperature magnetisation versus applied field loops for 5.4 at.% Co-doped ITO films grown using a heater temperature of 300°C under various oxygen partial pressures. Corresponding carrier concentrations are also given.

netisation loops (using a VSM) along with the corresponding carrier concentrations at room temperature for 5.4 at.% Co-doped ITO films grown under a number of different oxygen partial pressures. It clearly shows the reduction in the overall magnetisation of the film as the oxygen partial pressure rises. As we know from the previous chapter from our work on the ITO system, there are a number of film properties which are influenced by the oxygen partial pressure during the growth stage. The first obvious reason for the reduction in the strength of the magnetic signal is likely to be due to the decreasing carrier concentration with increasing levels of oxygen. As stated above, those films which were semiconducting were found to be diamagnetic. Earlier we discussed predictions by Raebiger *et al.* where it is said that In_2O_3 will only show room temperature ferromagnetism in the company of extrinsic Sn and TM doping, provided the condition of the concentration of free carriers reaches half that of the Cr dopant concentration (however, we have shown here that Co-doped In_2O_3 films without extrinsic Sn doping are ferromagnetic at room temperature) [13]. In the case of Raebiger's predictions, this carrier concentration was equivalent to 3.0×10^{20} cm^{-3}. The carrier concentration of the Co-doped ITO films showing semiconducting behaviour was typically 0.9 - 2.0×10^{19} cm^{-3}. Therefore, we can only estimate that somewhere between the region of 2.0×10^{19} cm^{-3} - 2.0×10^{20} cm^{-3}, there is a transition from a diamagnetic semiconductor to a metallic-like oxide ferromagnet for our Co-doped ITO films. Oxygen vacancies are perceived by many to have a strong role to play in the origins of ferromagnetism in these materials, and so the rising levels of oxygen will naturally disrupt their influence as a result of the filling of oxygen vacancies.

No detailed structural analysis was performed on these samples, however, in chap-

ter 4 it was found that increasing levels of oxygen during the growth process led to a reduction in the vertical grain size of the films. This is likely to lead to more point defects in the films. Some believe that defects can improve the strength of the magnetic response in the DMO materials, and have shown that moving towards epitaxy can suppress the ferromagnetism [67]. Perhaps in the case here however, the magnetic response benefits from improved crystallinity.

Increasing levels of oxygen during the growth process will surely increase the chances of forming Co oxide clusters and the likelihood of a reduction in the magnetic response of the samples. The majority of the likely candidates for Co oxide clustering e.g. Co_3O_4 and Co_2O_3, generally have ferromagnetic Curie temperatures of below 40 K and so, if present, will not show any ferromagnetic response at room temperature.

5.6.5 Dependence on the growth temperature

The majority of the results above describe data collected for films using relatively high heater temperatures (generally ≥ 300°C), however, the scenario whereby the films were grown unheated was also investigated. These films exhibited typical semiconducting characteristics with a room temperature resistivity of the order of 10^{-2} Ωcm. The magnetic response of the films could be modelled using a Brillouin function, i.e. that of a paramagnetic or superparamagnetic material. This suggests that some heating is required during the deposition process in order to promote a ferromagnetic response from the films, and may be linked to factors such as the microstructure, density of oxygen vacancies, *etc.* In addition, it could be that the Co atoms are not successful in substituting for the In atoms under these growth conditions.

5.6.6 Magnetic ITO . . . ?

The possibility of pure, undoped ITO being ferromagnetic was also investigated very briefly. Two identical pure ITO(10) samples, of thickness 300 nm, were grown under identical conditions to those described above (see section 5.6.3) for the Co-doped samples and measured using SQUID magnetometry at 2 and 290 K. Rather surprisingly a small magnetic moment, albeit very weak, at both 2 and 290 K is observed (see Fig. 5.15). There is a minimal change in magnetisation between 2 and 290 K. The magnetisation at room temperature (≈ 0.22 emu/cm^3) is comparable to, yet lower than that of the 1.6 at.% Co-doped ITO sample at 290 K (0.35 emu/cm^3). Others who have observed room temperature ferromagnetism in undoped In_2O_3 report values of 0.30 emu/cm^3 (200 nm thick films) [15], 0.70 emu/cm^3 (600 nm thick films) [31] and even as high as 1.40 emu/cm^3 (100 nm thick films) [69]. To most onlookers, the obvious explanation for these results would be contamination. There are not too many experimental cross-checks which are readily available to confirm whether these results

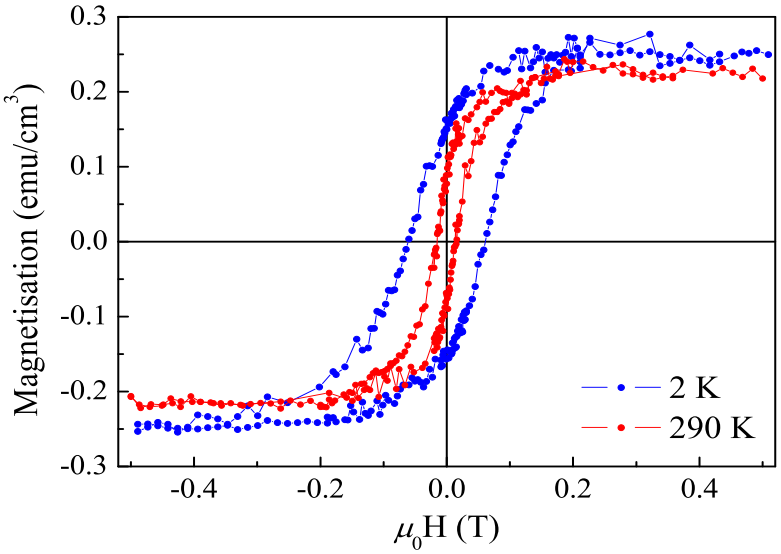

Figure 5.15: Magnetisation curves for a pure, undoped ITO(10) film grown under indentical conditions to the Co-doped ITO samples at 2 and 290 K.

are valid or not. In section 5.3.1 we discussed the results of Panguluri *et al.* where it was shown that pure In_2O_3 has a sizeable spin polarisation [15]. Another option would be to study the oxygen K-edge in detail using XMCD, but again, this is not an easy task, due to low signal levels (the moment per oxygen atom is likely to be very small) and the difficulty in being granted beam time.

As Coey *et al.* [62] and others have suggested, the role of the transition metal doping is questionable. Hong *et al.* [31] report that there is a strong thickness dependence on the magnetisation in their undoped oxide films suggesting that the magnetism is likely to be oxygen vacancy or defect related. Perhaps we do need to rejudge the role that TM doping has on introducing ferromagnetism in oxides: does the doping really introduce ferromagnetism? Or, in fact, does it just enhance the magnetism that already exists in the oxide hosts when in thin film form? Certainly in our case it seems that the addition of Co does enhance the magnetism we come to observe.

5.6.7 Transport Measurements

The carrier concentration is these films at 10 and 290 K was typically in the 10^{20} - 10^{21} cm^{-3} range, with electron mobilities between 8 - 10 cm^{2}V^{-1}s^{-1}. The anomalous Hall effect was not observed in any of the films even at 10 K. This suggests that the degree of spin polarisation in these materials may be relatively low.

Figure 5.16 shows a typical in-plane MR curve for a Co-doped (5.4 at.%) ITO film at 10 K. A negative MR is observed for field up to ±5 T, with a maximum of -0.17%.

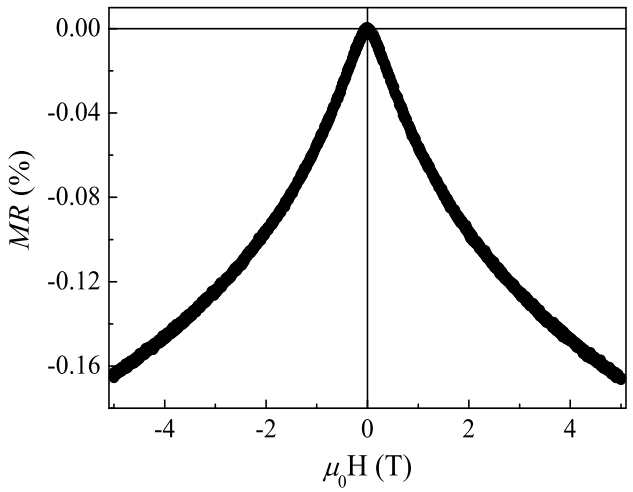

Figure 5.16: Magnetoresistance curve at 10 K for a 5.4 at.% Co-doped ITO(10) sample.

The MR curves are extremely similar to those shown in the pure ITO(10) samples shown in Fig. 4.4 implying that the addition of Co has little effect on the magnetoresistance behaviour. The negative MR can be attributed to electron scattering by spin disorder. Looking back at the hysteresis loops for this sample [Fig. 5.13 (a)] we recall a small remanent magnetisation, indicating that the moments are not well ordered in the remanent state. Therefore, as the magnetic field increases, these magnetic spins will become increasingly aligned, thereby reducing the spin disorder scattering [68]. Hence, the resistance is expected to become smaller with increasing applied field, resulting in the observed negative MR. No MR was recorded at 290 K.

As we discussed in section 2.3.1, magnetotransport measurements can be used as an indicator as to whether a material is undertaking the role of an efficient spin polariser. The positive contribution is most frequently quoted as being due to the field induced spin-splitting of the conduction band and the population change this causes. The negative MR is attributed to a reduction in spin scattering with increasing magnetic field. Since the overall MR seen is determined by a competition between the negative and positive mechanisms, this means that in the Co-doped ITO(10) (and in fact even in those with no Sn and only 5 at.% Sn) weak localisation effects and spin-disorder scattering dominate the *s-d* exchange interaction in our films.

5.6.8 Annealing tests

The effects of annealing on the magnetisation and magnetotransport behaviour of Co-doped ITO films have also been investigated. Here we focus solely on 5.4 at.% Co-doped films which have been grown in the same conditions as those described in section 5.6.3.

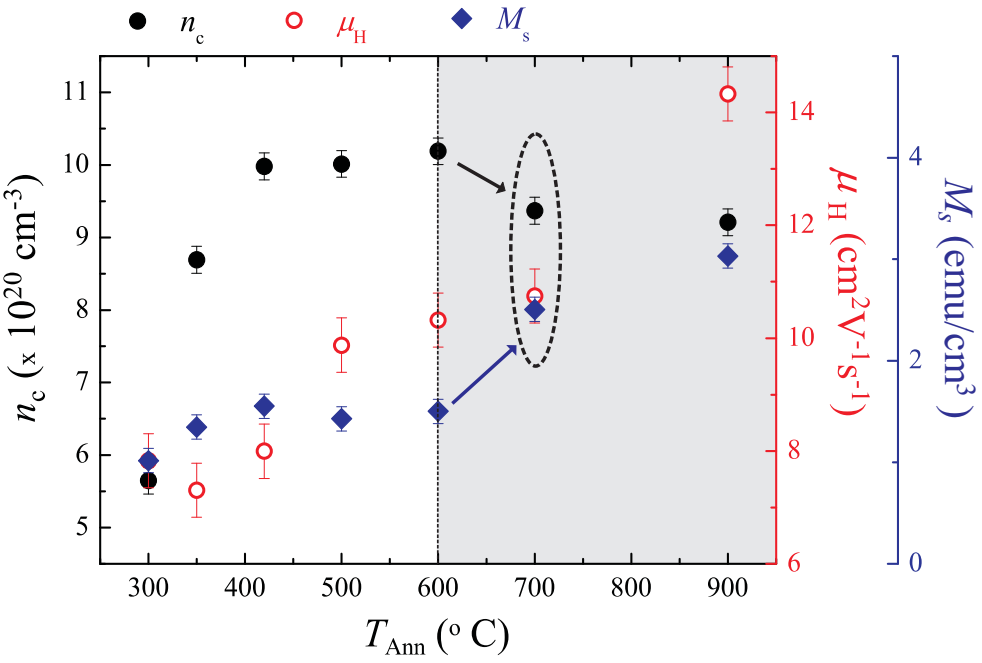

Figure 5.17: Summary of the transport properties (carrier concentration, n_c, and mobility, μ_H) and magnetisation (M_s) at room temperature for 5.4 at.% Co-doped ITO films as a function of the heater temperature, T_{Ann} (°C). Note that 300°C is the as-deposited condition. The grey shaded area signifies the region where T_{Ann}>600°C and we suspect the presence of ferromagnetic Co clusters. The data points encased within the dotted oval signifies that this sample was later used for further experiments using XMCD (see chapter 6).

Films were annealed in UHV conditions within the same chamber in which they were deposited. Films were annealed at different heater temperatures (T_{Ann}) for a fixed time of 2 hours.

θ-2θ XRD studies revealed no secondary Co phases. This does not rule out the possibility of these phases being present. The dilute levels of these materials makes it extremely difficult to identify any parasitic phases.

Figure 5.17 shows the dependence of the film carrier concentration, mobility and magnetisation at room temperature on T_{Ann}. Between 300≤T_{Ann}(°C)≤600, the carrier concentration and magnetisation show a clear correlation, as they follow a similar path as a function of the annealing temperature. After the initial annealing stage at 400°C, magnetisation seems to saturate, however, rises suddenly for T_{Ann}>600°C (grey shaded area) reaching a maximum magnetisation of 3.03 emu/cm^3 at T_{Ann}=900°C. This is accompanied by a drop in the carrier concentration, but is not large enough outside the error range to be considered too significant. There was no suggestion of the presence of superparamagnetic particles from the magnetisation loops. The coercive field progressively increased with annealing temperature, starting at approximately 7.5 mT for the as-deposited sample and rising to 32 mT for the sample annealed at 900°C.

ZFC-FC Magnetisation versus temperature curves for the sample annealed at 700°C,

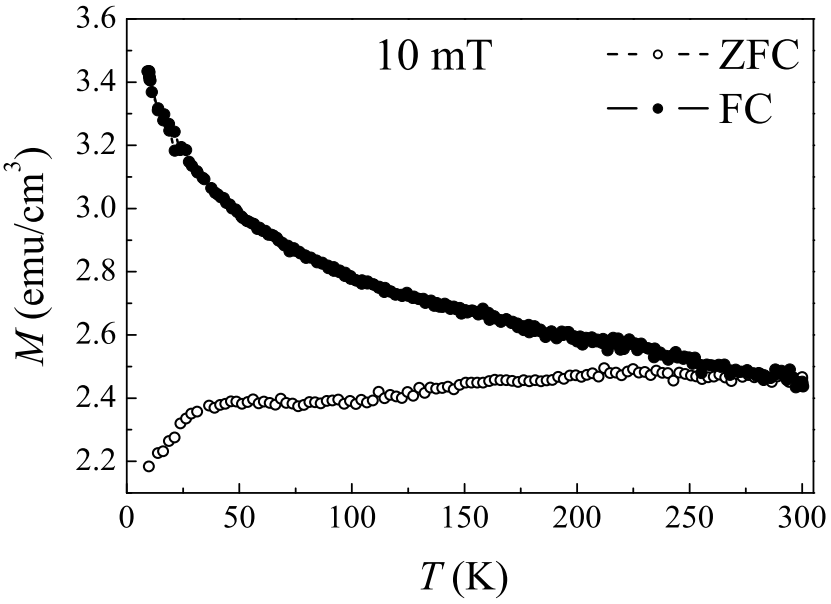

Figure 5.18: ZFC-FC magnetisation versus temperature curves for a 5.4 at.% Co-doped ITO sample annealed at 700°C for 2 hours. The applied field was 10 mT.

taken using a SQUID magnetometer, are shown in Fig. 5.18. There is a clear separation between the ZFC and FC curves, which coalesce at approximately 272 K. This is the value for T_B which can now be used to estimate the cluster size using Eqn. 2.8. Assuming spherical shaped clusters, the calculation yields a particle radius of 3.36 nm. Note that the ZFC curve is very broad and may even indicate multiple values for T_B. This suggests that there may be a broad distribution of particle sizes.

Therefore, in the case of the samples annealed at T_{Ann}>600°C, we believe that the source of magnetism is extrinsic in the form of ferromagnetic, metallic Co clusters. In particular, the sample annealed at 700°C shows clear signs of secondary metallic Co segregation, and in fact is investigated further in chapter 6 using XMCD.

No significant changes in the magnetoresistive response were seen when comparing the as-deposited and annealed samples. A negative MR was recorded, and is displayed as a function of temperature for the sample annealed at 700°C in Fig. 5.19. No MR was observed at 290 K.

From these annealing experiments it would not be too out of place to presume that there is some correlation between carrier concentration and the magnetisation. Samples annealed between $300 \leq T_{Ann}(^{\circ}\mathrm{C}) \leq 600$ are good evidence for this. Exposing the samples to 700°C (and above) for prolonged periods only leads to undesirable effects in terms of achieving intrinsic ferromagnetic properties. The AHE was not observed in any of these samples.

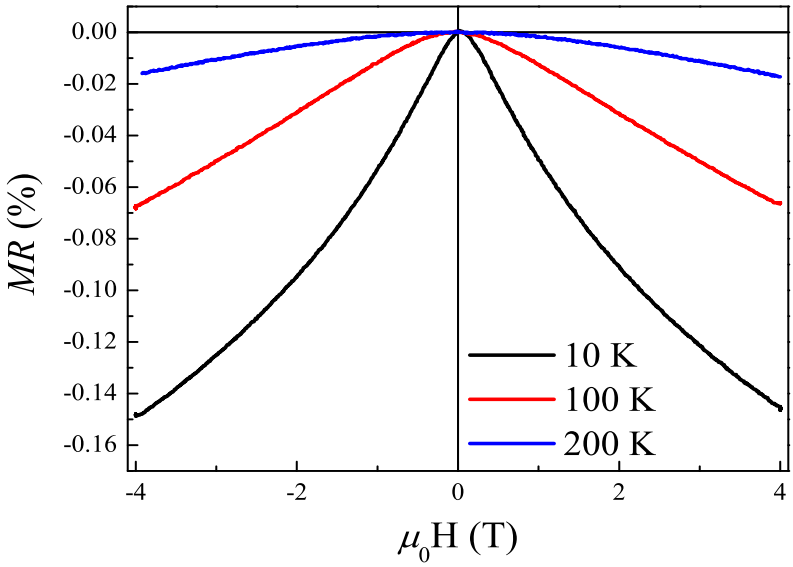

Figure 5.19: Magnetoresistance as a function of temperature for a 5.4 at.% Co-doped ITO film annealed at 700°C for 2 hours.

5.7 Summary and Conclusions

This chapter has highlighted the key aspects of dilute magnetic oxide materials and brought the controversies and experimental difficulties that overshadow the topic to the readers' attention.

It was found that only those films doped with Co exhibited reproducible ferromagnetic behaviour beyond room temperature. Ferromagnetism was found in Co-doped In_2O_3 and 5 and 10 at.% Sn-doped In_2O_3, however the results presented are predominantly concerned with the Co-doped 10 at.% Sn-doped In_2O_3 films. The ferromagnetic response was found to increase with increasing levels of Sn doping which was accompanied by a rise in the carrier concentration.

X-ray diffraction studies reveal that the out-of-plane lattice parameter decreases upon Co doping, suggesting that the Co ions are substituting for In ions and not forming metal Co clusters. This is supported by the absence of any secondary Co metal or Co oxide phases in the θ-2θ x-ray scan. However, it is made clear that this alone is not strong enough evidence to suggest that the samples are completely Co cluster free.

Magnetometry revealed that the ITO(10) films doped with 1.6, 3.0 and 5.4 at.% Co were all ferromagnetic beyond room temperature, with no sign of a superparamagnetic blocking temperature from magnetisation versus temperature scans. T_C was estimated to be approximately 500 K in each case from the dual phase fitting. Samples grown in oxygen deficient environments were found to be more magnetic than those grown using higher levels of oxygen. The rising magnetic response was accompanied

by higher carrier concentrations, i.e. only those films which had metallic-like conducting properties exhibited ferromagnetism, generally with carrier concentrations $\geq 10^{20}$ cm^{-3}. Films grown at room temperature were found to be superparamagnetic even when deposited in highly oxygen deficient atmospheres, suggesting that some level of heating is required during the growth process.

Rather surprisingly, a reproducible weak ferromagnetic response was measured above room temperature for a 300 nm thick pure (non-TM doped) ITO(10) film. This result brings the role that transition metal dopants play in the observation of ferromagnetism into major dispute, and supports a defect-related origin for magnetism.

Annealing a set of 5.4 at.% Co-doped ITO(10) films under UHV conditions at various annealing temperatures revealed that both the carrier concentration and magnetisation increase in tandem up to an annealing temperature of 600°C. It is believed that further annealing beyond 600°C leads to Co metal segregation and the formation of metal Co clusters. This is accompanied by a sharp rise in the magnetisation which continues as the annealing temperature is increased further. The presence of superparamagnetic particles is supported by the observation of a superparamagnetic blocking temperature from magnetisation versus temperature measurements.

The anomalous Hall effect was not observed in any of these samples reported in this chapter. This suggests that the Co:ITO system is likely to be a weak spin polariser. This is supported by very low values for magnetoresistance even at temperatures as low as 10 K. No magnetoresistance observed at room temperature.

Some of the data gathered here may be considered solid enough evidence to suggest that the magnetism observed in these films could be correlated to the carrier concentration, therefore pointing towards a carrier-mediated mechanism for ferromagnetism. However, the observation of room temperature ferromagnetism from the pure ITO samples is confusing. For this reason, I refrain from expressing the magnetisation in terms of Bohr magnetons per Co atom (μ_B/Co), which is often the standard method of expressing the magnetisation. It implies that the magnetisation is solely a consequence of the transition metal doping, which from our results, may or may not be the case. With this in mind, one way to try and make head-way of these issues is to try and understand the role of the transition metal dopants. As discussed, XRD, magnetometry and magnetotransport characterisation alone does not suffice when trying to elucidate the physical mechanisms behind the magnetism in these systems - more powerful techniques are called for to give greater detail on the dopant distribution and chemical states. In the following two chapters, characterisation of Co-doped In_2O_3 and ITO thin films are carried out using two different forms of magnetic circular dichroism: first, using x-rays (chapter 6), and second, using an optical light source (chapter 7).

Bibliography

[1] T. Mizokawa, T. Nambu, A. Fujimori, T. Fukumura, M. Kawasaki, Phys. Rev. B65, 085209, (2001).

[2] E. H. Hall, Amer. J. Math. 2, 287, (1879).

[3] H. Toyosaki, T. Fukumura, Y. Yamada, K. Nakajima, T. Chikyow, T. Hasegawa, H. Koinuma, M. Kawasaki, Nature Mater. 3, 221, (2004).

[4] H. Toyosaki, T. Fukumura, Y. Yamada, M. Kawasaki, Appl. Phys. Lett. 86, 182503, (2005).

[5] K. Ueno, T. Fukumura, H. Toyosaki, M. Nakano, M. Kawasaki, Appl. Phys. Lett. 90,072103, (2007).

[6] H. S. Hsu, C. P. Lin, H. Chou, J. C. A. Huang, Appl. Phys. Lett. 93, 142507, (2008).

[7] S. X. Zhang, W. Yu, S. B. Ogale, S. R. Shinde, D. C. Kundaliya, W. K. Tse, S. Y. Young, J. S. Higgins, L. G. Salamanca-Riba, M. Herrera, L. F. Fu, N. D. Browning, R. L. Greene, T. Venkatesan, Phys. Rev. B 76, 085323, (2007).

[8] S. R. Shinde, S. B. Ogale, J. S. Higgins, H. Zheng, A. J. Millis, V. N. Kulkarni, R. Ramesh, R. L. Greene, and T. Venkatesan, Phys. Rev. Lett. 92, 166601, (2004).

[9] Q. Xu, H. Schmidt, S. Zhou, K. Potzger, M. Helm, H. Hochmuth, M. Lorenz, A. Setzer, P. esquinazi, C. Meinecke, M. Grundmann, Appl. Phys. Lett. 92, 082508, (2008).

[10] T. Fukumura, H. Toyosaki, Y. Yamada, Semicond. Sci. Technol. 20, S103S111, (2005).

[11] J. Philip, A. Punnoose, B.I. Kim, K. M. Reddy, S. Layne, J. O. Holmes, B. Satapati, P. R. Leclair, T. S. Santos, J. S. Moodera, Nature Mater. 5, (2006).

[12] H. S. Kim, S. H. Ji, H. Kim, S. K. Hong, D. Kim, Y. E. Ihm, W. K. Choo, Solid State. Comm. 137, 41-43, (2006).

[13] H. Raebiger, S. Lany, A. Zunger, Phys. Rev. Lett. 101, 027203, (2008).

[14] F. X. Jiang, X. H. Xu, J. Zhang, X. C. Fan, H. S. Wu, G. A. Gehring, Appl. Phys. Lett. 96, 052503, (2010).

[15] R. P. Panguluri, P. Kharel, C. Subdakar, R. Naik, R. Suranarayanan, V. M. Naik, A. G. Petukhov, B. Nadgorny, G. Lawes, Phys. Rev. B 79, 165208, (2009).

[16] X. L. Wang, G. Peleckis, S. X. Dou, R. S. Liu, J. G. Zhu, J. Appl. Phys. 101, 09H121, (2007).

[17] J. He, S. Xu, Y. K. Yoo, Q. Xue, H. C. Lee, S. Cheng, X. D. Xiang, I. Takeuchi, Appl. Phys. Lett. 86, 052503, (2005).

[18] Z. G. Yu, J. He, S. Xu, Q. Xue, O. M. J. van't Erve, B. T. Jonker, M. A. Marcus, Y. K. Yoo, S. Cheng, X. D. Xiang, Phys. Rev. B 74, 165321, (2006).

[19] V. Brize, J. Sakai, N. H. Hong, Physica B, 379-382, (2007).

[20] J. Philip, N. Theodoropoulou, G. Berera, J. Moodera, B. Satpati, Appl. Phys. Lett. 85, 5, (2004).

[21] J. Stankiewicz, F. Villuendas, J. Bartomle, Phys. Rev. B 75, 235308, (2007).

[22] G. Subias, J. Stankiewicz, F. Villuendas, M. P. Lozano, J. Garcia, Phys. Rev. B 79, 094118, (2009).

[23] P. Kharel, C. Sudakar, M. B. Sahana, G. Lawes, R. Suryanarayanan, R. Naik, V. M. Naik, J. Appl. Phys. 101, 09H117, (2007).

[24] N. H. Hong, J. Sakai, N. T. Huong, V. Brize, Appl. Phys. Lett. 87, 102505, (2005).

[25] G. Peleckis, X. L. Wang, S. X. Dou, Appl. Phys. Lett. 89, 022501, (2006).

[26] T. Nakamura, K. Tanabe, K. Tsureishi, K. Tachibana, J. Appl. Phys. 101, 09H105, (2007).

[27] K. M. Reddy, J. Hays, S. Kundu, L. K. Dua, P. K. Biswas, C. Wang, V. Shutthanandan, M. H. Englehard, X. Mathew, A. Punnoose, J. Mater. Sci: Mater. Electron 18:1197-1201, (2007).

[28] G. Peleckis, X. L. Wang, S. X. Dou, Appl. Phys. Lett. 88, 132507, (2006).

[29] J. M. Baik, Y. Shoon, T. W. Kang, J. L. Lee, Jap. J. Appl. Phys., (2008).

[30] J. Stankiewicz, F. Villuendas, J. Bartolome, J. Sese, J. Magn. Magn. Mater. 310, 2084-2086, (2007).

[31] N. H. Hong, J. Sakai, N. Poirot, V. Brize, Phys. Rev. B 73, 132404, (2006).

[32] M. Venkatesan, R. D. Gunning, P. Stamenov, J. M. D. Coey, Appl. Phys. Lett. 103, 07D135, (2008).

[33] S. J. Pearton, C. Abernathy, M. E. Overberg, G. T. Thaler, D. P. Norton, N. Theodoropoulou, A. F. Hebard, Y. D. Park, F. Ren, J. Kim, L. A. Boatner, J. Appl. Phys. 93, 1, (2003).

[34] J. M. D. Coey, J. Appl. Phys. 97, 10D313, (2005).

[35] S. A. Chambers, Surf. Sci. Rep. 61, 345-381, (2006).

[36] F. Pan, C. Song, X. J. Liu, Y. C. Yang, F. Zeng, Mat. Sci. Eng. R 62, 1-35, (2008).

[37] M. Venkatesan, P. Stamenov, L. S. Dorneles, R. D. Gunning, B. Bernoux, J. M. D. Coey, Appl. Phys. Lett. 90, 242508, (2007).

[38] Z. W. Zhao, B. K. Tay, J. S. Chen, J. F. Hu, B. C. Lim, G. P. Li, Appl. Phys. Lett. 90, 152502, (2007).

[39] T. Deitl, T. Andrearczyk, A. Lipinska, M. Kiecana, M. Ttay, Y. Wu, Phys. Rev. B 76, 155312, (2007).

[40] G. S. Chang, E. Z. Kurmaev, D. W. Boukhvalov, L. D. Finkelstein, S. Colid, T. M. Pedersen, A. Moewes, A. Dinia, Phys. Rev. B 75, 195215, (2007).

[41] M. Kobayashi, Y. Ishida, J. l. Hwang, T. Mizokawa, A. Fujimori, K. Mamiya, J. Okamoto, Y. Takeda, T. Okane, Y. Saitoh, Y. Muramatsu, A. Tanaka, H. Saeki, H. Tabata, T. Kawai, Phys. Rev. B 72, 201201(R), (2005).

[42] N. Sanchez, S. Gallego, M. C. Munoz, Phys. Rev. Lett. 101, 067206, (2008).

[43] F. Schoofs, T. Fix, A. M. H. R. Hakimi, S. S. Dhesi, G. van der Laan, S. A. Cavill, S. Langridge, J. L. MacManus-Driscoll, M. G. Blamire, J. Appl. Phys. 108, 053911, (2010).

[44] R. Hanafin, T. Archer, S. Sanvito, Phys. Rev. B 81, 054441, (2010).

[45] T. C. Kaspar, T. Droubay, S. M. Heald, P. Nachimuthu, C. M. Wang, V. Shutthanandan, C. A. Johnson, D. R. Gamelin, S. A. Chambers, New J. Phys. 10, 055010, (2008).

[46] C. D. Pemmaraju, R. Hanafin, T. Archer, H. B. Braun, S. Sanvito, Phys. Rev. B 78, 054428, (2008).

[47] Y. Matsumoto, M. Murakami, T. Shono, T. Hasegawa, T. Fukumura, M. Kawasaki, P. Ahmet, T. Chikyow, S.-Y. Koshihara, H. Koinuma, Science 291, 854, (2001).

[48] Y. Matsumoto, M. Murakami, K. Hasegawa, T. Fukumura, M. Kawasaki, P. Ahmet, K. Nakajima, T. Chikyow, H. Koinuma, Appl. Surf. Sci. 189, 344, (2002).

[49] J. Y. Kim, J. H. Park, B. G. Park, H. J. Noh, S. J. Oh, J. S. Yang, D. H. Kim, S. D. Bu, T. W. Noh, H. J. Lin, H. H. Hsieh, C. T. Chen, Phys. Rev. Lett. 90, 1, (2003).

[50] D. H. Kim, J. S. Yang, Y. S. Kim, T. W. Noh, S. D. Bu, S. I. Baik, Y. W. Kim, Y. D. Park, S. J. Pearton, J. Y. Kim, J. H. Park, H. J. Lin, C. T. Chen, Y. J. Song, Phys. Rev. B 71, 014440, (2005).

[51] G. C. Han, P. Luo, Z. B. Guo, F.Un Nahar, M. Tay, Y. H. Wu, S. J. Wang, Thin Solid Films 505, 137-140, (2006).

[52] Y. J. Lee, M. P. de Jong, R. Jansen, Appl. Phys. Lett. 96, 082506, (2010).

[53] M. Venkatesan, C. B. Fitzgerald, J. M. D. Coey, Nature (London) 430, 630, (2004).

[54] J. M. D. Coey, M. Venkatesan, C. B. Fitzgerald, Nature, 4, (2005).

[55] N. H. Hong, J. Sakai, N. Poirot, V. Brize, Phys. Rev. B 73, 132404, (2005).

[56] D. Berardan, E. Guilmeau, D. Pelloquin, J. Magn. Magn. Mater. 320, 9830989, (2008).

[57] D. W. Abraham, M. M. Frank, S. Guha, Appl. Phys. Lett. 87, 252502, (2005).

[58] J. M. D. Coey, Curr. Opin. Solid State and Materials Science 10, 8392, (2006).

[59] S. B. Ogale, R. J. Choudhary, J. P. Buban, S. E. Lofland, S. R. Shinde, S. N. Kale, V. N. Kulkarni, J. Higgins, C. Lanci, J. R. Simpson, N. D. Browning, S. Das Sarma, H. D. Drew, R. L. Greene, T. Venkatesan, Phys. Rev. Lett. 91, 7, (2003)

[60] J. M. D. Coey, M. Venkatesan, C. B. Fitzgerald, L. S. Dorneles, P. Stamenov, J. G. Lunney, J. Magn. Magn. Mater 290, 1405-7, (2005).

[61] M. A. Garcia, E. Fernandez Pinel, J. de la Venta, A. Quesada, V. Bouzas, J. F. Fernandez, J. J. Romero, M. S. Martin Gonzalez, J. L. Costa-Kramer, J. Appl. Phys. 105, 013925, (2009).

[62] J. M. D. Coey, K. Wongsaprom, J. Alaria, M. Venkastesan, J. Phys. D: Appl. Phys. 41, 134012, (2008).

[63] J. M. D. Coey, P. Stamenov, R. D. Gunning, M. Venkatesan, K. Paul, New J. Physics 12, 053025, (2010).

[64] M. Opel, K.-W. Nielsen, S. Bauer, S. T. B. Goennenwein, J. C. Cezar, D. Schmeisser, J. Simon, W. Mader, and R. Gross, Eur. Phys. J. B 63, 437, (2008).

[65] E. P. Wohlfarth, J. Appl. Phys. 39, 2, (1968).

[66] G. A. Gehring, Private discussion

[67] T. C. Kaspar, S. M. Heald, C. M. Wang, J. D. Bryan, T. Droubay, V. Shutthanandan, S. Thevuthasan, D. E. McCready, A. J. Kellock, D. R. Gamelin, S. A. Chambers, Phys. Rev. Lett. 95, 217203, (2005).

[68] Y. Shapira and R. L. Krautz, Phys. Rev. B 10, 4781, (1974).

[69] C. Y. Park, S. G. Yoon, Y. H. Jo, S. C. Shin, Appl. Phys. Lett. 95, 122502, (2009).

Chapter 6

X-ray Absorption and magnetic circular dichroism characterisation of Co-doped Indium Tin Oxide thin films

This chapter introduces the concepts behind x-ray absorption and x-ray magnetic circular dichroism and describes some of the results obtained by others who have also investigated dilute magnetic oxide systems using these techniques. Our results obtained using Beamline I06 at Diamond Light Source are then presented concentrating mainly on an as-deposited 5.4 at.% Co-doped ITO thin film.

6.1 Introduction

In chapter 5 we have established that the origin of magnetism in dilute magnetic oxide systems is still an area which puzzles much of the scientific community. An ideal intrinsic DMO exhibits ferromagnetism as a result of a coupling interaction between localised moments at the substituted sites mediated by charge carriers of the host oxide. The need for more rigorous characterisation of the DMO materials have also been described in chapter 5.

Here we perform element specific measurements on Co-doped ITO(10) films using x-ray magnetic circular dichroism (XMCD). The majority of previous element specific XMCD measurements at the Co $L_{2,3}$ edges have been performed on $Zn_{1-x}Co_xO$ thin films [1–5]. Our results here concentrate on the 5.4 at.% Co-doped ITO(10) film characterised in chapter 5 and are the first set of results which describe the origins of magnetism in TM-doped ITO using advanced element specific techniques such as XMCD.

6.2 X-Ray Absorption Spectroscopy

X-ray Absorption Spectroscopy (XAS) is a technique used to probe the electronic configuration of a specific element within a material. Scanning the photon energy over the chosen element's absorption edge results in a sharp increase in the x-ray absorption. Electrons from an initial core state are promoted to the lowest unfilled state with allowed symmetry, just above the Fermi level. After absorption, the atom relaxes by one of two channels. The first involves the Auger process, where an intermediate electron recombines with the core hole and the energy of the excitation is carried away by the ejection of a secondary electron. The other channel is fluorescent photon emission, the inverse of the absorption process, where the excited electron recombines with the core hole and emits a photon.

Figure 6.1 shows the L-edge absorption spectra of Fe, Co and Ni in metal and oxide form. This is a $2p \rightarrow 3d$ transition with $2p^6 3d^N$ and $2p^5 3d^{N+1}$ initial and final states. L-edge absorption studies are best suited to probe magnetic properties which are governed by the $3d$ valence electrons (as is the case for transition metals) for the following reasons;

1. The dipole transition excites the $2p$ electron into the localised $3d$ shell, which has the magnetic moment.

2. The absorption spectrum is dominated by dipole transitions from the core $2p$ level to the empty $3d$ states which have a large Coloumb interaction between the levels and therefore gives information on the local electronic structure.

3. Spectra can give information about the oxidation state and symmetry of the $3d$

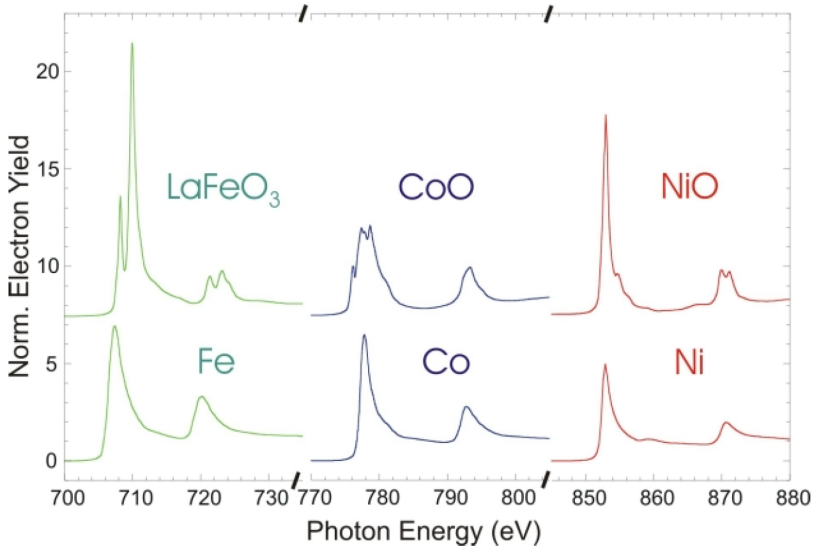

Figure 6.1: L-edge x-ray absorption edge spectra of Fe, Co and Ni in the form of the elemental metals and as oxides. The two main structures are called the L_3 (lower energy) and L_2 absorption edges. From reference [6].

transition metal ions.

4. The $2p$ and $3d$ core levels have high spin-orbit coupling resulting in very intense spectral peaks.

5. The $2p_{3/2}$ and $2p_{1/2}$ spectral parts are clearly separated by the core-hole spin-orbit interaction.

6. Core-hole lifetime broadening is small, resulting in sharp "multiplet" structures.

Metal spectra generally show two broad peaks which reflect the width of the empty d-band states. The oxides on the other hand exhibit a fine structure, often referred to as a "multiplet" structure. These empty oxide states are more localised than metal states. A strong coupling interaction between the spin and orbital momentum of different $3d$ valence electrons in the electronic ground state gives rise to a multitude of degenerate final states. All final states which are resolvable show up as multiplets in the absorption spectra.

6.3 Principles behind XMCD

XMCD, the difference in core-level absorption between right (ρ_+) and left (ρ_-) circularly polarised x-rays ($\rho_{XMCD} = \rho_- - \rho_+$), is an element and site specific probe of magnetism [8]. Since the absorption of polarised light leads to spin selectivity, (ρ_+) or (ρ_-) light preferentially probes the spin up and down states above the Fermi level.

Further, the XMCD sum rules [9] (see 6.3.1) can be applied to separate the contribution of spin and orbital contributions to the magnetic moment [10]. XMCD therefore provides a direct probe of the nature of ferromagnetism in DMOs, in particular the role that the TM ions play.

6.3.1 Origin of the XMCD effect

The microscopic origin of the XMCD effect is explained by electronic transitions from spin-orbit split initial $2p$ states to exchange-split $3d$ final states (Fig. 6.2). A model, termed the "two step" model, proposed by Stohr and Wu [11] explains the origin of XMCD at the $L_{2,3}$ edges of $3d$ transition metals. Firstly, the interaction of circularly polarised x-rays with the p shell electrons leads to the excitation of spin-polarised electrons with a spin and/or orbital momentum from a localised atomic inner shell. In the second step, the $3d$ shell serves as the detector of the spin or orbital momentum of the excited electron. For transition metals, the $3d$ final states are exchange split and there is an imbalance in the number of available unoccupied $3d$ spin-up and spin-down states. Therefore, the absorption of ρ_+ and ρ_- is different. In the case of non-magnetic materials, the $3d$ band will not be exchange-split (i.e. equal population of spin-up and spin-down) so that the transition intensities are identical for ρ_+ and ρ_-. In this scenario there will be no XMCD effect. Therefore, we can conclude that to be able to detect an XMCD effect at all, it is essential that the measured sample must have both strong spin-orbit interactions (to clearly separate the $2p_{3/2}$ and $2p_{1/2}$ spectral parts) and spin polarisation (d-band splitting).

The XMCD spectrum is calculated as the difference between the two measured XAS (ρ_+ and ρ_-), i.e. $\rho_{XMCD} = \rho_- - \rho_+$. Figure 6.3 (a) shows the typical absorption spectra for left and right circularly polarised light at the Co $L_{2,3}$ edge for a Co thin film [10]. It shows the Co $2p \rightarrow 3d$ transitions which results in two observable peaks (L_3 and L_2) due to the spin-orbit splitting of p-orbitals; L_3 corresponding to $2p_{3/2} \rightarrow 3d$ transition, and the L_2 corresponding to $2p_{1/2} \rightarrow 3d$ transition. The XMCD spectrum is opposite in sign at the L_3 and L_2 edge because of the opposite sign of the spin-orbit coupling in the $2p$ states: $1+s$ for $2p_{3/2}$ and 1-s for $2p_{1/2}$ (the orbital angular momentum number for a p orbital is equal to 1 and the total angular momentum number, j is a combination of orbital and spin angular momenta, $j = l + s$). The dichroism is given in Fig. 6.3 (b) which shows up with opposite signs at the two Co absorption edges.

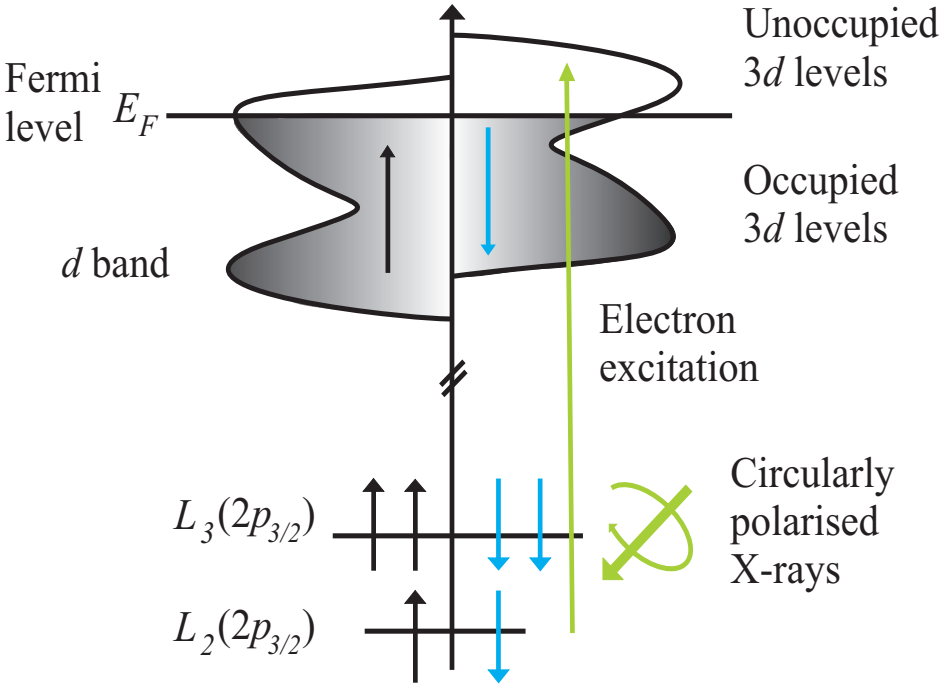

Figure 6.2: Schematic representation of the spin-dependent absorption process in the "two-step" model.

6.3.2 XMCD sum rules

The known spin polarisation of the $2p \rightarrow 3d$ transitions can be used as a probe to quantitatively measure the spin polarisation of the density of unoccupied valence states, which is directly linked with the spin magnetic moment. Due to the opposite sign at the L_3 and L_2 edges, the contributions from spin and orbital magnetic moments define an orthonormal basis for a measured XMCD spectrum. It can therefore be used to decompose a signal into its constituent spin (μ_S) and orbital (μ_L) components, described by the sum rules, and can be written as;

$$\mu_L = -\frac{4\int_{L3}\rho_{XMCD}\partial\omega}{3\int_{L3+L2}(\rho_- + \rho_+)\partial\omega}\cdot\frac{n_h}{p_{pol}} = -\frac{4q}{3r}\cdot\frac{n_h}{p_{pol}} \tag{6.1}$$

and

$$\mu_S = -\frac{6\int_{L3}\rho_{XMCD}\partial\omega - 4\int_{L3+L2}\rho_{XMCD}\partial\omega}{\int_{L3+L2}(\rho_- + \rho_+)\partial\omega}\cdot\frac{n_h}{p_{pol}} + 7 < T_z > = -\frac{6p-4q}{r}\cdot\frac{n_h}{p_{pol}} + 7 < T_z > \tag{6.2}$$

where n_h is the number of holes in the $3d$ band, and p_{pol} is the degree of the polarization of the light (roughly equal to unity at Diamond Light Source synchrotron facility), $< T_z >$ is the expectation value of the magnetic dipole operator (assumed to be zero in the bulk of cubic crystals), and,

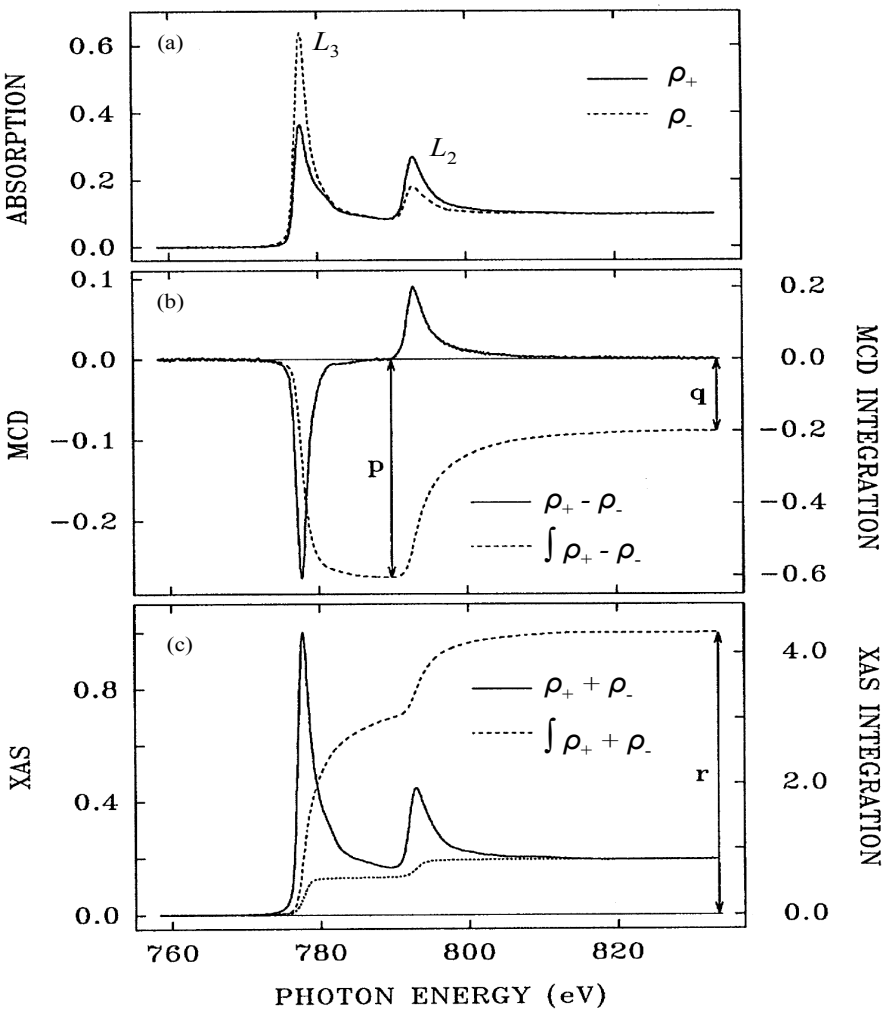

Figure 6.3: $L_{2,3}$-edge XAS and XMCD spectra for Co under an applied magnetic field of 0.05 T. (a) the XAS absorption spectra, (b) and (c) show the XMCD and summed XAS spectra and their integrations (dotted lines) calculated from the spectra shown in (a). p and q shown in (b) and the r shown in (c) are the three integrals required for the sum rule analysis. After reference [10].

$$p = \int_{L3} \rho_{XMCD} \partial\omega, q = \int_{L3+L2} \rho_{XMCD} \partial\omega, r = \int_{L3+L2} (\rho_- + \rho_+) \partial\omega \qquad (6.3)$$

which are clearly defined in Figs. 6.3 (b) and (c).

For a more comprehensive review of the XMCD processes, the reader is directed towards more detailed reviews [10, 12, 13].

6.3.3 Detection Methods

The XAS measurements can be made in a variety of ways. For a detailed review of these methods, the reader is referred to reference [14] (see Fig. 6.4). The results presented in this thesis use the total electron (TEY) and fluorescence yield (FY) methods. In the TEY method, the absorption spectra is obtained by monitoring all excited photoelectrons created during the absorption process. The electron yield is typically measured directly using a channeltron electron multiplier, or indirectly as the photocurrent of electrons flowing to the sample via the ground (the drain current). Since electrons are only emitted from the surface of the sample this technique is a surface sensitive technique only, with an escape or probing depth of the order of less than 10 nm and provides information representative of the near-surface region [14]. Therefore, for thick films, the spectra may not be representative of the bulk behaviour of the material. The FY mode can probe depths of the order of hundreds of nm [14]. When photoelectrons vacate the sample, positively charged holes are left behind. These holes are subsequently filled by Auger electrons from outer shells and x-ray fluorescence decay. The fluorescence signal is detected using a photodiode detector located close to the sample surface. TEY and FY modes of measurements are recorded simultaneously.

6.4 Previous Work

As stated earlier, the majority of previous element specific XMCD measurements at the Co $L_{2,3}$ edges have been performed on $Zn_{1-x}Co_xO$ [1–5]. Kobayashi *et al.* [2] were the first to investigate the role of the Co dopants in Co-doped ZnO concluding the coexistence of two magnetic phases emanating from the Co ions: the first, a very small fraction of ferromagnetic Co, and the second, strongly antiferromagnetically coupled Co. The magnetic field dependence of the spin (M_{spin}), orbital ($M_{orbital}$) and total (M_{tot}) magnetic moments of Co (estimated using the XMCD sum rules) indicate that there are both paramagnetic (signal which increases linearly with the applied field) and ferromagnetic (signal which persists at zero applied field) contributions to the overall XMCD spectrum (Fig. 6.5). The authors also conclude after some careful analytical subtractions that the XMCD line shape of both the paramagnetic and ferromagnetic components show similar multiplet structures, very different to that of pure Co metal,

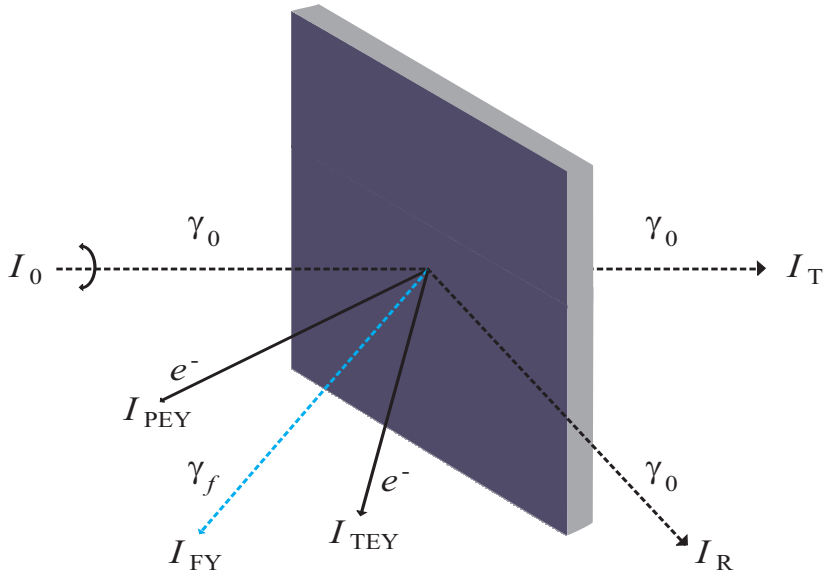

Figure 6.4: Experimental geometries showing five different methods for measuring XAS and XMCD spectra, where I_0 is the incident radiation, I_T is the transmitted flux, I_R the reflected flux, I_{TEY} the total electron yield, I_{FY} the fluorescence yield and I_{PEY} the partial electron yield. Adapted from reference [14].

therefore indicating that only a fraction of the doped transition metal ions are ferrromagnetic.

Gacic *et al.* performed a more detailed investigation into 5 at.% Co-doped ZnO and undoped ZnO [3]. As in the investigations performed by Kobayashi *et al.*, multiplet-like spectral features were observed in the XAS and XMCD spectra, however the dependence on temperature was very different. In the case of Gacic *et al.* the XMCD signal and moment calculated via the application of the sum rules reduced drastically as a function of increasing temperature [Fig. 6.6 (b)] resembling behaviour typical of a paramagnet and suggested a weak interaction between the Co ions. The field dependence of the calculated moment (m_s) gives no indication of ferromagnetic Co either as they see a perfectly linear dependence with no sign of remanent magnetisation. These results therefore contradict the findings of Kobayashi *et al.* with no evidence for any antiferromagnetic interaction between the dispersed Co ions. Measurements at the Zn $L_{2,3}$ edge confirmed that no magnetic moment was present on the Zn ions. However, these results were only made in TEY mode, and therefore only describe the properties at the very near-surface region.

Barla *et al.* furthered this work by performing XAS and XMCD measurements in both TEY and FY modes, therefore probing the bulk of the sample, in $Zn_{0.90}Co_{0.10}O$ and $Zn_{0.75}Co_{0.25}O$ thin films [4]. They confirm the results of Gacic *et al.* showing the purely paramagnetic nature of the Co dopants down to 2 K with no evidence of ferromagnetic metallic clusters. From these findings, both Gacic and Barla exclude transition metal Co dopants as the sole source of room temperature magnetism, and instead suggest a defect- or oxygen-related mechanism, similar to that suggested for

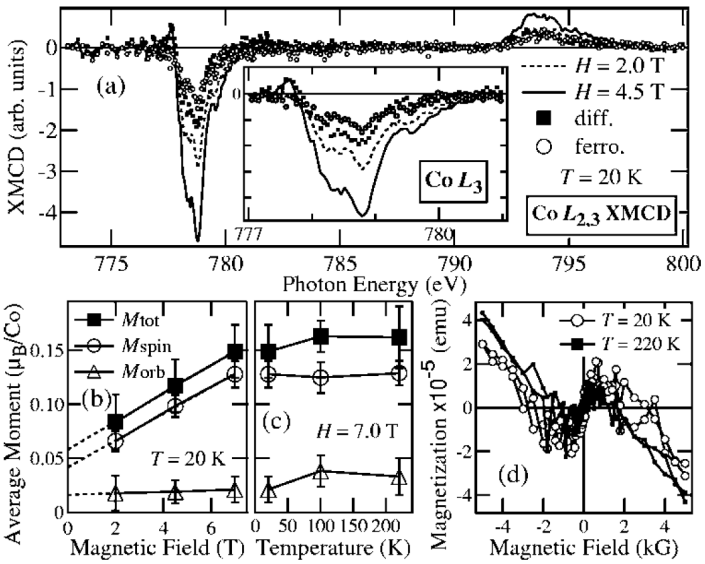

Figure 6.5: Magnetic field and temperature dependences of the Co $L_{2,3}$ XMCD spectra of $Zn_{0.95}Co_{0.05}O$. (a) XMCD spectra under different magnetic fields at 20 K. Average magnetic moments M_{spin}, M_{orb}, and M_{tot} as functions of magnetic field (b) and temperature (c), estimated using the XMCD sum rules, (d) Magnetization curves measured by a SQUID magnetometer. After reference [2].

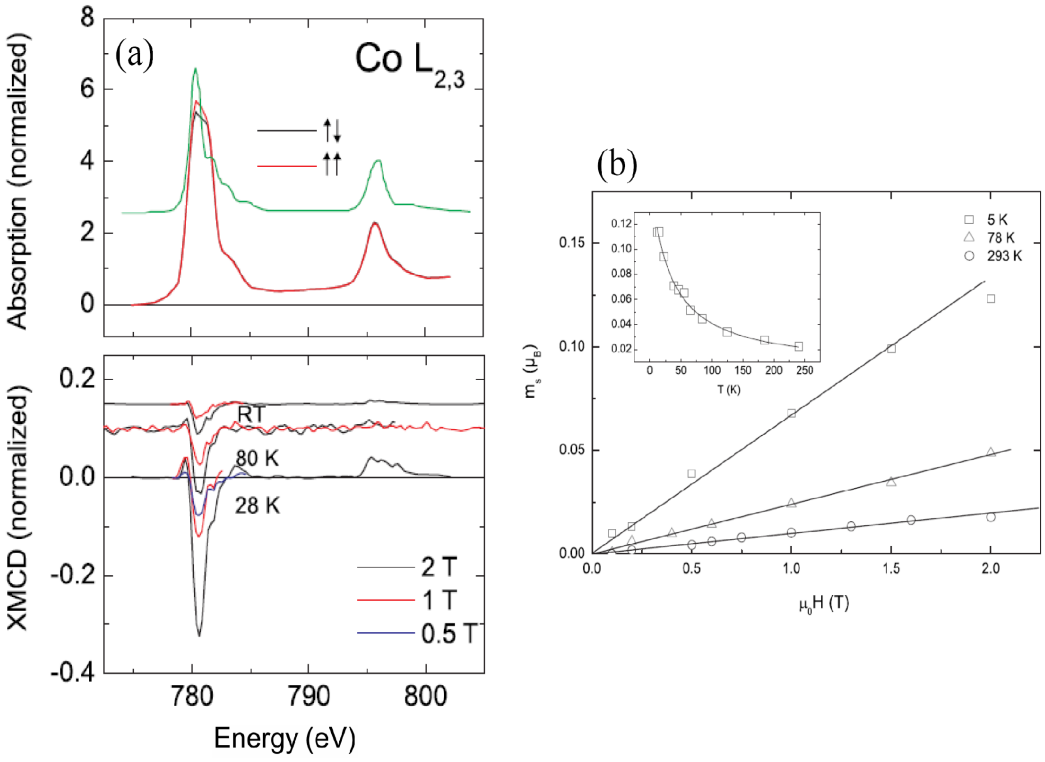

Figure 6.6: (a) XAS (top panel) and XMCD (bottom panel) spectra at the Co $L_{2,3}$ edges of a 5% Co doped ZnO thin film sample, (b) Field-dependent Co XMCD magnetic moments for three different temperatures. The inset shows the temperature dependent Co XMCD magnetisation and a corresponding Curie-Weiss law fit. After reference [3].

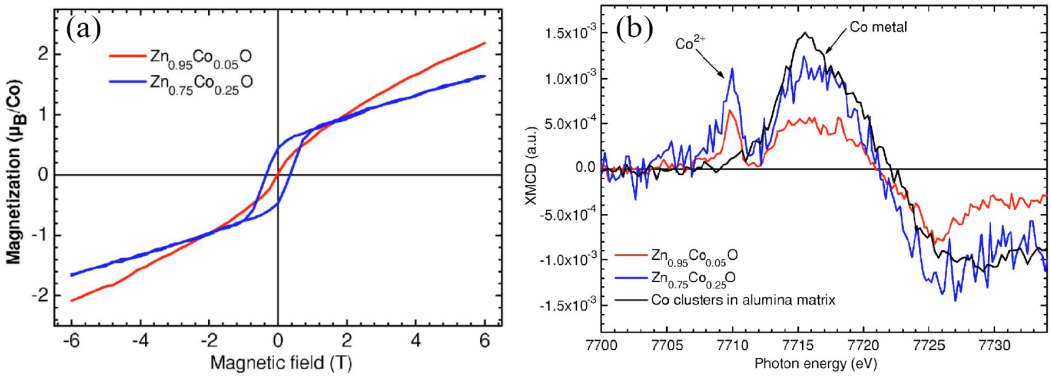

Figure 6.7: (a) XMCD magnetisation loops measured at the Co L_3 edge for $Zn_{0.95}Co_{0.05}O$ (red), $Zn_{0.75}Co_{0.25}O$ (blue), (b) XMCD spectra measured at the Co K edge for $Zn_{0.95}Co_{0.05}O$ (red), $Zn_{0.75}Co_{0.25}O$ (blue), and Co metallic clusters (black) embedded in an alumina matrix. FY spectra were recorded at T = 10 K and a 6 T applied field. After reference [5].

undoped, ferromagnetic oxides like HfO_2 [15].

The most comprehensive study of transition-metal doped ZnO using XAS and XMCD characterisation techniques was performed by Tietze *et al.* [1]. In addition to the focus at the Co $L_{2,3}$ edge, measurements were also performed at the oxygen K-edge. Once again, only paramagnetic Co was found both in TEY and FY modes, and in all cases only spectra consistent with a multiplet description of Co d^7 configuration in tetrahedral coordination were observed. The measurements at the O K-edge showed no sign of magnetisation. Having not found any element-specific signature of ferromagnetism, Tietze *et al.* suggest oxygen vacancies as a possible mediator for ferromagnetism in these materials.

Each of the experimental results described above show that within the dilute limit of Co in ZnO, the Co dopants successfully substitute for Zn lattice sites. Theoretical simulations performed to fit many of the XMCD spectra at the Co $L_{2,3}$ edge suggested that Co is tetrahedrally coordinated within the matrix in the $3d^7$ state.

Rode *et al.* investigated the ferromagnetic Co-doped ZnO system where low (5 %) and high (25 %) Co doping was used [5]. Figure 6.7 summarises the main findings of the report. Here we see that XMCD magnetisation loops at the Co $L_{2,3}$ edge reveal that in the lower doping regime, the magnetisation behaviour is paramagnetic (compounded by the multiplet XAS and XMCD line structure which implies ionic Co), whereas in the higher doping regime, it is clearly ferromagnetic with magnetisation persisting at remanence [Fig. 6.7 (a)]. In fact, the magnetisation loop in the highly doped regime also gives a paramagnetic component at higher fields (above 1 T) as is seen in the lower doping regime. This was confirmed by simply performing XAS and XMCD measurements at low (remanence) and high fields. Not only did the XMCD signal persist at remanence, but it also gave a different line shape, one that resembled that of pure Co metal, confirming that the origin of magnetism in the highly doped

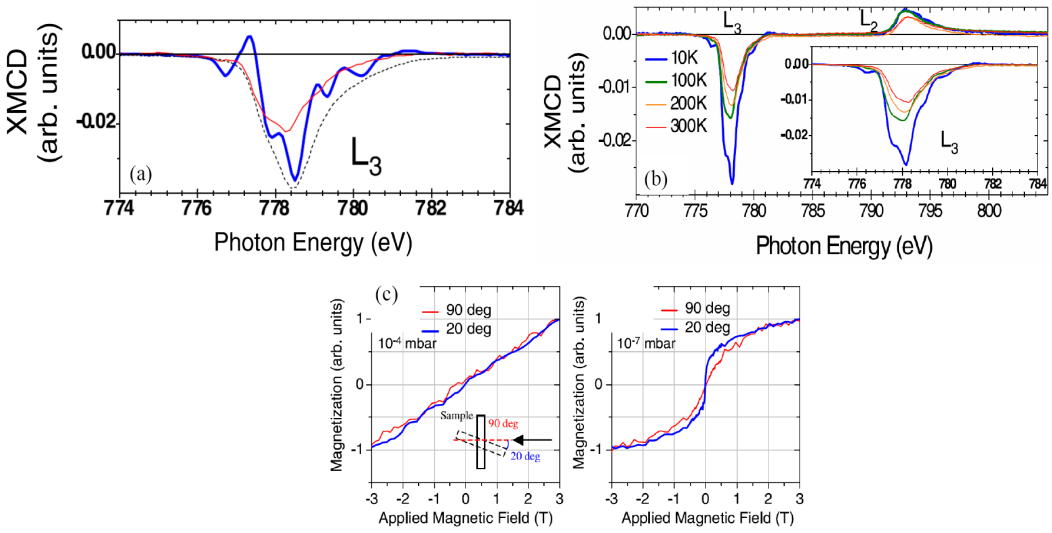

Figure 6.8: (a) Co $L_{2,3}$ edge XMCD spectra recorded in TEY mode at 10 K with an applied magnetic field of 3 T for films grown at 10^{-7} (red) and 10^{-4} (blue) mbar. The dotted black line shows a reference of metallic cobalt, (b) XMCD spectra in TEY mode for a sample grown at 10^{-6} mbar as a function of temperature with an applied magnetic field of up to 3 T. The inset simply provides an expanded view of the Co L_3 edge as a function of temperature, (c) XMCD magnetisation loop measured in TEY mode at Co L_3 edge for a high oxygen pressure film (left) and for a low oxygen pressure film (right) recorded for an angle between the applied magnetic field and the sample surface of 90° and 20° respectively. The applied magnetic field and the photon wavevector are both along the black arrow. After reference [7].

samples was metallic Co clustering. Taking the investigation a step further, XAS and XMCD measurements were performed at 10 K in a 6 T field at the Co K-edge, therefore probing the $1s \rightarrow 4p$ transitions, in FY mode. In each scenario, both low and high doping regimes, two clear dichroic peaks were observed, one corresponding to Co^{2+} ions and the other to metallic Co [see Fig. 6.7 (b)]. This was a hugely significant result and proved the coexistence of magnetic phases, even in the low doping regime sample.

Extensive investigations into the Co-doped (La, Sr)TiO_3 (LSTO) system via XAS and XMCD measurements have been performed by Copie *et al.* [7]. Two samples with identical Co doping level (2 %) were grown in different oxygen partial pressures: one high (10^{-4} mbar) and one low (10^{-7} mbar). Like Rode *et al.* they too claim evidence of mixed phases of ionic Co^{2+} and metallic Co clustering, particularly in the sample grown in low oxygen pressure. This is seen clearly in Fig. 6.8 (a) (solid red line) where the sharp multiplet line features are beginning to disappear once the oxygen partial pressure is reduced, and the XMCD spectrum starts to resemble that of pure metallic Co (dotted black line). Further evidence for metallic Co clustering was found when analysing the temperature dependence of the XMCD line structure [Fig. 6.8 (b)]. Here the authors conclude that the progressive vanishing of the fine multiplet structure is indicative of poor ionic behaviour.

6.5 Experimental Results

In order to probe the magnetic nature of Co-doped ITO in greater detail, XAS and XMCD measurements were performed at the In and Sn $M_{2,3}$, Co $L_{2,3}$- and oxygen K-edges on an as-deposited 5.4 at.% Co-doped ITO(10) sample (described earlier in chapter 5). The sample surface orientation was set at 45° to the incident beam. The magnetic field, in all XMCD measurements here, was applied in a direction parallel to the incident x-ray beam. The XAS spectra were recorded in both TEY and FY modes in order to measure the surface and bulk components, respectively.

6.5.1 In and Sn $M_{2,3}$ edges

In order to investigate the possibility of magnetic polarisation at the In and Sn lattice sites, XAS and XMCD spectra were recorded at the In and Sn $M_{2,3}$ edges. Both In^{3+} and Sn^{4+} have an electronic configuration of $4d^{10}$ and we do not expect any magnetic moment to be present at all. Figures 6.9 (a) and 6.9 (b) show the XAS and XMCD spectra measured in TEY mode at the In and Sn M_2 edges respectively at 2 K under an applied magnetic field of 4 T. No evidence of dichroic behavior at the In or Sn M_2 edges can be seen within the detection limits of the instrument. This excludes the presence of any detectable ferromagnetic polarisation of the In and Sn s and d states. The same behavior was observed at both edges at 300 K also under an applied magnetic field of 4 T.

6.5.2 Co $L_{2,3}$ edge

The XAS and XMCD spectra measured at 2 K in a 4 T field at the Co $L_{2,3}$ edge using TEY are shown in Fig. 6.10. The absorption edges appear due to a Co $2p \longrightarrow 3d$ transition. This transition provides clues on the density of unoccupied Co $3d$ states, therefore probing the $3d$ magnetism of Co. A large XMCD signal is present at the L_3 edge, indicating a significant magnetic moment at the Co^{2+} sites in the applied magnetic field. The XMCD asymmetries $[(\rho_+ - \rho_-)/(\rho_+ + \rho_-)]$ at 2 K were estimated as 5.5% and 14.2% respectively for TEY and FY spectra. TEY is generally lower than FY and is consistent with the fact that there is a lower volume fraction of Co dopants and magnetic coupling near the surface region of the film. The pronounced multiplet structure at the Co $L_{2,3}$ edges is typical of Co in a localised state. By comparing the XAS and XMCD spectra to those of metallic Co [10] (see Fig. 6.11), we conclude that Co clusters are absent in the surface region. The multiplet features observed are very similar to those reported in other Co-doped oxide systems [1–5, 7, 16, 17]. Furthermore, the fine structure of the XMCD spectra appears to be maintained as the temperature approaches room temperature and is shown in Fig. 6.10 (c). This is contrary to that observed in Co-doped LSTO where it was suggested that the gradual loss in fine struc-

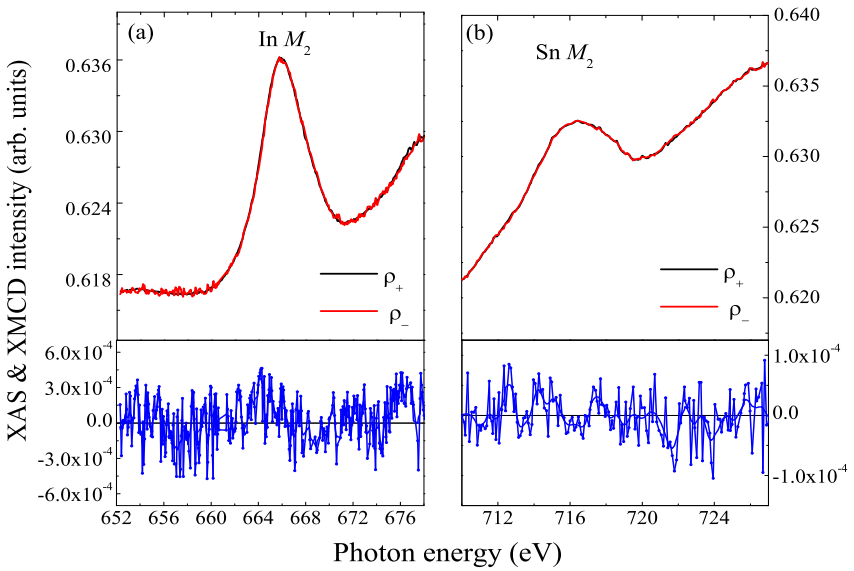

Figure 6.9: XAS and XMCD spectra in TEY mode at 2 K under an applied field of 4 T at the (a) In M_2 edge and (b) Sn M_2 edges, along with the raw XMCD data (solid blue circles) and a smoothed extrapolation (solid blue lines).

ture could be interpreted as a signature of poor ionic behavior and could indicate the presence of metallic Co clusters [7].

XAS recorded using FY mode [inset, Fig. 6.10 (a)] also exhibits pronounced multiplet features implying that the bulk of the film is also free from clustering. Fig. 6.12 (a) and (b) display the XAS and XMCD spectra for a 5.4 at.% Co-doped ITO film measured in FY mode at both 2 and 300 K. Multiplet features are visible in both cases, however, perhaps more so at 300 K. Even at 2 K, the XMCD spectrum does not coincide with that of pure metallic Co. In addition, the fact that the L_3 peak becomes increasingly multiplet-like with temperature implies that the samples are not superparamagnetic in any way. The observation of multiplet features in the FY XMCD spectra is hugely significant as it suggests that the bulk of the film is free from metal Co inclusions.

To corroborate the experimental results, the XAS and XMCD spectra were calculated (by Geerit van der Laan of Diamond Light Source) for the octahedral site symmetry of the Co ion (assuming Co substitutes for In^{3+}). Figure 6.10 (b) shows the calculated results, which are in excellent agreement with the experimental data. The spectra show the electric-dipole allowed transitions between the ground-state Co $3d^7$ $t_{2g}^5 e_g^2$ ($^4T_{1g}$) and the final-state $2p^5 3d^8$ configuration in octahedral symmetry with crystal field parameter $10D_q = 0.7$ eV split by first-order spin-orbit interaction and in the presence of a magnetic exchange field of $g\mu_B H = 1$ meV, where g is the spectroscopic splitting factor (set as 2.0023 for free electrons), μ_B is the Bohr magneton

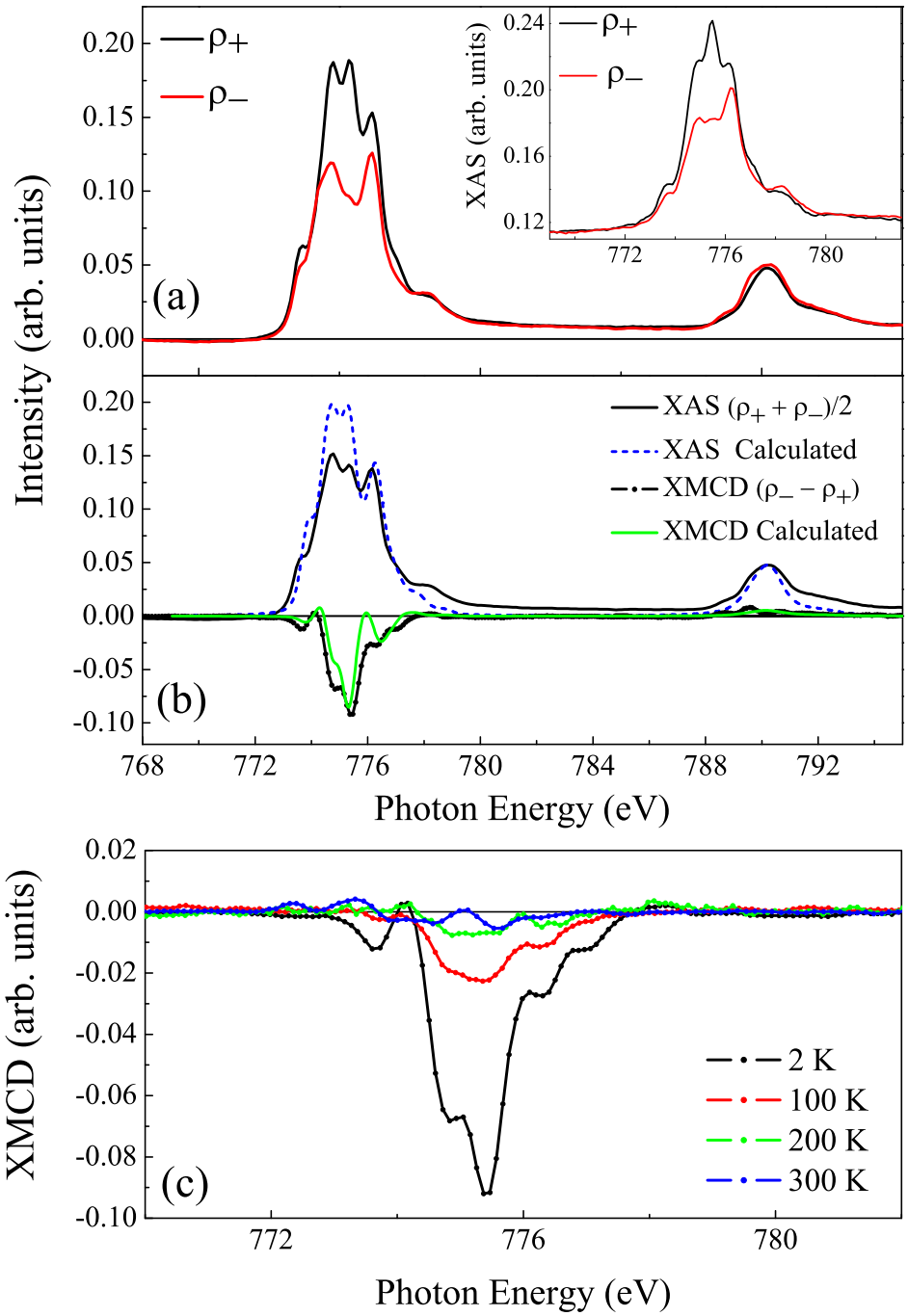

Figure 6.10: Co $L_{2,3}$ edge for a 5.4 at. % Co-doped ITO film at 2 K under an applied magnetic field of 4 T; (a) TEY XAS for right (ρ_+) and left (ρ_-) circularly polarised light. Inset: FY XAS spectra for right (ρ_+) and left (ρ_-) circularly polarised light under the same conditions, (b) average experimental TEY XAS and the calculated XAS spectra along with the experimental XMCD spectrum and calculated XMCD spectrum for octahedral Co^{2+} ($10D_q = 0.70$ eV), (c) TEY XMCD spectra at the Co L_2 edge of a 5.4 at. % Co-doped ITO film as a function of temperature under an applied magnetic field of 4 T.

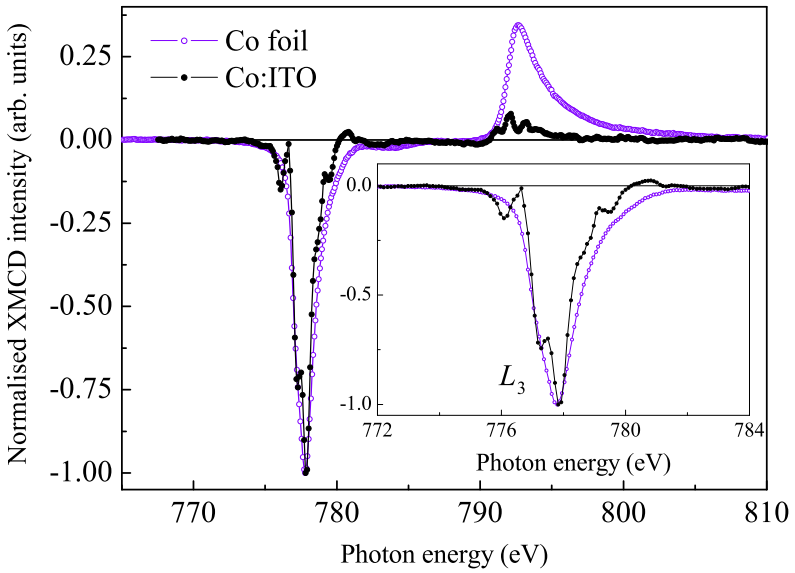

Figure 6.11: Comparison of the TEY XMCD spectra of a Co metal foil (open violet circles) and a 5.4 at.% Co-doped sample (closed black circles) at 2 K under an applied magnetic field of 4 T. Inset: an expanded view of the Co L_3 edge for each sample.

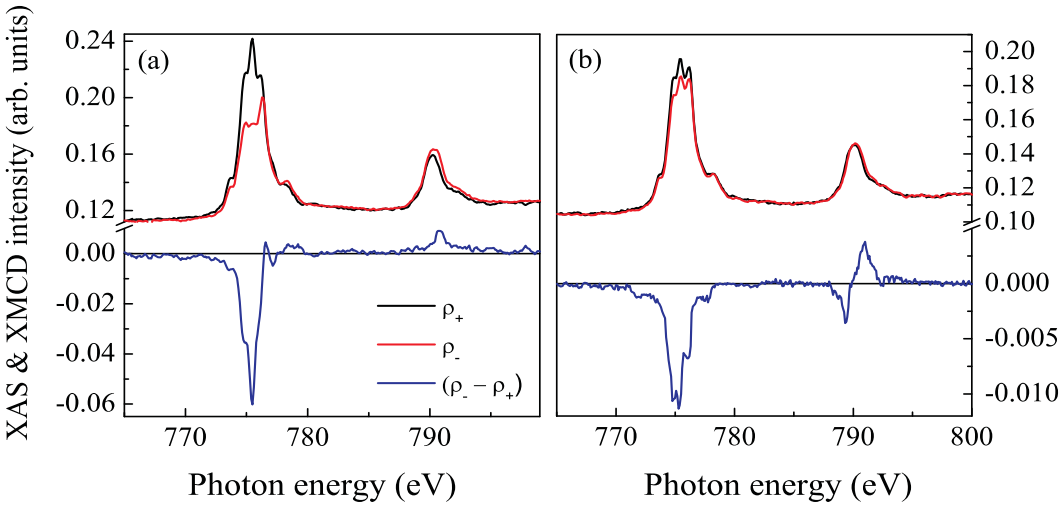

Figure 6.12: XAS and XMCD in FY mode at the Co $L_{2,3}$ edge for a 5.4 at. % Co-doped ITO film at (a) 2 K and (b) 300 K under an applied magnetic field of 4 T.

and H is the applied magnetic field. The wave functions of ground and final states were calculated in intermediate coupling using Cowan's Hartree-Fock (HF) code with relativistic correction following the method described in Ref. [18]. The Slater and spin-orbit parameters were as tabulated in Refs. [18, 19]. Interatomic screening and mixing was taken into account by reducing the atomic values of the Slater integrals $F_k(3d,3d)$, $F_k(2p,3d)$, and $G_k(2p,3d)$ to 70%, 80%, and 65%, respectively. The $2p$ spin-orbit interaction was scaled to 97% of the HF value. The calculated line spectra were broadened by a Lorentzian of $\Gamma = 0.10$ (0.40) eV for the L_3 (L_2) edge to account for intrinsic line width broadening and a Gaussian of $\sigma = 0.20$ eV for the instrumental broadening.

Element-specific magnetisation curves were recorded using XMCD in TEY and FY mode at 2, 100, 200 and 300 K by sweeping the magnetic field and maintaining the incident photon energy at 777.3 eV. Figure 6.13 (b) shows the magnetisation curve measured in FY mode at 2 K. Note that this measurement does not give an absolute value for the moment on an individual Co^{2+} ion, but provides an indication of the field dependence of the Co moment in 5.4 at.% Co-doped ITO. Similar results were obtained in TEY mode, confirming that we observe no difference in the magnetic properties of the surface and throughout the bulk of the sample. The curve can be modelled well with a Brillouin function (Eqn. 6.4) to describe paramagnetic behavior, where $y{=}g\mu_B JH/k_B T$ and m_s is the saturation magnetisation. The curve shows no ferromagnetic or remanent behavior for the Co^{2+} ions at any of the given temperatures. The fit yields a total angular momentum, J, of 0.761 and an effective total (recall that $J = L + S$) magnetic moment $p_{total} = g[J(J{+}1)]^{1/2}$ of $2.32\mu_B$/Co.

$$M_{XMCD} = m_s \left[\left(\frac{2J+1}{2J} \right) \coth \left[\frac{(2J+1)y}{2J} \right] - \left(\frac{1}{2J} \right) \coth \left(\frac{y}{2J} \right) \right] \qquad (6.4)$$

Theoretically, $S = 3/2$, $L = 3$ and therefore $J = 9/2$ for Co^{2+} in the $3d^7$ configuration. This yields a calculated theoretical total moment of $p_{total} = 6.63\mu_B$. The value we find experimentally is much lower, however is within reasonable agreement with the spin-only value ($3.87\mu_B$, calculated using $p_{spin} = 2[S(S{+}1)]^{1/2}$) expected for paramagnetic Co ions in the upper spin state [20]. Therefore, it is clear that the spin-only values are in much better agreement with experiment than the values calculated using the total angular momentum. This phenomenon is known as "quenching" of the orbital angular momentum (L is reduced to zero), and is a result of the electric field (crystal field) generated by the surrounding ions in the solid.

A more complete plot of the XMCD magnetisation curves is shown in Fig. 6.14, where data is plotted at each of the temperature intervals along with their respective Brillouin fits. The plot supports the data presented in Fig. 6.13 (c) where the XMCD magnetisation decreases as the temperature increases.

Fig 6.13 (a) shows the respective XAS and XMCD spectra in FY mode at the Co $L_{2,3}$ edge at 300 K in the remanent state (0 T). The sample was first magnetised at 4 T

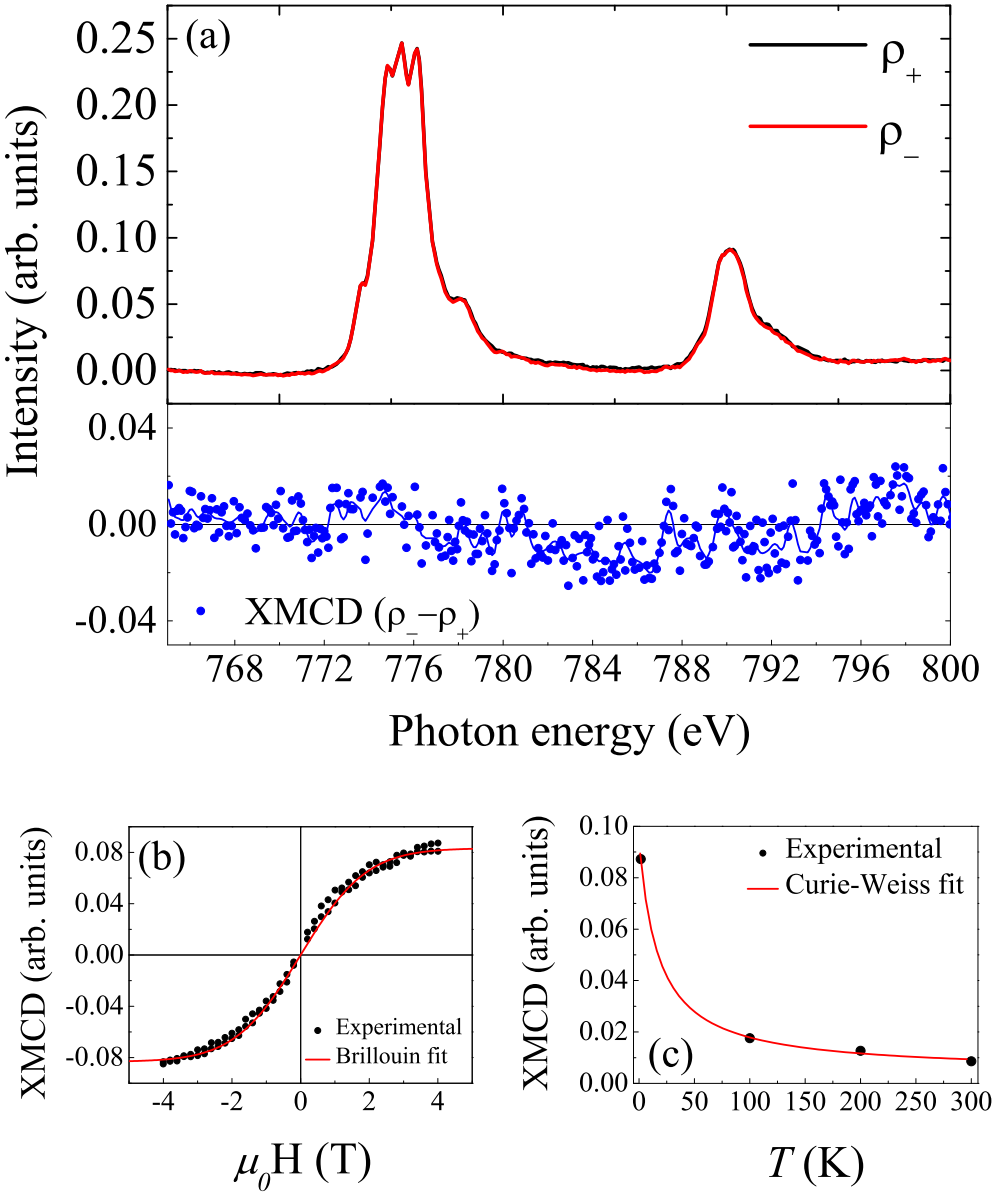

Figure 6.13: (a) XAS and XMCD spectra at the Co $L_{2,3}$ edge in FY mode at remanence (0 T) and 300 K. The XMCD is shown in the lower panel (solid blue circle with solid blue line), (b) Magnetisation curve of a 5.4 at. % Co-doped ITO measured at the Co $L_{2,3}$ edge in FY mode at 2 K (solid black circles), along with the fit to a Brillouin function (solid red line), and (c) temperature dependence of the FY XMCD signal at an applied magnetic field of 4 T (solid black circles), along with the fit to a modified Curie-Weiss law (solid red line).

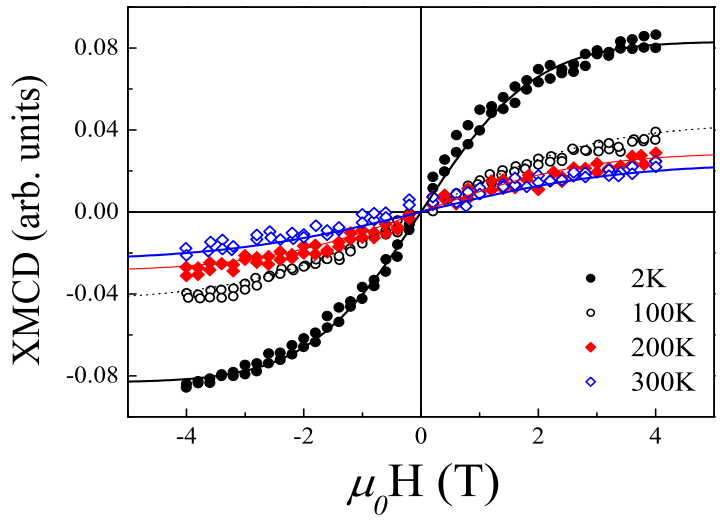

Figure 6.14: XMCD magnetisation curve for a 5.4 at. % Co-doped ITO measured at the Co $L_{2,3}$ edge in FY mode at 2, 100, 200 and 300 K respectively, along with corresponding fits to a Brillouin function (solid and dotted lines).

before being ramped down to 0 T for measuring. No XMCD signal could be detected which is consistent with the XMCD magnetisation curve discussed above, where no remanent XMCD effect is expected. The same was seen in the TEY measurements. Therefore, we can conclude that the specific contribution of Co $3d$ ions to the total bulk ferromagnetism measured in 5.4 at.% Co-doped ITO is purely paramagnetic, i.e. we can assume that the Co ions are not exchange-coupled with each other.

The temperature dependence of the XMCD measured in FY for the Co^{2+} ions in an applied field of 4 T is shown in Fig. 6.13 (c), and follows a modified Curie-Weiss law. From these findings, we conclude that there is strong evidence that the Co ions are not directly responsible for the ferromagnetism observed in the film.

Copie *et al.* also observed a similar "s-like" shaped XMCD magnetisation curve, much like the data presented in Fig. 6.13 (b) [7]. They, however, observe some anisotropy and claim that this may indicate ferromagnetic behaviour regardless of the fact that there is no hysteresis. Together with the metallic-like Co XMCD spectra, they suggest a non-negligible contribution to the magnetic signal arising from Co clusters in a metallic state. Rode *et al.* also measured a closed XMCD magnetisation loop in their $Zn_{0.95}Co_{0.05}O$ film, but analysis at the Co K-edge revealed the coexistence of two magnetic phases: a paramagnetic phase associated with ionic Co and an extrinsic ferromagnetic phase associated with Co metal clusters [5]. We believe that the preservation of the multiplet line structure in the XMCD spectra and paramagnetic dependence of the XMCD signal over the entire temperature range up to 300 K in our sample is good evidence to suggest that within the detection limits of our instruments,

metallic and ferromagnetic or superparamagnetic Co clusters are not present within this system.

Quantitative information regarding μ_L and μ_S components to the total magnetic moment (μ_{XMCD}) were calculated by applying the sum rules [9, 10], where we have included the magnetic dipole term $<\mu_T>$. Their dependence on temperature shown in Figs. 6.15 (a) and (b). We have assumed a pure $3d^7$ configuration for the Co atoms, which sets the number of holes in the $3d$ shell to 3. Values for μ_{XMCD} are taken at an applied magnetic field of 4 T in TEY mode. The magnitude of μ_L and μ_S are relatively high in comparison to some reports with comparable levels of Co doping in ZnO [3, 4]. This could be due to the different crystal field effects on the Co^{2+} ions in the ITO matrix. The value for μ_{XMCD} at 2 K (2.32 μ_B/Co) calculated from the sum rules is in excellent agreement with that estimated using the Brillouin fit in Fig. 6.13 (b). In addition to this, the ratio μ_L/μ_S of the experimental data (0.31) is in excellent agreement with that extracted from the theoretical calculations (0.29). This is further evidence for Co being in a 2+ state and substituting for In in the ITO matrix.

The data recorded in FY mode are qualitatively similar. However, due to self absorption effects which affect the relative intensity of $L_{2,3}$ peak, along with the differences in the matrix elements and selections rules for TEY and FY, application of the XMCD sum rules is meaningless here. They do however, qualitatively confirm the absence of Co clusters throughout the bulk of the film and the decreasing magnetic moment with increasing temperature.

6.5.3 Summary

We have studied the origin of magnetic ordering in the Co-doped ITO system. The line shape of both the XAS and XMCD spectra we obtain show clear multiplet features over a wide range of temperatures suggesting that we have Co existing in an ionic state. The absence of dichroism at remanence at the Co $L_{2,3}$ edge and the modelling of the XMCD magnetisation loops using a Brillouin function points towards paramagnetic behaviour thus excluding their significant contribution to the ferromagnetism. This is supported further by the clear difference in comparison to the SQUID magnetometry measurements. In contrast to the XMCD magnetisation loop at 2 K, the magnetic hysteresis loop [see Fig. 5.13 (a)] shows a curve with saturation field of approximately 0.40 - 0.50 T with a large coercive field. The XMCD magnetisation curve only shows signs of saturating beyond our measurement range of 4 T. This clearly shows that the two techniques are probing different phenomena and at the same time complementing each other in trying to determine the origins of the ferromagnetism in our samples.

These results suggest that the ferromagnetism we observe in Co-doped ITO is not related to the $3d$ electronic states. This is rather contradictory to theoretical models used to explain the magnetic properties in the DMO systems. Like those before, we be-

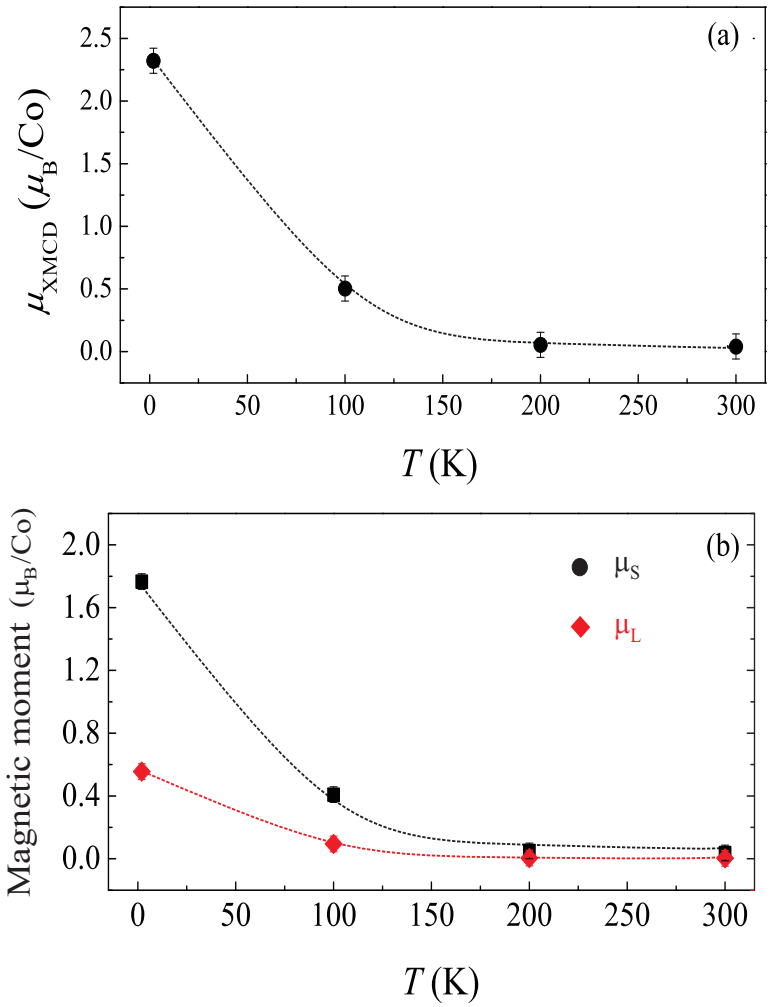

Figure 6.15: (a) Temperature dependence of calculated total magnetic moment (μ_S+μ_L), μ_{XMCD}, using normalised TEY XMCD spectrum and the application of the XMCD sum rules, (b) Temperature dependence of the orbital (μ_L) and spin (μ_S) magnetic moments moments. The dotted lines are a guide to the eye.

lieve that these findings may point towards the likelihood that the bulk ferromagnetism observed from the SQUID magnetometry measurements may be oxygen-mediated, e.g., oxygen vacancies or oxygen-induced defects. Oxygen K-edge XAS data would certainly be capable of providing useful information on whether the features could be signatures of oxygen related lattice defects. Certain atomic defects in structures, such as oxygen vacancies with trapped electrons or holes, may contain low-lying triplet states that are capable of overlapping to form an impurity band [22]. These magnetic defects may interact through long-range interactions mediated by the impurity band to create a ferromagnetic ground state. Therefore, further studies are required to definitively observe dichroism at oxygen sites at remanence (see section 6.7). This would confirm the presence of a spontaneous ferromagnetic contribution.

6.6 Influence of annealing : Studies at the Co $L_{2,3}$ edge

Annealing of the Co-doped ITO films significantly changed the magnetic properties, and was described previously in chapter 5. Differences were also observed in the line shapes of the XAS and XMCD line spectra as shown in Fig. 6.16 where we present the TEY XAS and XMCD spectra for for a pure Co foil (top), and as-deposited (middle) and annealed (in UHV for 2 hours at 700°C) (bottom) 5.4 at.% Co-doped ITO films at 2 K under an applied magnetic field of 4 T. After annealing at 700°C the multiplet features at the L_3 peak are less pronounced. Figure 6.16 (b) shows the corresponding XMCD spectra. The annealed sample looks to have features which are in between that of metallic and ionic Co. This suggests that we may have a mixture of metallic and ionic Co present at the near-surface region of the sample after annealing.

Confirmation of the presence of metallic Co was obtained from the XAS and XMCD spectra measured in FY mode and is shown in Fig. 6.17. Comparison of the XMCD spectra for the as-deposited and annealed samples clearly shows that the multiplet structures have been almost completely smeared out after annealing. The line shape of the spectrum now resembles that of metallic Co and therefore suggests that the bulk of the film contains metallic Co. This is consistent with the observation of a superparamagnetic T_B shown in Fig. 5.18. The arrows in Fig. 6.17 (a) indicate the emergence of two new features in the XAS spectrum which only appear after the annealing treatment. These new features may indicate different hybridisation of Co states to oxygen or In after the annealing process.

To probe the origins of the magnetism in the annealed sample further, XAS and XMCD measurements were performed at remanence. The multiplet fine structure were seen in both TEY and FY XAS spectra, however, no XMCD signal was detected in TEY. A very weak dichroic effect was observed in the FY spectra but was plagued

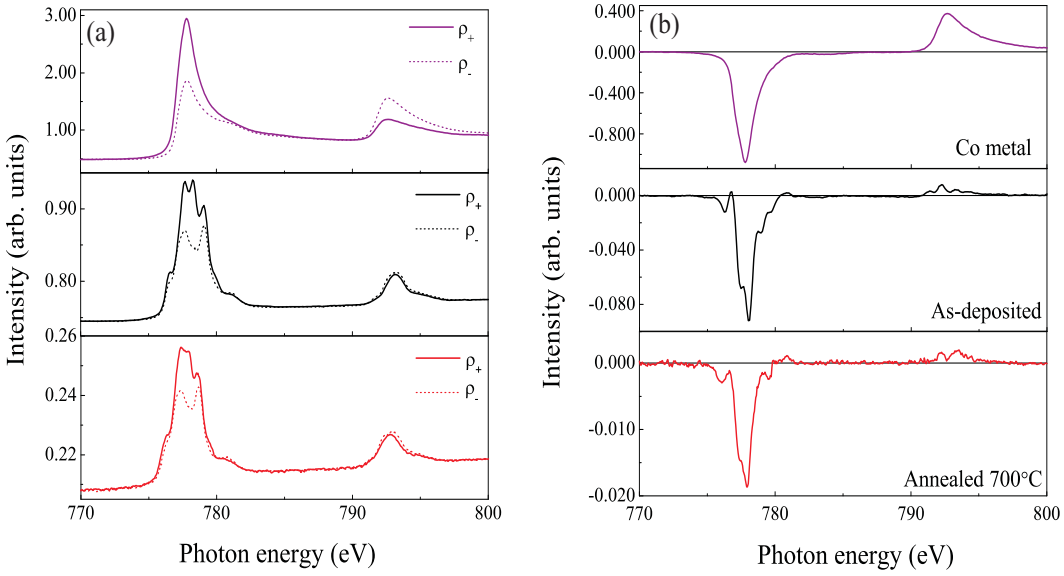

Figure 6.16: TEY XAS (a) and XMCD (b) spectra for Co metal (top), as-deposited (middle) and annealed (bottom) 5.4 at.% Co-doped ITO at 2 K in an applied magnetic field of 4 T.

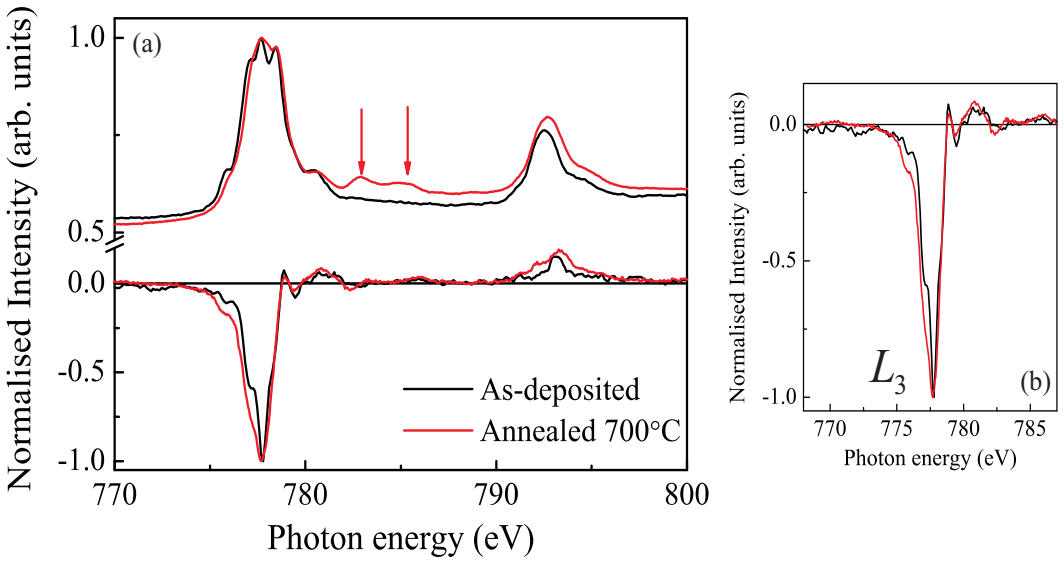

Figure 6.17: (a) Normalised FY average XAS and XMCD spectra for an as-deposited and annealed 5.4 at.% Co-doped ITO sample at 2 K in an applied magnetic field of 4 T; (b) an expanded view of the Co L_3 peak for the each sample.

Table 6.1: Summary of the spin (μ_S) and orbital (μ_L) components to the total magnetic moment (μ_{XMCD}) at 2 K in an applied magnetic field of 4 T calculated using the sum rules.

Sample	Number of holes	μ_S (μ_B/Co)	μ_L (μ_B/Co)	μ_{XMCD} (μ_B/Co)
Co foil	2.49	1.55±0.11	0.14±0.04	1.69±0.12
As-deposited	3.00	1.76±0.09	0.56±0.03	2.32±0.09
Annealed	3.00	1.72±0.12	0.41±0.04	2.13±0.13

with noise so that it was difficult to determine whether the multiplet features were present or not. The observation of a remanent signal is indicative of a ferromagnetic component. In the as-deposited samples, it was shown that there was no dichroism in TEY or FY at remanence confirming the paramagnetic nature of the Co^{2+} ions (recall Figs. 6.13 (b) and 6.14).

Applying the XMCD sum rules to the TEY spectra at 2 K and 4 T for the annealed sample gives a μ_{XMCD} of 2.13±0.10 μ_B/Co which is lower than that for the as-deposited sample (2.32 μ_B/Co). Table 6.1 summarises the results for each sample using the sum rule analysis. For the Co foil the number of holes used for our calculations was 2.49 (as used in ref. [10]), but in the case of the Co-doped samples, the number of holes was set to 3. Our value for the total moment for the Co foil is in excellent agreement with that of the theoretical value for Co metal (1.72 μ_B). Within the error estimations it is evident that the as-deposited and annealed samples have a similar spin moment, but there is a greater reduction in the orbital moment for the annealed sample. The quenching in the orbital moment may be due to a lowering in the degeneracy of the states arising from the change in crystal field around the Co sites due to the clustering of the Co dopants. As we mentioned in section 6.5.2, the estimated total moments from the sum rules are lower than that expected for Co^{2+} in the upper spin state. Rode *et al.* also observed similar reductions in the sum rule calculated magnetic moments [5]. They suggest that the origins of the reduction are difficult to explain but that it may be due to factors such as the lack of magnetic saturation, antiferromagnetic interactions between nearest neighbor Co^{2+} ions, and even the presence of Co metal clusters which have a lower Co magnetic moment (1.72 μ_B).

The rise in magnetisation upon UHV annealing can therefore be largely ascribed to the creation of metallic Co clusters.

6.7 Oxygen *K*-edge

Nefedov *et al.* showed that from XMCD magnetisation curves in Co-doped TiO_2 that the O K-edge showed clear hysteresis with switching fields identical to those recorded at the Co $L_{2,3}$ edge [23]. This result implied that the oxygen atoms in close proximity to the Co atoms become spin polarised, even in samples where Co clustering was not detected. This result suggested that oxygen polarisation can play an important role in the existence of long range magnetic order in TM-doped oxide systems. Thakur *et al.* have also observed an appreciable XMCD signal in the O $2p$ region in undoped MoO_2 thin films which also exhibit room temperature ferromagnetic properties [24]. This was attributed to a strong hybridisation between the O $2p$ - Mo $4d$ levels and thus a charge transfer from the O $2p$ orbitals to the Mo $4d$ orbitals.

The measurement sample (20 - 30 averages) for our O K-edge studies was very large in order to account for the fact that dichroic effects were expected to be very low compared to that at the Co $L_{2,3}$ edge. Earlier we showed the paramagnetic behaviour at the Co L-edge, and therefore the absence of Co $3d$ polarisation at remanence [Fig. 6.13 (a)]. Figure 6.18 shows the XAS and XMCD spectra in TEY mode for a 5.4 at.% Co-doped ITO film at 2 K after applied magnetic fields of ± 4 T at the O K-edge. A very pronounced peak in the XAS spectra at approximately 529.60 eV is observed, extremely similar to that seen by Abbamonte *et al.* in $La_{2-x}Ba_xCuO_4$ [25]. A sizeable XMCD signal, with line shape features similar to others who report dichroism at the O K-edge is produced.

XMCD requires the breaking of time-reversal symmetry and the presence of a spin-orbit interaction. The XMCD signal is due to electric-dipole and, in some cases, electric-quadrupole transitions between a deep core state and an empty conduction state. However, in some cases it is possible that one can observe another effect, largely due to the interference between electric-dipole and electric-quadrupole transitions. This gives a dichroic signal with a very similar line shape to that of an XMCD dichroism, however, its intensity is much smaller in comparison. One way to determine whether these effects are magnetic in origin is to see whether the dichroic signal "flips" when the applied magnetic field has been reversed (but the polarisation of the x-rays remain constant). Also, by using a normal incidence geometry, we can exclude non-XMCD effects such as linear dichroic contribution, *etc.*, in order to determine whether the features we see are truly magnetic dichroic effects or not. As can be seen from Fig. 6.18, the XMCD signal flips on reversal of the applied magnetic field.

We believe that the magnetic polarisation of the O $2p$ levels is a result of the intense hybridisation between the Co and O orbitals. As in the case of Co-doped TiO_2, the oxygen atoms that are in close proximity of the Co atoms become polarised upon application of a magnetic field [23]. The XMCD magnetisation loops in TEY mode at 2 K for positive (ρ_+) and negative (ρ_-) polarisation are shown in Fig. 6.19. The slope of

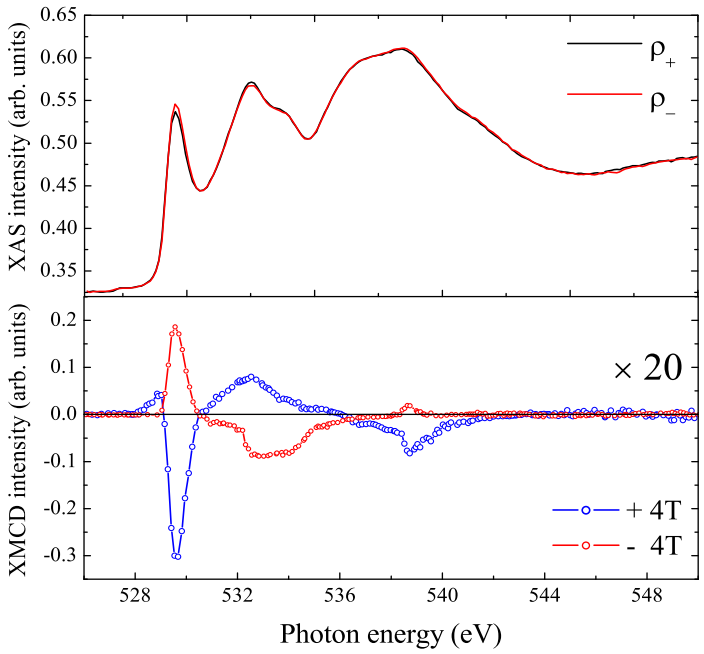

Figure 6.18: TEY XAS and XMCD spectra at the O K-edge at 2 K under applied magnetic fields of 4 and -4 T respectively.

the magnetisation curve flips upon reversal of the polarisation as expected. It is clear that the dependence of the XMCD signal at the O K-edge is paramagnetic, as is the case for the Co. This is further evidence that the Co and O orbitals are overlapping.

6.8 Summary and Conclusions

In summary, we have used XAS and XMCD characterisation at the In $M_{2,3}$, Sn $M_{2,3}$, Co $L_{2,3}$ and O K-edges in Co-doped ITO to study the origin of the magnetism over a range of temperatures and applied magnetic fields. Element specific hysteresis loops recorded at the Co $L_{2,3}$ edge indicate a clear paramagnetic contribution to the overall magnetic moment of the Co-doped ITO film and confirm the presence of non-coupled Co^{2+} ions substituting for the In ions. Multiplet features in the Co $L_{2,3}$ edge XAS measured in both TEY and FY mode from 2 to 300 K indicate that the Co atoms are in a divalent state, therefore non-metallic in nature throughout the entire film, and thus substituting for the In ions. Therefore, within the detection limits of the techniques, and from all the information we have through our exhaustive characterisation efforts, we believe that there is no contribution to the observed ferromagnetism solely from the Co dopants. No XMCD could be detected at the In or Sn M_2 edges, thus excluding the presence of a large magnetic polarisation of the In and Sn sublattices. Therefore

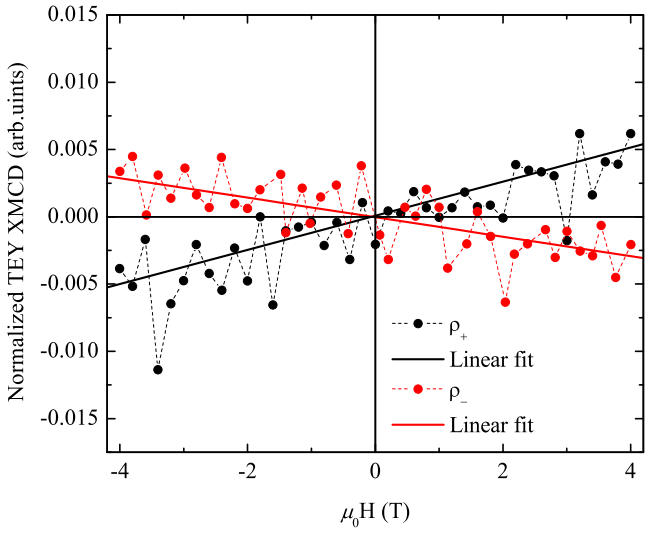

Figure 6.19: TEY XMCD magnetisation curve at the O K-edge in positive (ρ_+) and negative (ρ_-) polarization at 2 K.

the ferromagnetic moment observed in the Co-doped ITO films cannot be ascribed to the Co and In sublattices.

Upon UHV annealing, XAS and XMCD in both TEY and FY modes display features which suggest a mixed phase of both Co^{2+} ions and metallic Co. This confirms the results from annealing in chapter 5 where it was believed that Co metal segregation had taken place leading to an enhanced ferromagnetic response.

Magnetic dichroism was also observed at the O K-edge at 2 K, indicative of spin polarisation of oxygen atoms in the ITO host matrix. Not enough detailed experiments were performed to investigate whether there was any remanent magnetisation on the oxygen atoms, due to the experimental difficulty to confirm the presence of a genuine dichroic signal in the first place. However, for now the magnetic dichroism at the O K-edge can be attributed to the strong hybridisation between Co $3d$ and oxygen $2p$ orbitals.

So, what is the source of magnetism in these films if no remanent magnetisation is measured at the In, Sn, Co or O absorption edges? Through the process of elimination, what remains is atomic defects (either TM- or O-induced) such as interstitial defects, oxygen vacancies, *etc.*

On this evidence, the Co dopants alone are not responsible for the ferromagnetic response in these films. The only way this issue can be resolved would be to perform XMCD measurements at the Co K-edge, probing deeper energy levels, as was carried out by Rode *et al.* [5].

In the next chapter however, we use optical MCD which can provide useful information on which energy states in the solid may be involved in the magnetism.

Bibliography

[1] T. Tietze, M. Gacic, G. Schutz, G. Jakob, S. Bruck, E. Goering, New J. Phys. 10, 055009, (2008)

[2] M. Kobayashi, Y. Ishida, J. l. Hwang, T. Mizokawa, A. Fujimori, K. Mamiya, J. Okamoto, Y. Takeda, T. Okane, Y. Saitoh, Y. Muramatsu, A. Tanaka, H. Saeki, H. Tabata, T. Kawai, Phys. Rev. B 72, 201201(R), (2005)

[3] M. Gacic, G. Jakob, C. Herbort, H. Adrian, T. Tietze, S. Brck, E. Goering, Phys. Rev. B 75, 205206, (2007).

[4] A. Barla, G. Schmerber, E. Beaurepaire, A. Dinia, H. Bieber, S. Colis, F. Scheurer, J.-P. Kappler, P. Imperia, F. Nolting, F. Wilhelm, A. Rogalev, D. Mller, J. J. Grob, Phys. Rev. B 76, 125201, (2007)

[5] K. Rode, R. Mattana, A. Anane, V. Cros, E. Jacquet, J.-P. Contour, F. Petroff, A. Fert, M.-A. Arrio, Ph. Sainctavit, P. Bencok, F. Wilhelm, N. B. Brookes, A. Rogalev, Appl. Phys. Lett. 92, 012509, (2008).

[6] See: http://ssrl.slac.stanford.edu/stohr/xmcd.htm

[7] O. Copie, K. Rode, R. Mattana, M. Bibes, V. Cros, G. Herranz, A. Anane, R. Ranchal, E. Jacquet, K. Bouzehouane, M.-A. Arrio, P. Bencok, N. B. Brookes, F. Petroff, A. Barthlmy, J. Phys.: Condens. Matter 21, 406001, (2009).

[8] G. Schutz, W. Wagner, W. Wilhelm, P. Kienle, R. Zeller, R. Frahm, G. Materlik, Phys. Rev. Lett. 58, 737, (1987).

[9] B. T. Thole, P. Carra, F. Sette, G. van der Laan, Phys. Rev. Lett. 68, 1943, (1992)

[10] C. T. Chen, Y. U. Idzerda, H.-J. Lin, N. V. Smith, G. Meigs, E. Chaban, G. H. Ho, E. Pellegrin, F. Sette, Phys. Rev. Lett. 75, 152, (1995).

[11] J.Stohr and Y.Wu, "New Directions in Research with Third-Generation Soft X-Ray Synchrotron Radiation Sources", NATO ASI Series, Series E: Applied Sciences, Vol. 254, Eds. A.S.Schlachter and F.J.Wuilleumier, pg. 221-250, (1994).

[12] J. Stohr, J. Electron Spectrosc. Relat. Phenom. 75, 253, (1995)

[13] J. Stohr, J. Magn. Magn. Mater. 200, 470-497, (1999)

[14] Y. U. Idzerda, C. T. Chen, H. J. Lin, G. Meigs, G. H. Ho, C. C. Kao, Nucl. Instr. and Meth. in Phys. Res. A 347, 134-141, (1994)

[15] M. Venkatesan, C. B. Fitzgerald, and J. M. D. Coey, Nature, 430, 630, (2004)

[16] N. R. S. Farley, K. W. Edmonds, A. A. Freeman, G. van der Laan, C. R. Staddon, D. H. Gregory, and B. L. Gallagher, New J. Phys. 10, 055012, (2008).

[17] G. van der Laan, E. Arenholz, R. V. Chopdekar, Y. Suzuki, Phys. Rev. B 77, 064407, (2008).

[18] G. van der Laan and B. T. Thole, Phys. Rev. B 43, 13401, (1991).

[19] G. van der Laan and I. W. Kirkman, J. Phys.: Condens. Matter 4, 4189, (1992)

[20] S. Blundell, Magnetism in Condensed Matter, Oxford University Press, Oxford, p. 49, (2001).

[21] P. Gambardella, S. S. Dhesi, S. Gardonio, C. Grazioli, P. Ohresser, C. Carbone, Phys. Rev. Lett. 88, 047202, (2002).

[22] S. Krishnamurthy, C. McGuinness, L. S. Dorneles, M. Venkatesan, J. M. D. Coey, J. G. Lunney, C. H. Patterson, K. E. Smith, T. Learmonth, P.-A. Glans, T. Schmitt, and J.-H. Guo, J. Appl. Phys. 99, 08M111, (2006).

[23] A. Nefedov, N. Akdogan, H. Zabel, R. I. Khaibullin, L. Tagirov, Appl. Phys. Lett. 89, 182509, (2006)

[24] P. Thakur, J. C. Cezar, N. B. Brookes, R. J. Choudary, R. Prakash, D. M. Phase, K. H. Chae, R. Kumar, Appl. Phys. Lett. 94, 062501, (2009)

[25] P. Abbamonte, A. Rusydi S. Smadici, G. D. Gu, G. A. Sawatky, D. L. Feng, Nat. Phys. 1, (2005)

Chapter 7

Optical magnetic circular dichroism characterisation of Co-doped Indium Oxide thin films

The results in this chapter were performed in collaboration with the Magnetic Oxides group at the University of Sheffield. The majority of the work described is concerned with Co-doped In_2O_3 films, but also gives preliminary results from ITO(10) films also doped with Co. We present further evidence that the ferromagnetism in these materials is not solely from the Co dopants, rather it may be related to localised donor states associated with oxygen vacancies.

7.1 Introduction

In chapter 6 we have made it clear that magnetic circular dichroism is one of the most powerful tools available to unravel the mysteries surrounding dilute magnetic oxides.

Magneto-optics, MO, investigates the way light is modified when it passes through a magnetic crystal. The nature of the material's magnetic states can be investigated by measuring the properties of circularly polarised light transmitted through the material. MO spectroscopy is a direct method for evaluating the *s,p-d* exchange interactions within DMS materials [1]. The *s,p-d* exchange interactions induce a spin-dependent modification of the host semiconductor band structure in the presence of an applied magnetic field, that is, the Zeeman splitting [recall Fig. 5. 2 (b)]. A strong MO signal implies a strong *s,p-d* exchange interaction. Having reviewed the previous work on other DMOs using this technique, we then present our own MO data.

Here we present optical MCD (O-MCD) measurements on Co-doped (doping levels 1.0 - 5.0 at.%) In_2O_3 and ITO(10) samples grown using DC magnetron co-sputtering under the same conditions described in chapter 5. However, the films were grown upon *c*-plane sapphire due to the undesirable birefringent properties of *r*-plane sapphire. In addition, optical absorption spectra of the Co-doped In_2O_3 films are also given.

7.2 Principles of Magneto-optics

If we consider light passing through a material of thickness t, the material will have a refractive index, $\tilde{n}$, that is made up of real and imaginary parts.

$$\tilde{n} = n_0 + ik \tag{7.1}$$

Linearly polarised light is made up of equal parts of left (LCP) and right circularly polarised (RCP) light, as shown in Fig. 7.1 (a). It can be decomposed into these two states and passed through a magnetic medium. This would mean Eqn. 7.1 now being written as;

$$\tilde{n}_{\pm} = n_{0\pm} + ik_{\pm} \tag{7.2}$$

where the LCP light is equivalent to the negative and the RCP light the positive terms. RCP and LCP light cause charges in a material to rotate in opposite senses. Each polarisation therefore produces a contribution to the orbital angular momentum having an opposite sign. If the system is then exposed to a magnetic field this gives rise to spin-polarisation along the magnetic field direction. The spin-orbit interaction then leads to an energy contribution for the two circular polarisations having the same magnitude but opposite sign and therefore, RCP and LCP light will propagate through the medium with different speeds. An MO effect is seen when, upon recombination, the refractive index of LCP and RCP are not equal, i.e. where $\tilde{n}_+ \neq \tilde{n}_-$, and there is a phase-lag between the two light beams. This is shown in Fig. 7.1 (b) where the

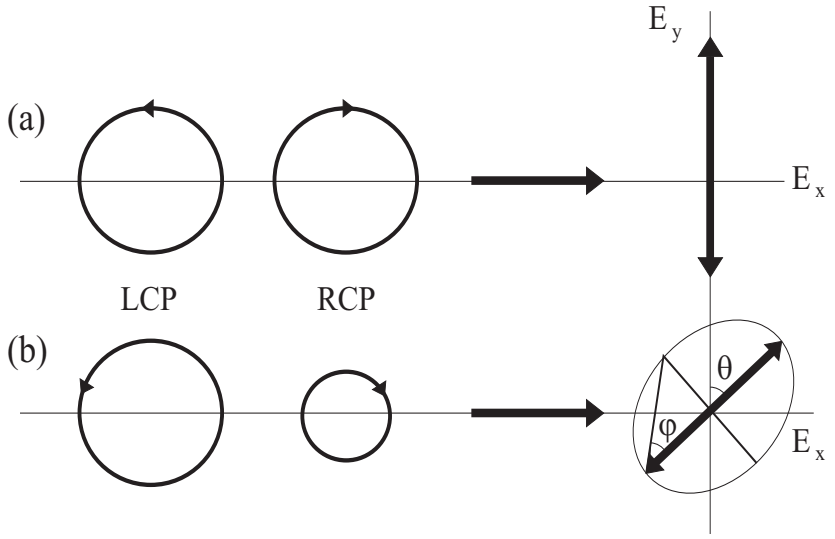

Figure 7.1: (a) Linear light made up of equal parts of LCP and RCP. (b) If these are unequal after being incident upon a sample in a magnetic field, the transmitted or reflected light will be elliptically polarised and rotated. Adapted from A. J. Behan thesis [2].

light is elliptically polarised by a rotation of angle θ and change in intensity. This occurs as a result of the relative changes in phase and amplitude (due to a difference in attenuation rates for LCP and RCP light) of LCP and RCP light. Therefore, the presence of a spin-orbit coupling is of paramount importance for the orbital moment to reflect information about the magnetism of a system.

The ellipticity and rotation of circularly polarised light results in MO effects such as the Faraday effect and MCD [3]. The Faraday effect is a measurement of the difference in refractive indices for LCP and RCP light: it is the rotation of the plane of polarisation for polarised light as it propagates through a medium in the direction of an applied magnetic field. The effect is dependent on a weighted average over all transitions in the crystal, so that it is finite in spectral regions when the crystal is not absorbing.

The MCD is the difference in intensity for left and right circularly polarised light at a frequency ω. Since it is only dependent upon transitions at ω, it is only non-zero if the crystal is absorbing. This however, makes it very useful when determining the nature of a magnetic state. For this reason, it is the MCD that we are most interested in. The Faraday effect can therefore be used as a check that any MCD observed is not just because a material is absorbing strongly at its band edge. Both of these MO quantities are obtained when measuring in transmission mode. Measurements made in reflection give another MO effect called the Kerr effect, but is outside the scope of this thesis.

The quantum selection rules that dictate the electronic dipole transitions ($\Delta l = \pm 1$) leads to two possible origins of an optical MCD effect. The first is that we have a

spin-split valence or conduction band so that the absorption coefficients for LCP and RCP light are different. The second is a difference in the strength of the transition intensity for LCP and RCP light which will occur is there is a difference in orbital state population.

The XMCD and O-MCD techniques are different in terms of their physics but are complementary to each other in trying to explain the origins of magnetism in these materials. Whilst XMCD is element specific and can therefore give information on the magnetic nature of individual elements, it cannot tell us anything about which energy states are involved in the magnetism. O-MCD is primarily concerned with the energy states of the solid and the band gap and can therefore provide clues as which energy states are important in producing a magnetic signal. Correlating absorption spectra with that of the MCD as a function of energy is an excellent way of doing this, as we know that MCD will only occur if an absorption takes place. However, as we will explain later, we are still left not knowing where these states are located within the film.

7.3 Previous results

The previous work presented here focuses on those investigations carried out on ZnO-based DMOs. To my knowledge, no such studies regarding magneto-optical effects in TM-doped In_2O_3 are available. The major work carried out on the TM-doped ZnO system has been performed by Ando *et al.* [5,6] and the Magnetic Oxides group at the University of Sheffield [7,8].

The first detailed study of magneto-optical effects in TM-doped ZnO was performed by Ando *et al.* where a large array of TM dopants (Sc, Ti, V, Cr, Mn, Co, Ni and Cu) were used to dope ZnO, grown using PLD [6]. Undoped ZnO was found to give a weak and positive diamagnetic signal near the ZnO band gap energy of 3.4 eV. Samples doped with Sc, Ti, V and Cr showed no enhancement in the MCD signal compared to that of pure ZnO. However, those samples doped with Mn, Co, Ni and Cu all showed sizeable MCD effects at both 5 and 270 K. The $Zn_{1-x}Co_{0.016}O$ sample gave the largest MCD signal [see Fig. 7.2 (a)]. In addition, the Co-doped sample shows clear MCD structures near to a photon energy of 2.0 eV which are clear signatures of the intraionic d-d^* of Co^{2+} symmetry sites in tetrahedral coordination.

The temperature dependence of the Co-doped sample near 3.4 eV [Fig. 7.2 (b)] shows that the large negative signal at 5 K decreases with increasing temperature and that the MCD becomes positive at higher temperatures, however, much smaller. Evidence that this temperature dependence is induced by the transition metal comes from the fact that the undoped ZnO MCD signal is almost completely independent of temperature. Ando interprets the MCD signal at the band edge as being a consequence of conduction and valence band splitting. A sizable sp-d exchange interaction should lead to a pronounced MCD signal. The strength of the sp-d exchange interaction is

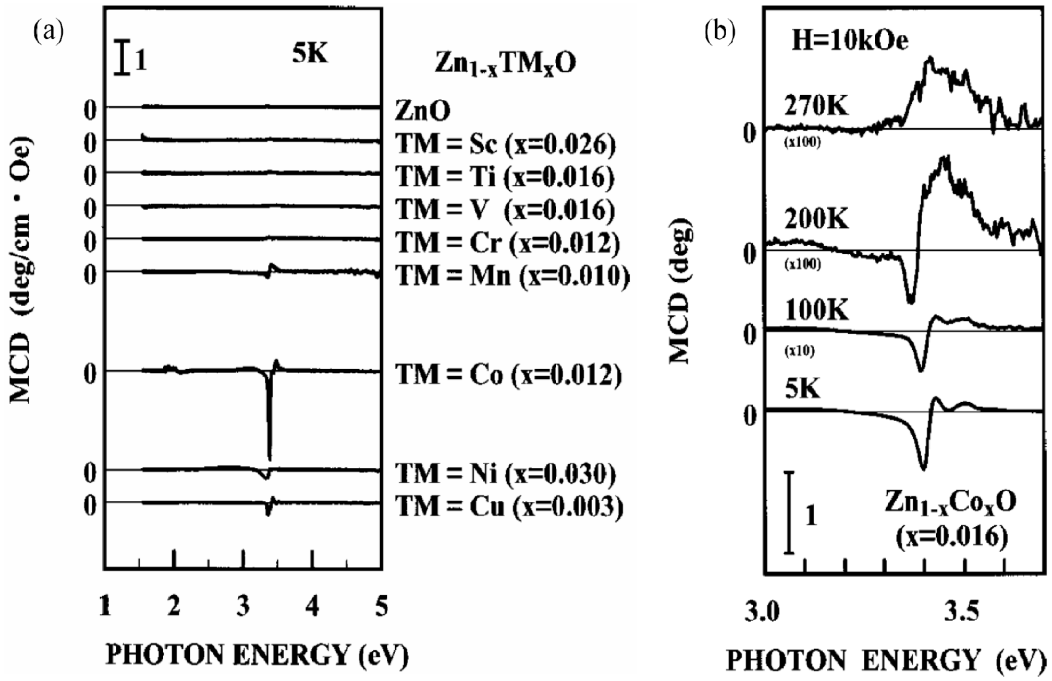

Figure 7.2: (a) MCD spectra of $Zn_{1-x}TM_xO$ (TM=Sc, Ti, V, Cr, Mn, Co, Ni, and Cu) films at 5 K, (b) MCD spectral shape of $Zn_{1-x}Co_{0.016}O$ under a magnetic field of 10 kOe at various temperatures. After reference [6].

explained as being dependent upon the number of $3d$ electrons present.

A similar study was carried out by Neal *et al.* where the ZnO system was doped with a variety of TM dopants (Co, Mn, Ti, V) [7]. The MCD spectra along with absorption spectra, and Faraday spectrum for the Ti-doped sample, are shown in Fig. 7.3 (a). Each show an edge at the band gap in the absorption spectra along with a corresponding MCD signal. The ferromagnetic nature of the band edge MCD is confirmed by the observation of open MCD hysteresis loops for the Co-, V-, and Ti-doped samples at room temperature (see Fig. 7.3 (d) for Co-doped sample). As was observed by Ando *et al.* the Co-doped ZnO sample shows a negative excitonic feature at low temperatures [see Fig. 7.3 (b)] which weakens rapidly as the temperature is increased, due to its paramagnetic nature and the fact that the number of carriers increases leading to exciton screening.

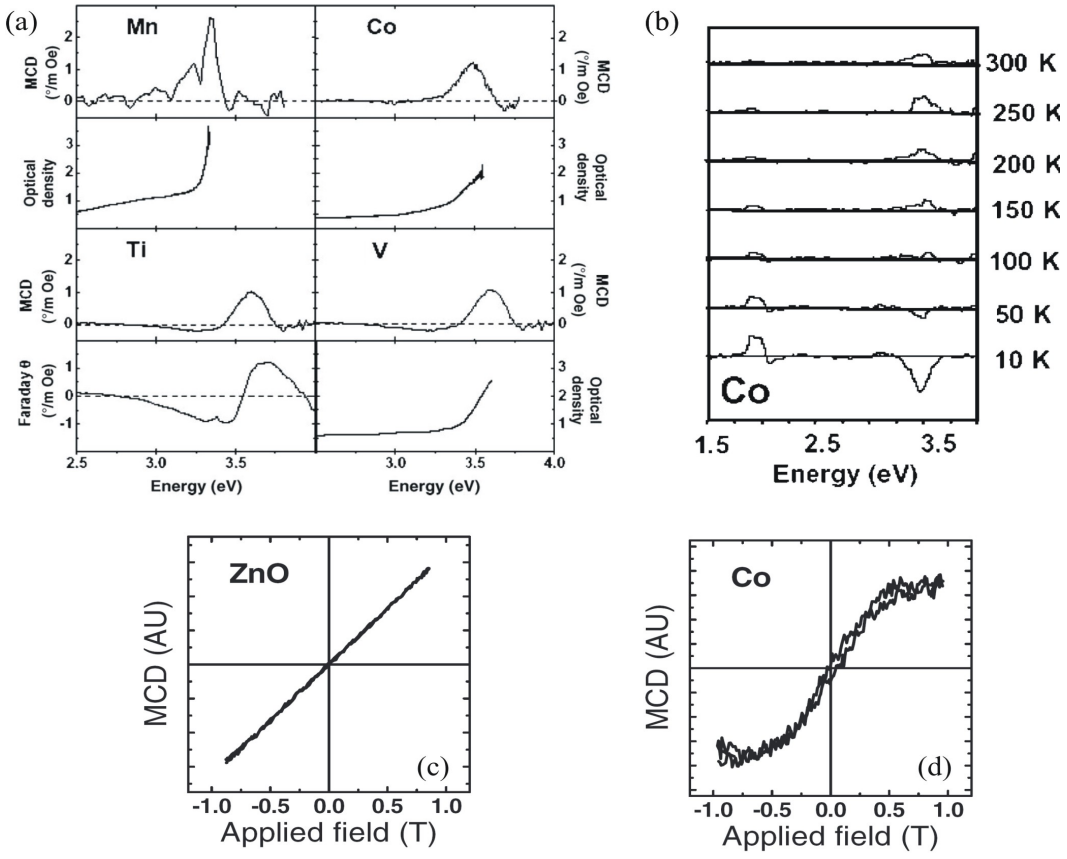

Figure 7.3: (a) Room temperature MCD measurements for ZnO doped samples with a variety of TM dopants, together with the absorption spectra and Faraday rotation in the case of Ti-doped ZnO, (b) Temperature dependence of the MCD of $Zn_{0.98}Co_{0.02}O$, and, (c) and (d) MCD hysteresis loops obtained at room temperature and an energy of 3.4 eV for a pure ZnO film (c) and a Co-doped ZnO film (d). After reference [7].

7.4 Experimental results

7.4.1 Co-doped In_2O_3

Film thickness ranged from 210 - 230 nm to ensure a sizable MCD signal close to the band edge. If the sample is too thin the light will pass through with little interaction, whilst if it is too thick, not enough light will be transmitted above the band edge for a signal to be measured.

Magnetic and Magnetotransport properties

Each of the samples were found to be magnetic at both low and above room temperature. The films were all n-type as expected since they had been grown in an oxygen deficient environment. The resistivities of all the films rose rapidly as the temperature was lowered, indicating semiconducting behaviour, and obeyed the variable range hopping law at temperatures below 50 K. The transport measurements taken at room temperature are summarised in Fig. 7.4. The carrier concentration is reduced for films with 1.0<Co (at.%)<4.0 in comparison with the pure In_2O_3 (4.53×10^{19} cm^{-3}), as we would expect if the Co dopants are in the Co^{2+} state and acting as acceptors. Within this doping range the carrier concentration is relatively constant with minimal variation in the saturation magnetisation. At 5 at.% doping, the carrier concentration has increased and has almost returned to the value of pure In_2O_3; this is accompanied by a sudden rise in the saturation magnetisation. The mobility dropped monotonically with doping between 1.0 at.% and 5.0 at.%; from 3.34 cm^2 V^{-1} s^{-1} to 0.95 cm^2 V^{-1} s^{-1}.

The total magnetisation that can arise from spin-polarised free electrons is $n_c\mu_B$. This is of the order of 0.10 emu/cm^3 for carrier densities of approximately 10^{19} cm^{-3}, which is more than a factor of 10 smaller than the observed values given in Fig. 7.4. We thus deduce that the ferromagnetism cannot be attributed to the free electrons. Given that we have argued above that the ferromagnetism is not due to the Co^{2+} ions either (chapter 6), we therefore need to look at the possible contribution from localised donor states. These are best analysed by optical methods.

Absorption properties

Figure 7.5 (a) presents the optical absorption coefficient for Co-doped In_2O_3 with doping levels of 1.0, 3.0 and 5.0 at.%. The band edge of the In_2O_3 is apparent, together with a shoulder from approximately 2.8 eV down to 2.5 eV. This shoulder is not observed in undoped films, and we therefore attribute it to donor states that have been partially ionised through the compensating effect of the Co^{2+} acceptors substituting for In^{3+}. The donor levels are observable in absorption after doping with Co since

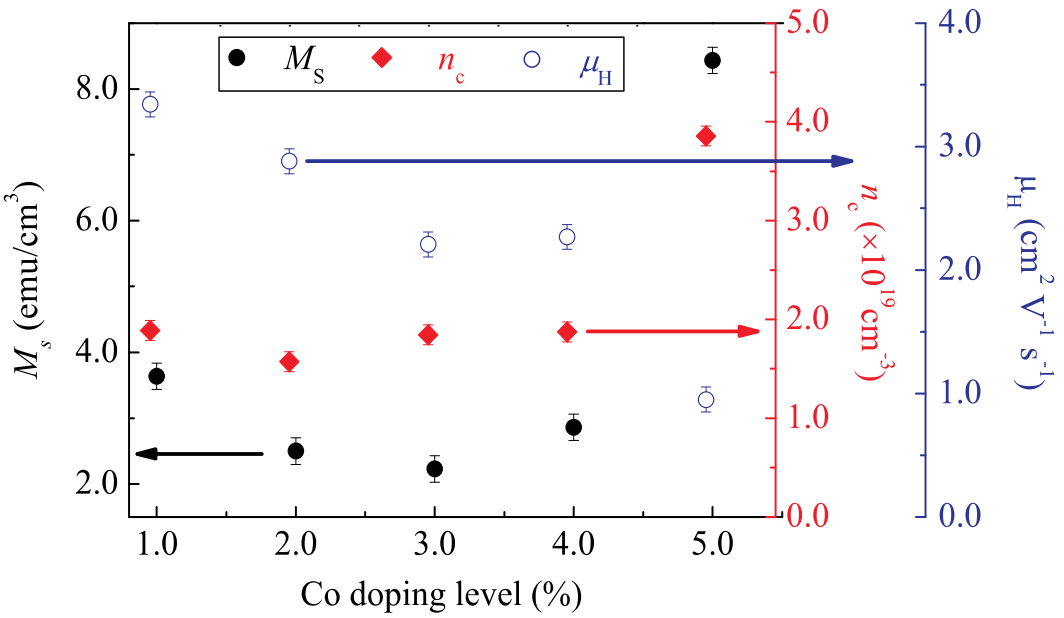

Figure 7.4: Summary of the magnetisation and transport behaviour of Co-doped In_2O_3 thin films at 290 K.

transitions from the valence band are now possible to these partially empty states. The most likely origin of these donor levels is oxygen vacancy states which have been calculated to lie $\sim$ 0.9 eV below the band edge [9].

Figure 7.5 (b) shows the "Tauc" plots for 0.0 - 5.0 at.% Co-doped In_2O_3 samples. The Tauc plot is a method used to determine the optical band gap energy, E_g, having first determined the absorption coefficient, α. Using the relationship $\alpha \sim \sqrt{h\nu - E_g}$ and plotting $(\alpha h\nu)^2$ against the photon energy, one can estimate E_g. It is clear that there is a gradual decrease in E_g as the concentration of Co doping increases. The inset of Fig. 7.5 (b) summarises the dependence of E_g, extracted from the absorption measurements, as a consequence of the Co doping. The pure In_2O_3 has a considerably larger E_g than those which have been doped with Co. After the initial doping stage where just 1.0 at.% Co has been added, E_g falls rapidly. Subsequent doping however results in a monotonic decrease in E_g. This is further evidence for substitution of Co^{2+} ions at In^{3+} sites instead of forming metallic clusters. There is a notable increase in the slope of the absorption edge between the pure, undoped In_2O_3 and Co-doped In_2O_3 samples and suggests that a now much heavier band is contributing to the absorption as a result of the Co doping.

O-MCD characterisation

Strong evidence that these donor states are related to the ferromagnetism was obtained by O-MCD spectroscopy. The magneto-optical measurements were carried out using photon energies between 1.5 and 4.2 eV. Low temperature measurements were conducted within a cryostat with a temperature cooling range of 10 - 300 K. The mag-

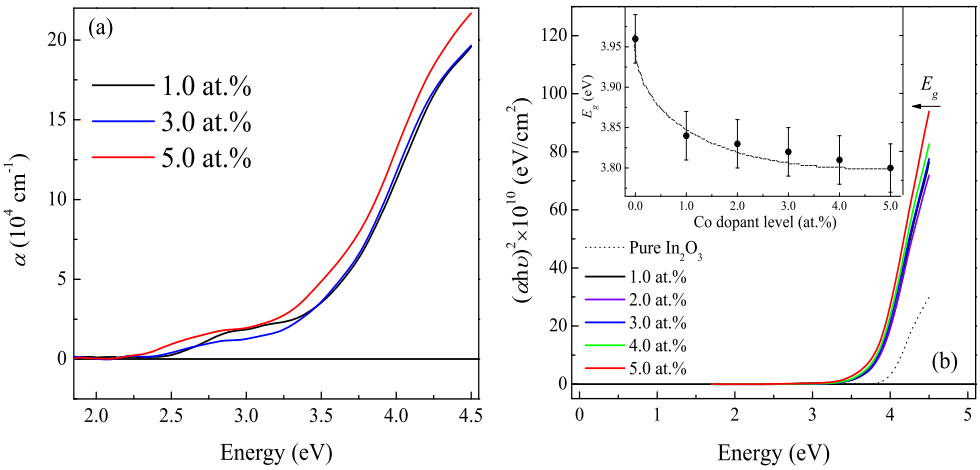

Figure 7.5: (a) Effect of Co doping on the optical absorption spectra for Co-doped In_2O_3 thin films at room temperature. (b) Tauc plots for Co-doped In_2O_3 films. The arrow indicates the direction of the shift in the band gap energy, E_g. Inset: dependence of E_g as a function of the Co doping level estimated using the Tauc plots.

netic field applied was 1.8 T at room temperature but was reduced to 0.5 T when using the cryostat.

Figure 7.6 shows the effect of Co-doping on the room temperature O-MCD spectra for a set of Co-doped In_2O_3 films. The data presented here are the spectra of the films obtained after the MCD of a blank substrate has been subtracted. A clear MCD signal emerges, peaking at the band edge for each of the samples, which gains intensity with increasing magnetisation (refer to Fig. 7.4). The observation of an MCD signal at the onset of absorption is good evidence for a spin-split conduction band. The intensity of the MCD is determined both by the strength of the absorption at a particular energy and the extent to which that state is magnetically polarised. The observation that the MCD is rising for energies above 2.5 eV demonstrates that these transitions which gave rise to the shoulder on the absorption edge involve spin-polarised states. No equivalent MCD signal was observed for pure In_2O_3 films.

The origin of the MCD signal was explored in more detail by investigating its temperature dependence. Figure 7.7 portrays the MCD signal for the 5.0 at.% Co-doped sample from 10 K to 300 K. The ratio of the magnitude of the MCD at 10 K and 300 K agrees very well with the reduction of the magnetisation between 5 K and 300 K. The fact that the MCD and the magnetisation have the same temperature dependence is strong evidence to support the contention that the observed magnetisation originates from the same donor states as those involved in the optical transitions.

Co^{2+} ions in octahedral coordination give rise to a broad MCD signal [10] near 2.0 eV which we believe is too weak to be detected. The observed signal in this energy range does not have the correct dependence on cobalt concentration or temperature to

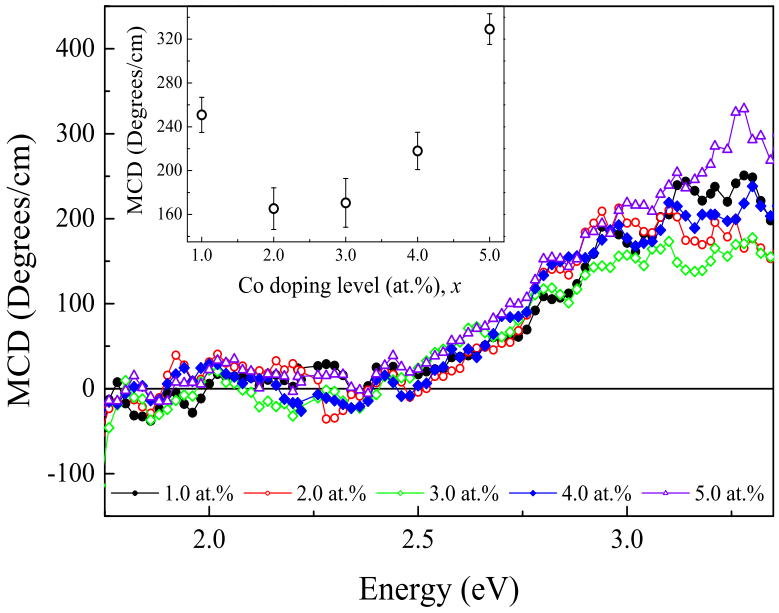

Figure 7.6: O-MCD spectra for the entire Co doping range (1.0-5.0 at.%) at room temperature for Co-doped In_2O_3 thin films. Inset: MCD signal at 3.28 eV plotted as a function of the Co doping level.

separate it from the noise. However the shape of the MCD spectrum at 300 K does rule out a sizeable contribution from metallic cobalt [11, 12] or CoO [13] and there is no temperature dependence to indicate Co_3O_4 and Co_2O_3 where the transition temperatures are below 40 K [14].

We believe that the transition metal ions are acting as acceptors and ionising a sufficient fraction of the donors to produce a partially occupied narrow donor band, much like in the sketches shown in chapter 2 in reference to Coey's work. Therefore, the inevitable hybridisation of the broad donor band with the $3d$ band is the origin of the magnetism in our Co-doped In_2O_3 films. However, we are unable to determine the location of these donor states - they may be distributed evenly through the material or concentrated at the grain boundaries as has been suggested by other studies [15, 16].

7.4.2 Co-doped ITO(10)

Ferromagnetic 1.0 - 5.0 at.% Co-doped ITO(10) thin films were investigated in much the same way as the Co-doped In_2O_3 samples described above in 7.4.1. The films were metallic over the entire temperature range with carrier concentrations typically in the range of 10^{20} cm^{-3}.

Figure 7.8 (a) shows the room temperature O-MCD spectra as a function of Co

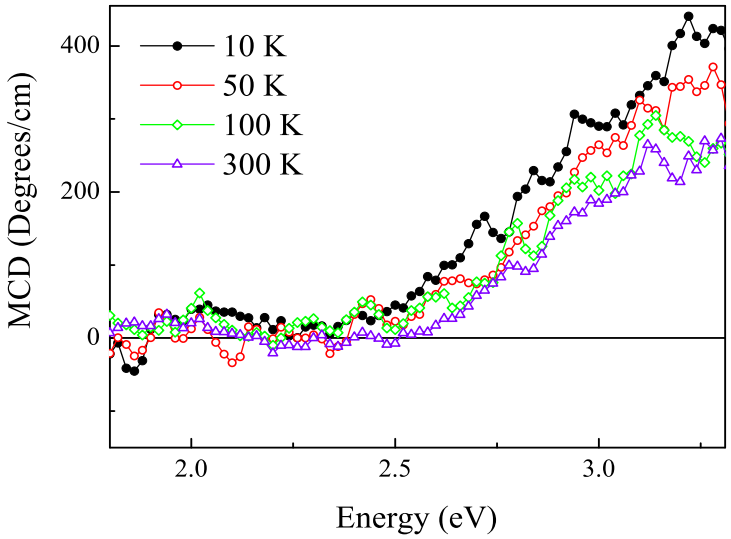

Figure 7.7: Temperature dependence of the O-MCD for a 5.0 at.% Co doped In_2O_3 sample.

doping from 1.0 - 5.0 at.% in Co-doped ITO(10) films. All spectra have been corrected for by subtracting the measured signal from a *c*-plane sapphire substrate. A clear MCD signal emerges, peaking at the band edge for each of the samples, which monotonically gains intensity with increasing levels of Co doping [Fig. 7.8 (b)]. Notice that the onset of MCD and therefore absorption occurs at a slightly higher energy, 2.75 eV instead of 2.50 eV is the case of the Co-doped In_2O_3 films. This suggests that the band gap energy has increased or that the energy level of the donor states has shifted upon doping with Sn. One of the major reasons for shifting of the band gap can be related to changes in the lattice constant. Compression of the lattice will widen the bands and therefore will widen the gaps. The changing lattice will overide the influence of the Sn donor band that will form just below the conduction band, which would normally reduce the band gap (recall section 4.2). The MCD signal appeared to be correlated to the magnetisation as is clear from a comparison between Figs 7.8 (b) and (c).

Figure 7.8 (d) portrays the temperature dependence of the MCD signal as a function of temperature for a 5.0 at.% Co-doped ITO(10) film. The sample behaved in a very similar way to the 5.0 at.% Co-doped In_2O_3 sample described earlier, i.e. decreasing temperature led to a continual rise in MCD intensity.

Magnetisation in samples containing additional Sn doping is generally larger than those without Sn doping (section 5.6.2) and we now know that the MCD scales with the strength of the total film magnetisation. The larger values for magnetisation and MCD in the Sn doped samples confirms this.

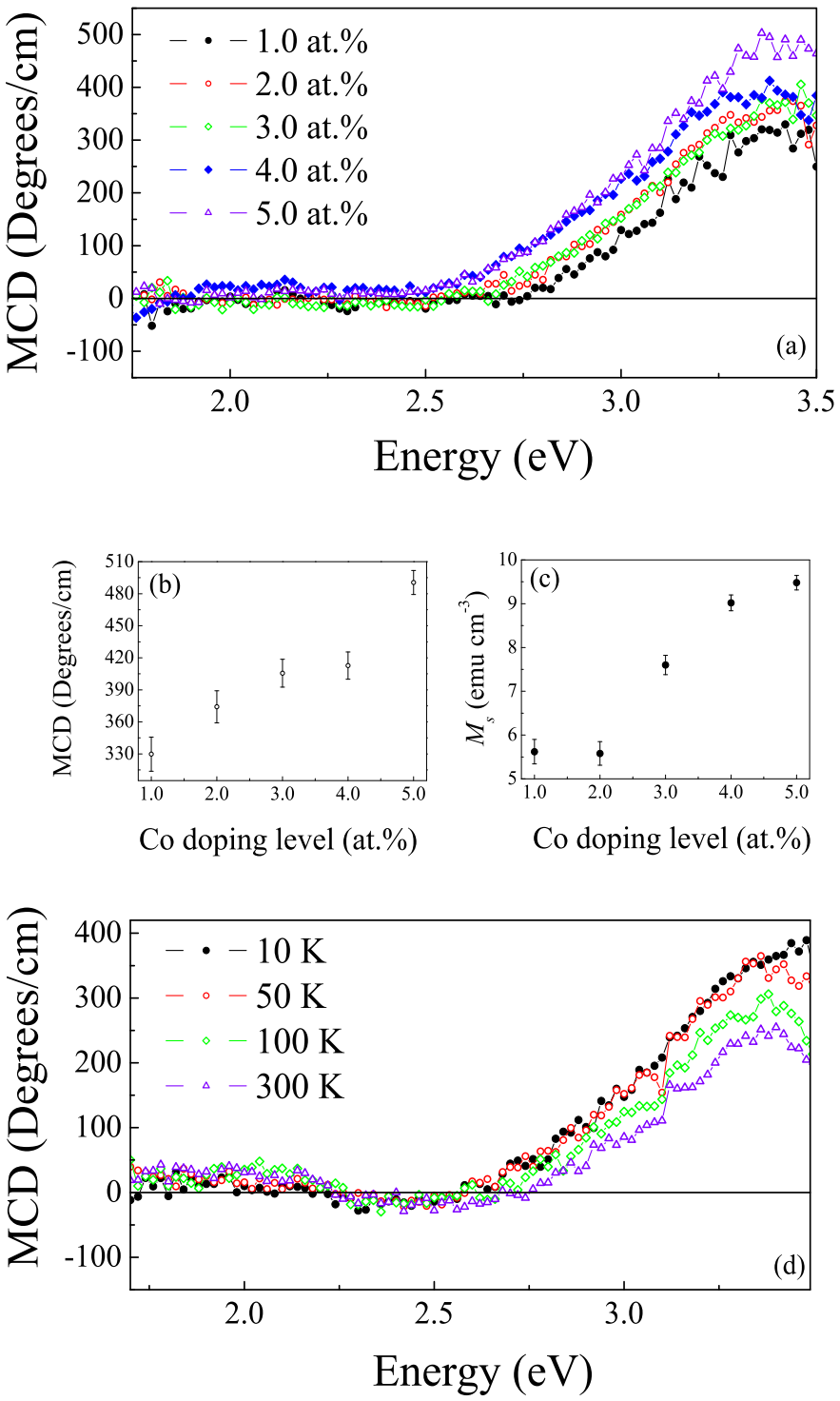

Figure 7.8: (a) Room temperature O-MCD spectra for 1.0-5.0 at.% Co-doped ITO(10) films; Dependence of room temperature O-MCD signal at 3.28 eV (b) and magnetisation, M_s, (c) on the Co doping level; (d) Temperature dependence of the O-MCD spectra for a 5.0 at.% Co-doped ITO(10) film.

7.5 Summary and Conclusions

In summary, we have shown that the ferromagnetism observed in semiconducting Co-doped In_2O_3 films is not related to the formation of secondary metallic Co clusters, similar to the findings described in chapter 6 using XMCD. Taken together, our data show that the magnetism may be due to polarised electrons in localised donor states, most likely related to oxygen vacancy defect states. Therefore, we can think of the origins of magnetism in these films in terms of Coey's band pictures where we have a hybridisation and charge transfer of electrons from a broad donor/defect-derived impurity band to a band of unoccupied $3d$ states at the Fermi level. The evidence for this comes from the fact that the optical MCD shows a strong dependence on the bulk magnetisation both as a function of temperature and as a function of the Co doping. This suggests that the states that we see optically in the absorption spectra are in fact the states that are giving rise to the magnetisation. We believe that the same localised donor states are also present in the Co-doped ITO samples. The presence of Sn however will have an influence on the donor state energy levels and is evident from the shift in band gap energy and magnitude of the magnetisation and MCD compared to samples without additional Sn doing. We expect that similar mechanisms might be important in other DMOs.

Bibliography

[1] K. Ando, Springer Series in Solid-State Science, Vol. 128, edited by S. Sugano and N. Kojima, p. 211, (Springer, Berlin, 2000).

[2] A. J. Behan, PhD Thesis, Characterisation of Doped ZnO Thin Films for Spintronic Applications, University of Sheffield, (2008).

[3] F. J. Kahn and P. S. Pershan, Phys. Rev. 186, 3, (1969).

[4] K. Ando, Appl. Phys. Lett. 82, 1, (2003).

[5] K. Ando, H. Saito, Z. Jin, T. Fukumura, M. Kawsaki, Y. Matsumoto, H. Koinuma, Appl. Phys. Lett. 78, 18, (2001).

[6] K. Ando, H. Saito, Z. Jin, T. Fukumura, M. Kawsaki, Y. Matsumoto, H. Koinuma, J. Appl. Lett. 89, 11, (2001).

[7] J. R. Neal, A. J. Behan, R. M. Ibrahim, H. J. Blythe, M. Ziese, A. M. Fox, G. A. Gehring, Phys. Rev. Lett. 96, 197208, (2006).

[8] A.J. Behan, J.R. Neal, R.M. Ibrahim, A. Mokhtari, M. Ziese, H.J. Blythe, A.M. Fox, G.A. Gehring, J. Magn. Magn. Mater., 310, 21582160, (2007).

[9] 26. L. M. Tang, L. L. Wang, D. Wang, J. Z. Liu, K. Q. Chen, J. Appl Phys. 107, 083704, (2010).

[10] I. N. Douglas, Phys. Stat. Sol. (b) 73, 641, (1976).

[11] C. Clavero, A. Cebollada, G. Armelles, Y. Huttel, J. Arbiol, F. Peiro, A. Cornet, Phys. Rev. B 72, 02441, (2005).

[12] D. Score et al J. Phys.: Conf. Ser. 200, 062024, (2010).

[13] M. A. White, S. T. Ochsenbein, D. R. Gamelin, Chem. Mater. 20, 7107-7116, (2008).

[14] Y. Ichiyanagi, J. Magn. Magn. Mater., 272-276, e1245-e1246, (2004); S. A. Makhlouf, J. Magn. Magn. Mater., 246, 184-190, (2002).

[15] J. M. D. Coey, P. Stamenov, R. D. Gunning, M. Venkatesan, K. Paul, New Journal of Physics 12, 053025, (2010).

[16] B. B. Straumal, A. A. Mazilkin, S. G. Protasova, A. A. Myatiev, P. B. Straumal, G. Schutz, P. A. van Aken, E. Goering, B. Baretzky, Phys. Rev. B. 79, 205206, (2009).

Chapter 8

Co/ITO multilayers

Giant magnetoresistance in multilayered Co/ITO thin-films can occur even at room temperature, but the crucial role played by superparamagnetic regions at the Co/ITO interface to the magnetotransport properties has remained unclear. By growing a series of $[Co/ITO]_{\times N}$ multilayers with bilayer repeat number, N, varying from 2 up to 40, and ITO thickness in the 1.20 - 4.20 nm range we have disentangled the various magnetic contributions which most strongly influence the physical properties of this system. The results show that ITO is a promising material for integration within oxide-based spintronic devices.

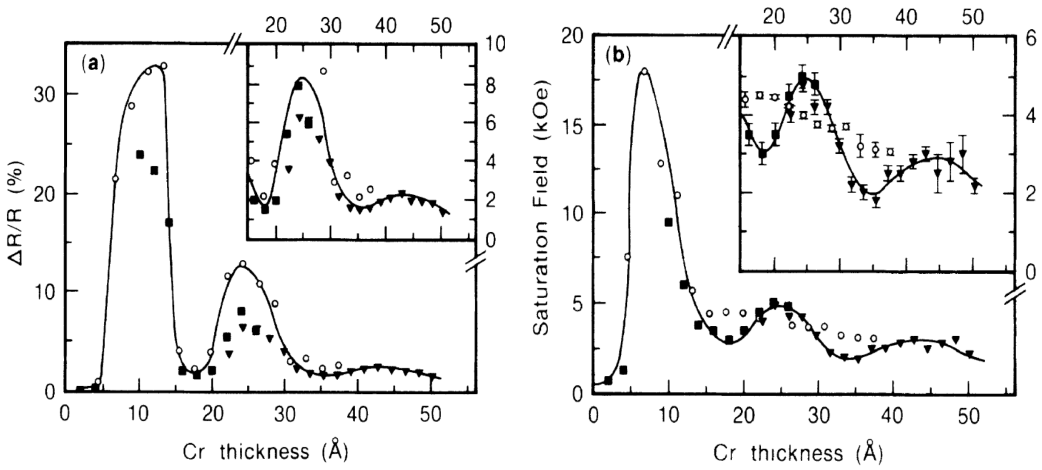

Figure 8.1: Magnetoresistance (a) and magnetisation saturation field (b) of sputter deposited Si (111)/Cr (10 nm)/[Fe (2 nm)/Cr (t_{Cr} nm)]$_N$/Cr (5nm) (N = 20 or 30) multilayers measured at 4.2 K. After reference [3].

8.1 Introduction

Exchange coupling of ferromagnetic (FM) metals through a non-magnetic (NM) spacer in layered structures is of considerable interest, both from a phenomenological and technological viewpoint. The most striking discoveries in these systems are the observation of giant magnetoresistance (GMR) [1], antiferromagnetic (AF) interlayer exchange coupling [2] as well as oscillations in the GMR ratio as a function of NM spacer layer thickness [3]. The following sections aim to introduce the GMR effect and its origins as well as some of the most influential factors which can affect the behaviour of these FM/NM layered systems.

8.1.1 The Giant Magnetoresistance effect

In 1988 Baibich *et al.* observed magnetoresistance changes as large as 50% at low temperatures in Fe/Cr multilayer structures [1]. The Fe layers were antiferromagnetically coupled across the Cr spacer layers, and the large change in resistance was found to be due to the change in the relative orientation of the ferromagnetic layers from antiparallel to parallel alignment as the field was increased. In order to achieve a large resistance change it was important for the Fe layers to be antiparallel in the absence of an applied field. In addition, it was found that the interlayer coupling oscillated between ferromagnetic and antiferrromagnetic depending on the thickness of the Cr interlayer [3–5] (see Fig. 8.1). The effect has since been seen in a number of other FM/NM systems such as Co/Cu and Co/Ru [5, 6].

The GMR effect in magnetic multilayers is the dependence of the resistance on the relative angles between the magnetisation direction of successive FM layers. The effect exploits the spin-dependence of the electrical conduction in FM metals and spin-

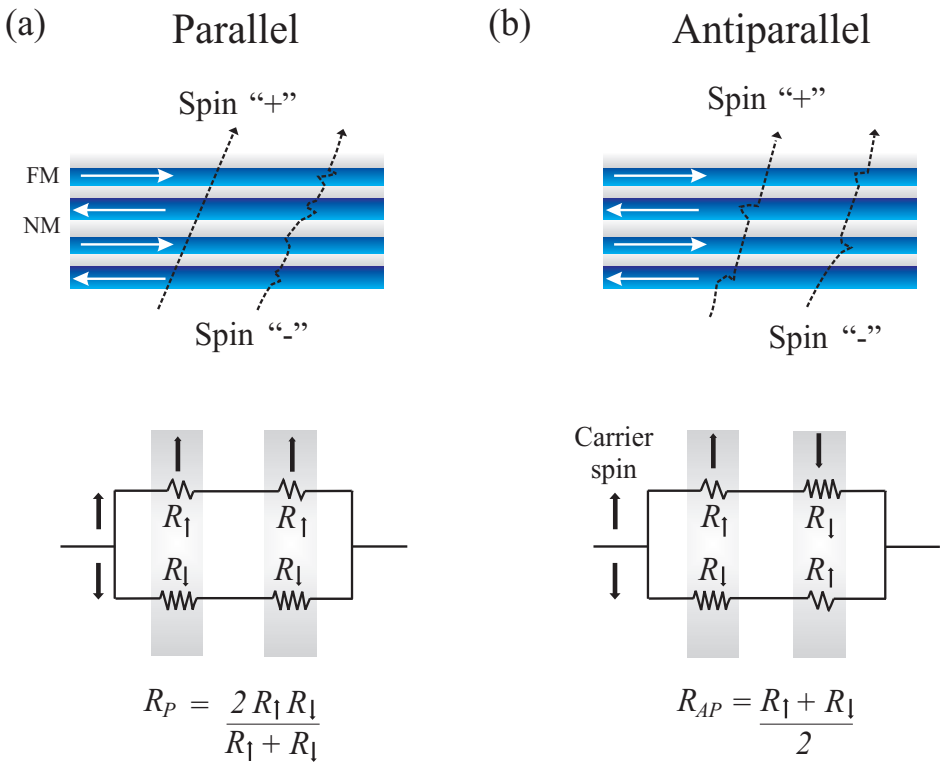

Figure 8.2: (Top panel) Electron transport in FM/NM multilayers for parallel (a) and antiparallel (b) alignments of magnetisation. Typical trajectories of spin "+" and spin "-" electrons are indicated by dashed lines; (Bottom panel) Effective resistor scheme that gives the parallel and antiparallel resistances of the multilayer.

dependent scattering at the interfaces. As explained in chapter 2, the essence of an MR response is the change in electrical resistance as a reaction to an applied magnetic field. In multilayered systems, the magnetisation of the respective FM layers will be altered upon application of a magnetic field. The GMR ratio can therefore be defined as

$$\frac{\Delta R}{R} = \frac{R_{AP} - R_P}{R_P} \tag{8.1}$$

where R_P and R_{AP} are the resistances in the parallel and antiparallel states respectively.

The GMR effect is best described by the two current model, based on a model of the electrical conduction in ferromagnetic metals by Mott [7] which was introduced in section 2.3.1. Here, the conductance of ferromagnetic materials can be viewed as the sum of separate contributions from electrons with opposite spin directions. There is a dissimilar scattering rate for the two electron channels due to a difference in the available energy states at the Fermi level. Figure 8.2 illustrates the origin of the GMR effect for a periodic FM/NM multilayer, depicting typical trajectories of diffusively scattered electrons with opposite spin directions.

In Fig. 8.2 (a), electrons for which in the parallel state the scattering probability is smallest are called the spin "+" electrons. In the parallel state the spin "+" contribu-

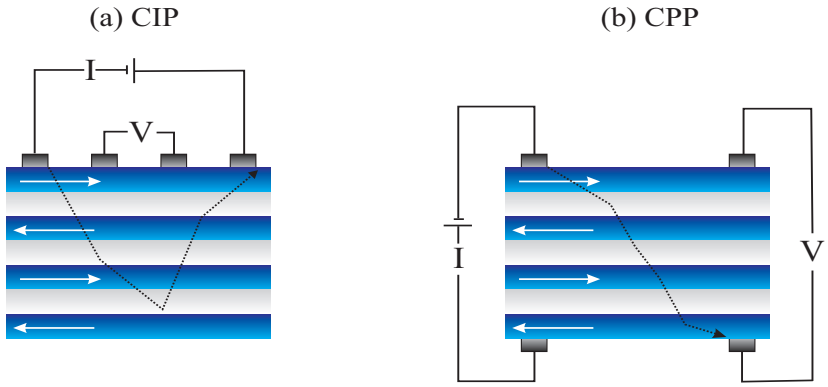

Figure 8.3: Schematic diagram of the CIP (a) and CPP (b) geometries of GMR.

tion to the conductance is much larger than the spin "-" contribution. In contrast, in the antiparallel state [Fig. 8.2 (b)], both spin "+" and spin "-" scatter strongly within the FM layers and results in a larger antiparallel resistance. Therefore, each layer acts as a spin-selective valve (see chapter 10), i.e. its magnetisation determines which spin polarisation ("+" or "-") it will transmit most easily .

Within a simple model for the GMR effect, R_P and R_{AP} in the antiparallel and parallel configurations can be found from the resistor schemes illustrated in the bottom panel of Fig. 8.2. This series resistor model leads to a GMR ratio equal to

$$\frac{\Delta R}{R} = \frac{(R_\downarrow - R_\uparrow)^2}{4R_\downarrow R_\uparrow}. \tag{8.2}$$

A number of semi-classical and quantum-mechanical approaches to explaining the GMR effect have been made by a host of authors [9, 10], but are beyond the scope of this thesis.

It is possible to measure the GMR in either the Current-In-Plane (CIP) or Current-Perpendicular-to-Plane (CPP) configuration, as shown in Figure 8.3. The CIP measurement requires no patterning and is therefore easier to perform on thin films (this technique was used in this chapter to measure the GMR properties of Co/ITO multilayers) and is characterised by the same drop in electrical resistance of the thin film sample when a magnetic field is applied. However, for the electrons to sample all of the different layers the requirement is that the mean free path of the electrons is longer than the sum of the layer thicknesses. The CPP configuration gives easier access to many of the fundamental parameters of the system [11], but is more complex to achieve experimentally (see chapter 10). The critical length scale is usually the spin-diffusion length. As we shall discuss later in chapter 10, CPP GMR measurements are governed by spin accumulation effects, however, this is not the case in the CPP geometry since the current flow is parallel to the layers and instead depends on the differential mobilities of the spin-up and spin-down electrons. The CIP geometry has the disadvantage of a lower GMR relative to the CPP measurement.

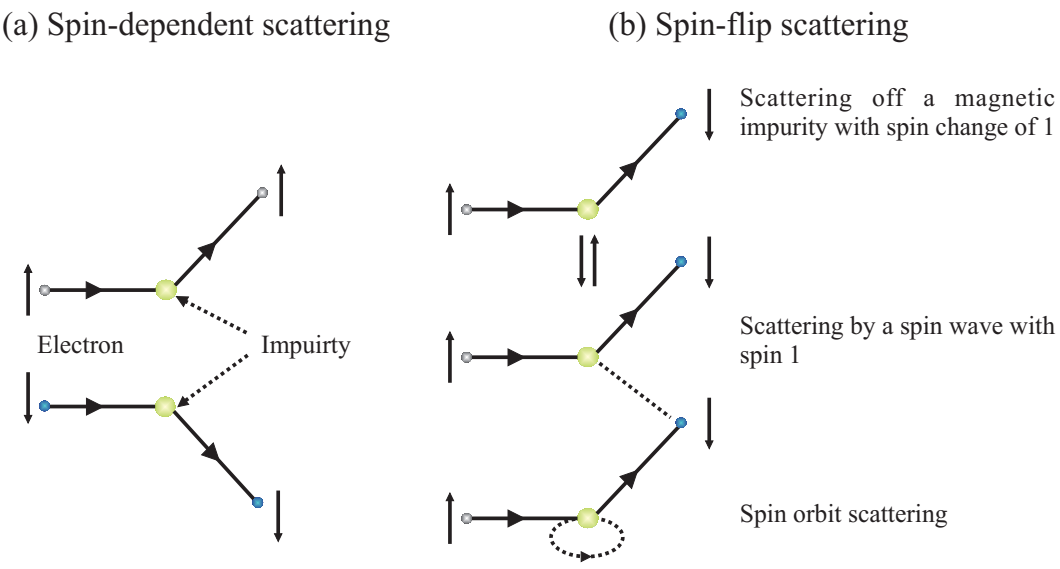

Figure 8.4: Different types of scattering in magnetic multilayers, (a) spin-dependent scattering, and (b) spin-flip scattering.

8.1.2 Importance of spin-dependent scattering

The GMR effect is based upon spin-dependent scattering. We are mainly concerned with elastic (energy conserving) scattering. In each scattering event only the direction of propagation of electrons changes. It is essential to distinguish between spin-dependent scattering which causes the GMR and spin-flip scattering which is detrimental to the GMR. The two major forms of scattering are shown in Fig. 8.4. In the case of spin-dependent scattering the orientation of the electron spin is conserved in each scattering event but the probabilities of scattering for electrons with up and down spin projections are different. On the other hand, when an electron undergoes a spin-flip scattering, its spin orientation changes from up to down (or vice versa) and, at the same time, the spin of the scattering centre changes so that the total spin is conserved.

There are a number of crucial factors that lead to the spin-dependent scattering

all of which derive from the fact that ferromagnetic materials have a spin-split band structure (recall section 2.1.3). The *sp* and *d* bands are strongly hybridised where the *d* band is only partially filled and therefore has a number of available unoccupied states. This gives the *s* electrons (which dominate the conduction in 3*d* TMs) options to scatter into the unoccupied states of the part-filled *d* band, thus reducing the mean free path of the electrons. This explains why the the conductivity of noble metals is considerably higher compared to ferromagnetic transition metals.

Another consequence of the spin-split *d* bands is a difference in the density of states at the Fermi energy level for spin-up and spin-down electrons and therefore a different scattering probability for each. Spin-dependent scattering which originates from the relative shift in the spin-up and spin-down bands takes place at the interface between

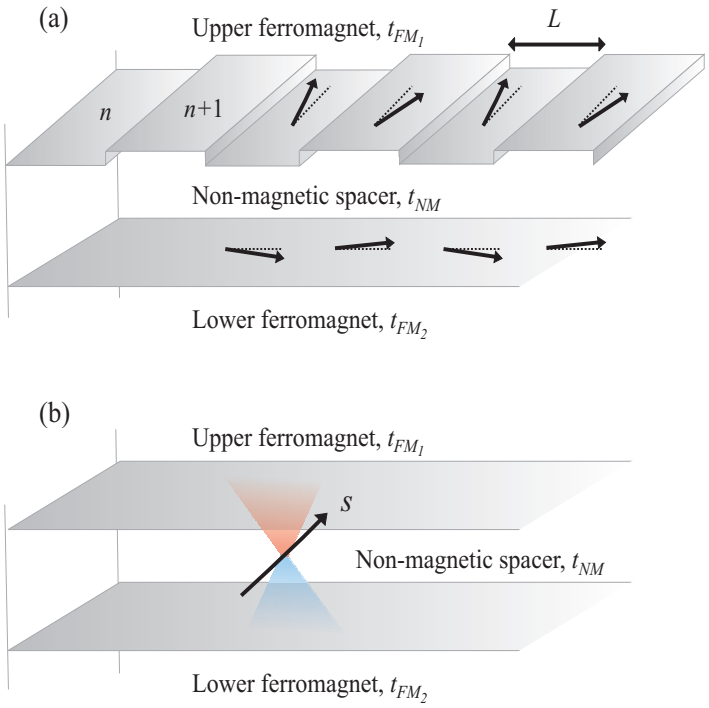

Figure 8.5: Two of the commonly invoked models for biquadratic coupling: (a) Thickness fluctuations and biquadratic coupling. For a trilayer where the spacer layer thickness varies periodically between n and n+1, the bold arrows show the local variation in the direction of the magnetisation. n-layer thick regions are taken to be anitferromagnetic and the magnetisations rotate away from each other. n+1 layer thick regions are considered as ferromagnetically coupled regions and the magnetisations align towards each other; (b) the loose spin model.

the FM and NM layers. This interfacial spin-dependent scattering arises from the band structure, for example, if there is a matching of the electronic potentials in one spin direction and not in the other. Therefore, for optimum interfacial spin-dependent scattering we require a good match between the bands of the magnetic layers and those of the spacer layer in one spin channel and as large as possible mismatch in the other spin channel.

There are several sources of spin-flip scattering (spin-independent scattering). Often these scattering events are results of microstructural imperfections such as stray impurities, vacancies, defects, roughness and dislocations. Also shown in Fig. 8.4 (b) are spin-flip processes which take place due to scattering with spin-waves and collisions with impurities where a spin-orbit interaction may take place. As we shall discuss in detail later, interdiffusion at interfaces where the elements are miscible can complicate the situation further. Not only will this have repercussions on the scattering processes, but also on the interlayer exchange coupling (see section 8.1.3). Since all these processes mix the up and down spin channels ("spin mixing"), they are detrimental to the GMR.

8.1.3 Interlayer Exchange Coupling

Interlayer exchange coupling (IEC) is concerned with the alignment of ferromagnetic layers that are separated by a spacer layer, much like the schematics shown in Fig. 8.2. The interest in IEC was revamped after observations made by Parkin *et al.* [3] where such coupling was found to oscillate with the spacer layer thickness. The two main forms of coupling are known as the "bilinear" and "biquadratic" coupling.

Phenomenologically, the IEC energy per unit area ($E_{1,2}$) between two FM layers (FM_1 and FM_2) separated by a spacer of thickness t_{NM}, can be written in the following form;

$$E_{1,2}(t_{NM}) = -J_1(t_{NM})\cos\alpha_{1,2} - J_2(t_{NM})\cos^2\alpha_{1,2} \tag{8.3}$$

where α refers to the relative magnetisation orientations of FM_1 and FM_2, and J_1 and J_2 are the bilinear and biquadratic coupling constants. If we consider a trilayer structure, when the two FM layers of thickness t_{FM} are aligned antiferromagnetically, the coupling between the layers can be determined according to the equation;

$$cJ_1 = -\mu_0 H_{SAT} M_{FM} t_{FM} \tag{8.4}$$

in which $c = 1$ or 2 and is a constant which depends on the order of magnetic re-orientation, M_{FM} is the total magnetisation and $\mu_0 H_{SAT}$ is the saturation field. In the case where repeated bilayers are used, e.g. a multilayer stack, J_1 is further halved to take into account that two surfaces of each FM layer are being coupled.

Two general approaches have been taken to explain bilinear IEC; the first, an extension of the RKKY coupling model [12], and the second, based on the consideration of quantum confinement [13] arising from the periodic modulations of the superlattice structures. Detailed reviews of the bilinear IEC effect can be found in reference [14].

Biquadratic coupling is a more complex matter. Discrepancies between experimental and theoretical values for J_2 have led to attempts of explaining biquadratic coupling by extrinsic effects. Slonczewski [15], and later Demokritov *et al.* [16], looked to solve the problem by taking into account microstructural factors such as spacer layer fluctuations, formulating rough interface models. Considering the hypothetical surfaces shown in Fig. 8.5 (a), with a terrace of width L within the spacer layer, both models conclude that J_2 is directly proportional to L, i.e. J_2 increases with L up to a limit (obviously, beyond a critical limit, L will be so wide that we have a non-terraced continuous layer) .

Slonczweski later proposed another model which better explained the unexpected strong temperature dependence of the biquadratic coupling [17], where he considered the case in which magnetic impurities were present in the spacer or at its interfaces, as shown in Fig. 8.5 (b), where a small arrow of spin S is in the NM layer. Such impurities interact with the two FM layers on both sides of the NM and mediate the interaction of the two FM layers. There is no direct exchange coupling, only indirect exchange coupling (RKKY-type) mediated by the spacer layer electrons.

Another form of coupling which will compete with the IEC is that due to the

presence of pinholes, or the break in the spacer layer giving direct exchange coupling between the two FM layers. Since there is direct contact between the FM layers, pinhole coupling is ferromagnetic.

8.2 Previous Work

The contributions towards the total GMR signal are not always straightforward, and there are a number of FM/NM multilayer systems where the GMR signal exhibits a very strong non-saturating behaviour explained by the coexistence of FM and SPM regions [18]. In this scenario, the SPM regions are magnetically decoupled from the FM regions of the magnetic layers. Typically, the magnitude of the total GMR is lower than in systems which are free from the SPM contribution. These systems can be modelled well using the Wiser-Hickey model [19,20], usually prescribed to granular systems, whereby the total GMR signal constitutes three separate components which depend on the path of the spin-dependent scattering event of each electron. In conventional GMR, where there is no contribution from SPM particles, scattering will typically take place between $FM_1 \rightarrow NM \rightarrow FM_2$. However, the presence of SPM particles will result in an electron scattering path of $FM_1 \rightleftharpoons NM \rightleftharpoons SPM$ and the emergence of a high-field contribution to the total GMR. The quality of the multilayers has been shown to influence the SPM term in the total GMR signal: lower surface roughness of the substrate has been found to decrease the SPM contribution [21].

The relevant pioneering work for the phenomena observed here have been briefly explained in earlier sections, however, are all concerned with metal based multilayers. Here we are interested in FM metal/oxide interfaces. Chen *et al.* have produced work on Fe- and Co/ITO multilayers [22, 23]. In particular, oscillations in the GMR as a function of ITO spacer thickness are observed and the origins of the GMR response is explained as having its origins from ferromagnetic and interfacial superparamagnetic contributions. However, the work does not go into any great detail about the presence of superparamagnetic particles at the interface. The results presented in this chapter aim to shed some light on these issues.

8.3 Experimental Results

All $[\mathrm{Co/ITO}]_{\times N}$ multilayers (ITO(10) composition) were prepared at room temperature on unheated 5×10 mm^2 area r-plane sapphire substrates by DC magnetron sputtering in a diffusion pumped UHV system. Prior to film growth, the system's base pressure was better than 1×10^{-6} Pa. Films were sputtered in 1.50 ± 0.01 Pa of Ar with each layer grown in sequence and without breaking vacuum by rotating the substrates below

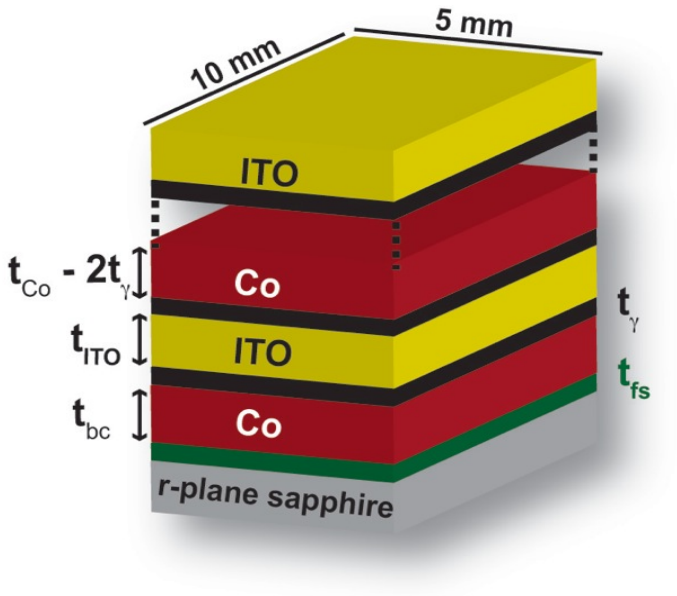

Figure 8.6: Illustration of a Co/ITO multilayer, where t_{ITO} is the ITO layer thickness, t_γ is the thickness of the magnetically dead layer at the Co/ITO interface, t_{fs} is the thickness of the magnetically dead layer at the Co/r-plane sapphire interface, t_{bc} is the equivalent bottom Co layer thickness (= t_{Co} - t_{fs} - t_γ) and t_{Co} is the equivalent thickness of subsequent Co layers.

stationary Co and ITO targets (as described in sections 3.3 and 3.4). The gas flow was approximately 0.10±0.01 Pa/s. The deposition rates for the ITO and Co targets were 0.02 and 0.04 nm/W/pass at 1 rpm calibrated in 1.50±0.01 Pa respectively. A power of 10 and 15 W was applied to the ITO and Co targets.

Because the lattice parameter for ITO is 1.012 nm, the minimum ITO thickness (t_{ITO}) used was 1.20 nm so that the risks of discontinuities and fluctuations, the formation of magnetic pinholes and/or the presence of loose spins could be minimised. Stacks where the bilayer repeat number was varied (N = 2 - 40) had an ITO thickness of t_{ITO} = 3.0 nm. In those stacks where N = 10, the ITO thickness was systematically varied between each sample in the (1.20 - 4.20±0.10) nm range. The thickness of the Co layer remained constant for all multilayers at (1.20±0.1) nm. In Fig. 8.6 an illustration of a $[Co/ITO]_{\times N}$ multilayer used in these experiments is shown.

8.3.1 Magnetic Dead Layers

Interfacial intermixing between the Co and ITO layers was investigated. For FM/oxide systems, an equivalent thickness of the FM (in this case Co) can be assumed whereby the FM atoms are surrounded by a host of O atoms, resulting in the FM atoms becoming oxidised. This can happen for one of two reasons; (1) due to oxygen diffusion

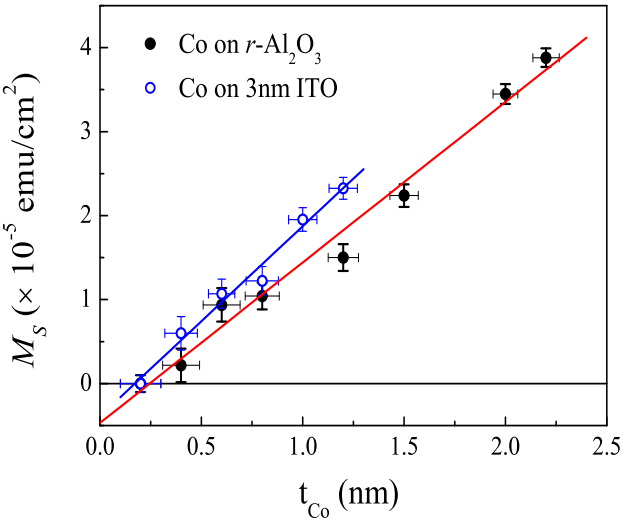

Figure 8.7: Moment per unit area versus Co thickness deposited onto r-plane sapphire substrates (closed circles) and on a 3.0 nm layer of ITO (open circles). Solid lines linear least-square fits to the experimental data used to extrapolate the dead layer thicknesses.

into the Co layer, and (2) due to stray Co atoms diffusing into the oxide layer. We define this region in our Co/ITO system as the magnetically dead layer (MDL) and more precisely can be thought of as a length scale over which there is little or no magnetic exchange. The quality of the interfaces is therefore important as we would expect increasing levels of discontinuity in the Co or ITO layers to increase the thickness of the MDL. Potentially, the MDL can be detrimental since their magnetic and electronic properties will differ from those of the metallic Co atoms in a ferromagnetic and metallic crystal. Investigation into the possibility of an MDL being present and its potential scale was carried out by measuring the magnetisation, M_s, per unit surface area as a function of Co layer thickness, t_{Co} (nm), on a number of samples where a 3.0 nm layer of ITO had been deposited onto r-plane sapphire substrates. All samples were capped with 2.0 nm of gold to prevent further oxidation of the Co layer. The MDL thickness per interface, t_γ (see Fig. 8.6), was extrapolated as the point where the linear fit intersected the x-axis ($M_s = 0$) and was found to be approximately (0.17±0.15) nm (Fig. 8.7) similar to that found in Co/ZrO_2 [24] and Co/MgO multilayers [25].

The behavior of the first Co layer deposited at the surface of the r-plane sapphire substrate has also been considered. We have found through systematic variation of the Co layer thickness (0.2 - 5.0 nm) onto r-plane sapphire substrates that an MDL of (0.22±0.15) nm [(t_{fs} (Fig. 8.6)] exists at the Co-r-plane sapphire interface (Fig. 8.7). This implies that the first Co layer is mostly redundant as almost half of it is magnetically inert due to the MDL formed at both the substrate and ITO interfaces.

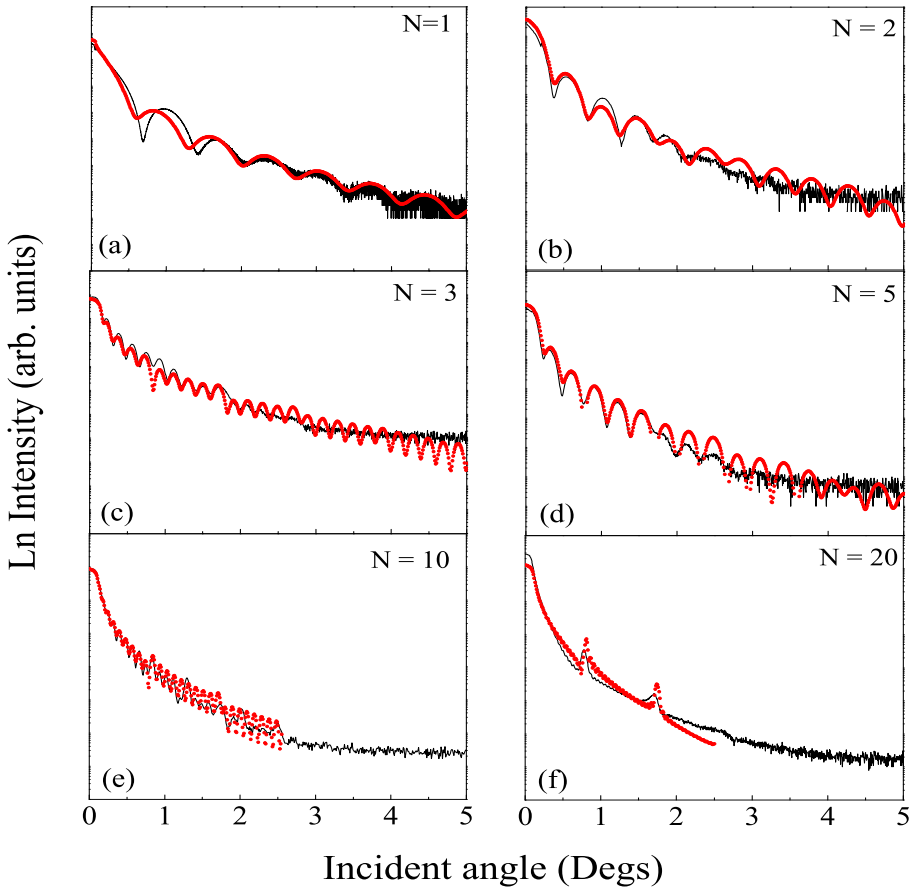

Figure 8.8: Low angle reflectivity for $[Co/ITO]_N$ multilayers with varying N between 1 to 20. Solid black lines represent measured data, and the solid red circles are the corresponding simulations.

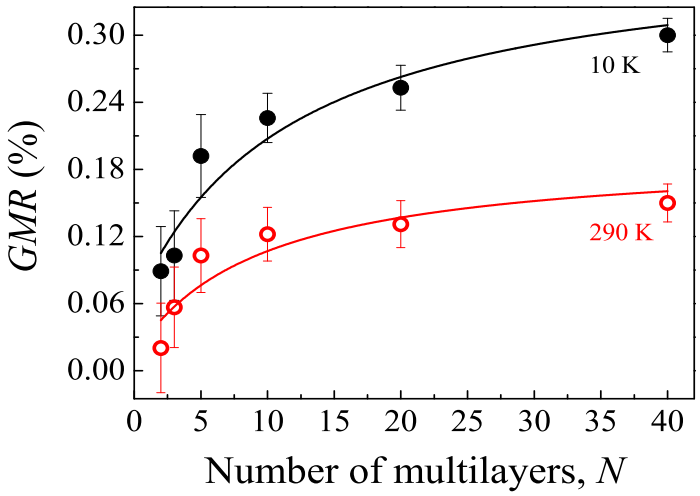

Figure 8.9: Absolute GMR dependence on the number of bilayer repeats, N, in $[\text{Co}(1.20\text{nm})/\text{ITO}(3.00\text{nm})]_N$ multilayers at 10 K (closed circles) and 290 K (open circles). The solid lines correspond to fits made using the Fuchs-Sondheimer model.

8.3.2 Varying the number of repeat bilayers, N

Structural properties

The number of bilayers, N, in the multilayers is varied to understand the influence of interfacial features on the overall multilayer performance. Generally N is kept rather large in other FM/NM multilayers, typically N>20, and has been reported to play a significant role in achieving large values for GMR [3, 26].

Figures 8.8 (a) - 8.8 (f) show the low-angle x-ray reflectivity (LAR) measurements for the build up of N from 1 to 20 with comparative simulation fits. The main assumption made when attempting to simulate the experimental data was that the quality of the layers improved as they moved further away from the substrate. The typical ranges used for the roughness parameters from start to finish for the fittings were 0.40 - 0.10 nm for Co and 0.60 - 0.20 nm for the ITO layers. There is excellent agreement between the experimental and simulated data up to $N = 10$ after which the experimental data starts to deviate from the simulation. After $N = 20$, the total stack thickness is verging on the limit of obtaining good low angle data and may also be nearing the maximum acceptable roughness. $N = 40$ (not shown) reveals no discernable Kiessig fringes, but does show two multilayer Bragg peak reflections.

Magnetotransport properties

The thickness (equivalent N) dependence of our MR data was fitted using the Fuchs-Sondheimer model [27,28] following the method applied in reference [29]. All boundary conditions are assumed to be diffusive, such that the measured effective resistivity, ρ^*,

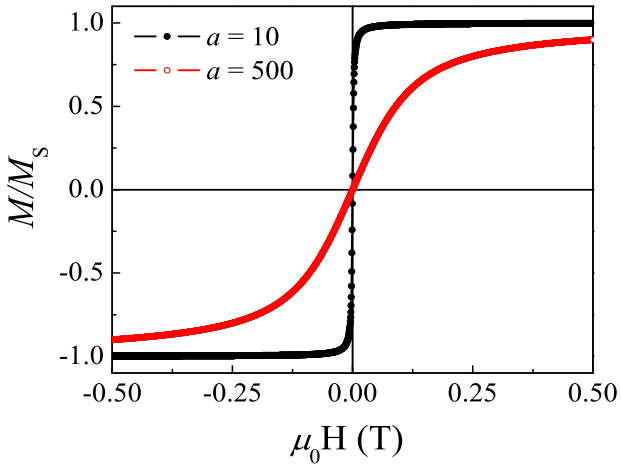

Figure 8.10: Sensitivity of the shape of the magnetisation at 290 K on the Langevin parameter, a, in Eq. 8.7.

corresponds to

$$\rho^* = \rho\left[1 + \frac{3\ell}{8t}\right], \tag{8.5}$$

where t is the thickness of the film which leads to a bulk scattering resistivity ρ and a mean free path ℓ. The first term relates to bulk scattering, while the second term corresponds to additional scattering at surfaces. According to this equation, resistivity of any given film will show finite size effects with characteristic bulk resistivity and mean free path. The GMR ratio can then be defined as

$$GMR = \frac{\rho_0^* - \rho_H^*}{\rho_0^*}, \tag{8.6}$$

where ρ_H^* and ρ_0^* are resistivities in an in-plane applied magnetic field (μ_0H) and zero magnetic field respectively. Eqn. 8.6 has been used to fit the thickness dependence of the Co/ITO stacks. Fig. 8.9 shows the thickness dependence of the multilayers with corresponding fits to Eqn. 8.6. The bulk resistivities in an applied magnetic field and zero field were determined from straight line fits of $\rho^* t$ against t using Eqn. 8.5. The free fit parameters in Eqn. 8.6 (once Eqn. 8.5 has been substituted accordingly) were ℓ_0 and ℓ_H. We obtained values of 17.0 nm and 4.7 nm for ℓ_0 at 10 and 290 K respectively. The corresponding ℓ_H values were 25.1 nm and 31.1 nm at 10 and 290 K. Notice that the values obtained here agree well with ones reported elsewhere for Co/Cu multilayers [29]. The temperature dependence of the values for the mean free path seem to be unrealistic; in a metallic system it is reasonable to expect an increasing mean free path with decreasing temperature. However, this not the case in our multilayers. Considering that similar analysis by Marrows *et al.* on Co/Cu multilayers resulted with similar unphysical temperature dependence in the mean free path of the multilayers, we assume that these unphysical values are a result of the limitations in

the Fuchs-Sondheimer model. The most interesting result of the Fuchs-Sondheimer model fitting is the prediction of finite size effects in GMR for our multilayers.

GMR achieved in similar Co/ITO multilayers was considerably higher than the GMR we obtain here [23]. We believe that this is due to high levels of spin-independent interfacial scattering between the Co and ITO layers in our samples. We expect that the interfacial region between Co and ITO is expected to have a frustrated magnetic structure which is possibly superparamagnetic or spin glass type. Large scattering effects makes it very difficult to interpret the resistance data and so analysis of the magnetic data may be a more fruitful avenue to gain information on the different magnetic contributions to the physical properties of the multilayers (see section below).

Magnetic Modelling

It is well documented that ultra thin films of Co exhibit superparamagnetism [30]. Since in our films t_{Co} is approximately (1.20±0.10) nm, we expect a SPM contribution to the overall magnetisation.

The magnetic properties of the [Co/ITO] stacks could be modelled assuming we have a two-phase system with SPM and FM components contributing to the magnetic and magnetotransport properties. Since magnetisation measurements are volume sensitive, the volume fraction of each phase can be extracted.

The Langevin function describes the field dependence of the magnetisation of both ferromagnets and superparamagnets [31, 32]:

$$M(H) = M_S[coth(H/a_{SPM}) - a_{SPM}/\mu_0 H], \tag{8.7}$$

where M_s is the saturation magnetisation as before, T is the absolute temperature and a is the Langevin parameter. The value of the Langevin parameter will define the shape of the field dependence of the magnetisation as illustrated in Fig. 8.10. For a_{SPM}=10, the magnetisation curve has a relatively low magnetisation saturation field similar to those observed in ferromagnetic materials, while larger values for a_{SPM}, such as 500, produce a non-saturating magnetisation curve similar to those observed in superparamagnetic materials. Therefore, one can write an expression which can describe the magnetisation of a system which contains ferromagnetic and superparamagnetic phases:

$$M(H) = fM_S[coth(H/a_{FM}) - a_{FM}/\mu_0 H] + (1-f)M_S[coth(H/a_{SPM}) - a_{SPM}/\mu_0 H], \tag{8.8}$$

Here a_{FM} and a_{SPM} are the Langevin parameters for the ferromagnetic and superparamagnetic phases, f is the ferromagnetic volume fraction and M_s, T and μ_0H are as before. In Eqn. 8.8 a value of $f = 1$ means the sample contains only a ferromagnetic phase, while $f = 0$ corresponds to a case where the superparamagnetic phase is the

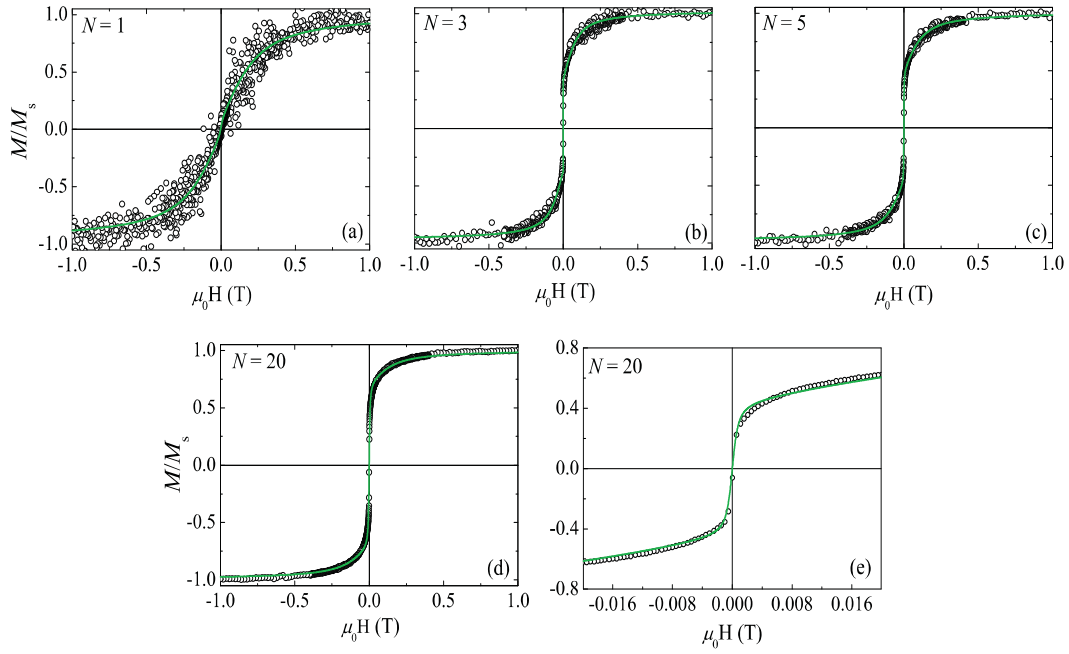

Figure 8.11: Normalised magnetisation curves for a selection of $[\text{Co/ITO}]_N$ ML stacks where (a) $N = 1$, (b) $N = 3$, (c) N=5, (d) $N = 20$, and (e) low-field region of a stack where $N = 20$, along with model fits (solid green line).

lone phase in the system. To investigate the possibility of a SPM contribution in our samples, normalised M-$\mu_0 H$ loops were fit to Eqn. 8.8.

Figs. 8.11 (a) - 8.11 (c) show the magnetisation curves for a selection of $[\text{Co/ITO}]_{\times N}$ multilayers along with fits using the model described above. The fits are excellent at both low and high magnetic fields which is consistent with the presence of a contribution to the magnetisation and GMR from SPM particles. a_{FM} is varied between 8-20 while a_{SPM} was fixed at 320, and f was used as the fitting parameter. The values of f for all stacks is given in Figure 8.12. It is interesting that the ferromagnetic volume fraction increases rapidly when the number of stacks is increased to 10 and almost reaches saturation when N>10. This could be due to an improved interface between the Co and ITO for a larger number of stacks, where the quality of the bilayers improves as the distance from the substrate interface increases and is consistent with the assumptions made to fit the LAR data. This has also been observed in Co/Cu multilayers [6]. It is expected that the SPM phase forms at the interface of the film with the substrate or the FM/ITO interface. Therefore, it is reasonable to assume that the SPM volume fraction is related to the roughness and quality of the Co/ITO interfaces.

8.3.3 Varying the ITO spacer layer thickness, t_{ITO}

$[\text{Co(1.20nm)/ITO}(t_{ITO})]_{10}$ multilayers were all semiconducting over the temperature range of 5 - 300 K. The observation of semiconducting behaviour for the entire stack

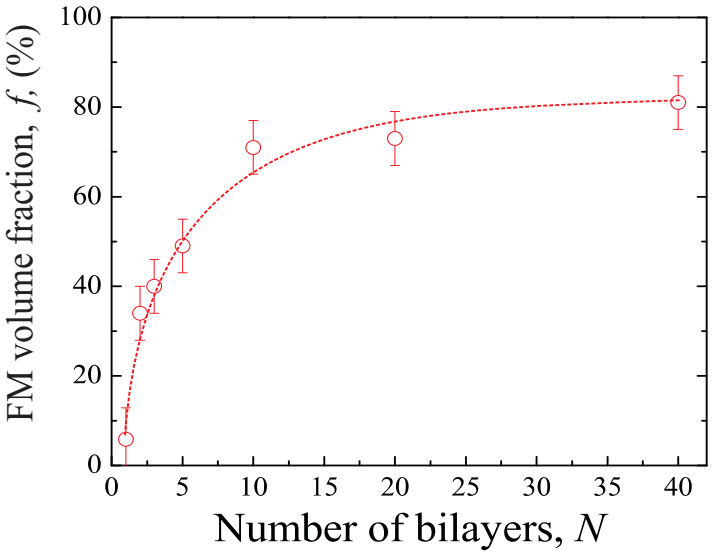

Figure 8.12: Ferromagnetic volume fraction, f, as a function of the number of bilayer repeats, N.

suggests that a high degree of electron scattering between the layers and the higher resistivity of the ITO layers plays a dominant role in determining the transport properties of these multilayers.

The temperature evolution of the GMR for a $[\mathrm{Co(1.20nm)/ITO(1.65nm)}]_{10}$ multilayer is shown in Fig. 8.13. As shown in the inset of Fig. 8.13, pronounced hysteresis is seen in the GMR and indeed in the the magnetic hysteresis loops (see later) at 5 - 10 K. As the temperature begins to rise, the GMR switching field and magnetic coercive field decrease in tandem, as expected. A similar dependence on temperature is observed in all $[\mathrm{Co(1.20nm)/ITO(t}_{ITO})]_{10}$ multilayers. The magnitude of the GMR signal also decreases as the temperature increases as we would expect, and is also shown in the main panel of Fig. 8.13 (solid black circles with black line).

To rule out any contribution from AMR, measurements were made having rotated the in-plane field by 90° with respect to the current. The resulting curves for field parallel or perpendicular to the current were identical, thus eliminating a significant AMR contribution. The absence of an AMR contribution is not what we would have expected, regardless of the very low GMR values. We believe that one of the major origins in the low GMR signal observed is due to magnetic spin frustrations as a result of a fierce competition between respective magnetic phases. It is possible that these magnetic frustrations are also responsible for the lack of an AMR contribution to the total GMR. The frustrations may act to suppress or eliminate spin-orbit coupling interactions between neighbouring Co layers. Alternatively, the absence of a detectable AMR signal could be related to the lack of clearly defined current paths and so rotating the field or current with respect to each other would not be expected to have any effect.

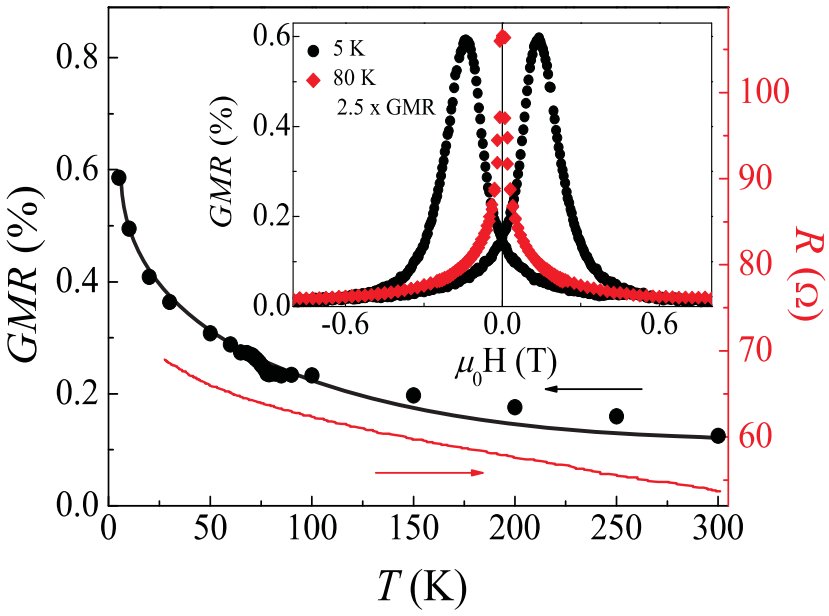

Figure 8.13: (a) GMR (closed circles) and resistance (line) as a function of increasing temperature for a $[Co(1.20nm)/ITO(1.25nm)]_{10}$ multilayer. Arrows indicate data axes. Inset (a) shows the GMR of the same stack at 5 (closed circles) and 80 K (closed diamonds). The GMR at 80 K has been multiplied by a factor of 2.5. Solid lines serve to guide the eye.

Figures 8.14 (a) - 8.14 (c) illustrate the oscillatory nature of magnetisation saturation field ($\mu_0 H_{SAT-M}$) at 290 K and the magnitude of GMR at both 10 K and 290 K. $\mu_0 H_{SAT-M}$ was estimated directly from the magnetisation loops and defined as the point at which the measured magnetisation signal deviates more than the assigned error in magnetisation. The oscillatory nature of the saturation magnetisation and GMR can be modelled by considering oscillatory exchange coupling due to RKKY interactions across a NM spacer thickness t_S;

$$J(t_s) = \frac{J_0}{t_s^2} \sin\left(\frac{2\pi t_s}{\Lambda} + \Psi\right) \frac{t_s/L}{\sinh(t_s L)} \tag{8.9}$$

where J_0 is the interlayer exchange coupling strength (erg/cm^2), Λ and Ψ are the period and phase of the oscillation and L is an attenuation length [33]. Table 8.1 summarises the fitting parameters that resulted from the fits for the magnetisation saturation field and GMR at both 10 and 290 K. Two clear oscillations were identified: the first at 1.65 nm and the second at approximately 3.0 nm. After the second oscillation peak, GMR becomes very low even at 10 K and begins to fall steadily with increasing t_{ITO}. The oscillations seen in $\mu_0 H_{SAT-M}$ and GMR, both at 10 K and 290 K, coincide. A further weak oscillation is seen however in the $\mu_0 H_{SAT-M}$ at approximately 4.0 nm, indicating an oscillation period of $\Lambda \approx 1.40$ nm. This value is in reasonably good agreement with that estimated using Eqn. 8.9 (see table 8.1). The discrepancy between the values for J_0 are due to differences in the saturation fields between the M-$\mu_0 H$ and GMR curves.

From $\mu_0 H_{SAT-M}$ we can estimate the AF interlayer exchange coupling energy, J_{AF},

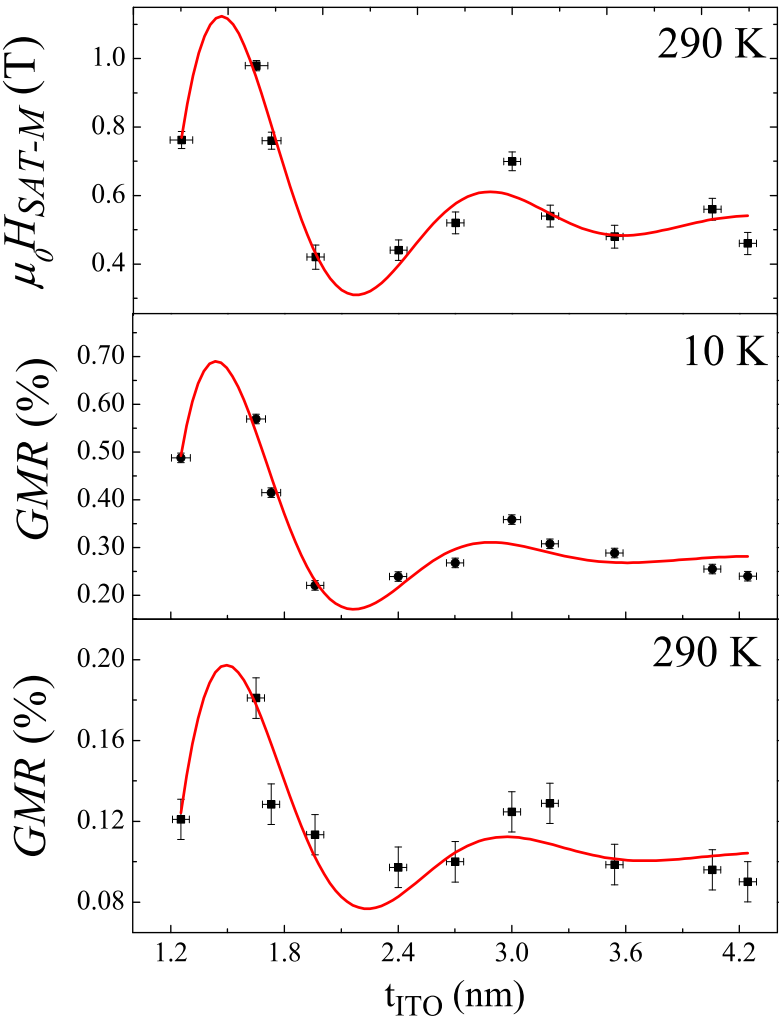

Figure 8.14: Dependence of the magnetisation saturation field, $\mu_0 H_{SAT-M}$, at 290 K (a), and (b) GMR at 10 and 290 K, as a function of the ITO spacer layer thickness for $[Co/ITO]_{10}$ multilayers. The solid lines are fits to Eqn. 8.9.

Table 8.1: Summary of the fitting results and parameters using the RKKY equation described in Eqn. 8.9 to model the results shown in Fig. 8.14. * represents the fitting results at 290 K obtained from the magnetisation data.

Temperature (K)	J_0 (erg/cm^2)	Λ (nm)	Ψ (nm)	L (nm)	p (arb. units)
10	-1.57	1.43	4.23	0.78	0.28
290	-0.36	1.46	4.15	0.88	0.11
290*	-1.75	1.40	4.05	1.19	0.52

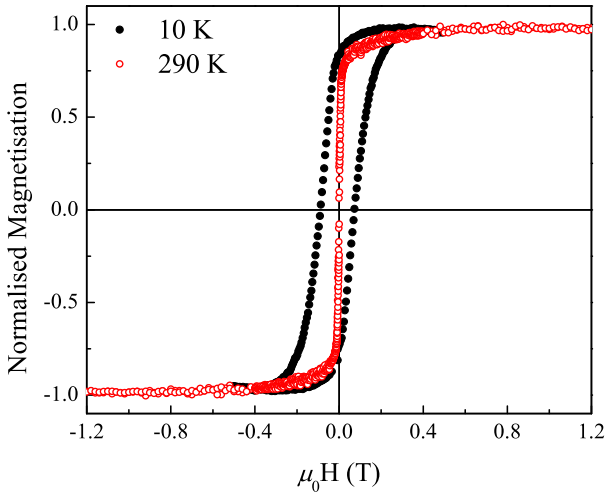

Figure 8.15: Normalised magnetisation versus applied field for a multilayer stack with $N = 10$ and $t_{ITO} = 1.20$ nm at 10 (solid black circles) and 290 K (open red circles).

between the Co layers using Eqn. 8.4. The magnitude of J_{AF} follows the same path as $\mu_0 H_{SAT-M}$ as t_{ITO} is varied, with the maximum J_{AF} corresponding to -0.26 erg cm^{-2} at 290 K for [Co(1.20nm)/ITO(1.65nm)]$_{10}$ at the peak of the first AF oscillation which is in good agreement with the value obtained from the fittings using Eqn. 8.9 (-0.36 erg cm^{-2}), and approximately 1.7 times larger than that reported in Co/Cu [5].

Large magnetisation saturation fields, compared to pure thin film Co, combined with low magnetic remanence and coercive field observed in the [Co(1.20nm)/ITO(t_{ITO})]$_{10}$ multilayers, suggest that there is a non-negligible contribution to the magnetotransport properties of the stacked structures from stray or loose SPM Co particles which are present in the ITO spacer layer. A comparison of the GMR and magnetisation curves shows that $\mu_0 H_{SAT-GMR} > \mu_0 H_{SAT-M}$. We attribute this discrepancy in saturation fields to large interfacial scattering of conduction electrons and the difficulty for mo-

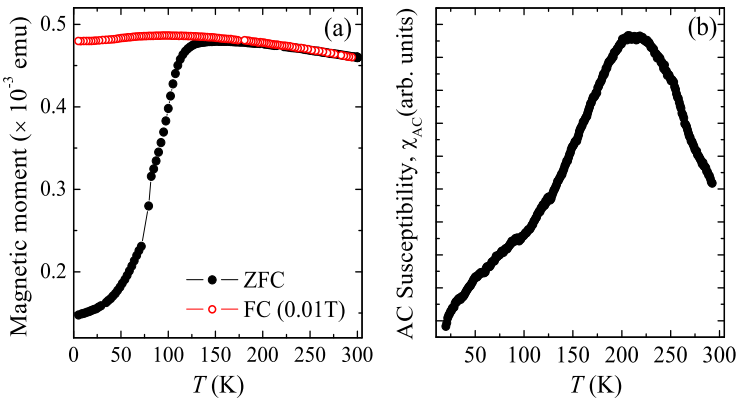

Figure 8.16: (a) Magnetisation versus temperature scan in the field cooled (FC) (open circles) and zero-field cooled (ZFC) (closed circles) modes for a $[\text{Co}(1.20\text{nm})/\text{ITO}(1.25\text{nm})]_{10}$ stack in an applied field of 0.01 T, and (b) Real component of the AC susceptibility, χ_{AC}, as a function of temperature for the same $[\text{Co}(1.20\text{nm})/\text{ITO}(1.25\text{nm})]_{10}$ stack. The AC field of 0.787 mT was applied parallel to the film plane at a frequency of 376 Hz. The measurements were taken in a 0.01 T DC field.

ments to align in a parallel fashion within respective FM layers due to a high degree of magnetic frustration.

Figure 8.15 compares the normalised M-$\mu_0 H$ loops for a multilayer with $N =$ 10 and $t_{ITO} = 1.20$ nm at 10 and 290 K. It has already been shown that there is a certain SPM contribution to these M-$\mu_0 H$ loops at higher temperatures. At low temperatures, the M-$\mu_0 H$ shows a clear hysteresis with a coercive field of approximately 0.20 T. Therefore, we expect to see some SPM signature in the magnetisation versus temperature scans. Confirmation of the presence of SPM Co through the ITO spacer was carried out via standard ZFC-FC magnetisation versus temperature scans from 5 - 300 K in an applied magnetic field of 0.01 T using a SQUID [Fig. 8.16 (a)]. It is clear that a T_B is present at approximately 140 K.

Further evidence for the presence of SPM particles was gathered from measurements of the real component of the AC susceptibility as a function of AC frequency [Fig. 8.16 (b)]. The peak observed indicates a T_B of approximately 210 K. The difference in values for T_B are due to the fact that T_B for superparamagnetic particles depends on the time scale of the experimental technique, and it is therefore expected to be different in DC (SQUID) and AC measurements. T_B may also depend on the shape and particle size distribution. Using the information from the temperature dependence of magnetisation and AC susceptibility we can apply Eqn. 2.8 to estimate the Co particle radius (using $K_{Co} = 4.9 \times 10^6$ ergs cm^{-3} and measurement time $t = 10$ s). Assuming spherical particles, this yields a value of approximately 1.30 nm. Other multilayers with different ITO spacer thicknesses also produced similar results.

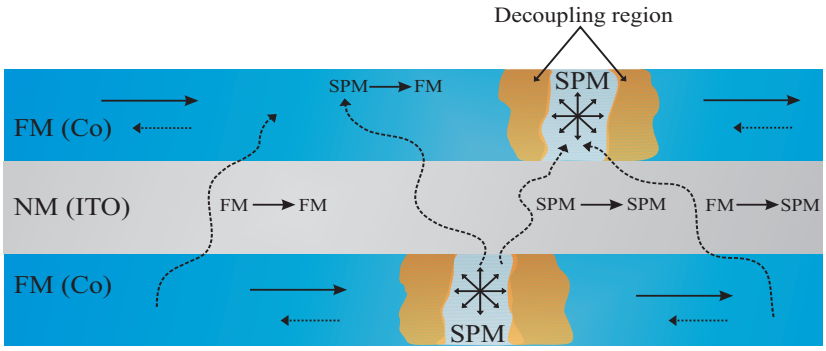

Figure 8.17: Schematic illustration of the SPM isolated island model. The sold-line and dashed-line straight arrows indicate the directions of the magnetisations lying in the plane of the FM Co layer. The significance of the shorter dashed arrows refers to the fact that the magnetisations in successive layers are not aligned in antiparallel fashion. The multi-arrow stars within the SPM regions represent the temporary fluctuations of the orientation of their magnetic moments. Wavy arrows indicate the possible trajectories of electrons between FM and SPM regions that can contribute to the GMR. Adapted from [35].

The bulk characterisation features for identifying a magnetically frustrated system such as a spin glass (recall section 2.1.5) or superparamagnet are very similar, however, we are confident that the phenomena observed in these multilayers are of superparamagnetic origin. Spin glasses are usually alloyed materials, e.g. $Cu_{1-x}Mn_x$, whereas in the case here, we have ultrathin Co layers separated by ITO. At most we are likely to have discontinuous Co layers forming islands or stray Co particles dispersed within the ITO spacer (see section 8.3.4). Also, spin glasses will usually show a cooperative phase transition [34], while superparamagnets show a gradual blocking of the superparamagnetic particles. The freezing temperature of spin glasses is rarely as large as the peak points in Fig 8.16 which serves as further evidence for superparamagnetism. The best way to distinguish between the two would be to perform muon spin rotation, relaxation and resonance measurements, where a spin glass will give very specific relaxation times.

8.3.4 Considerations of the possible spatial distribution of superparamagnetic particles

The results above unambiguously confirm the presence of SPM regions in these multilayers, which are believed to be decoupled from the FM parts of the magnetic layers. However, it is not easy to determine the location of the magnetically separated SPM regions. Based on models by Bakonyi *et al.* [35] it is believed that two possible scenarios can be proposed to explain the SPM contributions to both the magnetic and magnetotransport behaviour in these multilayers: the *isolated island model* and the *interfacial loose-spin model* (analogous to the model described by Slonczewski [15, 17]).

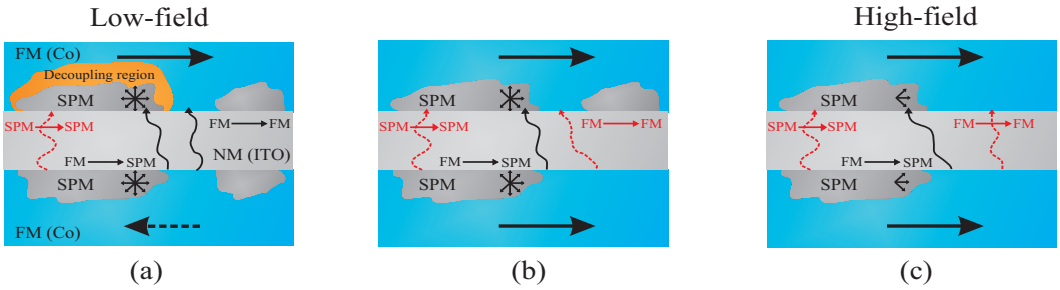

Figure 8.18: Schematic illustration of the loose-spin model, where SPM regions are present at the interfaces between FM and NM layers at low (a), intermediate (b) and high (c) applied magnetic fields. The features can all be defined as in Fig. 8.16. The star-like arrow arrangements indicate the random temporal fluctuations in SPM particle magnetisation which gradually align with higher magnetic fields (c). Solid wavy arrows indicate electron paths which will contribute to the magnetoresistance, whereas those which are dotted represent ineffective paths. Adapted from [35].

The possibility of intermixing between the Co and ITO layers has been proven in section 8.3.1. In the extreme case, this may lead to the formation of small magnetic islands separated by non-magnetic material from the FM part of the magnetic layer. These separating regions may be alloys of Co-ITO and may be non-magnetic. These are referred to as decoupling regions between the FM and SPM parts of the FM layer. Due to their probable nanoscale size, the isolated islands may exhibit SPM behaviour. A schematic illustration of the dynamics involved within this model scenario is depicted in Fig. 8.17. Note that this is an over-simplified picture, and that possible fluctuations in FM and NM layer thicknesses have been neglected, which is likely to not be the case.

The other possibility is to assume the presence of *loose* spins located between FM and NM layers. This is depicted in Fig. 8.18 where each of the possible electron paths leading to spin-dependent scattering are specified. At low applied magnetic fields, where there is partial antiparallel alignment of the weakly coupled or non-coupled FM layers, the resulting GMR curve will be a result of FM→SPM (or SPM→FM) and FM→FM transitions, whereas at higher fields, where the FM layers and SPM regions are strongly aligned (above the magnetic saturation field), only FM→SPM and SPM→FM transitions remain effective. The intermixing between the Co and ITO layers could potentially result in the formation of such interfacial loose-spin regions, adding to the magnetic frustration throughout the FM Co layers, and thus the overall low values for GMR.

Therefore, it is hard to convince oneself that the layers in these multilayer structures are strictly continuous. If the interfacial layers were continuous, it is difficult to understand how the surface spins can be decoupled from the rest of the magnetic layer.

8.3.5 Annealing effects on stack magnetoresistance

We have found that the electrical properties of ITO are very sensitive to the temperature at which it is grown (chapter 4). Our studies show that an increasing growth temperature results in ITO films with lower resistivity (due to increasing carrier concentration and mobility), and is in agreement with others who have found similar trends [36]. In an attempt to improve the electrical conductivity of the ITO such as to reduce the resistivity mismatch between Co and ITO, a $[Co(1.20nm)/ITO(3.00nm)]_{20}$ stack was annealed using a heater temperature of 300 °C under UHV conditions for 2 hours. Total stack resistivity at 10 K was reduced from $7.2\times10^{-4}\Omega$cm for the as-deposited stack to $2.1\times10^{-4}\Omega$cm upon annealing, yet still follows the path of a semiconducting system over a range of temperatures. However, as we anticipated, there has been significant interdiffusion between the Co and ITO layers, as confirmed by LAR measurements before and after annealing treatment.

The LAR spectra shown in the inset of Fig. 8.19 (a) show reduced clarity in the Keissig fringes and major reduction in the Bragg peak intensities. In fact, the second Bragg peak has disappeared in the case of the annealed sample. This clearly indicates interdiffusion as a reduction in Bragg peak intensity would normally signify a change in density. The density of Co (8.79 g cm^{-3}) is larger than that of ITO (7.11 g cm^{-3}), and upon mixing, is likely to have increased the density of ITO. The improved conductive properties are likely to be due to both the improved crystalline quality of the ITO layers as well as the probable creation of metallic Co conducting paths which run through the ITO layers.

Annealing resulted in a significant reduction in the GMR from 0.25% to 0.05% [Fig. 8.19 (b)]. The reduction in GMR is likely to be due to the destruction of the interfaces upon annealing. The total saturation magnetisation also fell upon annealing, and again is likely to be linked to the breakdown of the interfaces

8.4 Summary and Conclusions

We have systematically studied the transport and magnetic properties of Co/ITO multilayers as a function of the number of Co/ITO repeats and semiconducting ITO spacer layer thickness. We have shown that alternating Co and ITO layers can produce a giant magnetoresistance effect which persists above room temperature. The magnetic hysteresis loops imply a significant contribution arising from superparamagnetic particles along with a ferromagnetic phase. Using a simple magnetic model where we have included the contribution made by superparamagnetic particles, we were able to separate the different magnetic phase constituents. The occurrence of multiple magnetic contributions in our multilayers suggests that there is a high degree of magnetic frustration throughout the ultrathin Co layers. As the thickness of the non-magnetic ITO

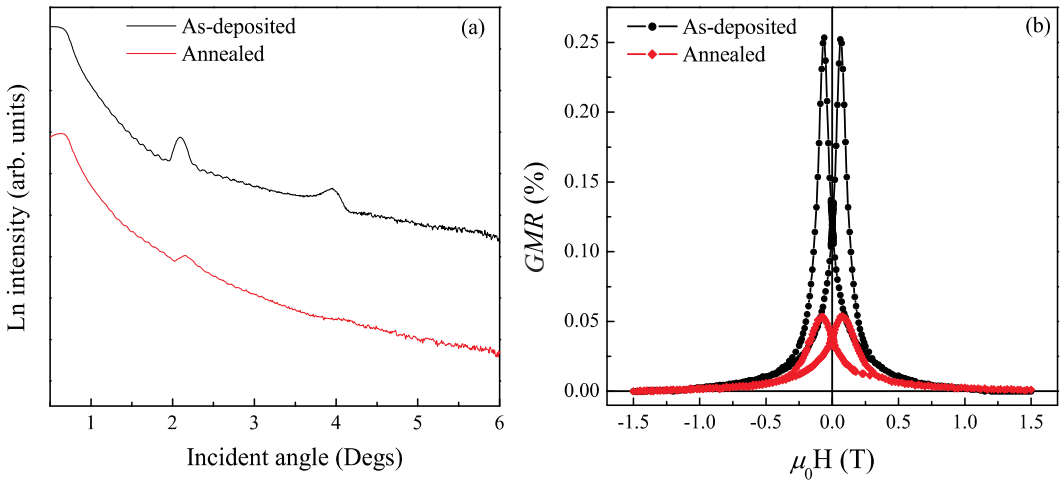

Figure 8.19: (a) LAR measurements for an as-deposited (black) and annealed (red) (T_{Ann} = 300°C) [Co(1.20nm)/ITO(3.00nm)]$_{20}$ stack. (b) corresponding GMR curves for the same stacks at 10 K.

is varied between 1.20 - 4.20 nm both the magnetisation saturation field and GMR oscillate with the ITO thickness implying RKKY interaction.

The quality of the Co/ITO interfaces and layers is still unknown. Due to high levels of spin disorder within the thin Co layers, it is highly likely that there is a significant amount of spin-independent/flipping scattering at the Co/ITO interfaces. This results in the interfacial spin-dependent scattering averaging to zero, thus giving little or no contribution to the GMR. High resolution cross-section TEM would certainly shed some light on the situation. The possibility of magnetically isolated SPM islands within the magnetic layer plane and SPM loose-spins present at the interfaces between the FM and NM layers has been discussed, however, locating these regions is difficult.

Bibliography

[1] M. N. Baibich, J. M. Broto, A. Fert, F. Nguyen Van Dau, F. Petroff, P. Etienne, G. Creuzet, A. Friederich, J. Chazelas, Phys. Rev. Lett. 61, 2472, (1988).

[2] P. Grunberg, R. Schreiber, Y. Pang, M. O. Brodsky, and H. Sowers, Phys. Rev. Lett. 57, 2442, (1986).

[3] S. S. P. Parkin, N. More, K. P. Roche, Phys. Rev. Lett. 64, 19, 2304, (1990).

[4] S.S.P. Parkin, Phys. Rev. Lett., 67, 3598, (1991).

[5] S.S.P. Parkin, R. Bhadra, K. P. Roche, Phys. Rev. Lett. 66, 2152 (1991).

[6] A. Paul, T. Damm, D. E. Burgler, S. Stein, H. Kohlstedt, P. Grunberg, J. Phys. : Condens. Matter, 15, 2471-2491, (2003).

[7] N. F. Mott, Proc. R. Soc. A 153, 699, (1936).

[8] A. Fert, P. Grunberg, A. Barthelemy, J. Magn. Magn. Mater. 140, 1, (1995).

[9] R. E. Camley, J. Barnas, Phys. Rev. Lett. 63, 664-667, (1989).

[10] P. M. Levy, S. F. Zhang, A. Fert, Phys. Rev. Lett. 65, 1643-1646, (1990).

[11] T. Valet and A. Fert, Phys. Rev. B 48, 7099, (1993).

[12] P. Bruno, C. Chappert, Phys. Rev. Lett. 67, 1602-1605, 2592, (1991); P. Bruno, C. Chappert, Phys. Rev. B. 46, 261-270, (1992).

[13] P. Lang, L. Nordstrm, R. Zeller, P.H. Dederichs, Phys. Rev. Lett. 71, 1927-1930, (1993); L. Nordstrm, P. Lang, R. Zeller, P.H. Dederichs, Phys. Rev. B. 50, 13058-13061, (1994).

[14] P. Bruno, J. Magn. Magn. Mater. 121, 248-252, (1993); P. Bruno, J. Phys.: Condens. Matter. 11, 9403-9419, (1999).

[15] J. C. Slonczewski, Phys. Rev. Lett. 67, 3172-3175, (1991).

[16] S. Demokritov, E. Tsymbal, P. Grunberg, W. Zinn, I. K. Schuller, Phys. Rev. B 49, 720-023, (1994).

[17] J. C. Slonczewski, J. Appl. Phys. 73, 5957-5962, (1993).

[18] I. Bakonyi, L. Pter, Z. Rolik, K. Kiss-Szab, Z. Kupay, J. Tth, L. F. Kiss, J. Pdr, Phys. Rev. B, 054427, (2004).

[19] N. Wiser, J. Magn. Magn. Mater. 159, 119 (1996).

[20] B.J. Hickey, M.A. Howson, S.O. Musa, and N. Wiser, Phys. Rev. B 51, 667 (1995).

[21] A. Cziraki, L. Peter, V. Weihnacht, J. Toth, E. Simon, J. Padar, L. Pogany, C.M. Schneider, T. Gemming, K. Wetzig, G. Tichy, I. Bakonyi, J. Nanosci. Nanotechnol. 6, 2000 (2006).

[22] T. Yu, X. Li, D. Li, S. Hao, L. Wang, Z. Zhang, G. Wu, X. Zhang, Q. Li, P. Chen, J. Magn. and Mag. Mat., 320, 2185-2189, (2008).

[23] L. Lu, G. Lu, Z. Zhang, C. Gao, T. Yu, P. Chen, Solid. State. Comm. 149, 47-48, (2009).

[24] O. Proux, J. S. Micha, J. R. Regnard, A. Traverse, B. Dieny, F. Ernult, P. Bayle-Guillemaud, J. LHazemann, L. Giacomoni, J. Phys.: Condens. Matter 15, 72377252, (2003).

[25] K. Oguz, P. Jivrajka, M. Venkatesan, G. Feng, J. M. D. Coey, J. Appl. Phys. 103, 07B526, (2008).

[26] H. Kano, K. Kagawa, A. Suzuki, A. Okabe, K. Hayashi, K. Aso, Appl. Phys. Lett. 63, 2839, (1993).

[27] K. Fuchs, Proc. Camb. Phil. Soc. 34 100, (1938).

[28] E. H. Sondheimer, Adv. Phys. 1, 1, (1952).

[29] C. H. Marrows, M. Perez, B. J. Hickey, J. Phys.: Condens. Matter 18, 243, (2006).

[30] J. Xu, M. A. Howson, B. J. Hickey, D. Greig, E. Kolb, P. Veillet, N. Wiser, Phys. Rev. B. 55, 1, (1997).

[31] D. C. Jiles, J. Magn. and Mag. Mat., 242-245, 116-124 (2002).

[32] M. Mordjaoui, B. Boudjema, M. Chabane, R. Daira, J. Computer Sci. 3(6): 399-405 (2007).

[33] J. Dubowik, B. Szymanski, F. Stobiecki, K. Roll, Phys. Stat. Sol. (a), 196, 86, (2003).

[34] S. Blundell, Magnetism in Condensed Matter, Oxford University Press, Oxford, p. 93, (2001).

[35] I. Bakonyi, J. Toth, L. F. Kiss, E. Toth-Kadar, L. Peter, A. Dinia, J. Magn. Magn. Mater. 269, 156-167, (2004); I. Bakonyi, L. Peter, V. Weihnacht, J. Toth, L. F. Kiss, C. M. Schneider, J. Optoelectron. Adv. Mater. 7, 589, (2005).

[36] H. Kim, C. M. Gilmore, A. Pique, J. S. Horowitz, H. Mattoussi, H. Murata, Z. H. Kafafi, D. B. Chrisey, J. Appl. Phys. 86, 11, (1999).

Chapter 9

Cu-buffered [Co/ITO] multilayers

We now investigate the influence of inserting an additional 1 nm thick Cu buffer layer at each Co/ITO interface within the multilayers described in chapter 8. In particular we look at how this can affect the magnetotransport behaviour of the multilayers. GMR rises immediately upon the insertion of Cu buffer layers and is attributed to interfacial doping at the Co/Cu interface. Annealing results in a large increase in GMR, believed to be a result of gradual Cu diffusion into the ITO layers which forms a graded interface between adjacent Cu and ITO layers. Further annealing at progressively higher temperatures resulted in a gradual decline in GMR as the interfaces break down.

9.1 Introduction

Following on from the results discussed in chapter 8, a new component is now added to the [Co/ITO] multilayer structure; Cu buffer layers have been inserted at each and every Co/ITO interface with a view to prevent the undesirable diffusion of magnetic impurities into the NM spacer layer. Co/Cu multilayers and interfaces are one of the most extensively studied systems and so are considered compatible for the purposes of this investigation. They have been reported to form high quality interfaces with little evidence of intermixing. However, this is very much dependent on the preparation technique used to make the multilayers. Already in chapter 8, the models described for the SPM contribution to GMR (in section 8.3.4) were originally based on Co/Cu multilayers which had been deposited using an electrodeposition process [1].

9.2 Experimental Results

A series of $[Co/Cu/ITO/Cu]_{20}$ films were prepared on unheated r-plane sapphire substrates by DC magnetron sputtering under identical conditions (chamber base pressure, sputtering pressure, target power, etc.) to those described in chapter 8 (ITO(10) composition). The deposition rate for the Cu target was 0.10 nm/W/pass at 1 rpm calibrated at 1.50±0.01 Pa. The respective layer thicknesses were 1.30±0.10 nm for Co, 3.00±0.10 nm for ITO and 1.00±0.10 nm for the additional Cu buffer layers. UHV annealing took place in the same system in which the samples were prepared at various heater temperatures (T_{Ann}). Each annealing stage lasted 1 hour.

9.2.1 Magnetotransport measurements and magnetometry

Figure 9.1 shows a selection of GMR curves for as-deposited and annealed multilayers with and without additional Cu buffers. The insertion of a 1 nm Cu buffer layer at each Co/ITO interface led to an immediate increase in GMR in the as-deposited samples, from 0.25% to 0.64% at 10 K and 0.11% to 0.44% at room temperature (Fig. 9.2, dotted encasing and arrow). Annealing these structures in a UHV environment led to a steady rise in the GMR signal at both 10 and 290 K. A maximum GMR of 2.18% at 10 K was measured after using a heater temperature of 300°C. Further annealing led to a gradual decline in GMR. These results are summarised in Fig. 9.2.

Similar results were obtained in Co/Cu multilayers after annealing, however, a sharper fall in GMR was observed for $T_{Ann} > 400$°C until GMR was completely destroyed when annealed above 700°C [2]. Khalyapin *et al.* however, observed an immediate drop in GMR in their Co/Cu multilayers if annealed at $T_{Ann} = 100$°C for just 15 minutes [3]. Annealing for a longer period of 1.5 hours resulted in a complete disappearance of the GMR. My preliminary results on Co/Cu multilayers also show an

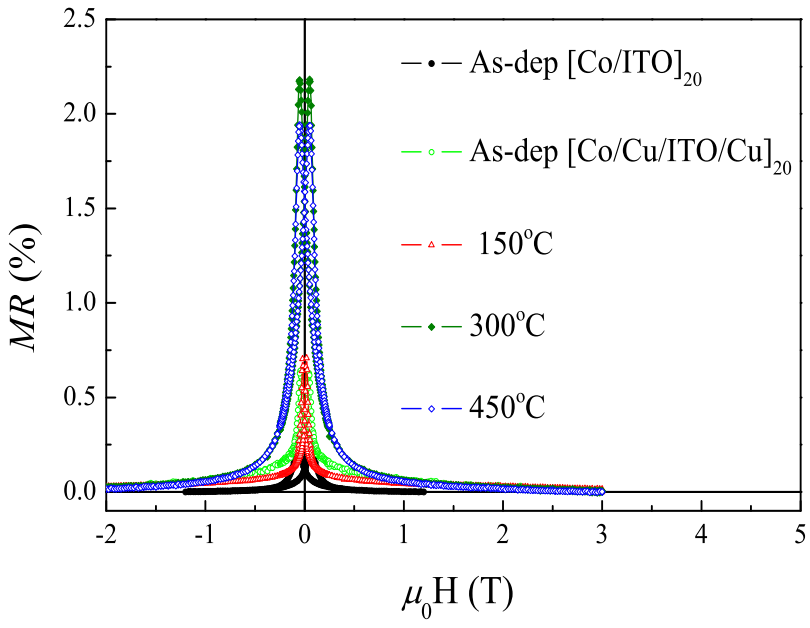

Figure 9.1: Magnetoresistance curves for an as-deposited $[Co/ITO]_{20}$ (from chapter 8) and as-deposited $[Co/Cu/ITO/Cu]_{20}$ multilayers at 10 K and corresponding magnetoresistance curves for Cu-buffered multilayers which have been annealed at various T_{Ann}.

immediate fall in GMR upon annealing for 1 hour using $T_{Ann} = 100°C$.

Any contributions from AMR were dismissed having rotated the in-plane field by 90° with respect to the current as was performed for the [Co/ITO] multilayers in chapter 8.

Magnetometry measurements show that the absolute moment of the Cu-buffered multilayers increases gradually upon annealing up to a heater temperature of 300°C, after which it saturates. This suggests that the magnetic properties of the Co layers do not degrade upon annealing. A test on a capped 5 nm film of pure Co was carried out where we simply measured the magnetisation before and after UHV annealing of a film grown under identical conditions to those described for the multilayers. Similarly, the 5 nm Co film was annealed at three different heater temperatures (150, 300 and 450°C). After the first annealing stage, the saturation magnetisation increased by approximately 14%, after which it saturated even after two further anneals. In the [Co/ITO] multilayer stacks where no Cu buffer was present (chapter 8), annealing led to a reduction in the saturation magnetisation, likely to be due to the promotion of intermixing as a result of oxygen diffusion from the ITO towards the Co layer. In the scenario where Cu is present, we believe that the Cu buffer layer acts as a barrier to prevent oxygen from reaching the Co layer and vice versa.

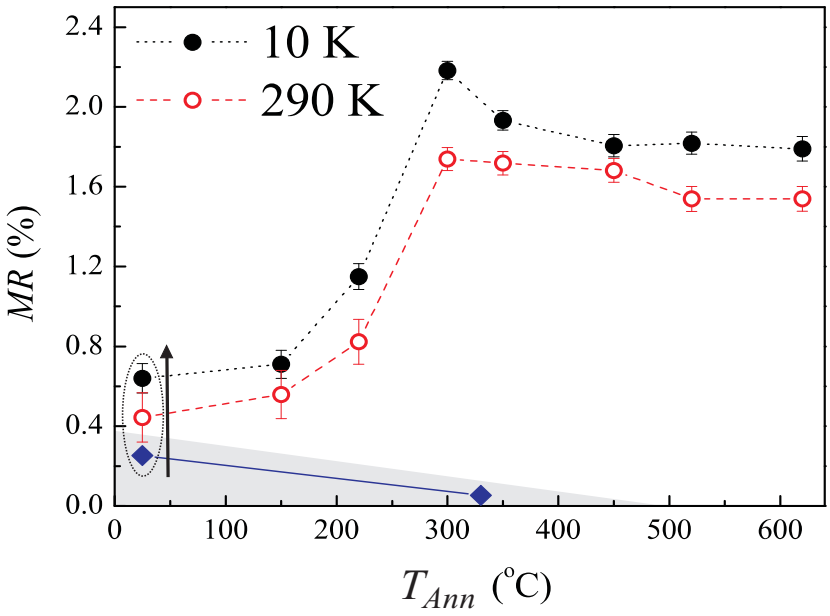

Figure 9.2: Magnetoresistance as a function of T_{Ann} in $[Co/Cu/ITO/Cu]_{20}$ multilayers at both 10 K (solid black circles) and 290 K (open red circles). The shaded region shows the magnetoresistance measured in $[Co/ITO]_{20}$ multilayers for an as-deposited sample and after annealing at $T_{Ann} = 300°C$ (solid blue circles). The arrow shows the increase in magnetoresistance upon addition of the Cu buffers.

9.2.2 Structural properties

The dramatic decrease in GMR upon annealing of the $[Co/ITO]_{20}$ multilayers (chapter 8) was attributed to the subsequent breakdown of Co/ITO interfaces, confirmed by the observation of suppressed Bragg reflection peaks and Keissig fringes by LAR measurements. This was considered sufficient evidence to suggest that there was some level of interdiffusion between Co and ITO layers resulting in a more granular system.

θ-2θ scans [Fig. 9.3 (a)] for the Cu-buffered multilayers revealed that the as-deposited stacks were amorphous, however, on annealing, they became increasingly crystalline demonstrated by the emergence of a strong ITO (222) peak which becomes stronger as the annealing temperature increases [Figs. 9.3 (b) and (c)]. There were no Bragg peak reflections which were identified as belonging to Cu or Co after any of the annealing stages. The average lattice parameter of the ITO estimated at each stage of annealing was 1.010 nm, which is relatively small compared to the typical value of 1.012 nm for ITO. This suggests that ITO grown on top of Cu and Co is highly strained. A systematic shift towards lower incident angles of the ITO (222) would have implied a systematic change in lattice parameter, providing clues regarding the possible diffusion between Cu and ITO. Unfortunately, no information regarding this issue could be obtained from our scans.

Figure 9.4 shows the LAR pattern obtained for an as-deposited and annealed $[Co/Cu/ITO/Cu]_{20}$ multilayer. In the as-deposited samples, there are no signs of Kies-

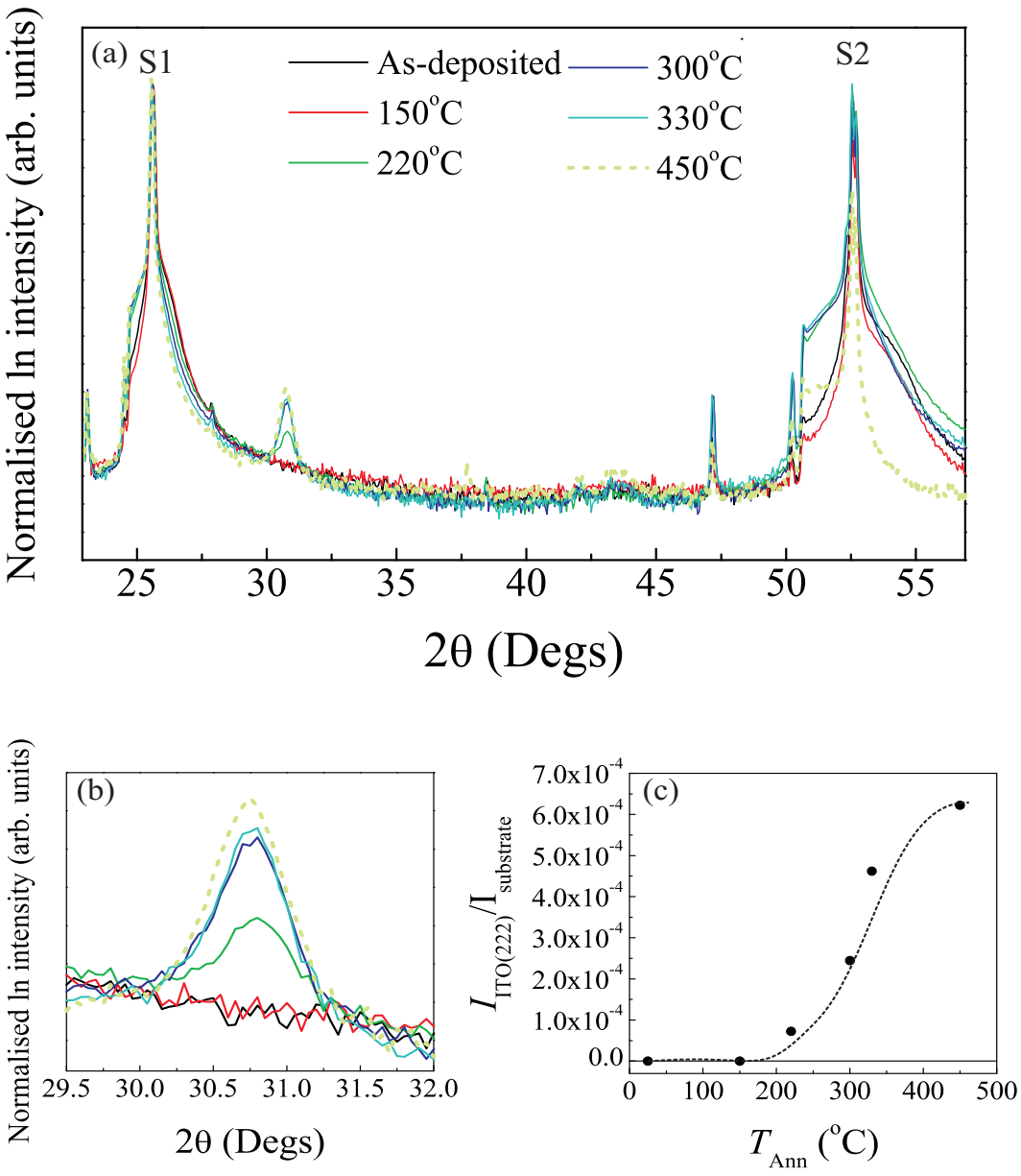

Figure 9.3: Effects of heater temperature on $[Co/Cu/ITO/Cu]_{20}$ multilayers, (a) θ-2θ diffractograms, (b) expanded view of the θ-2θ diffractograms at the ITO (222) reflection peak, and, (c) ITO (222) reflection peak intensity normalised to the first substrate peak (S1).

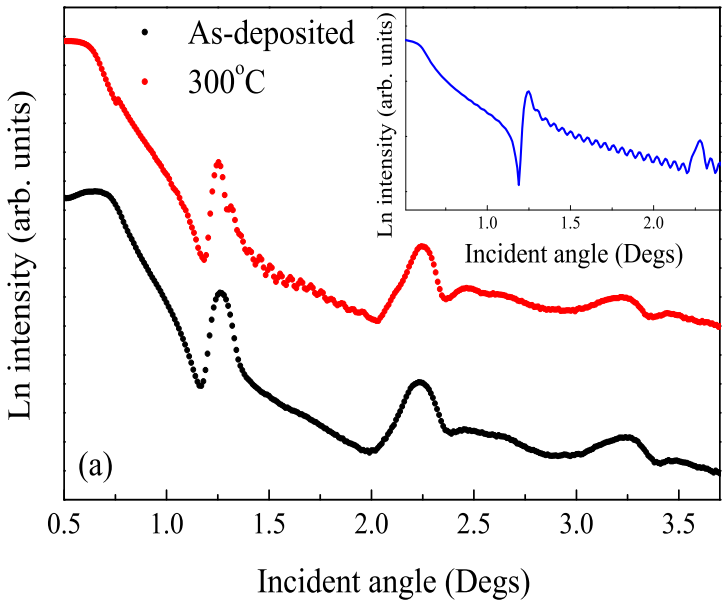

Figure 9.4: Low-angle reflectivity scans for an as-deposited (black circles) and annealed (300°C) (red circles) $[Co/Cu/ITO/Cu]_{20}$ multilayer. Inset: simulated data of the $[Co/Cu/ITO/Cu]_{20}$ multilayer.

sig fringes, however, there are pronounced first, second and third order Bragg reflection peaks, a good indicator of a well-defined multilayer structure. It is not until the third annealing stage (300°C) that Keissig fringes become clear and the LAR pattern observed resembles the simulated pattern (Fig. 9.4, inset). Further annealing resulted in the gradual disappearance of the Keissig fringes.

9.2.3 Discussion

To investigate what may be happening upon annealing in these multilayers, a series of Cu-doped (3.3 - 16.0 at.%) ITO(10) and undoped ITO(10) thin films were grown. These films were grown under the same conditions as the multilayers, i.e. on unheated r-plane sapphire substrates. The room temperature transport properties of these films are summarised in Fig. 9.5; the shaded regions show the changes in the transport properties having been annealed in UHV using a heater temperature of 300°C. Surprisingly, the transport properties of ITO deteriorated upon Cu doping in the room temperature as-grown samples where we see a rise in total film resistivity, a fall in carrier mobility and minimal changes in carrier concentration with increasing Cu doping levels. All as-grown Cu-doped ITO films were semiconducting, as determined from standard resistance versus temperature measurements, however, the pure, undoped ITO sample showed metallic behavior. In addition, the as-grown Cu-doped ITO films were all amorphous,

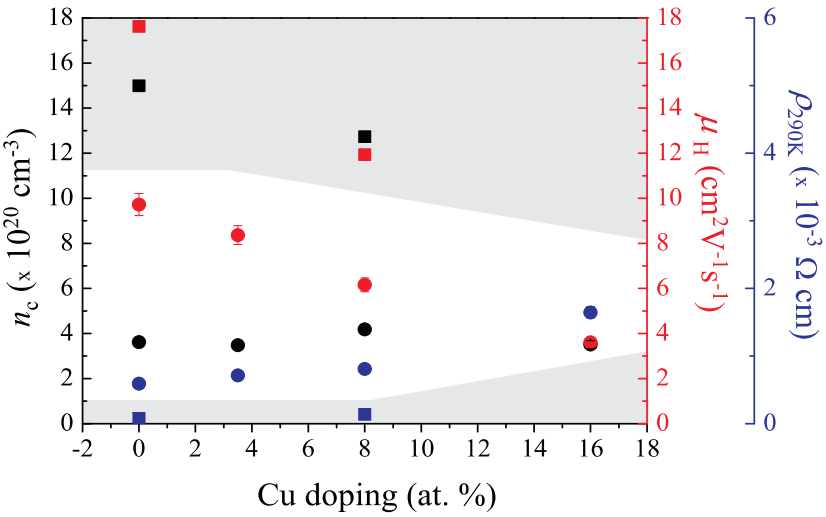

Figure 9.5: Summary of the transport properties [carrier concentration, n_c, (black circles), carrier mobility, μ_H, (red circles) film resistivity, ρ, (blue circles)] of as-deposited Cu-doped ITO(10) films grown using dc magnetron sputtering at room temperature. The shaded regions represent the values after annealing using T_{Ann} = 300°C (data points now solid squares with the same colour scheme).

whereas the pure ITO sample showed a very weak ITO (222) peak. Upon annealing, the Cu-doped ITO films become more crystalline, showing the ITO (222) peak, however, there were still no signs of any Cu peaks which implies that the Cu and ITO may have now mixed. Therefore, it is highly likely that the Cu and ITO mix upon annealing in the multilayers at heater temperatures of at least 300°C. The electrical properties of both the pure ITO and 8.0 at.% Cu-doped ITO improve upon annealing (solid squares inside the shaded region of Fig.9.5).

In the as-deposited state, the rise in GMR of the multilayers may be related to interfacial-doping of the Co interface by the additional Cu buffer layer [4, 5]. The structural quality of the stack, in particular, the roughness, plays an important role in determining the continuity across the layers. Layer fluctuations provide pathways for interdiffusion or penetration of stray atoms into unwanted regions. It has been shown in Co/Cu-based spin valves and multilayers that Cu impurities within the Co layer close to the interface can lead to a rise in GMR. Conversely, Co impurities in the Cu spacer layer strongly reduce the GMR signal if they are located close to the interface [5]. Therefore, these effects are penetration depth dependent, and so the quality of the layers in our stacks is of vital importance.

It may be possible that the mixing between the Cu and ITO layers leads to a graded interface so that an ultra-thin layer of Cu-doped ITO exists at the Cu/ITO interface. This results in improved electrical properties and the likelihood of reduced bulk scattering of electrons due to a decrease in the resistivity mismatch between

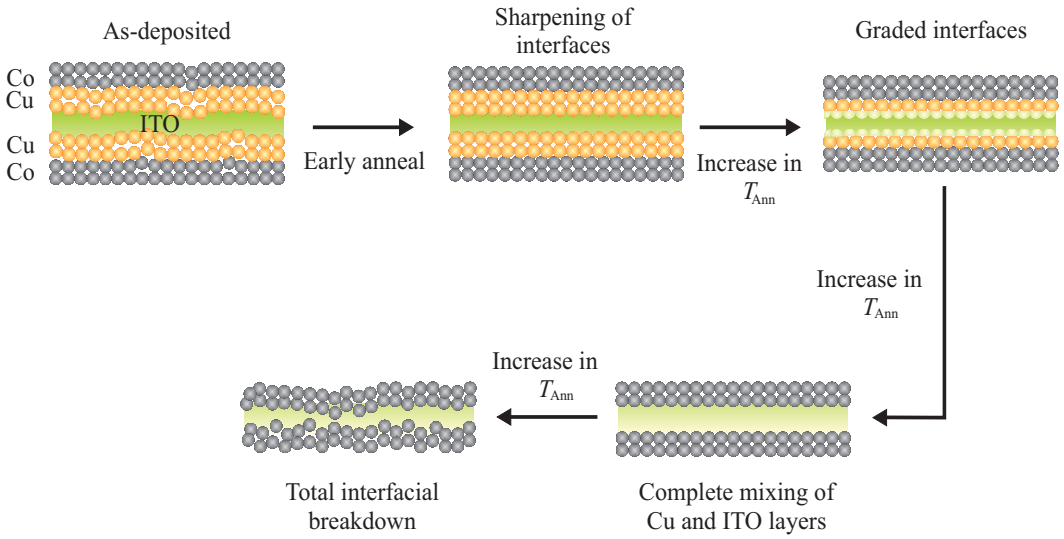

Figure 9.6: Illustrated interpretation of the influence of Cu buffer layers at the Co/ITO interface and the subsequent effects of annealing.

Cu, Cu-ITO and ITO. In addition, the annealing process results in greater crystalline quality in each layer which will undoubtedly result in greater electron transport.

From the LAR measurements, we see that the Cu-buffered multilayers have pronounced Keissig fringes only after a particular annealing temperature, which coincides with the maximum value recorded for GMR. This result is similar to Hecker *et al.* who argue that the initial rise in GMR in their Co/Cu multilayers correlates with the sharpening of the interfaces [2]. Thereafter, with further annealing, the features in the LAR measurements begin to deteriorate, as does the magnetoresistance due to the breakdown of interfaces. If the Cu/ITO interfaces have now mixed completely, it is highly likely that the Co atoms will begin to migrate towards the neighboring oxide when annealed. The Co may either remain as stray, isolated Co atoms or become clusters within the oxide layer, interacting superparamagnetically, therefore leading to spin-independent scattering, and thus a reduction in GMR. Fig. 9.6 provides an illustrative summary of these points.

9.3 Summary and Conclusions

The combination of interfacial-doping at the Co/Cu interface and the creation of the graded Cu/Cu-ITO interface along with improved magnetic properties of the Co layers upon annealing leads to enhanced GMR signal in Cu-buffered $[Co/ITO]_{20}$ multilayers. Further annealing leads to a breakdown of the interfaces and a reduction in the measured GMR signal.

This work still has a great deal of unanswered questions particularly regarding the

state of the interfaces at each annealing stage. Therefore, the conclusions we make here are speculative and based only on the limited knowledge we have available to us at the current time.

Bibliography

[1] I. Bakonyi, J. Toth, L. F. Kiss, E. Toth-Kadar, L. Peter, A. Dinia, J. Magn. Magn. Mater. 269, 156-167, (2004); I. Bakonyi, L. Peter, V. Weihnacht, J. Toth, L. F. Kiss, C. M. Schneider, J. Optoelectron. Adv. Mater. 7, 589, (2005).

[2] M. Hecker, J. Thomas, D. Tietjen, S. Baunack, C. M. Schneider, A. Qiu, N. Cramer, R. E. Camely, Z. Celinski, J. Phys. D: Appl. Phys. 36, 564, (2003).

[3] D. L. Khalyapin, P. D. Kim, J. Kim, I. A. Tupanov, A. Y. Beten'kova, G. V. Bondarenko, T. N. Isaeva, I. Kim, Physics of the Solid State, 52, 1787, 9, (2010).

[4] M. Perez, C. H. Marrows, B. J. Hickey, Europhys. Lett., **54**, 262-268, (2001)

[5] C. H. Marrows and B. J. Hickey, Phys. Rev. B, **63**, 220405(R), (2001)

Chapter 10

Estimating the Spin Diffusion Length of Semiconducting Indium Tin Oxide

This chapter is concerned with exploring the feasibility of integrating ITO within spintronic devices. We begin by introducing semiconducting ITO thin films into conventional spin valve structures and provide an overview of the steps involved to fabricate current-perpendicular-to-plane nanopillar junctions. From this we have estimated the room temperature spin diffusion length of semiconducting ITO. The next stage involves the insertion of two thin Cu buffer layers on either side of the ITO spacer layer in the spin valve resulting in a marked improvement in the GMR. Finally, we attempt to substitute the metallic ferromagnet in the spin valve structure with a dilute magnetic oxide.

10.1 Introduction

In FM/NM multilayers and spin valves (SV) with FM/NM/FM structure, the magnitude of the GMR strongly depends on the spin scattering asymmetries of the FM layer and FM/NM interfaces as well as the length over which an electron spin information is conserved throughout the NM spacer layer [1]. The electron spin diffusion length of the NM spacer, λ_{sdl}, in thin films is a fundamental measure of spin conservation and ultimately determines the performance of magnetic sensor-based devices. Valet and Fert produced a phenomenological model (VF model) which describes CPP-GMR from Boltzmann's equations [1]. As explained in the VF model of CPP-GMR, spin polarised currents flowing perpendicularly to the layers induce spin accumulation effects and the final result is that the length scale governing the thickness dependence is λ_{sdl}.

Finding an all-purpose NM semiconducting oxide to build spintronic devices is the first and most difficult challenge. The material should have high electron carrier mobility and bipolar transport properties. In addition, it should be structurally and chemically compatible with the neighbouring layers. As we have shown in chapters 5 through 7, further doping of ITO with various transition metals has now been widely studied with reports of ferromagnetism above room temperature. However, in addition to ferromagnetism at room temperature, practical implementation of FM ITO into spintronic devices requires minimal interfacial spin scattering and long λ_{sdl}. The observation of oscillatory GMR in $[Co/ITO]_{10}$ multilayers in chapter 8 at room temperature and spin injection in CoFe-ITO based junctions [2] indicates a coherent transfer of spin information through thin layers of ITO; however, the length scale over which efficient spin information can be transmitted through ITO is still unclear with little understanding of the spin dynamics at the FM/ITO interface. Provided that the spin polarisation is maintained across the ITO layer, a spin valve effect is expected: polarised carriers injected from one electrode reach the other electrode and the resistance of the heterostructure depends on the relative orientations of the electrode magnetisation.

10.2 Spin Valves

10.2.1 Spin Valve structures

The fields required to rotate the magnetic moments from parallel to anti-parallel (or vice-versa) in chapters 8 and 9 are relatively large and unsuited for use in magnetic memory applications. Dieny *et al.* provided a solution to this dilemma [3]. Instead of relying on interlayer exchange coupling to achieve parallel/antiparallel magnetisation configurations, Dieny *et al.* employed a structure where two FM layers were *decoupled* from each other via the use of a relatively thick NM spacer layer. In this scenario, the saturation fields could effectively be reduced to that of the individual FM layers.

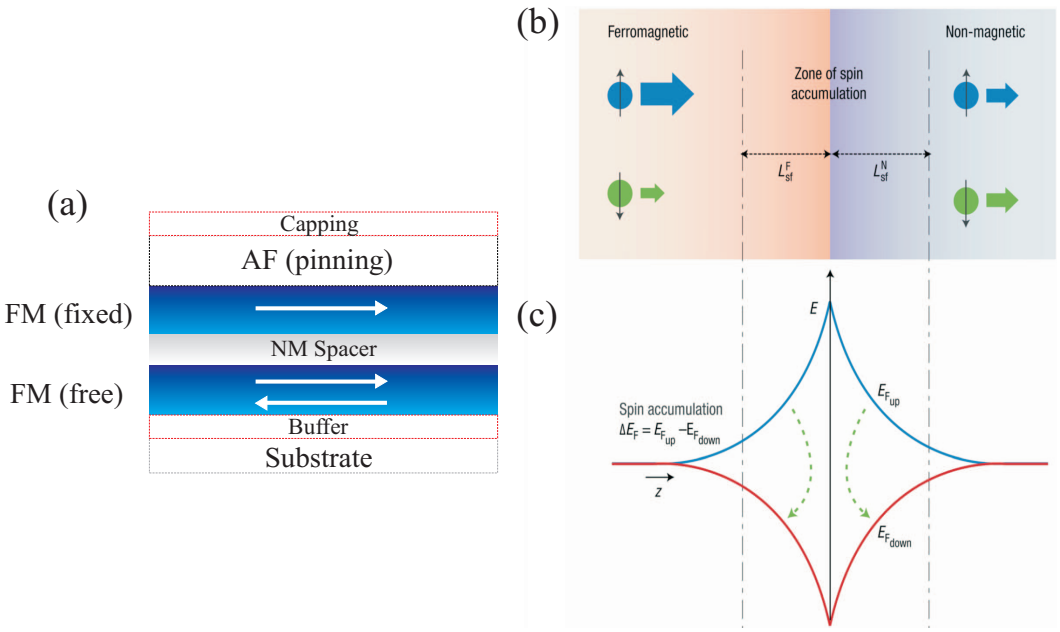

Figure 10.1: (a) Schematic illustration of a typical spin valve structure. The core components are those of the fixed and free ferromagnetic layers either side of a non-magnetic spacer. Those layers outlined with dotted lines are additional components to the structure which are often utilised, however, are not used in this study; (Right) Simplified representation of the spin accumulation at an interface between a ferromagnetic metal and a non magnetic layer assuming no interfacial resistances, (b) Incoming and outgoing spin-up and spin-down currents (c) Splitting of the chemical potentials, E_{Fup} and E_{Fdown}, in the interface region (spin accumulation). The arrows symbolise the spin flips induced by this out of equilibrium distribution. These spin-flips govern the progressive depolarisation of the current. ${L_{sf}}^F$ and ${L_{sf}}^N$ are the spin diffusion lengths of the ferromagnetic and non-magnetic layers, respectively. (b) and (c) taken from reference [5].

This structure is illustrated in Fig. 10.1 (a) and is known as a simple spin-valve (SV). Differential scattering of electrons in FM layers gives rise to a GMR signal in these heterostructures in much the same way as the multilayers.

There are a number of variations on the SV structure. If the two FM layers are made of different materials (a pseudo-spin-valve) the different coercive fields can be exploited: the softer FM layer can switch its magnetisation with a relatively small applied field, with the magnetisation of the harder material unaffected. This gives rise to the antiparallel state with higher resistance. In this case the spacer layer is relatively thick, and is used to decouple the ferromagnetic layers to prevent them from switching at the same field. A detailed review of CPP SVs can be found in reference [4].

10.2.2 Spin accumulation effects

Spin accumulation effects govern the propagation of a spin-polarised current through any succession of magnetic and nonmagnetic materials. Figures 10.1 (b) and (c) provide a simplified illustration of the principles behind spin accumulation which occurs when electrons cross a FM/NM interface. In Fig. 10.1 (b) the incoming electrons are predominantly of the spin up direction whereas the outgoing electrons are carried equally by both up and down spins. As a result, there is an accumulation of spin up electrons at the interface which diffuses on both sides of the FM/NM interface to a distance of the order of the λ_{sdl}. This process can also be described in terms of the splitting of spin up and spin down Fermi energies [see Fig. 10.1 (c)]. The imbalance of electron distribution in the spin accumulation zone generates spin-flips and provides the mechanism for the adjustment between the incoming and outgoing spin currents. The spin polarisation of current decays exponentially as it travels through the spin accumulation zone.

To summarise, there is a broad zone of spin accumulation which extends on both sides of the ferromagnetic layer to the distance of λ_{sdl} and in which the current is progressively depolarised by the spin-flips generated by the spin accumulation.

10.2.3 Controlling Spin Valve performance

To review all the work performed on SV structures in recent years would be outside the scope of this thesis. The intense research surrounding this area is naturally boosted by the huge prospects and potential of employing these structures in magnetic storage technology and miniaturised devices. Below is a summary of some of the important parameters which can influence the GMR performance of the spin valve structures.

If the magnetic layers are made thinner, it has been reported that the GMR decreases [6] and is found for multilayer and spin valve structures.

A discussion on multilayer or stacked structure systems would never be complete without considering the quality of the microstructure at the interfaces. As we have already discussed in chapter 8, rough samples are generally accompanied by the presence of interfacial mixing. This is particularly relevant for sputtered films, where grain boundaries may act as transport channels for diffusion across different layers. In general, the scenario where there is interfacial intermixing leads to a situation where momentum scattering (spin-independent scattering) dominates leading to a reduction in device performance.

An ideal spin valve structure will have FM layers which are totally decoupled from each other, but due to microstructural defects and imperfections in the FM layers or at the interfaces, this is never achieved in practice. Magnetic bridges or pinholes result as a consequence of these imperfections leading to FM coupling between the layers. Stray fields emanating from domain walls of a FM layer can act as local barriers to

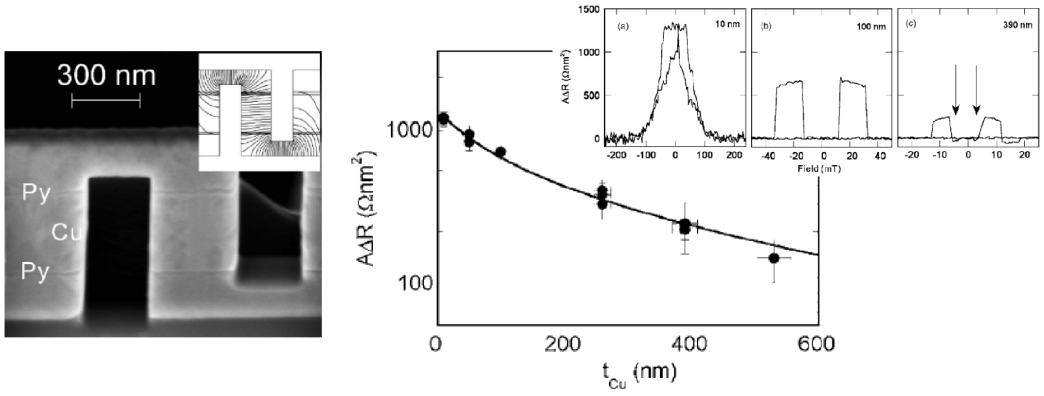

Figure 10.2: An SEM micrograph of a Py/Cu/Py spin valve (inset shows a finite element simulation of the equipotential lines across the device). The right hand panel shows the compiled GMR results of all the devices with a Valet-Fert model fit (solid line). The inset shows typical CPP GMR curves of a selection of spin valves with differing Cu spacer layer thickness. After reference [7].

the wall motions in the adjacent FM layers, resulting in coupling between FM layers across spacer layers.

10.3 Previous Work

The use of CPP measurements on sub-micron nanopillar spin valves to estimate the spin diffusion length of a non-magnetic spacer layer material has been done in the past. Through measurements of $Ni_{80}Fe_{20}$(Py)/Cu/Py CPP spin valves, Leung *et al.* used this technique to estimate the spin diffusion length of Cu at 77 K to be 600±245 nm [7] (see Fig. 10.2).

Investigations into the spin diffusion lengths of oxide materials are fairly scarce. Recently Pallecchi *et al.* have estimated the spin diffusion length of Cu_2O to be approximately 40 nm at 10 K [8]. The investigators tried to solve this problem in two ways using two different trilayer spin valve structures: an $La_{0.7}Sr_{0.3}MnO_3$(LSMO)/Cu_2O/Co trilayer, and an all-oxide LSMO/Cu_2O/LSMO trilayer. Measurements involving the all-oxide structure proved unsuccessful as it was difficult to attribute the magnetoresistance features to genuine spin transport across the Cu_2O layer. The estimation for the spin diffusion length was made using the LSMO/Cu_2O/Co trilayers (using Cu_2O thicknesses of 5, 50, 75 and 100 nm). Figure 10.3 shows typical magnetoresistance curves obtained for a LSMO/Cu_2O(50 nm)/Co trilayer over a range of temperatures. A rather interesting observation made by the authors is that the spin diffusion length of Cu_2O is relatively insensitive to the temperature and claim that this is more to do with the fact that the LSMO has a reduced spin polarisation efficiency at higher temperatures as it approaches its ferromagnetic Curie temperature.

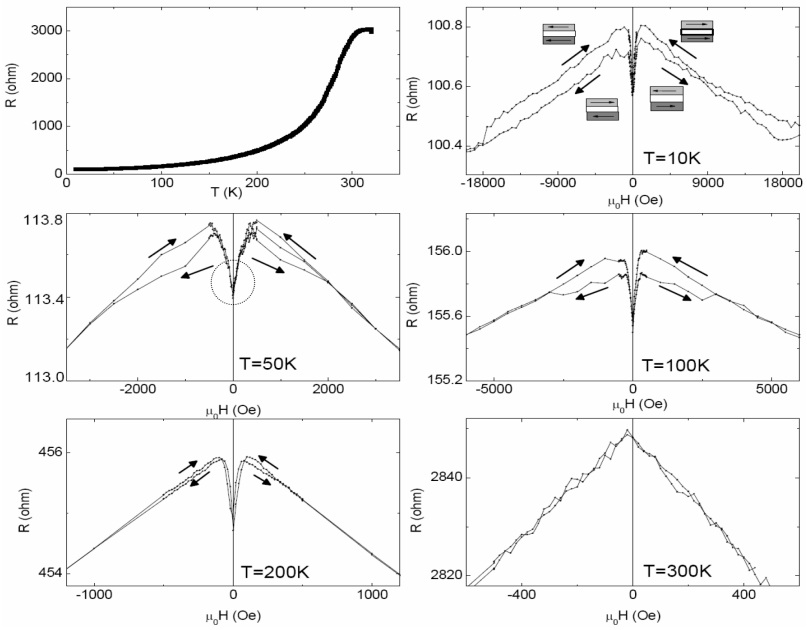

Figure 10.3: Upper panel: resistance versus temperature across a LSMO/Cu_2O/Co trilayer with Cu_2O thickness of 50 nm. The other panels show the resistance versus magnetic field across the trilayer at different temperatures. Arrows indicate the direction of the field sweep. The dotted circled area indicates the contribution to the GMR from AMR. After reference [8].

Ghosh *et al.* have used time-resolved optical techniques to explore electron spin dynamics in bulk and epilayer samples of *n*-type ZnO as a function of temperature and magnetic field [9]. In the bulk sample, the spin coherence time extends to very long times at low temperatures (approximately 20 ns). In the epilayers, the spin coherence time increases with carrier concentration, but is much smaller than in the bulk. However, spin precession in the epilayers persists until room temperature (see Fig 10.4).

10.4 Fabrication of the Spin valve structures

A series of Cu(200nm)/Co(20nm)/ITO(t nm)/Co(5nm)/Cu(200nm) SV structures were prepared on unheated Si (100)/SiO_2 substrates in a UHV system by DC magnetron sputtering in 1.5 Pa of Ar. The system's base pressure before depositing was better than 1×10^{-6} Pa. Substrates with an area of 6×11 mm^2 were mounted on a circular sample table below stationary Cu, Co, and ITO targets. The total ITO thickness, t, was linearly varied between each sample in the 0 to 20 nm range by controlling the rotation speed of a substrate as it passed below the ITO target, as described in section 3.3.

There are two distinct paths that can be taken towards fabrication of nanometre-scale structures for the study of spin electronic properties: the usual top-down approach

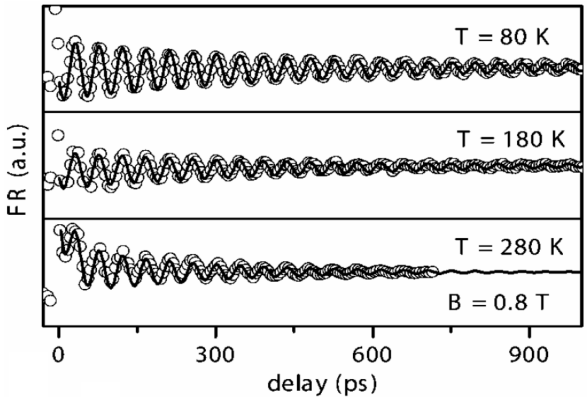

Figure 10.4: Temperature dependence of time-resolved Faraday rotation of the spin precession on a ZnO sample at three temperatures for an applied field of 0.8 T. After reference [9].

uses lithographic patterning techniques to define device structures by the removal of unwanted material and to mask the subsequent growth of different layers; the alternative bottom-up route requires directed additive assembly of subunits. The devices reported in this thesis have have been fabricated using a top-down approach, patterning thin film heterostructures using novel 3D focused ion beam (FIB) lithography. All the layers are deposited in a single UHV cycle, therefore achieving excellent interface cleanliness.

10.4.1 Patterning to micron scale tracks

Optical lithography

Optical lithography or photolithography is a process used in microfabrication to selectively remove parts of a thin film or the bulk of a substrate. It uses light to transfer a geometric pattern from a photo-mask to a light-sensitive chemical photoresist on the substrate. A series of chemical treatments and developing then engraves the exposure pattern into the material underneath the photoresist. A positive "DQN" photoresist deemed appropriate for the desired feature sizes (4 μm) was chosen. The resist is spun onto a sample and subsequently baked-out on a hot-plate to remove the solvent and to set the resin. The process of exposure to high intensity ultra-violet (UV) light results in the resist undergoing a complex chemical change. The exposed regions now become extremely soluble in alkaline solutions, compared to the non-exposed parts. Regions that were not subjected to high intensity UV light will remain stable so that only a fraction of the surface is dissolved. This leaves behind a photoresist pattern which resembles the mask.

The standard lithographic technique used for this work is outlined below and illustrated in Fig. 10.5.

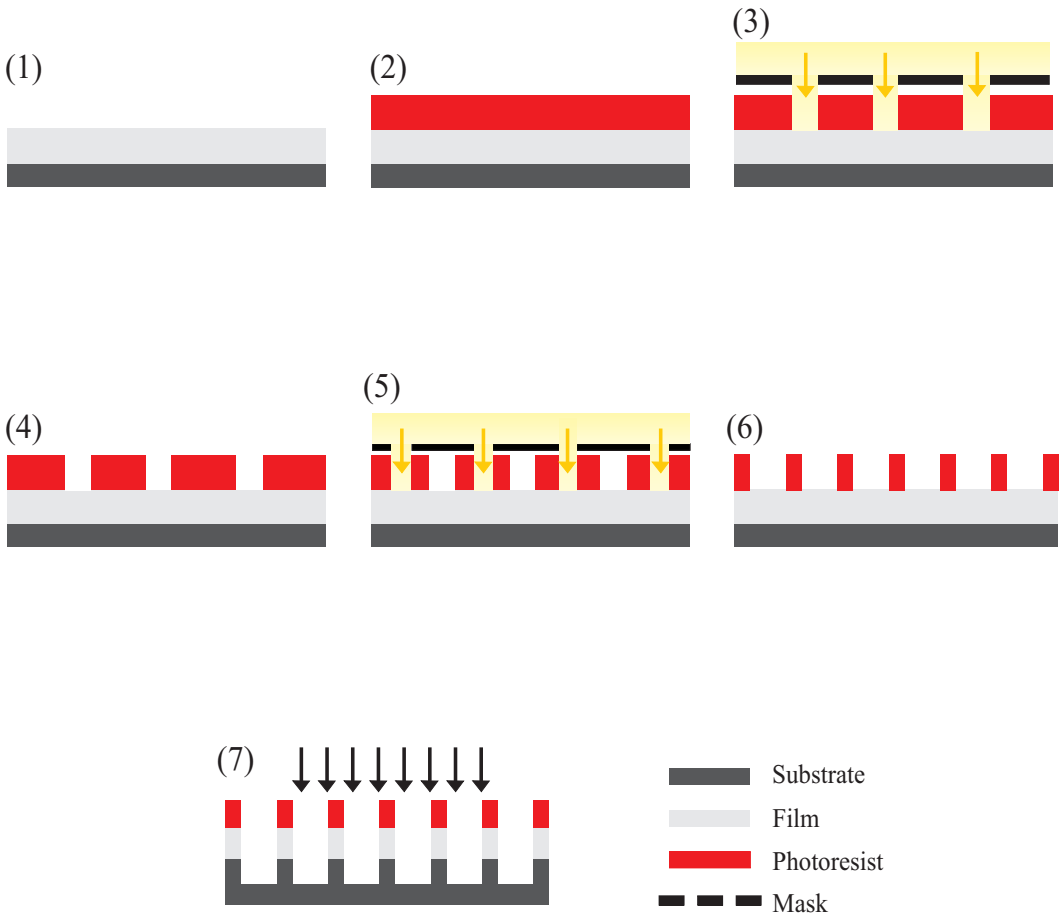

Figure 10.5: Schematic illustration of the mask pattern transfer by optical lithography to define 4 μm tracks. (1) film or layered stacks structure has been deposited onto a substrate, (2) photoresist is spun onto the substrate surface, (3) initial edge bead pattern is engraved into the resist via exposure to ultraviolet light through a mask pattern, (4) the resist is developed leaving behind a photoresist pattern on the surface of the substrate for more intricate patterning, (5) photoresist again exposed to ultraviolet light through a mask where smaller features (4 μm scale) are engraved into the resist, (6) photoresist is developed for a second time, leaving behind the final photoresist pattern on the surface, (7) Ar ion beam milling removes the material which still remains around the final pattern and the resist is removed with acetone.

1. the sample was cleaned by soaking in acetone and then isopropanol for 2 minutes and dried using a nitrogen air gun.

2. the sample was then placed on a small platform in a spinner. Photoresist was applied using a pipette to the surface of the sample, whilst actively trying to avoid any air bubbles becoming trapped (this would affect the photoresist surface quality and cause many problems in the subsequent patterning stages).

3. the sample was spun using a program set to 6000 rpm for 30 seconds. Photoresist of thickness ~ 3 μm settles around the central region of the sample. Thicker edge-beads are found around the perimeter of the sample.

4. the sample was then transferred to a hot-plate to bake for 2 minutes allowing the solvent to evaporate and the photoresist to harden.

5. using an edge-bead removal mask, the sample was then exposed to high intensity UV light for 90 seconds.

6. the photoresist was developed in an alkaline KOH:H_2O solution with a 3:2 ratio for approximately 40 seconds and subsequently rinsed in water.

7. using a high resolution mask with the final pattern the samples were exposed to high intensity UV light for a second time for 8 seconds to define the device area.

8. stage 6 was repeated but with interval inspection under a light microscope while taking paying particular attention to the 4 μm tracks: if edge-sharp the pattern was good; if the track edges were rough, faded or absent, the photoresist was removed with acetone and the entire process started again.

The mask aligner used operates in the contact mode, such that the mask is pressed against the photoresist. Therefore, it is imperative that the mask itself and the substrate are clean, i.e. any dust or excessive photoresist on the surface must be removed otherwise defects are generated in the photoresist, or, if the surface is not uniform, the undulating surface will not result in even contact from the mask, leaving behind poorly defined features.

Mask design

Two masks were used in the photolithography process, the first for the removal of unwanted photoresist edge-beads, and the second containing the high resolution device area pattern itself. Figure 10.6 (a) shows an illustration of the final mask pattern used. The pattern permits the fabrication of 14 devices on one sample [Fig. 10.6 (b)].

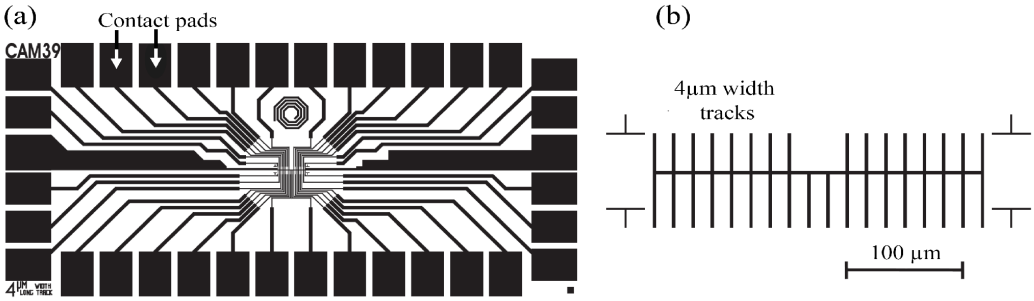

Figure 10.6: (a) CAM39 mask design used for these experiments, (b) an expanded view of the device area.

Ion milling

Ion milling is a non-selective, anisotropic process which uses high energy ions to bombard the sample surface and erode away unwanted material from a surface. In this case, it is used to remove unwanted material around the resist pattern. The resist itself is also milled away, however, its erosion rate is considerably lower than that of metal. The instrument used for these experiments was a broad-beam Ar ion miller. The typical base pressure of the system was 1×10^{-9} Torr. Electrons are emitted from an ion gun ionising a neutral gas intake of Ar to Ar^+. This ionised gas is accelerated across a potential difference of 500 V towards the surface of the sample with a pressure of 4×10^{-4} mBar. More precisely, the input gas is actually a mixture of Ar with 2 $\%O_2$. The role of oxygen is essentially to improve the etch rate of the photoresist, which results in the etch profile being more uniform, and to also aid the reduction in the redeposition of photoresist products. The average mill time used was approximately 23 minutes and was enough to effectively remove all the unwanted material around the masked photoresist pattern. After the milling was complete the remaining photoresist was removed by ultrasonically cleaning the sample in acetone for 20 seconds and finally dried with a jet of nitrogen gas.

10.5 Focused ion beam processing of devices

10.5.1 The process

The focused ion beam (FIB) system used in these experiments was an FEI200 series FIB XP 2.25 which utilises Gallium ions (Ga^+) ejected from a liquid Ga source, with a minimum spot size of approximately 10 nm [10]. The ion beam is generated from a liquid-metal (maintained in a high-vacuum of 1×10^{-5} Pa) source by the application of a large electric field. The large electric field causes the emission of positively charged ions from a liquid gallium cone, which is formed on the tip of a hot tungsten filament [11]. The ion beam energy is typically between 10 and 50 keV, with beam currents varying

between 1 pA and 10 nA. It is possible to alter the beam current, allowing both a fine beam for high-resolution imaging on sensitive areas and a high energy beam for fast and the less delicate stages of milling. Typical beam currents used in this work were 11 pA for high resolution cleaning, and 150 pA for trench milling and larger cuts. Figure 10.7 (a) shows an illustration of the focused ion beam column.

Once the sample is mounted and loaded within the chamber (pumped down to a high vacuum pressure of $< 10^{-3}$ Pa), the Ga source is switched on - this now allows images to be taken (using secondary electrons). The first stages of the operation, before any milling takes place, is to align the beam, i.e. focusing and stigmatism correction.

The physical process of the ion beam milling effect is similar to that described in the previous section. It is a site-specific technique and so allows us to define very small features (here we are fabricating devices of the order of hundreds of nanometers). The Ga^+ primary ion beam hits the sample surface and sputters a small amount of material, which leaves the surface as either neutral atoms (enabling milling) or secondary ions (enabling imaging) [see Fig. 10.7 (b)]. Milling and imaging (particularly the imaging process which exposes larger areas to the Ga beam) can result in a number of undesirable effects such as electron charging, displacement of atoms at the surface, and the implantation of Ga^+ [11]. Ion implantation can be a great problem for ferromagnets - over milling the ferromagnet, in our case Co, with a Ga^+ beam is known to severely reduce ferromagnetic Curie temperature and the spin asymmetry [13]. Therefore, it is important to optimise the processing of these devices when using a FIB microscope, otherwise we risk compromising the device performance.

10.5.2 Device fabrication

The three-dimensional technique for creating CPP devices used for these studies was developed by C. Bell *et al.* for studying the device transport properties of superconductor/ferromagnet structures [14, 15]. In the present work this specific technique is extended to produce nanoscale spin valve junctions for the characterisation of the CPP properties.

Within the chamber of the FIB microscope, a sample holder is screwed onto a sample carriage. The carriage has three degrees of freedom (z, y, and θ). In order to facilitate both top-cuts and side-cuts of the 4 μm tracks, a custom made 45° wedge holder (designed by D. J. Kang) was used, as illustrated in Fig. 10.8 (a) - (c).

The process of fabricating a three-dimensional nanopillar step device is outlined in Fig. 10.9 (a) - (d). The first stage uses a high beam current of 150 pA milling away the 4 μm track so that its width is reduced to approximately 500 - 700 nm range using an angle of $\theta = 45°$ and $\phi = 0°$. The milling is monitored closely using an end-point detection measurement. During the track thinning step, sputtered material

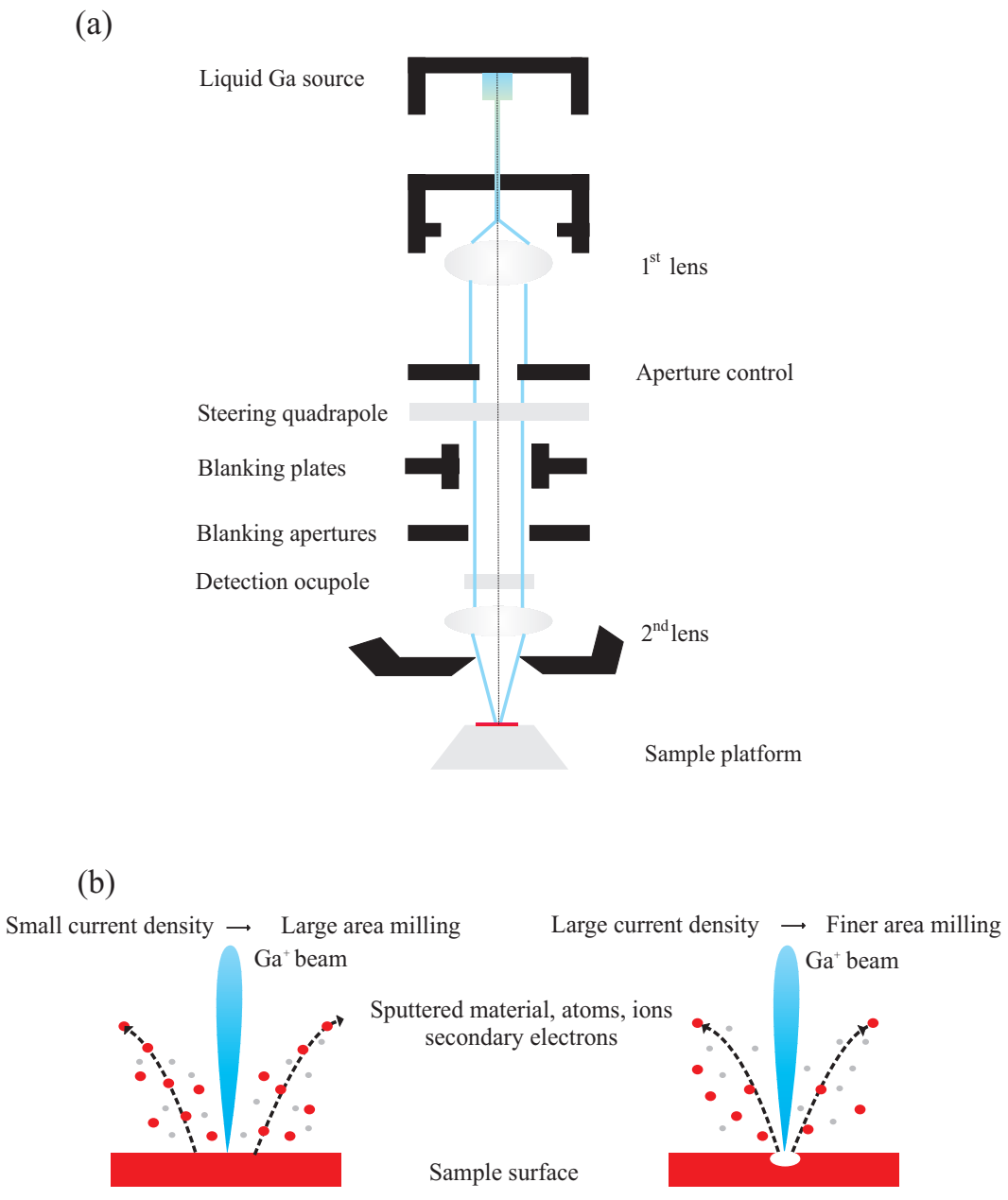

Figure 10.7: (a) Illustration of the ion beam column, adapted from reference J. W. A. Robinson thesis [12], (b) Imaging (left) and milling (right) illustrations for a focused ion beam microscope, adapted from reference [11].

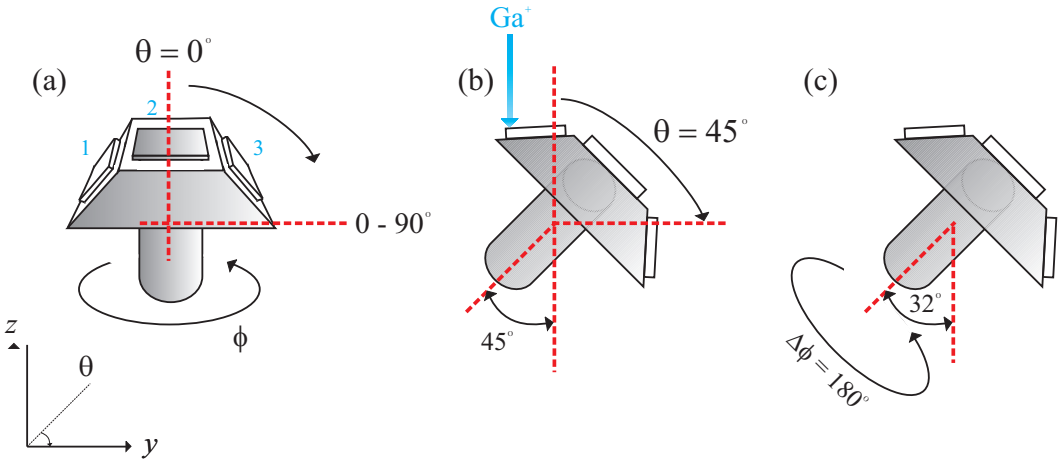

Figure 10.8: Schematic of the sample holder used in FIB; (a) the sample holder with two axes of rotation, where $0°\leq\phi\leq360°$ and $0°\leq90°$, (b) milling of a sample where θ=45° and ϕ=0°, (c) side-cuts are made with $\theta\approx32°$. Blue numbers 1-3 indicate that it is possible to mount and load 3 samples at a time for processing.

is redeposited onto the sidewalls. This redeposited material will change the electrical transport properties of the device, providing alternative current pathways. The sidewalls of the narrowed track are therefore cleaned with a beam current of 11 pA, using the standard cleaning tool which repeatedly steps in a single pixel wide line. The cleaning process will also remove excessive gallium that was implanted during the narrowing stage, where a higher beam current was used. The final track width after the cleaning treatment is then $\leq$ 500 nm (Fig. 10.10). The sample was then rotated to $\phi = 180°$, $\mu = 40°$ so that the isolated side-cuts could be made using a beam current of 11 pA, giving the final device step structure. Beam drift was a problem at this stage and had to be monitored carefully. Generally, before making any of the side-cuts, the process would be stalled for approximately 1 minute until satisfied that the beam position had stabilised. The side cuts in the device force the current vertically through the barrier, hence giving us the CPP configuration (Fig. 10.11).

The effect on the magnetic properties of thin films when patterned into nanoscale features of varying aspect ratio and shape is of course critical technologically. Tsymbal has given a theoretical approach to the influence that the aspect ratio has on the magnetostatic coupling [16]. The magnetoresistance obtained in small and narrow shapes is expected to be enhanced. Already we have discussed the findings of Kaminsky *et al.* [13] who found that direct Ga implantation can modify magnetic thin films, reducing the coercivity even to the extent that the ferromagnetism at room temperature can be destroyed. In contrast, Ozkaya *et al.* found that the coercive field of Py increased upon Ga^+ implantation, which they attribute to magnetostrictive stresses induced in the film, as well as a slight change in the composition of the Ni:Fe ratio [17]. However, Xiong *et al.* conducted very similar studies using Py, and found that objects in soft magnetic materials can be fabricated down to as low as 100 nm with no significant

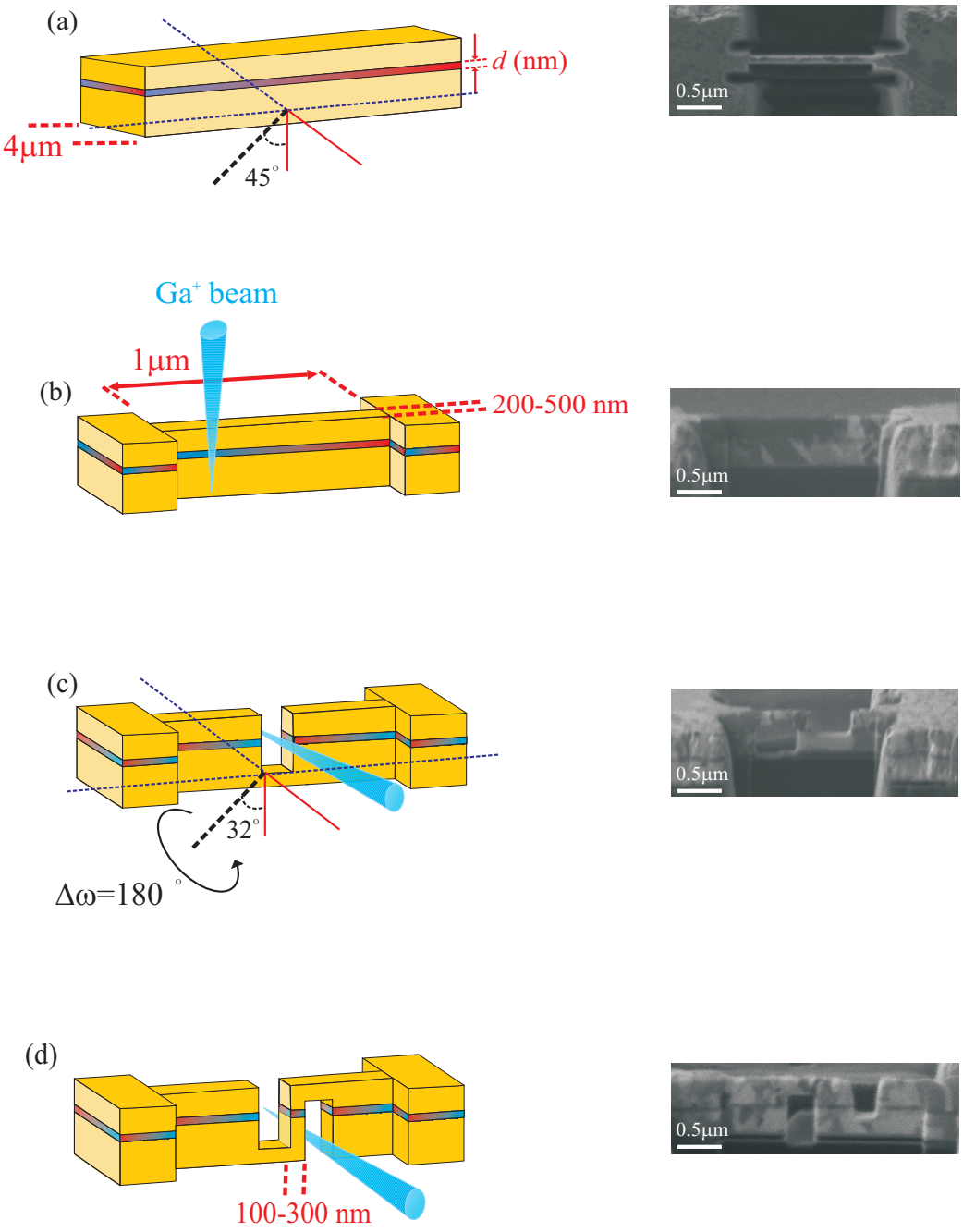

Figure 10.9: Three-dimensional FIB procedure for nanopillar device fabrication; (a) the initial micron scale track, (b) the 4 μm wide track is narrowed with a 150 pA Ga^+ beam followed by sidewall cleaning with 11 pA beam current, (c) sample stage is rotated so that the first and second (d) side cuts can be made. Adapted from references [12, 14].

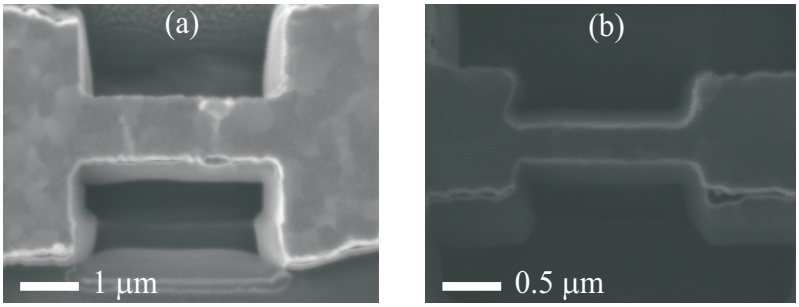

Figure 10.10: (a) Track narrowed with 150 pA (b) after further cleaning and narrowing with an 11 pA beam.

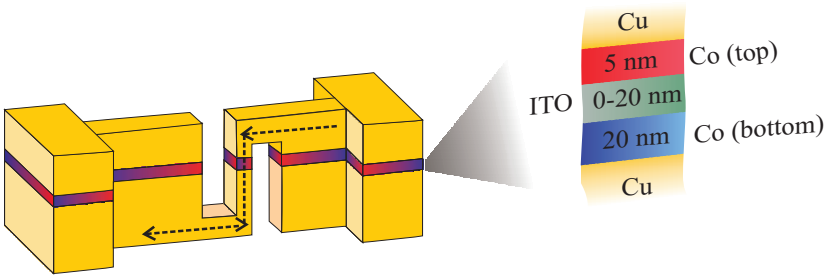

Figure 10.11: Nanopillar device structure design used for these experiments. To the right of the structure is an expanded view of the respective layers in the "active" region of the spin valve. The dotted arrows indicate the general principle of CPP-GMR measurements where the current is forced to flow perpendicularly through an isolated active region composing of two ferromagnetic layers separated by a non-magnetic spacer, via two thick Cu electrodes.

effect on the magnetic properties [18]. The FIB is also known to increase the temperature locally when milling material. Therefore, we must take great care over the exposure and milling times so as to not over-expose a particular region for a prolonged period of time. It has been quantified previously that large doses of the order of 10^{16} ions/cm^2 are required before significant removal of material begins [17]. We expect that within the time scales used for fabrication in this work, milling only damages the top most Cu electrode layer.

Wu *et al.* have simulated typical nanopillar device structures using a FEMLAB finite element simulation technique to optimise the geometry of the CPP devices [19]. The simulation models the current flow and current density of a conducting metal with a specific geometry. The current flow in the optimal nanopillar geometry is shown in Fig. 10.12 (b) and shows that it is perpendicular to the plane of the magnetic active region. Fig. 10.12 (c) also shows that the nanopillars are subject to resistive heating

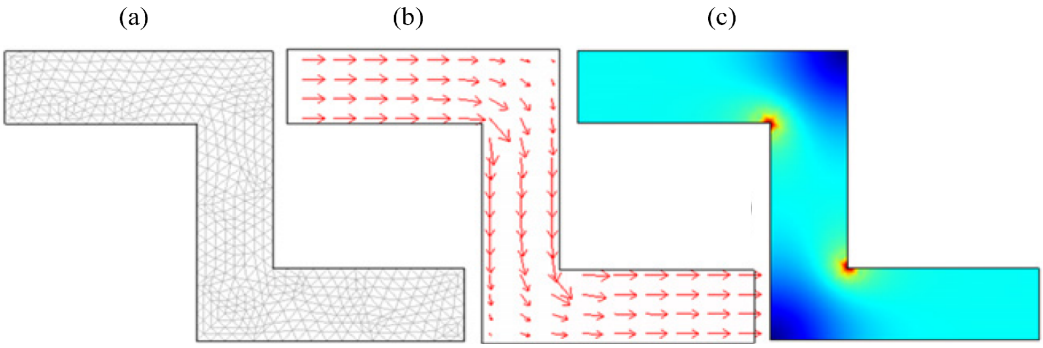

Figure 10.12: Finite element simulation of the optimized nanopillar showing (a) mesh map, (b) current flow and (c) resistive heating. After reference [19].

and subsequent damage if the applied current is too high. Magnetic and surface morphology characterisation of the structures also suggested that using 200 nm thick Cu electrode leads is the optimum (as used here in these experiments).

10.6 Experimental Results

10.6.1 Cu(200nm)/Co(20nm)/ITO(t nm)/Co(5nm)/Cu(200nm) Spin valves

Figure 10.13 (a) shows a low-angle reflectivity scan of an active region stack, consisting of Co(20nm)/ITO(3nm)/Co(5nm). Like in the case of the [Co/ITO] multilayers investigated in chapter 8, the low-angle reflectivity data suggests Co/ITO interfaces of reasonable quality.

The magnetic properties of the samples were characterised in the VSM, from which the in-plane magnetisation as a function of applied magnetic field was determined. In Fig. 10.13 (b), we plot the magnetisation loop for an unpatterned film with and ITO thickness, t, of $t = 2$ nm at room temperature. It is clear that there is no complete antiparallel state but the discernable changes in gradient close to switching do suggest a certain degree of misalignment which is dependent on the magnetic field. Generally it is difficult to discern the different switching fields given that the area over which we are examining is so large (an unpatterned film) and effects such as large magnetostatic coupling and stray fields will be dominant.

The electrical resistance of the devices were measured as a function of an applied magnetic field (μ_0H) directed along a films' magnetic easy-axis and parallel to the Co/ITO interface. Measurements were performed at room temperature and 77 K using a four-terminal lock-in technique with an AC amplitude of ± 100 μA. The current propagated through the nanopillar from the free 5 nm Co layer first. In Fig. 10.14,

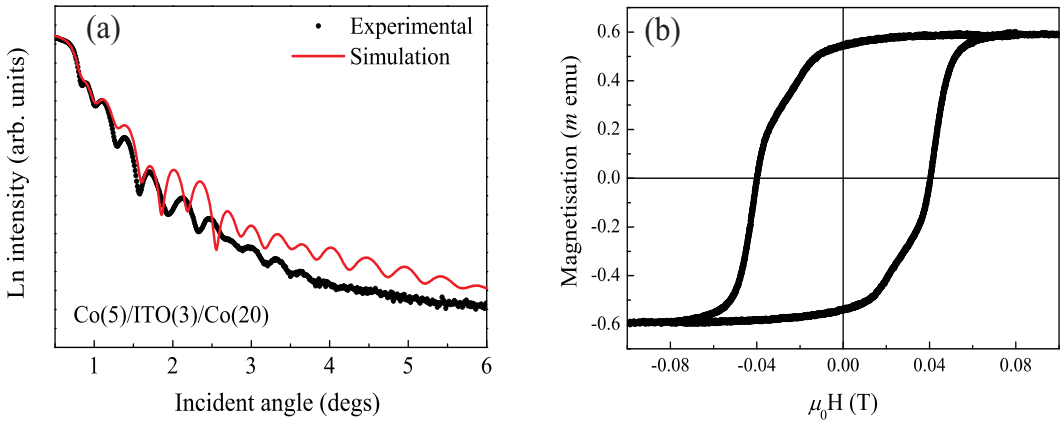

Figure 10.13: (a) Low-angle x-ray reflectivity measurement of a SV structure with t = 3 nm along with a simulated fit, and, (b) Room temperature magnetisation versus applied magnetic field for a SV structure where t = 2 nm.

we plot the typical GMR response (0.16%) of a device with t = 2 nm at room temperature (main panel). Due to the relatively large cross sectional areas of the devices, we expect an inhomogeneous magnetisation within the Co layers at low fields, which was later verified with three dimensional OBJECT ORIENTED MICROMAGNETIC FRAMEWORK (OOMMF) [20] simulations [stages (ii) and (iv) in Fig. 10.14]. The simulations were carried out assuming a nanopillar device with a cross-sectional area of 600×350 nm^2 (identical to that estimated for the actual nanopillar during the FIB processing) which has been divided into 5×5×2 nm^3 cells. The saturation magnetisation and uniaxial anisotropy for Co were set to 1400 emu cm^{-3} and 4.9×10^6 ergs cm^{-3}, respectively, and the damping coefficient was set to 0.5 as is usually done to obtain rapid convergence [21, 22]. The resulting simulated GMR loop for a SV structure with t = 2 nm is plotted on top of the experimental data for easy comparison.

We observe a close resemblance between the experimental and simulated GMR curves, with minimal differences in switching fields. The simulated GMR curve shows larger magnetostatic coupling at zero field compared to the experimental data. A possible explanation for this could be due to the uncertainties in measuring the device dimensions, which, if overestimated, can lead to significant changes in the degree of magnetostatic coupling present over the device area. Of particular interest is the magnetic configuration of the layers at low fields, since they can reveal the formation of any non-uniform magnetisation regions which may be annihilated at higher fields. These are labeled (ii) and (iv) on the GMR curves and illustrate the magnetic configuration of the two FM layers with respect to each other at an applied magnetic field of ±26 mT. Blue and red coloured regions indicate opposite orientations in the magnetisation. Here we can see that the top Co layer is beginning to switch and shows regions of non-uniform magnetisation, whereas the bottom Co layer remains fairly uniform, resulting in the angle between the magnetisation of the two layers being below 180°. This deviation from the strictly antiparallel state ultimately results in a lower GMR and could

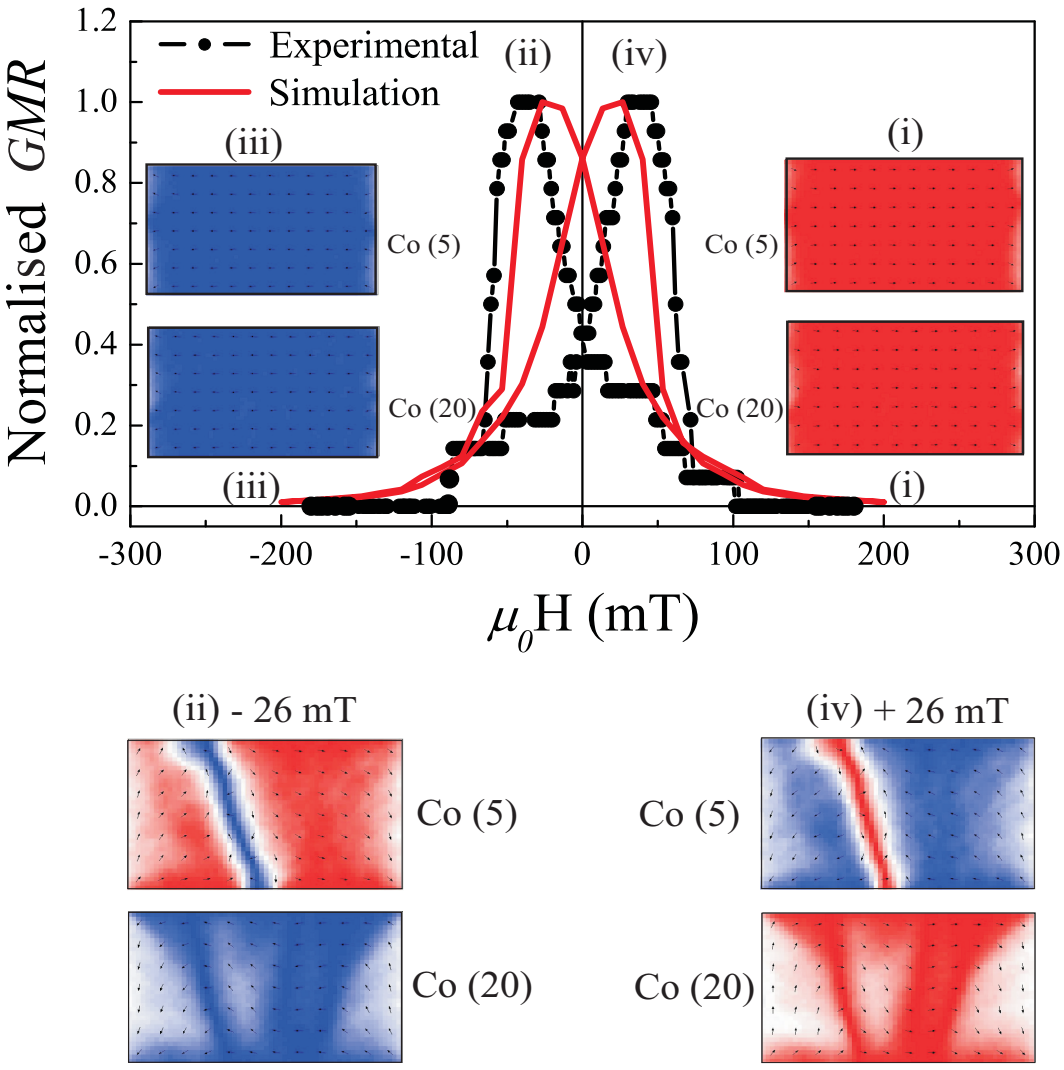

Figure 10.14: Normalised experimental and simulated GMR of a Co(5nm)/ITO(2nm)/Co(20nm) SV structure at room temperature. Labels (i)-(iv) represent specific stages of the GMR loop with respective micromagnetic OOMMF simulations. Stages (i) and (iii) represent the parallel state and therefore low resistance state of the Co layers. Stages (ii) and (iv) show the simulated magnetic configurations of the two Co layers at μ_0H = $\pm$26 mT at the onset of the antiparallel state.

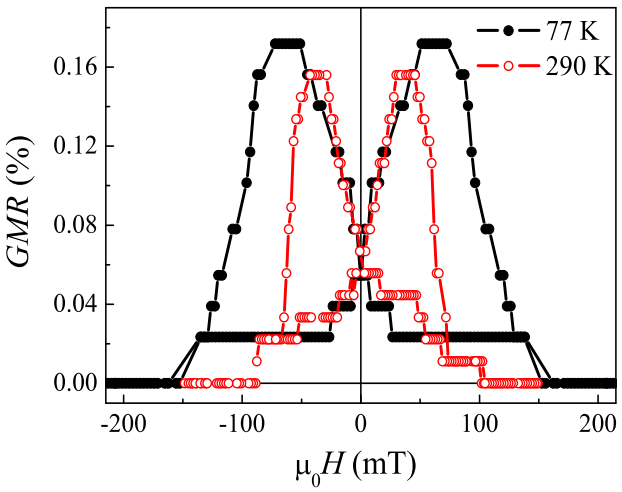

Figure 10.15: GMR curves for a spin valve structure with t= 2 nm at 77 and 290 K.

be a source of uncertainty in our measurements. Larger devices also contribute toward considerable magnetostatic coupling as evident from the orientation of the two layers at zero applied field in Fig. 10.14. The average magnetisation of the top and bottom Co layers are in between 0° and 180°, thus giving rise to an intermediate resistance state. This magnetostatic coupling combined with the non-uniform magnetisation of the FM layers affects sharp switching behaviour at low fields and will influence the shape of the GMR signal.

GMR increased as the temperature decreased from room temperature to 77 K. Furthermore, switching fields have increased with decreasing temperature resulting from the higher coercive fields at low temperatures. Figure 10.15 shows the rise in GMR from 0.16% to 0.18% for a SV structure where t = 2 nm.

Figure 10.16 shows the evolution of the GMR response at room temperature for a selection of devices as the thickness of the ITO spacer layer was increased from 0 to 7 nm. We can see that there is a strong magnetostatic coupling contribution to the GMR signal in all of the devices, but in particular, those with thinner ITO spacer layers. The short, flat region at the point of switching suggests the occurrence of the antiparallel alignment of the FM magnetisations.

AMR is considered a major concern for the majority of spin injection-based experiments [23]. If there was a contribution to the total GMR arising from AMR, then the most likely source would be from the FM Co layers. In order to eliminate the possibility of an AMR contribution from the Co to the total GMR signal measured, SV structures were fabricated with t = 0 nm. Measurements revealed no indication of a GMR or AMR response (Fig. 10.16 (a) - open black circles).

The switching fields in the GMR curves show an interesting variation with the ITO spacer thickness (Fig. 10.17). There is a slight increase in switching field from 1 to

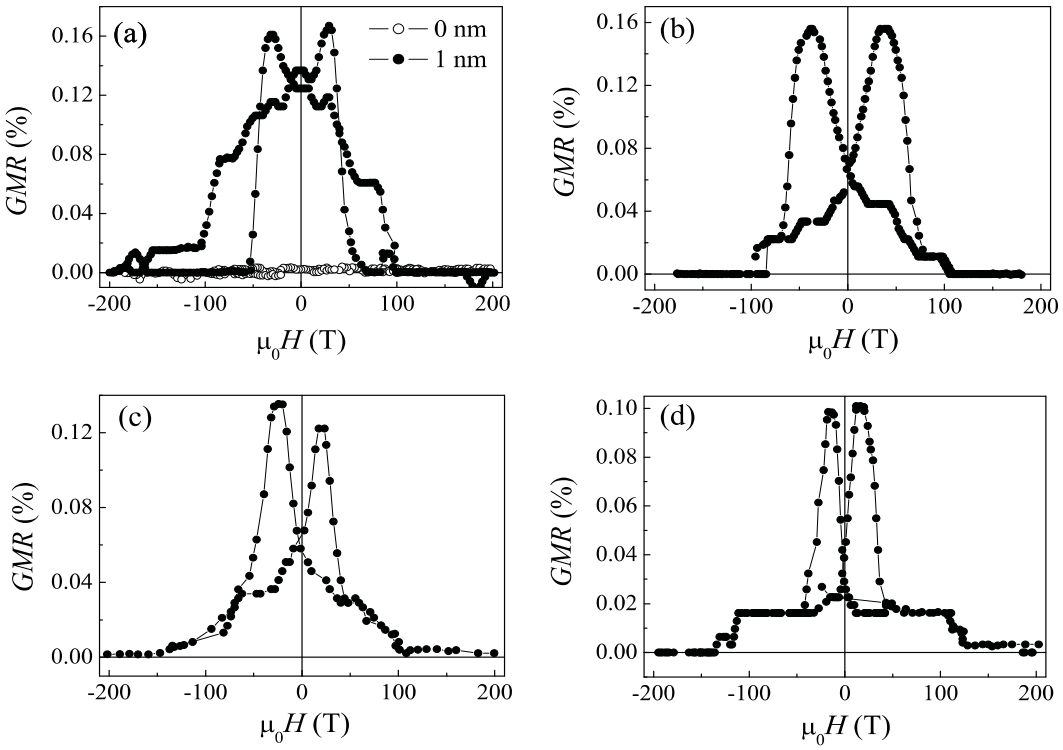

Figure 10.16: Evolution of the GMR response at 290 K as a function of ITO spacer thickness, t, where (a) $t = 1$ nm, (b) $t = 2$ nm, (c) $t = 3$ nm and (d) $t = 7$ nm. The open black circles in (a) shows the GMR response for $t = 0$ nm.

2 nm, after which, we see a gradual fall. This matches the trend seen in the coercive field values extrapolated from the magnetisation loops. Differences are likely to arise due to the physical difference between what is actually being probed. Magnetometry is a volume sensitive measurement and is carried out on unpatterned samples, whereas the magnetotransport properties were performed only after the micromachining had been carried out. Once patterned into a nanoscale structure, it is highly likely that the properties of the materials are going to change to some extent, both from the FIB process (exposure to doses of Ga^+ ions etc) itself and due to the influence of size effects.

No GMR was recorded in the devices for $t \geq 10$ nm, indicating that ${\lambda_{sdl}}^{ITO}$ for semiconducting ITO is less than 10 nm at room temperature. In Fig. 10.18, we plot the ITO thickness dependence of the area product with change in resistance ($A\Delta R$) of all the devices measured at room temperature where it is clearly shown that $A\Delta R$ decays exponentially with t. We compare this data to a simplified CPP-VF model [1] from which we estimate ${\lambda_{sdl}}^{ITO}$. This method also provides quantitative information regarding the spin asymmetry ratio, α, of bulk Co. We have assumed infinitely thick Co layers (assuming an upper limit of ${\lambda_{sdl}}^{Co} \approx 50$ nm at room temperature [24]) and for simplicity, did not include any Co/ITO interfacial resistances. t was expected to vary between $t < {\lambda_{sdl}}^{ITO}$ and $t \approx {\lambda_{sdl}}^{ITO}$. The VF equation was solved without any assumptions on t, and read as

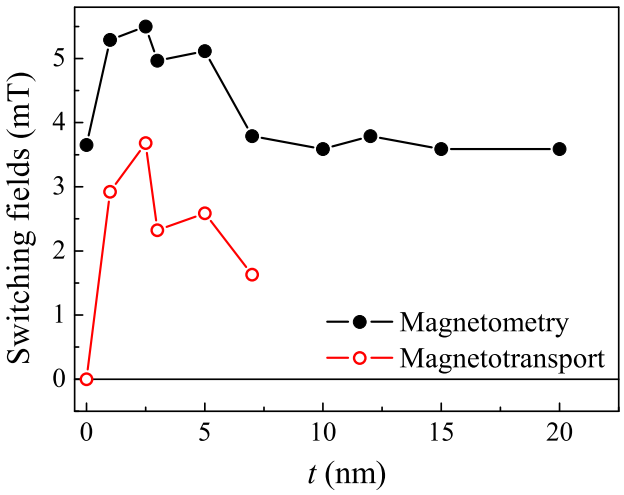

Figure 10.17: Switching fields extrapolated from magnetometry (solid black circles) and magnetotransport measurements (open red circles) at room temperature.

$$A\Delta R = \frac{4\alpha_{Co}^2 \rho_{ITO} \lambda_{sdl}^{ITO}}{\left[1 + \frac{\rho_{ITO}\lambda_{sdl}^{ITO}}{\rho_{Co}^{*}\lambda_{sdl}^{Co}}\right] \sinh\left(\frac{L}{\lambda_{sdl}^{ITO}}\right) + \frac{2\rho_{ITO}\lambda_{sdl}^{ITO}}{\rho_{Co}^{*}\lambda_{sdl}^{Co}} \cosh\left(\frac{L}{\lambda_{sdl}^{Co}}\right)} \tag{10.1}$$

where Co ${\rho_{Co}}^{*} = \rho_{Co}/$ (1-α^2) represents the normalised resistivity of Co [1] and L is the length of the active region Co/ITO/Co. The resistivity values employed were $\rho_{Co} = 63$ nΩm and $\rho_{ITO} = 10$ $\mu\Omega$m (measured from 200 nm thick films deposited in identical conditions). This resulted in $\alpha_{Co} = 0.55$. This value for α_{Co} required to fit the data is relatively small compared to those values found in the literature [7]. Using Eqn. 10.1, fits assuming different values for ${\lambda_{sdl}}^{ITO}$ (5 - 7 nm) have been performed. For low values of t the simulated curve with ${\lambda_{sdl}}^{ITO} = 7$ nm fits well while at higher values of t the curve corresponding to ${\lambda_{sdl}}^{ITO} = 5$ nm serves to describe the data better. This leads us to propose that ${\lambda_{sdl}}^{ITO}$ at room temperature is 6$\pm$1 nm.

From LAR measurements, we are confident that the quality of the Co/ITO interfaces are reasonable. However, we cannot completely exclude the possibility of interdiffusion at the interfaces which can result in additional electron scattering centers and should be accounted for in the calculations for ${\lambda_{sdl}}^{ITO}$. In fact, we know from the investigations described in chapter 8 that a magnetic dead layer may exist at the interface between Co and ITO. The introduction of impurities within the NM ITO spacer will shorten the mean free path of the charge carriers as well as shorten the spin-flip time via spin-orbit scattering. This will ultimately lead to λ_{sdl} diminishing rapidly.

In chapter 4 it is shown that the temperature at which ITO is grown can affect its morphology and structure, in particular the average grain size. θ-2θ x-ray studies

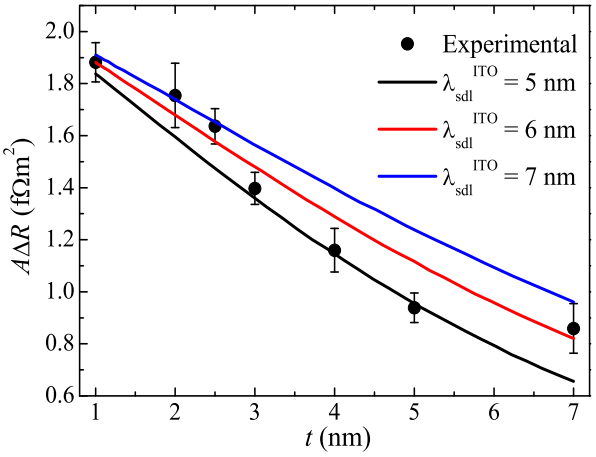

Figure 10.18: Compiled results for a series of Co/ITO/Co SV nanopillar devices at room temperature. The solid lines represent fits using the VF model.

show that ITO is amorphous on top of layers of Cu and Co, and so a smaller grain size and greater density of defects and grain boundaries is highly likely. This, for now, is unavoidable when using the sputtering set-up here. The application of heat during the deposition process is likely to cause many complications (interdiffusion, increased roughness profiles of initial Cu and Co layers, *etc*). Perhaps the rather modest GMR and estimation for the spin diffusion length of ITO is indicative of the critical role that interdiffusion of magnetic impurities in the NM ITO spacer layer, as well as the ITO microstructure, may have in spin depolarisation.

A further drawback is possibly related to the injection from a FM metal electrode (Co). When using FM transition metal electrodes the problem of resistance mismatch, which is responsible for severe depolarisation at the interface, has to be faced [25] leading to a resistance build-up at the interfaces. The result of this interface resistance is that the spin accumulation acts as a "bottle neck" for carrier injection, as a consequence of the fact that the spin carriers are also charge carriers [8]. Here, the interfacial resistance between Co and ITO has also been neglected. We justify this assumption on the basis that all the sample structures were prepared simultaneously *in situ*. However, the large resistivity mismatch between Co and ITO is ultimately an issue and the model needs to be developed further to account for this.

Furthermore, due to the formation of regions where there is an inhomogeneous distribution of the magnetisation within the fixed FM Co layer, the size of the devices is likely to have had a significant influence on the size of the GMR measured and $\lambda_{sdl}{}^{ITO}$ estimated.

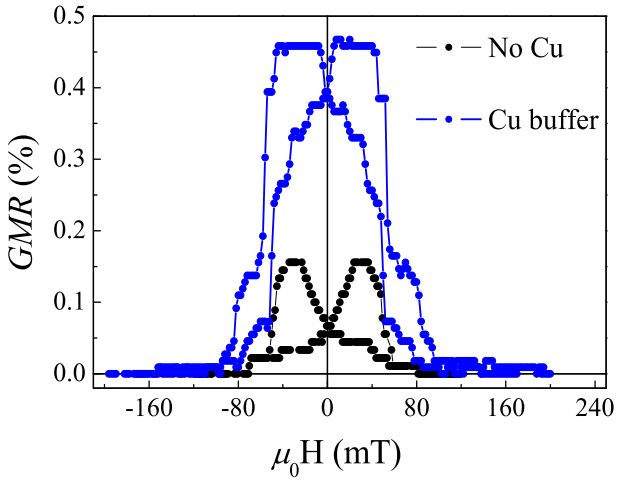

Figure 10.19: Room temperature GMR curves for a spin valve where $t = 2$ nm with (blue) and without (black) a 1 nm Cu buffer layer inserted at each Co/ITO interface.

10.6.2 Insertion of Cu buffer layers

A series of Cu(200nm)/Co(20nm)/Cu(1nm)/ITO(2nm)/Cu(1nm)/Co(5nm)/Cu(200nm) SV structures were prepared in much the same way as the spin valves discussed above.

Figure 10.19 shows the GMR curve for an as-deposited Cu buffered SV with $t = 2$ nm at room temperature along with the corresponding SV without the 1 nm Cu buffer layer inserted (from section 10.6.1). It is clear that the addition of the Cu buffer layer results in a significant increase in the room temperature GMR from approximately 0.16% in the case of the SV without the Cu buffer to 0.47% once the Cu buffer had been added. This is concurrent with the findings for the multilayers in chapter 9 in the as-deposited state where an immediate improvement to the GMR was observed once a Cu buffer layer had been inserted at each and every Co/ITO interface. This behaviour was attributed to possible interfacial doping at the Co/Cu interface and the prevention of stray Co scattering centres diffusing into the ITO spacer layer.

The stability of the spin valve devices was tested by monitoring its behavior over a range of applied DC bias currents. A DC bias current was switched on and held constant for 20 minutes and then turned off back to zero, after which the measurement commenced. The spin valve structures were stable even up to DC bias currents of ± 5 mA. In fact, the only changes observed were in the switching fields. Fig. 10.20 shows the linear dependence of the GMR switching field as a function of applied DC current. These values were extrapolated from minor loop measurements of the device between ± 5 mA. The behaviour of the switching field with current can be explained by considering an induced Oersted field on application of the current. The Oersted field should cancel each other out within the nanopillar junction. However, sometimes a remanent component may remain causing a shift in the switching fields [26].

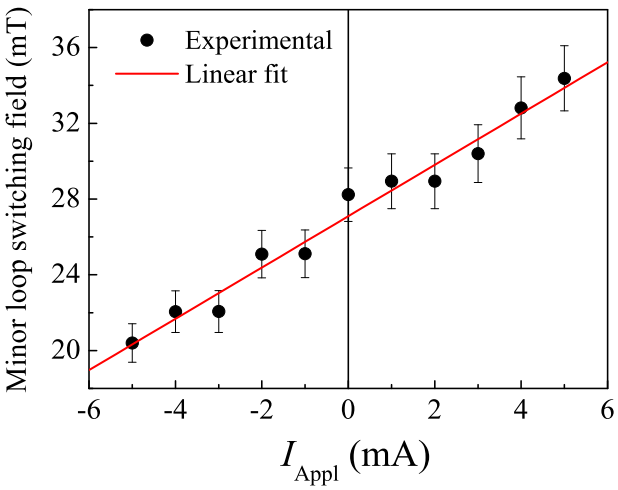

Figure 10.20: Linear dependence of the switching field as a function of the DC bias current.

With the intention of repeating what had been observed in the Cu buffered multilayer stacks (chapter 9), we also made an attempt to anneal these spin valve structures. Annealing was carried out via two avenues; (1) prior to the photolithography stage and (2) after the FIB patterning process, neither of which proved to be successful. Annealing before the photolithography stage resulted in poor mask contact due to the rising levels of surface roughness of the top Cu electrodes. Annealing post-photolithography and machining led to the extreme oxidation of the nanopillar structure so that the device resistance was now far too high to measure.

10.6.3 Spin valves with DMO electrodes : Preliminary results

It has been made very clear that the interest in spin injection through semiconducting materials stems from the fact that they are extremely versatile in terms of doping, microstructure, optical tuning, bipolar transport and above all, due to their ease-of-integration with conventional electronics.

Some of the potential problems associated with the Co/ITO/Co SV nanopillars have been discussed in section 10.6.1. An alternative option could be the replacement of the FM metal Co electrodes with a FM oxide like the Co-doped ITO materials developed in earlier chapters. Immediate advantages of doing this are the likelihood of favourable band alignment and low resistivity mismatch. Two routes were taken to investigate the possibility of carrying this out:

1. *In situ* shadow masking to make Co(5 at.%):ITO(200)/ITO(2)/Co(5)/Au(200) SVs on *r*-plane sapphire substrates (all thicknesses are in nm); (set A).

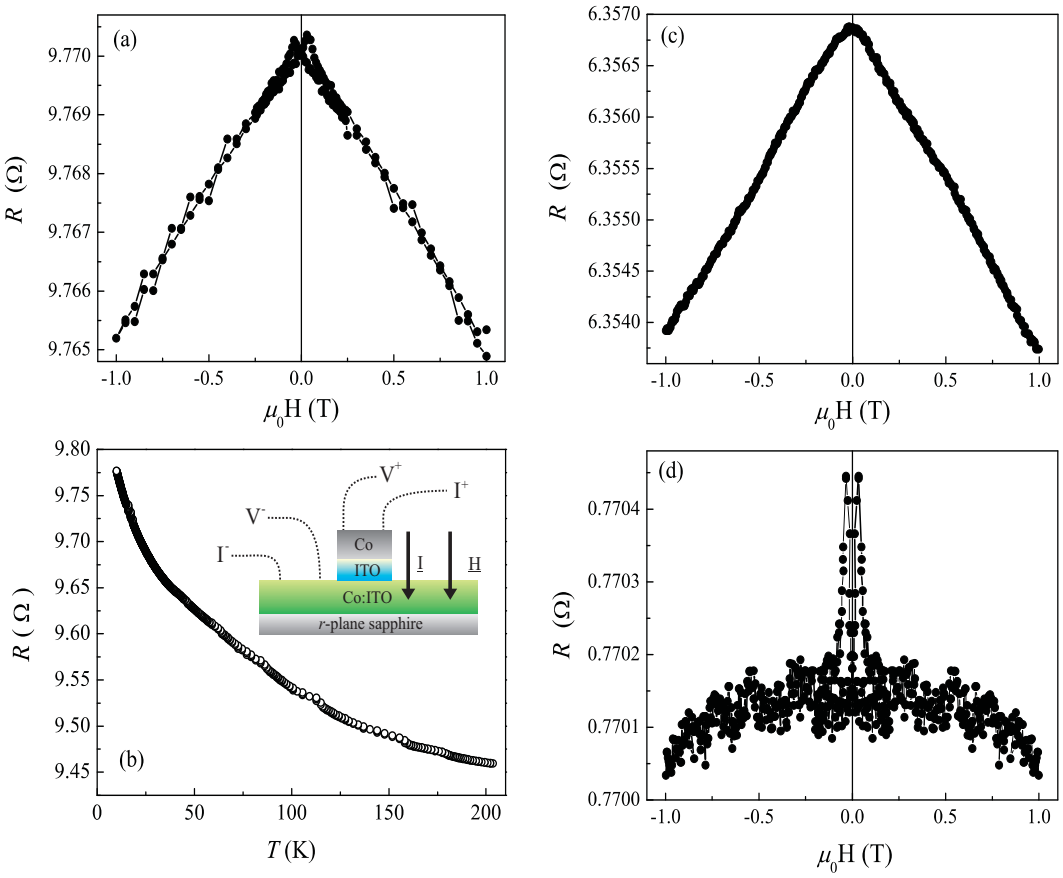

Figure 10.21: R versus μ_0H curves at 10 K for set A SV structures (with junction area of approximately 80 μm^2) for the entire device (a), bottom (c) and top (d) electrodes respectively measured using the configuration shown in the inset of (b). Resistance versus temperature variation is shown in (b) also measured using the same configuration shown in the inset. All measurements were made using $I \parallel \mu_0 H$.

2. FIB machined nanopillars of Cu(200)/Co(5 at.%):ITO(200)/ITO(2)/Co(5)/Cu(200) SVs onto SiO_2/Si substrates (all thicknesses are in nm); (set B).

Both routes involved using growth procedures very similar to those described in earlier sections of the thesis.

The compatibility of the growth conditions of the different elements is a key issue. From chapter 5 (section 5.6.5) we know that to obtain room temperature ferromagnetism in Co:ITO we require heater temperatures ≥ 300°C. Each of the other layers can be grown at room temperature. However, we also know that the crystalline quality and electrical properties of ITO are heavily affected by its growth temperature. To avoid interdiffusion between the two initial ITO-based layers no heat was applied after the deposition of the initial FM oxide electrode, i.e. the FM oxide was always the designated bottom FM electrode (first layer to be deposited).

Figure 10.21 shows representative R versus μ_0H measurements of a sample from set A with the applied current (I) flowing in a direction parallel to the applied magnetic field ($I \parallel \mu_0 H$) at 10 K along with device resistance as a function of temperature. The device resistance shows semiconducting-like properties [Fig. 10.21 (b)] as a function of temperature suggesting that the current is flowing through the entire device.

Emerging from the reversible negative magnetoresistance, there is a clear sign of spin valve hysteresis with two maxima symmetric either side of zero field [Fig. 10.21 (a)]. In order to better explore the origins of this magnetoreistance, similar measurements were carried out on the upper and lower electrodes at 10 K [Fig. 10.21 (c) and (d)]. The bottom Co:ITO electrode shows a weak negative MR with no hysteresis as we have seen in previous chapters, but the top Co electrode exhibits evident hysteresis. The hysteresis displayed in Fig. 10.21 (a) unfortunately cannot be unambiguously attributed to charge carriers through the ITO maintaining their spin polarisation. The switching fields of the curves showing hysteresis [Figs. 10.21 (a) and (d)] are identical and we therefore attribute the origins of this behaviour to a series contribution from top and bottom electrodes.

The results obtained from the FIB devices (set B) were also not so fruitful. The first major issue was the growth of Co:ITO on top of Cu which may cause many undesirable microstructural problems. The second was the FIB machining of thick oxide layers. This is likely to cause significant changes in the material properties. We have not addressed this issue in detail here, however has been investigated for LSMO films [27]. Depending on the radiation dosage, both the electrical and magnetic properties are at risk of becoming affected. Note that this will also apply to the ITO spacer layer used in the Co/ITO/Co SVs described in section 10.6.1. Figure 10.22 shows a typical R versus μ_0H curve at 10 K for a FIB machined SV. The changes in R as a function of applied magnetic field are very different to that of the larger devices from set A. Here we see a shift from negative to positive GMR at applied magnetic fields greater than 60 mT. Negative MR is an intrinsic property of the Co:ITO films grown when heated. The emergence of a positive contribution may be due to the damage caused by exposure to

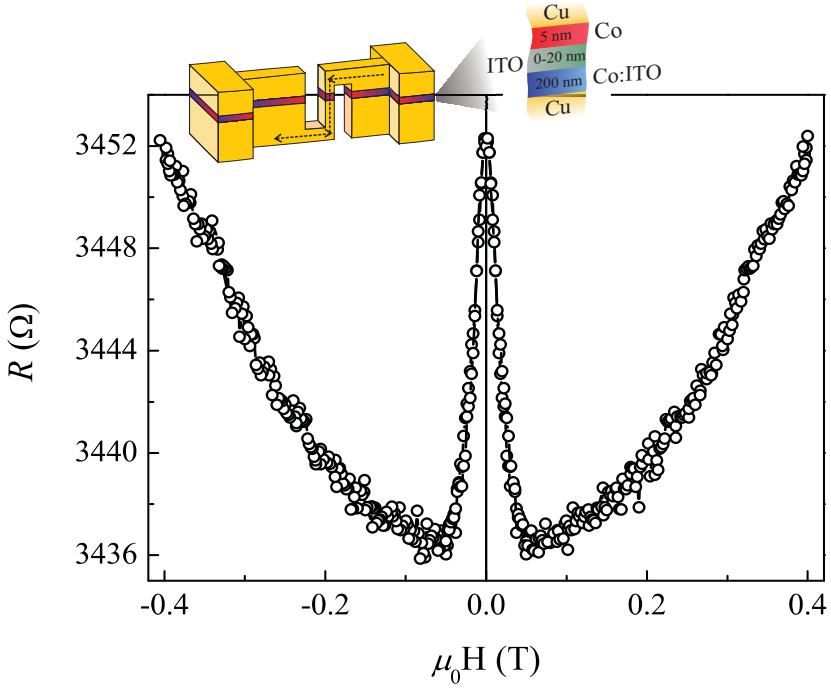

Figure 10.22: CPP R versus μ_0H measurement of a set B nanopillar device (with junction area of approximately 600 × 400 nm^2) at 10 K.

Ga ions during the FIB process. In addition, the size of the devices is likely to have a significant influence on the characteristic R versus μ_0H behaviour: the CPP- pillar GMR contribution will be much larger in the smaller devices. In the larger devices it is likely that we are only taking a measurement of the in-plane MR of the individual FM electrodes and not a genuine CPP effect.

10.7 Summary and Conclusions

Sub-micron spin valve devices with a range of semiconducting ITO spacer thickness have been fabricated and current-perpendicular to plane GMR measurements have been performed. Using a simplified VF model an estimate of the spin diffusion length of semiconducting ITO at room temperature of 6±1 nm has been made. The spin diffusion length of ITO may be improved by optimising its structural quality and physical properties. The addition of a 1 nm Cu buffer layer at each Co/ITO interface led to a significant rise in the room temperature GMR signal.

This work has taken a step toward realising transparent spintronics with the demonstration that spin polarised information can be injected and detected through ITO. However, once spin transport in ITO is fully explored and its limits identified, a full-crystalline oxide spin-injection device will be the ultimate target.

Our preliminary experiments where the metal FM Co electrodes were replaced by

the Co:ITO DMO were largely unsuccessful. The development of such devices are still in their infancy with many hurdles yet to be met, let alone overcome. The FIB process needs to optimised, especially parameters such as the Ga ion exposure time and dosage.

Bibliography

[1] T. Valet and A. Fert, Phys. Rev. B 48, 7099, (1993)

[2] Q. Wen, Y. Song, Q. Yang, H. Zhang, Rare Met. Mater. Eng. 25, 536, (2006).

[3] B. Dieny, V.S. Speriosu, S.S.P. Parkin, B.A. Gurney, D.R. Wilhoit and D. Mauri, Phys. Rev. B 43, 1297-1300, (1991).

[4] J. Bass and W. P. Pratt Jr., J. Magn. Magn. Mater. 200, 274, (1999).

[5] C. Chappert, A. Fert, F. Nguyen Van Dau, Nature Mater. 6, 813, (2007).

[6] D. J. Kubinski and H. Holloway, J. Appl. Phys. 79, 7395, (1996).

[7] C. W. Leung, C. Bell, G. Burnell, M. G. Blamire, Phys. Rev. B 72, 212409, (2005).

[8] I. Pallecchi, L. Pellegrino, N. Banerjee, M. Cantoni, A. Gadaleta, A. S. Siri, D. Marre, Phys. Rev. B 81, 165311, (2010).

[9] S. Ghosh, V. Sih, W. H. Lau, D. D. Awschalom, S.Y. Bae, S. Wang, S. Vaidya, G. Chapline, Appl. Phys. Lett. 86, 232507, (2005).

[10] FEI Company, *Focused Ion Beam Workstation Reference Guide*, (1996).

[11] S. Reyntjens and R. Puers, Journal Of Micromechanics And Microengineering, 11(4):287-300, (2001).

[12] J. W. A. Robinson, PhD Thesis, Zero to Pi Oscillations in Ferromagnetic Josephson Junctions, University of Cambridge, (2007).

[13] W. M. Kaminsky, G. A. C. Jones, N. K. Patel, W. E. Booij, M. G. Blamire, S. M. Gardiner, Y. B. Xu, J. A. C. Bland, Appl. Phys. Lett. 78, 1589, (2001)

[14] C. Bell, PhD Thesis, Nanoscale Josephson Junctions, University of Cambridge, (2004).

[15] C. Bell, G. Burnell, D-J. Kang, R. H. Hadfield, M. J. Kappers, M. G. Blamire, Nanotechnology, 14(6):630-632, (2003).

[16] E. Y. Tsymbal, Appl. Phys. Lett. 77, 17, (2000)

[17] D. Ozkaya, R. M. Langford, W. L. Chan, A. K. Petford-Long, J. Appl. Phys. 91, 9937, (2002).

[18] G. Xiong, D. A. Allwood, M. D. Cooke, R. P. Cowburn, Appl. Phys. Lett. 79, 3461, (2001).

[19] M. C. Wu, A. Aziz, J. D. S. Witt, M. C. Hickey, M. Ali, C. H. Marrows, B. J. Hickey, M. G. Blamire, Nanotech. 19, 485305, (2008).

[20] See, http://math.nist.gov/oommf, Version 1.2.0.4 of the software was used.

[21] S. H. Lim, S. H. Han, K. H. Shin, and H. J. Kim, J. Magn. Magn. Mater. 223, 192, (2001)

[22] S. Bedanta, E. Kentzinger, O. Petracic, W. Kleemann, U. Rcker, T. Brckel, A. Paul, S. Cardoso, and P. P. Freitas, Phys. Rev. B 74, 054426, (2006).

[23] Y. Ji, A. Hoffmann, J. S. Jiang, S. D. Bader, Appl. Phys. Lett. 85, 6218, (2004).

[24] L. Piraux, S. Dubois, A. Fert, and L. Belliard, Eur. Phys. J. B 4, 413, (1998).

[25] A. Fert, H. Jaffres, Phys. Rev. B 64, 184420, (2001).

[26] N. Banerjee, A. Aziz, M. Ali, J. W. A. Robinson, B. J. Hickey, M. G. Blamire, Phys. Rev. B. 82, 224402, (2010).

[27] I. Pallecchi, L. Pellegrino, E. Bellingeri, A. S. Siri, D. Marre, G. C. Gazzadi, J. Magn. Magn. Mater. 320, 1945, (2008).

Chapter 11

Summary and Conclusions

This dissertation provides a detailed and systematic study into the investigation of using In_2O_3 and ITO based materials for next generation spintronic applications. This was approached by first developing the In_2O_3 and ITO oxides and later a functional dilute magnetic oxide system. Thereafter, ITO was incorporated into device-like structures and tested for its efficiency as both a medium for spin polarised information to move through, but also as a spin injector.

The major findings of this comprehensive study are summarised in the following points:

1. A DMO has been developed using transparent and conducting Co-doped In_2O_3 and ITO thin films with a ferromagnetic Curie temperature in excess of room temperature (approximately 500 K).

2. XMCD and O-MCD exploration indicates that the Co dopants alone are not the sole source of ferromagnetism in these materials. In fact, the Co dopants in dilute form give a strictly paramagnetic response suggesting that the magnetism observed may be a result of polarised electrons in localised donor states within the host In_2O_3 and ITO oxide, most likely related to oxygen vacancy defect states. Therefore, the origins of magnetism in these films is related to a hybridisation and charge transfer of electrons from a broad donor/defect-derived impurity band to a band of unoccupied $3d$ states at the Fermi level. However, we are unable to determine the location of these donor states - they may be distributed evenly through the material or concentrated at the grain boundaries.

3. A unified theory capable of explaining the magnetic behaviour of the DMO systems still eludes us. It appears from our experimental results and those of others that different doped magnetic oxides may have different underlying mechanisms leading to the observed ferromagnetism. There may even be several competing ferromagnetic mechanisms at play in these DMO materials.

4. Co/ITO multilayers exhibited low GMR persisting to room temperature. Both the magnetoresistance and magnetisation saturation field oscillate with the ITO

spacer layer thickness consistent with RKKY interaction throughout the structure. From our magnetic modelling we believe that a significant portion of the magnetic and magnetotransport properties were a result of a superparamagnetic contribution. These superparamagnetic regions may be due to intermixing at the Co/ITO interfaces leading to stray Co particles within the ITO spacer layers. This highlights the importance of the quality of the interfaces between the layers in multilayer stacks and metal-oxide heterostructures.

5. Insertion of a 1 nm Cu buffer layer at each Co/ITO interface leads to an immediate rise in GMR. This is likely to be due to interfacial-doping at the Co/Cu interface. Upon annealing, GMR was found to increase as it is believed that a graded interface between the Cu and ITO has formed, hence reducing the burden of a high Fermi surface mismatch. Further annealing at higher temperatures led to a reduction in GMR, possibly due to enhanced atom mobility and interfacial mixing.

6. Further evidence of efficient spin transport through ITO at room temperature was provided by the estimation of a spin diffusion length in ITO of 6±1 nm using CPP-GMR measurements of Co/ITO/Co nanopillar junctions.

Overall, this research shows that ITO is a candidate material for transparent spintronics. This new level of understanding opens up the possibility of creating an all-oxide device.

Chapter 12

Future Directions and Outlook

12.1 TEM study of the DMO

There is a need for more detailed atomic characterisation on the dopant distribution and chemical states in the DMO systems. More extensive use of techniques such as high resolution TEM combined with element specific sensitive detection, e.g. electron energy loss spectroscopy, would be ideal and would complement characterisation using the synchrotron based techniques. High-resolution cross-sectional TEM on these samples would improve our knowledge of the material, and possibly help to put the argument about the possible presence of Co metal clustering to bed once and for all. These studies must take into account the observations made on various length scales, because even in the cases of clustered dopant samples, local TEM may look deceptively good. In chapter 5, preferential Co clustering close to the substrate/film interface was discussed. This would certainly be an area of interest. A combination of these techniques with the synchrotron and magneto-optical based methods could bring far greater clarity on the issues of importance in the field.

12.2 Photomagnetic effect

Recently, photoinduced magnetisation in various materials has been the focus of much attention [1–3], where ferromagnetism is induced or enhanced by the interaction with the incident light.

I have carried out some preliminary measurements investigating the photoconductive properties of pure In_2O_3 and ITO(10) thin films, i.e. the influence of light of various wavelengths on the electrical properties of the material. It was found that those films which were more insulating were more susceptible to changes in conductivity when exposed to different wavelengths of light. Figure 13.1 shows the conductivity gain (%) as a function of the wavelength of light for pure In_2O_3 which had been grown at 300°C and in relatively high levels of oxygen (0.20 Pa). It is clear that in each case, when the sample is exposed to light, the conductive properties of the sample improve and is

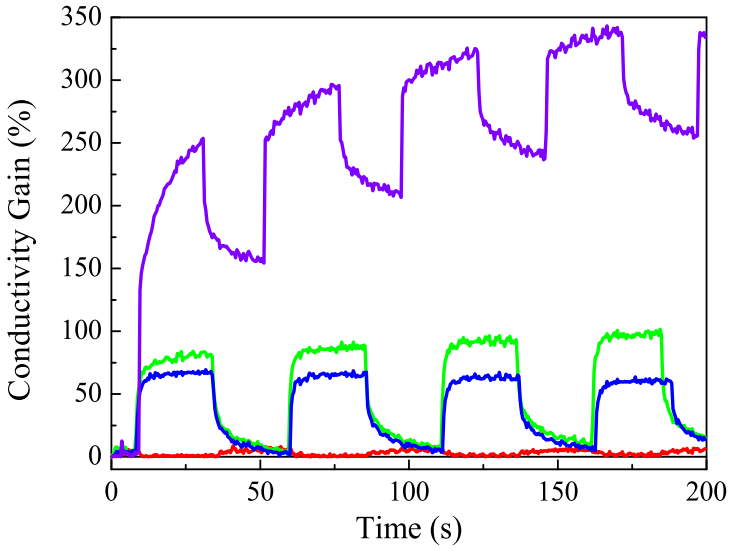

Figure 12.1: Photoconductive properties for pure In_2O_3 thin films grown at 300°C and 0.20 Pa of oxygen. The conductivity gain (%) is given as a function of the wavelength of light [Red (650 nm), Green (510 nm), Blue (475 nm) and ultraviolet (400 nm)].

likely to be related to photoexcitation of electron carriers. The largest effects are seen in those films exposed to ultraviolet light.

An interesting advance could be to investigate the influence that this may have on the magnetic properties of the films. Evidence described in earlier chapters suggested that there may be a correlation between the carrier concentration and the ferromagnetic response in our samples. Therefore, such an experiment may yield some interesting results, in particular, using the Co-doped In_2O_3 samples as these are far more insulating than those which have additional Sn doping. The measurements would involve monitoring the carrier concentration and ferromagnetic response before and after exposure to light. However, one problem which is evident from Fig. 13.1 is the time for the electrical resistance to return back to its original value after light exposure (relaxation time). Therefore, when performing these measurements it is first necessary to determine the relaxation time of the films for the particular wavelengths of light. This investigation may lead to a material with dynamic "on/off" control of the ferromagnetism.

12.3 Metal/ITO interfaces

This work has highlighted the importance of the interface between metal and oxide surfaces. The major issue of the presence of isolated SPM regions in the vicinity of the Co/ITO interface has been discussed but have not been located. More detailed

structural characterisation using high resolution TEM would certainly prove useful and would also provide information on the quality of the interfaces and the level of interdiffusion. Neutron diffraction studies may also be able to shed some light on the magnetic structure of the multilayers as we argue that the magnetic frustration is a result of multiple magnetic contributions. Perhaps the presence of Cu buffer layers not only has an influence on the structural properties of the multilayers but also the magnetic properties. If this is the case, then neutron diffraction studies may help to explain the behaviour in these samples.

12.4 Functional *all-oxide* device

The development of an all-oxide device which exploits both the conducting and magnetic nature of the Co:ITO DMO is still very much in its infancy. One of the major areas which is still in need of some serious development is that of the FIB processing of the oxide itself. A worthwhile future investigation should use the work of Pallecchi *et al.* [4] as a guideline for the systematic study of the effects of FIB radiation dosage on the electrical and magnetic properties of the pure and TM-doped ITO films.

Perhaps if there are still problems arising in obtaining genuine spin valve behaviour in these all-oxide devices, then the first question to be asked could be whether the Co:ITO is an efficient spin polariser at all. Therefore, it would be useful to try and quantify the magnitude of the spin polarisation of the Co:ITO DMO materials using Point Contact Andreev Reflection, similar to the study by Panguluri *et al.* [5]. If this can be quantified reliably then it may still be worth pursuing this material for future development.

Bibliography

[1] J. Fernandez-Rossier, C. Piermarocchi, P. Chen, A. H. MacDonald, L. J. Sham, Phys. Rev. Lett., 93, 127201, (2004).

[2] S. Mishra, G. S. Tripathi, S. Satpathy, Phys. Rev. B. 77, 125216, (2008).

[3] J. S. Bettinger, R. V. Chopdekar, Y. Suzuki, Appl. Phys. Lett., 94, 072505, (2009).

[4] I. Pallecchi, L. Pellegrino, E. Bellingeri, A. S. Siri, D. Marre, G. C. Gazzadi, J. Magn. Magn. Mater. 320, 1945, (2008).

[5] R. P. Panguluri, P. Kharel, C. Subdakar, R. Naik, R. Suranarayanan, V. M. Naik, A. G. Petukhov, B. Nadgorny, G. Lawes, Phys. Rev. B 79, 165208, (2009).

Appendix A

Abbreviations, Symbols & Physical constants

Abbreviations

AFM	Atomic force microscopy
AHE	Anomalous Hall effect
AMR	Anisotropic magnetoresistance
BMP	Bound Magnetic Polaron
CIP	Current in-plane
CPP	Current perpendicular-to-the-plane
DMO	Dilute magnetic oxide
DMS	Dilute magnetic semiconductor
FIB	Focused Ion Beam
FM	Ferromagnet
FY	Fluorescence yield
GMR	Giant magnetoresistance
ITO	Indium Tin Oxide
LAR	Low-angle X-ray reflectivity
MCD	Magnetic circular dichroism
MDL	Magnetic dead layer
MR	Magnetoresistance
NM	Non-magnetic
OHE	Ordinary Hall effect
O-MCD	Optical magnetic circular dichroism
OOMMF	Object Oriented Micromagnetic Framework
PLD	Pulsed laser deposition
RKKY	Rudeman-Kittel-Kasuya-Yosida
SPM	Superparamagnetic
SQUID	Superconducting quantum interference device
SV	Spin valve
TCO	Transparent conducting oxide
TCR	Temperature coefficient of resistance
TEY	Total electron yield
TM	Transition metal
UHV	Ultra high vacuum
VF	Valet-Fert
VSM	Vibrating sample magnetometer
XAS	X-ray absorption spectroscopy
XMCD	X-ray magnetic circular dichroism
XRD	X-ray diffraction

Constants

A	Area
g	Lande g factor
C	Curie constant
H	Applied magnetic field
H_c	Coercive field
I	Current
m^*	Effective mass of a charge carrier
m_s	Saturation magnetisation
m_r	Remanent magnetisation
N	Number of bilayer repeats
n_c	Carrier concentration
n_s	Sheet carrier concentration
q	charge
R	Resistance
R_s	Sheet resistance
T	Temperature
T_C	Ferromagnetic Curie temperature
T_B	Superparamagnetic blocking temperature
V_H	Hall voltage
V_0	Oxygen vacancy
χ	Magnetic susceptibility
β	Spin asymmetry ratio
λ_s	Spin diffusion length
μ_H	Carrier mobility
μ_L	Orbital moment
μ_S	Spin moment
$\tilde{n}$	Refractive index
ϕ_b	Grain boundary potential barrier
ρ	Resistivity
ρ_{xy}	Hall resistivity
ρ_+ / ρ_-	Right/Left circularly polarised light/X-rays
σ	Conductivity
θ	Curie-Weiss temperature

Physical constants

Boltzmann constant	k_B	$1{\times}38 \times 10^{-23}$ J K^{-1}
Bohr magneton	μ_B	9.27×10^{-24} J T^{-1}
Electron charge	q	1.602×10^{19} C
Electron mass	m_e	9.11×10^{-31} kg
Electron volt	eV	1.602×10^{-19} J
Permeability of vacuum	μ_0	$4\pi \times 10^{-7}$ H m^{-1}
Planck constant	h	6.63×10^{-34} J s
Reduced Planck constant	$\hbar$	1.05×10^{-34} J s

Appendix B

Published articles